

Effectiveness of Geotextiles/ Geogrids in Roadway Construction; Determine a Granular Equivalent (GE) Factor

Vernon R. Schaefer, Principal Investigator
Institute of Transportation
Iowa State University

NOVEMBER 2021

Research Project
Final Report 2021-26



To request this document in an alternative format, such as braille or large print, call [651-366-4718](tel:651-366-4718) or [1-800-657-3774](tel:1-800-657-3774) (Greater Minnesota) or email your request to ADArequest.dot@state.mn.us. Please request at least one week in advance.

Technical Report Documentation Page

1. Report No. MN 2021-26	2.	3. Recipients Accession No.	
4. Title and Subtitle Effectiveness of Geotextiles/Geogrids in Roadway Construction; Determine a Granular Equivalent (GE) Factor		5. Report Date November 2021	
		6.	
7. Author(s) Hossein Alimohammdi, Vernon R. Schaefer, Junxing Zheng, Charles T. Jahren, Guangfan Zheng, and David White		8. Performing Organization Report No.	
9. Performing Organization Name and Address Institute for Transportation Iowa State University Ames, IA 50011		10. Project/Task/Work Unit No.	
		11. Contract (C) or Grant (G) No. (c) 1034932	
12. Sponsoring Organization Name and Address Minnesota Department of Transportation Office of Research & Innovation 395 John Ireland Boulevard, MS 330 St. Paul, MN 55155-1899		13. Type of Report and Period Covered Final report	
		14. Sponsoring Agency Code	
15. Supplementary Notes https://www.mndot.gov/research/reports/2021/202126.pdf https://www.mndot.gov/research/reports/2021/202126A.pdf			
16. Abstract (Limit: 250 words) Geogrids have been widely used in roadway construction as reinforcement in pavement foundations. Geogrids have been effective in practice for reducing rutting damage, distributing traffic loads within the pavement foundation layers, increasing the resilient modulus of the base course, and stabilizing the subgrade layer. For this project, an integrated mobile accelerated test system (IMAS), an automated plate load test (APLT) device, and finite element simulation approaches were used to evaluate the effects of geogrid reinforcement. Test configurations were constructed by varying geogrid types (i.e., light-duty biaxial, heavy-duty biaxial, light-duty triaxial, and heavy-duty triaxial), geogrid locations in the base course (i.e., at the interface between the base and the subgrade or in the base course), and base aggregate thicknesses (6, 10, and 16 in) in the laboratory and in experimental field tests. The finite element method (FEM) models were calibrated based on the results from the experimental test sections. Then, the calibrated FEM models were used to determine granular equivalent (GE) values for the remaining sections. Testing results included resilient modulus, deflection, and permanent deformation of the pavement foundation to evaluate the structural benefits of geogrids as a function of the GE. The results of this research revealed that improvement in pavement performance using geosynthetic reinforcement depended on various factors and variables. A new formulation was proposed to predict the GE factor of geogrid reinforcement of flexible pavements. The products produced by this research include this report, which improves geogrid understanding, and a well-developed method to apply GE factors during pavement design. It is expected that one or more of the following benefits will be achieved during implementation: increased service life, reduced gravel and/or asphalt thickness, and reduced maintenance costs.			
17. Document Analysis/Descriptors Reinforcement (Engineering), Geogrids, Geosynthetics, Geotextiles, Granular bases, Foundations, Road construction, Subgrade (Pavements), Soil stabilization		18. Availability Statement No restrictions. Document available from: National Technical Information Services, Alexandria, Virginia 22312	
19. Security Class (this report) Unclassified	20. Security Class (this page) Unclassified	21. No. of Pages 212	22. Price

Effectiveness of Geotextiles/Geogrids in Roadway Construction; Determine a Granular Equivalent (GE) Factor

FINAL REPORT

Prepared by:

Hossein Alimohammadi, Vernon R. Schaefer, Junxing Zheng, Charles T. Jahren, and Guangfan Zheng
Department of Civil, Construction, and Environmental Engineering and the Institute for Transportation
Iowa State University, Ames, Iowa

David J. White
Ingios Geotechnics, Inc.

November 2021

Published by:

Minnesota Department of Transportation
Office of Research & Innovation
395 John Ireland Boulevard, MS 330
St. Paul, Minnesota 55155-1899

This report represents the results of research conducted by the authors and does not necessarily represent the views or policies of the Minnesota Department of Transportation or Iowa State University. This report does not contain a standard or specified technique.

The authors, the Minnesota Department of Transportation, and Iowa State University do not endorse products or manufacturers. Trade or manufacturers' names appear herein solely because they are considered essential to this report.

ACKNOWLEDGMENTS

The research team would like to thank the Minnesota Local Research Board for funding this project. The assistance of the members of the technical advisory panel is gratefully acknowledged: Terrance Beaudry, Jeff Johnson, Mike McCarty, Blake Nelson, Daniel Sarff, John Siekmeier, Joseph Stadheim, Bruce Tanquist, Joel Ulring, and Raul Velasquez. Early discussions with Jeff Johnson, Mike McCarty, and Dan Sarff helped set the direction of the research efforts. Their comments and suggestions were very helpful. John Siekmeier and Dr. Raul Velasquez provided substantial review of many of the interim task reports, which improved the reports; their suggestions are greatly appreciated.

At Iowa State University, Doug Wood, at the Structural Engineering Research Laboratory within the Civil, Construction and Environmental Engineering Department, provided great assistance with placement of strain gauges on the geogrids and data acquisition of data during the laboratory tests. Sue Stokke of InTrans provided technical editing of the final report and helped to improve the final product.

The field trials in Mankato were facilitated by Mike McCarty, at the city of Mankato. The field test sections were constructed by W. W. Blacktopping of Mankato. The company was very easy to work with and most accommodating in our field-testing efforts

TABLE OF CONTENTS

CHAPTER 1: Introduction, Background, and Literature Review.....	1
1.1 Performance Benefits of Geosynthetic Reinforcement in Flexible Pavements	2
1.2 Research Methodologies for Geosynthetic-Reinforced Pavements	3
1.3 Small- and Large-Scale Laboratory Tests	5
1.3.1 Analysis of Results in the Laboratory Test Database	11
1.4 Review of Full-Scale Field Studies.....	14
1.4.1 Quantifying Pavement Performance with Field Trials	14
1.4.2 Applications of Geosynthetic Reinforcement in Pavements.....	14
1.4.3 Literature Review of Geosynthetic-Reinforced Field Tests	16
1.4.4 Factors Affecting Geosynthetic Reinforcement Benefits	18
1.4.5 Comparison of the Results for Geosynthetic Reinforcement in Flexible Pavements	21
1.5 Summary Discussion of Factors Affecting Geosynthetic Reinforcement	26
CHAPTER 2: Laboratory Tests and RELATED LAB Data	28
2.1 IAMS Equipment	28
2.2 Test Sections, Configurations, Sensors, and Procedures for Performing the Tests	28
2.2.1 Test Sections.....	29
2.2.2 Test and Sensor Configurations.....	31
2.2.3 Loading Pattern	32
2.2.4 Geogrids, Aggregates, and Subgrade Soils	33
2.3 Test Preparation and Sensor Setup	34
2.3.1 Subgrade Preparation	34
2.3.2 Base Layer Preparation	35
2.3.3 Surface Layer Preparation	38
2.3.4 Sensors and Sensor Set-Up Procedure: Selection of the Instrumentation	40

2.3.5 Setting Up Strain Gauges on Geogrids	45
2.4 Results.....	46
2.4.1 Summary Plots.....	46
2.5 Detailed Results	61
2.5.1 Loading Pattern vs. Earth Pressure Cell Data	61
2.5.2 Loading Pattern vs. Strain.....	69
CHAPTER 3: Field Tests and related field Data	84
3.1 Field Test Section Plan and Construction	84
3.2 Introduction.....	84
3.3 Geogrid, Aggregates, and Subgrade Soils	87
3.3.1 Geogrids	87
3.3.2 Base Course Material Properties.....	87
3.4 Project Location and Test Locations	87
3.5 Site Conditions and Images	89
3.6 Automated Plate Load Testing	91
3.7 Performed QC/QA Tests in the Field	93
3.7.1 Light Falling Weight Deflectometer Tests on Top of the Subgrade Layers	93
3.7.2 Intelligent Compaction on Top of Subgrade and Base Layers.....	94
3.7.3 Dynamic Cone Penetrometer Tests on Top of Base layer	95
3.7.4 Sand Cone Compaction Test on Base layer	95
3.8 Summary Plots.....	96
CHAPTER 4: Geogrid Design Criteria.....	128
4.1 Review of Geosynthetic Flexible Pavement Design Methods	128
4.1.1 Introduction.....	128
4.1.2 Historical Reinforced Pavement Design Methods.....	128

4.1.3 Geogrid Design Basics.....	129
4.1.4 AASHTO and Manufacturer’s Design Methodologies and Their Software Descriptions.....	131
4.2 Laboratory and Field Tests Conducted and Their Brief Descriptions	139
4.3 Evaluation of Short-Term GE Factors for Geogrid Reinforced Sections	141
4.4 Evaluating Long-Term GE Factors for Geogrid Reinforcement in Flexible Pavements.....	145
4.5 Finite Element Evaluation of Short-Term GE Factors for Geogrid Reinforced Sections.....	149
4.5.1 Introduction.....	149
4.5.2 Finite Element Modeling	151
4.5.3 Geometry and Mesh Sizes.....	151
4.5.4 Material Input Parameters	152
4.5.5 Interface/Interlocking and Confinement Effect Modeling of Geogrid	153
4.5.6 Calibration of the FE Simulations by Mechanistic-Empirical Approach with IMAS Experimental Tests, Parametric Study	154
4.5.7 Developing GE Factors for Assessing Geogrid Reinforcement in Flexible Pavements.....	157
4.6 Cost-Benefit Analysis	160
4.6.1 Lifecycle Cost Analysis	160
4.6.2 Initial Cost Analysis.....	161
4.6.3 Maintenance/Rehabilitation Costs Analysis.....	164
4.6.4 Calculation of Lifecycle Cost Analysis (LCCA)	165
4.7 ensar Software Simulation and Calculation.....	169
4.7.1 Unreinforced Section.....	169
4.7.2 Section 1	170
4.7.3 Section 4.....	172
CHAPTER 5: Research Findings and Implementation of the Research in MnPave Software	175
5.1.1 First Method of Implementation of Research Findings in Incorporation of Geogrid in MnPave.....	175

5.1.2 Second Method of Implementation of Research Findings in Incorporation of Geogrid in MnPave.....	177
CHAPTER 6: Conclusions, Key Findings and Recommendations	180
6.1 Conclusions and Key Findings.....	181
6.2 Recommendations.....	183
References.....	184

LIST OF FIGURES

Figure 1. Three typical types of pavements.....	1
Figure 2. Mechanisms of geosynthetic reinforcement.....	3
Figure 3. The relationship among diverse facets of pavement design	4
Figure 4. Permanent rutting deformation development using light- and heavy-duty biaxial geogrids in different base course thicknesses.....	11
Figure 5. Maximum vertical stresses at the interface between subgrade and the aggregate base course layer for different thicknesses of base courses.....	12
Figure 6. Permanent surface deformation for different strength and geometry of geogrid located at different locations of sections	12
Figure 7. Permanent surface deformation for different stiffness of geogrid located at the base-subgrade interface and the effect of several geosynthetics layers	13
Figure 8. Integrated mobile accelerated test system for laboratory tests	28
Figure 9. IMAS laboratory test sections and finite element model sections.....	30
Figure 10. Test configuration in IMAS device	31
Figure 11. Normal distribution of loading pattern.....	33
Figure 12. Biaxial geogrid directions.....	33
Figure 13. Subgrade preparation procedures: a) add soil layer, b) compact soil with a hammer, c) level the soil layer with a tamper, d) add soil, layer by layer, and compact each layer, and e) perform measurement and final leveling of subgrade surface	35

Figure 14. Base layer preparation steps: a) place the geogrid, b) add aggregate on top of the geogrid, c) level and prepare the aggregate surface layer, and d) compact the aggregate layer	36
Figure 15. Application of 1 in. aggregate layer through the geogrid at the interface: a) aggregate layer placed with less than 1 in. thickness, b) aggregates entrapped in the geogrid apertures, c) thin layer of aggregate spread on top of the surface, d) geogrid placed on top of thin aggregate, e) aggregate added and spread across and through the top of the geogrid, and f) base materials placed on top, leveled, and prepared for compaction	36
Figure 16. Steps to compact the base layer: a) compactor used, b) prepare the compactor, c) level the aggregate surface, d) compact the base layer, and e) level the surface after compaction	38
Figure 17. Surface layer preparation steps: a) place a plastic cover layer on top of the aggregate, b) adjust the loading plate on the center of the aggregate layer, c) place the steel layer on top of the plastic cover layer, d) adjust the sensors, and e) set up the strain gauge data acquisition system	39
Figure 18. Steel surface plate installation: a) set first layer of steel plates and b) set the second layer of steel plates.....	40
Figure 19. Instrumentation: a) laser surface deformation sensor, b) pressure cell sensor, c) two types of strain gauges for biaxial and triaxial geogrids, and d) strain gauge data acquisition system.....	41
Figure 20. Installation of earth pressure cells: a) place the pressure cell and b) cover the pressure cell with sand	42
Figure 21. Position of strain gauges for: a) high duty biaxial, b) light-duty biaxial, c) high duty triaxial, and d) light-duty triaxial.....	45
Figure 22. Key setup steps for strain gauge installation on geogrids: a) apply the topcoat liquid on the strain gauges, b) add foam tape as protection, c) protect strain gauge wires by passing them through a plastic tube, d) set the geogrids in their positions, e) set up the data logger software, and f) compact the base layer with the plate compactor for 3 minutes and simultaneously record the strain gauge and sensor results to measure the effect of compaction on mobilization of the geogrid	46
Figure 23. Average strains in the compaction part for biaxial geogrids	47
Figure 24. Average strains in the compaction part for triaxial geogrids.....	48
Figure 25. GE1 strain gauge in direction 1	49
Figure 26. GE1 strain gauge in direction 2	49
Figure 27. GE2 strain gauge in direction 1	50
Figure 28. GE2 strain gauge in direction 2	50

Figure 29. GE4 strain gauge in direction 1	51
Figure 30. GE4 strain gauge in direction 2	51
Figure 31. GE5 strain gauge in direction 1	52
Figure 32. GE5 strain gauge in direction 2	52
Figure 33. GE7 strain gauge in direction 1	53
Figure 34. GE7 strain gauge in direction 2	53
Figure 35. GE12 strain gauge in direction 1	54
Figure 36. GE12 strain gauge in direction 2	54
Figure 37. GE15 strain gauge in direction 1	55
Figure 38. GE15 strain gauge in direction 2	55
Figure 39. Permanent deformation results of triaxial and biaxial geogrids	56
Figure 40. Pressure cell results for section GE0	57
Figure 41. Pressure cell results for section GE1	58
Figure 42. Pressure cell results for section GE2	58
Figure 43. Pressure cell results for section GE4	59
Figure 44. Pressure cell results for section GE5	59
Figure 45. Pressure cell results for section GE7	60
Figure 46. Pressure cell results for section GE12	60
Figure 47. Pressure cell results for section GE15	61
Figure 48. GE0 section loading vs. EPC results for time intervals: a) 0–500 sec, b) 2,000–2,500 sec, c) 30,000–30,500 sec, d) 45,000–45,500 sec, and e) 60,000–60,500 sec.....	62
Figure 49. GE1 section loading vs. EPC results for time intervals: a) 0–500 sec, b) 2,000–2,500 sec, c) 30,000–30,500 sec, d) 45,000–45,500 sec, and e) 60,000–60,500 sec.....	63
Figure 50. GE2 section loading vs. EPC results for time intervals: a) 0–500 sec, b) 2,000–2,500 sec, c) 30,000–30,500 sec, d) 45,000–45,500 sec, and e) 60,000–60,500 sec.....	64
Figure 51. GE5 section loading vs. EPC results for time intervals: a) 0–500 sec, b) 2,000–2,500 sec, c) 30,000–30,500 sec, d) 45,000–45,500 sec, and e) 60,000–60,500 sec.....	65

Figure 68. GE15 section loading vs. strain for direction 1 in time intervals: a) 0–500 sec, b) 2,000–2,500 sec, c) 30,000–30,500 sec, d) 45,000–45,500 sec, and e) 60,000–60,500 sec.....	82
Figure 69. GE15 section loading vs. strain for direction 2 in time intervals: a) 0–500 sec, b) 2,000–2,500 sec, c) 30,000–30,500 sec, d) 45,000–45,500 sec, and e) 60,000–60,500 sec.....	83
Figure 70. Field test sections.....	85
Figure 71. Project location in Mankato.....	88
Figure 72. Field location in Mankato	88
Figure 73. Field test sections in Mankato	89
Figure 74. a, b, and c) site condition and geogrid placement for construction, d) subgrade compaction around manhole in the road, e) compacted subgrade around the manhole, and f, g, h, and i) construction procedure for base and subgrade	91
Figure 75. a and b) APLT equipment and truck, c and d) APLT loading actuator structure and sensors, and e) APLT equipment.....	92
Figure 76. LFWD test on top of the subgrade layer in the field.....	94
Figure 77. Intelligent compaction on top of subgrade and base layers in the field	94
Figure 78. DCP tests on top of the base layer in the field.....	95
Figure 79. Sand cone compaction test on base layer in the field	96
Figure 80. Resilient modulus of aggregate base materials for all test sections in the field	97
Figure 81. Base resilient modulus of all test sections in the field.....	98
Figure 82. CBR results at top layer of all test sections in the field	99
Figure 83. Summary of test results for all test sections in the field	100
Figure 84. APLT results for Section 1, page 1 of 6.....	101
Figure 85. APLT results for Section 1, page 2 of 6.....	102
Figure 86. APLT results for Section 1, page 3 of 6.....	103
Figure 87. APLT results for Section 1, page 4 of 6.....	104
Figure 88. APLT results for Section 1, page 5 of 6.....	105
Figure 89. APLT results for Section 1, page 6 of 6.....	106

Figure 90. APLT results for Section 2, page 1 of 3.....	107
Figure 91. APLT results for Section 2, page 2 of 3.....	108
Figure 92. APLT results for Section 2, page 3 of 3.....	109
Figure 93. APLT results for Section 4, page 1 of 3.....	110
Figure 94. APLT results for Section 4, page 2 of 3.....	111
Figure 95. APLT results for Section 4, page 3 of 3.....	112
Figure 96. APLT results for Section 5, page 1 of 3.....	113
Figure 97. APLT results for Section 5, page 2 of 3.....	114
Figure 98. APLT results for Section 5, page 3 of 3.....	115
Figure 99. APLT results for Section 7, page 1 of 3.....	116
Figure 100. APLT results for Section 7, page 2 of 3.....	117
Figure 101. APLT results for Section 7, page 3 of 3.....	118
Figure 102. APLT results for Control section 2, page 1 of 3.....	119
Figure 103. APLT results for Control section 2, page 2 of 3.....	120
Figure 104. APLT results for Control section 2, page 3 of 3.....	121
Figure 105. APLT results for Section 5, page 1 of 6.....	122
Figure 106. APLT results for Section 5, page 2 of 6.....	123
Figure 107. APLT results for Section 5, page 3 of 6.....	124
Figure 108. APLT results for Section 5, page 4 of 6.....	125
Figure 109. APLT results for Section 5, page 5 of 6.....	126
Figure 110. APLT results for Section 5, page 6 of 6.....	127
Figure 111. Historical pavement design methods	129
Figure 112. Flexible pavement design chart proposed.....	132
Figure 113. Geogrid-reinforced base course for paved highway section using geogrids.....	133
Figure 114. TRB versus SN for perfect reinforcement model.....	134

Figure 115. Layer coefficient ratio vs. subgrade CBR.....	134
Figure 116. Improvement graph layer coefficient vs CBR of the subgrade	135
Figure 117. SpectraPave4	137
Figure 118. MnPave software	139
Figure 119. IMAS laboratory test sections and finite element model sections.....	140
Figure 120. a) IMAS for laboratory test and b) automated plate load test device for field test	141
Figure 121. Calibrated permanent deformation of experimental results with mechanistic-empirical approach in unreinforced section.....	146
Figure 122. Calibrated permanent deformation of experimental results with mechanistic-empirical approach in unreinforced section.....	147
Figure 123. a) Dimension size of FE models and b) Refined mesh size of the FE model elements	151
Figure 124. Calibrated permanent deformation of experimental test results with performed FE simulation sections evaluated by mechanistic empirical approach	155
Figure 125. Maintenance/rehabilitation versus road life time.....	165
Figure 126. Unreinforced section	170
Figure 127. Section 1.....	170
Figure 128. Section 1 comparison.....	171
Figure 129. Section 4.....	172
Figure 130. Section 4 comparison.....	173

LIST OF TABLES

Table 1. Test configurations, geosynthetic properties and locations, and layer thicknesses and properties.....	5
Table 2. Summary of major findings in the studies	8
Table 3. Summary of application benefits of geosynthetic reinforcement in pavements	15
Table 4. Test configurations and special features of field test studies.....	17
Table 5. Properties of geosynthetics and locations in the tests of various researchers	19

Table 6. Layer properties and factors in the literature.....	20
Table 7. Summary of major findings in the literature.....	22
Table 8. Ten loading distribution levels in IMAS tests	32
Table 9. Specifications of the plate compactor	37
Table 10. Conditions for various geosynthetic products	130
Table 11. Variables that influence the effect of reinforcement	130
Table 12. GE factors for geogrid-reinforced field test sections	144
Table 13. Mechanistic-Empirical calibration parameters	146
Table 14. GE factors for geogrid-reinforced laboratory sections	148
Table 15. Prony series parameters in FE simulations in Abaqus software	152
Table 16. Base course, and subgrade layers properties used in FE simulation	152
Table 17. The geogrid equivalent modulus (MPa) quantifying geogrid properties.....	153
Table 18. Maximum confining stress for different type and stiffness of geosynthetics	154
Table 19. Mechanistic-empirical calibration parameters	156
Table 20. Mechanistic-empirical calibration parameters	157
Table 21. Factors for geogrid reinforced sections	159
Table 22. Aggregate and hauling time costs for base material	161
Table 23. Geogrid costs for the material installation in the road sections.....	161
Table 24. Labor and equipment unit costs	162
Table 25. Weight of the aggregate materials required for construction.....	162
Table 26. Class 5 aggregate and labor cost of hauling the Class 5 aggregate for construction.....	162
Table 27. Labor and equipment required times for construction	163
Table 28. Equipment costs for each section for construction	163
Table 29. Labor costs of the sections for construction.....	163
Table 30. Equipment, Class 5 aggregate, and labor total costs for each geogrid type.....	163

Table 31. HMA maintenance/seal coat costs for seven-year cycle	164
Table 32. Cost analysis of each section separately	166
Table 33. GE gain factors for geogrid reinforced sections	176
Table 34. Base resilient modulus gain factor for geogrid reinforced sections	178

ACRONYMS AND ABBREVIATIONS

AASHTO	American Association of State Highway and Transportation Officials
ABC	aggregate base course
AC	asphalt concrete
ALF	accelerated loading facility
APT	accelerated performance testing
APLT	automated plate load test
BCR	base course reduction
CBR	California bearing ratio
CRCP	continuously reinforced concrete pavement
CRREL	Cold Regions Research & Engineering Laboratory
DCP	dynamic cone penetrometer
EPC	earth pressure cell
ESAL	equivalent single-axle load
FEM	finite element method
FERF	Frost Effects Research Facility
FWD	falling weight deflectometer
GE	granular equivalent

Gg	geogauge
GSC	geosynthetic structural coefficient
HMA	hot-mix asphalt
HVS	heavy vehicle simulator
IMAS	integrated mobile accelerated test system
JPCP	jointed plain concrete pavement
JRCP	jointed reinforced concrete pavement
LCCA	lifecycle cost analysis
LCR	layer coefficient ratio
LEA	layered elastic analysis
LVDT	linear variable differential transformer
LFWD	light falling weight deflectometer
LWD	lightweight deflectometer
MDD	multi-depth deflectometer
MDT	Montana Department of Transportation
ME	mechanistic-empirical
MEPDG	mechanistic-empirical pavement design guide
MnDOT	Minnesota Department of Transportation

MSL	mechanically stabilized layer
PCP	pre-stressed concrete pavement
PR	perfect-reinforced
PSPA	portable seismic property analyzer
QA/QC	quality assurance control and quality control
RAP	recycled asphalt pavement
RDD	rolling dynamic deflectometer
SN	structural number
TBR	traffic benefit ratio
TIF	traffic improvement factor
USCS	Unified Soil Classification System

EXECUTIVE SUMMARY

Geogrids have been widely used in roadway construction as reinforcement in pavement systems. Geogrids have been effective in practice for reducing rutting damage, distributing traffic loads within the pavement foundation layers, increasing the resilient modulus of the base course, and stabilizing the subgrade layer. Evaluating structural benefits of geogrids in the pavement structure depends on factors such as geogrid stiffness, geogrid rib shape, geogrid location, hot-mix asphalt (HMA) thicknesses, base aggregate stiffness and thicknesses, and subgrade stiffness.

This project was a comprehensive study of geogrid reinforcement for flexible pavements and included laboratory tests, field tests, and finite element simulations to evaluate geogrid reinforcement advantages and granular equivalent (GE) gain factors in reinforced pavements. The overall research methodology was proposed by a highly-qualified and multi-disciplinary team with expertise in pavement foundations, geogrids, field and laboratory testing, construction, and cost analysis at Iowa State University, Ingios Geotechnics, Inc., and the Minnesota Department of Transportation (MnDOT) through the project's Technical Advisory Panel.

This report fills the gaps in research performed by previous researchers and includes a comprehensive literature review. The GE factor is determined based on the results of the geosynthetic-reinforced foundations, and the unreinforced section is compared to those results obtained from the GE factors. A table of GE factors based on different parameters is presented in this report, according to the comparison of the results for the laboratory and experimental field tests, along with numerical studies. The results in this report can be used by designers to evaluate the geogrid reinforcement of flexible pavements in their designs.

Currently, there exist difficulties in quality assurance and quality control (QA/QC) testing of road systems, difficulties in evaluating the benefits of geosynthetic reinforcement of flexible pavements offering an environmentally friendly and potentially economical alternative solution to reinforce/stabilize roads built over weak subgrade soils, and the need to develop consistent standards and methodologies for geosynthetic reinforcement in pavement structure designs. Hence, this research seeks to evaluate and optimize the standard method of pavement design currently used by MnDOT and assess the performance benefits of geogrids in the pavement system. The MnDOT pavement design method is based on the concept of the GE factor. The GE factor is determined based on Class 5 aggregate base material and is used to assess the performance benefits of geogrids in the pavement system. This GE factor shows that, by using a layer of geogrid in the pavement, the thickness of the base course can be decreased, and by how much, compared to that of unreinforced sections.

Although MnDOT is assigning a GE factor of 2 inches to geogrid-reinforced flexible pavements, given the advances in geogrid materials, this GE value may underestimate the performance benefit of geogrids, resulting in overdesigning the thickness of the aggregate base layers. Furthermore, the mechanistic-empirical (ME) flexible pavement design program, MnPave, and other pavement design software programs do not currently contain a geogrid design module, so pavement design engineers use geogrid manufacturers' design methods as an alternative to analyzing and designing these pavement structures.

While use of MnPAVE is required for all pavement designs on the trunk highway system, FlexPAVE (R-Value/GE) is allowed and preferred for pavement designs by most local agencies on the county state-aid highway (CSAH) and municipal state-aid street (MSAS) systems, although use of MnPAVE is highly encouraged. MnPAVE currently includes geogrid as an option in the research mode, so this Minnesota Local Road Research Board (LRRB) sponsored project proposes other options to quantify geogrids using MnPAVE.

For this project, an integrated mobile accelerated test system (IMAS), an automated plate load test (APLT) device, and finite element simulation approaches were used to evaluate the reinforcement effects of geogrid reinforcement. Test configurations were constructed by varying geogrid types (i.e., light-duty biaxial, heavy-duty biaxial, light-duty triaxial, and heavy-duty triaxial), geogrid locations in the base course (i.e., at the interface between the base and the subgrade or in the base course), and base aggregate thicknesses in the laboratory and in experimental field tests.

Eight IMAS and APLT test sections were studied to evaluate the reinforced base course behavior using different types of geogrids in different locations. These sections were named GE0, GE1, GE2, GE4, GE5, GE7, GE12, and GE15. GE0 was the control section, so no geogrid was installed in this section.

A biaxial geogrid was used in GE1, GE2, and GE5, and a triaxial geogrid was used in GE4, GE7, GE12, and GE15. For GE1, GE2, GE4, and GE12, the geogrid products were placed at the interface between the base course layer and the subgrade layer; for GE5 and GE7, the geogrid was installed at the middle of the base course layer. Finite element method (FEM) models were later calibrated based on the results of these eight sections. Then, the calibrated FEM models were used to determine GE values for the remaining sections. The results of cyclic deformation, permanent deformation, elastic modulus, stiffness, resilient modulus, cyclic stresses, and the number of cycles calculated in real-time were also presented. Testing results were used to evaluate the structural benefits of geogrids as a function of the GE factor.

The results of this study reveal that improvement of pavement performance due to geosynthetic reinforcement relates to various factors and variables, including geogrid stiffness and geometry, geogrid location/depth, asphalt surface, aggregate thicknesses, and subgrade stiffness. Thereby, a new formulation is proposed to predict the GE factor for geogrid reinforcement of flexible pavements.

The benefit of this work is realizing and understanding the structural benefits of geogrids and being able to apply GE factors to pavement design to reduce the thickness of gravel and/or asphalt and, consequently, extend the service life and reduce maintenance costs for the pavement. It is expected that the appropriate use of geogrids can result in significant cost savings per project.

CHAPTER 1: INTRODUCTION, BACKGROUND, AND LITERATURE REVIEW

Pavement structures are built to resist environmental effects (e.g., temperature and moisture) and static and dynamic loads from vehicles by distributing the loads to underlying subgrade soils. Pavement structures enable ease, speed, safety, and efficiency of commuting for millions of daily vehicles and freight transportation traffic. Pavements can be categorized into three main types: flexible pavements consisting of hot-mix asphalt (HMA) and surface treatments; rigid pavements including jointed plain concrete pavement (JPCP), continuously reinforced concrete pavement (CRCP), jointed reinforced concrete pavement (JRCP), and pre-stressed concrete pavement (PCP); and composite pavements such as asphalt overlaid concrete and white topping (Paterson and Scullion 1990). Figure 1 shows examples of flexible, rigid, and composite pavements.



Figure 1. Three typical types of pavements

The United States has the largest road network in the world with a total length of 4,092,730 miles, including 2,674,825 miles of paved roads and 1,417,903 miles of unpaved roads. More than 95% of the paved roads are flexible pavements (FHWA 2019). In 2016, about \$60 billion was allocated to the highway budget for road maintenance, which increased 9% the next year (FHWA 2019). These statistics show that flexible pavements are critical for the transportation infrastructure in the United States.

A usual flexible pavement structure contains a surface asphalt layer and a base course layer consisting of granular or cement-treated materials built on top of a subgrade layer. Environmental effects and vehicle loads can cause the pavement to lose its initial stiffness and smoothness over time. Two common types of pavement distress are fatigue cracking and rutting.

One common type of fatigue cracking for flexible pavement can be defined as a series of interconnected cracks resembling the back of an alligator (alligator cracking), and rutting is the permanent longitudinal surface displacement along a wheel path. Each failure type is associated with a critical pavement response (Alimohammadi 2020, Alimohammadi et al. 2020a). For example, rutting is due to the accumulated vertical strain for each sublayer, and fatigue cracking is due to the tensile strain at the bottom of the HMA layer (Alimohammadi et al. 2020b).

The design and construction of flexible pavements built over weak or wet subgrades have always been objectives for pavement engineers. Cement or lime treatments are two common methods to stabilize or treat the upper part of a subgrade, depending on the subgrade soil types, to improve the engineering

strength or stiffness properties of the subgrade. However, geosynthetics offer an environmentally friendly and possibly economical solution for reinforcing or stabilizing roads built over weak or wet subgrade soil. In this case, geosynthetics, located either on top of the subgrade or within the unbound base course layer, work with the soil and granular materials to build a reinforced section (Saghebfar et al. 2016, Alimohammadi et al. 2020c).

1.1 PERFORMANCE BENEFITS OF GEOSYNTHETIC REINFORCEMENT IN FLEXIBLE PAVEMENTS

Geosynthetics provide a long-term and economical solution to a wide variety of engineering applications, such as base reinforcement and soil stabilization for pavement foundations, mechanical stabilization for earth structures (i.e., steepened slopes, retaining walls, or embankments), erosion and drainage control, landfill and waste-containment projects, root barriers, water retention, capillary mat drainage composites, and filtration (Ingle and Bhosale 2017).

The approach of using geosynthetics as reinforcement in pavement foundations was initiated in the 1970s (Cuelho and Perkins 2017). Since then, various geosynthetic types have been developed and used in pavement foundations. These geosynthetic types can be divided into eight different categories: geogrids, geotextiles, geonets, geo-membranes, geosynthetic clay liners, geofoam, geo-composites, and geocells.

Many studies have been carried out to examine the mechanisms of geosynthetic reinforcement. These mechanisms include lateral restraint, enhanced bearing capacity, tension membrane effects, and separation, which are described as follows (Zornberg and Gupta 2010, Cuelho and Perkins 2017).

- **Lateral Confinement:** Loads applied to the pavement establish a lateral spreading motion of the unbound base course layer. Tensile lateral strains are initiated in the base layer under the applied load as the base material moves down from the load. The geosynthetic confines the base aggregates, thus reducing and confining side movement caused by the load. The term lateral confinement consists of several factors of reinforcement as well as confining the side movement of base aggregate, increasing the stiffness of the base aggregate layer, reducing the shear stress in the subgrade soil layer, and developing the vertical stress distribution on the top of the subgrade. This mechanism of the reinforced base is illustrated in Figure 2(a).
- **Increasing the Bearing Capacity:** Improvement of the bearing capacity is attained by shifting the failure envelope from the relatively weak subgrade to the approximately stiff base layer of the pavement system, as illustrated in Figure 2(b). Therefore, bearing failure of the subgrade from punching failure without reinforcement is limited when reinforcement is used.
- **Tension Membrane:** The tension membrane effect is a result of vertical deformation that initiates a concave shape in the tensioned geogrid layer, as shown in Figure 2(c). The tension membrane effect can decrease the vertical stress acting on the subgrade. Commonly, a greater deformation is required for the mobilization of resistance of the tensile membrane as the stiffness of the geogrid

declines. Rutting depth and high stiffness of the geosynthetics are important to establish the membrane effect, thus enhancing the bearing capacity of the subgrade layer.

- **Separation:** One of the most significant mechanisms of geotextiles in pavements is separation. Due to the traffic loads, fine particles from the subgrade shift into the aggregate base layer, which leads to a drop in their desired properties. Mixing at the base course or subgrade zone causes a reduction in the effective base thickness and layer modulus, which can likely lead to structural failure of the pavement system. A geosynthetic layer between the subgrade and base interface provides a separator layer that may limit this intermixing. Figure 2(d) illustrates the separation effect.

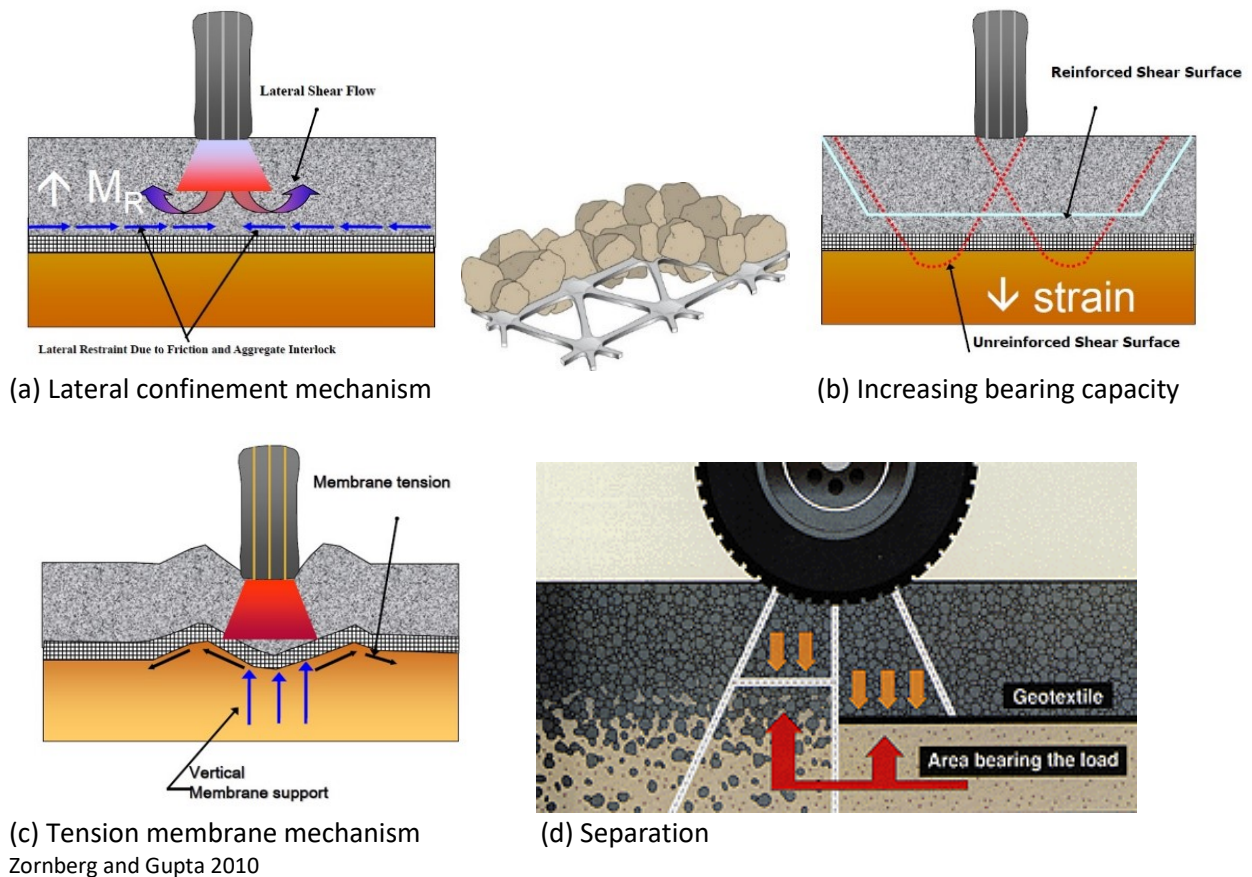
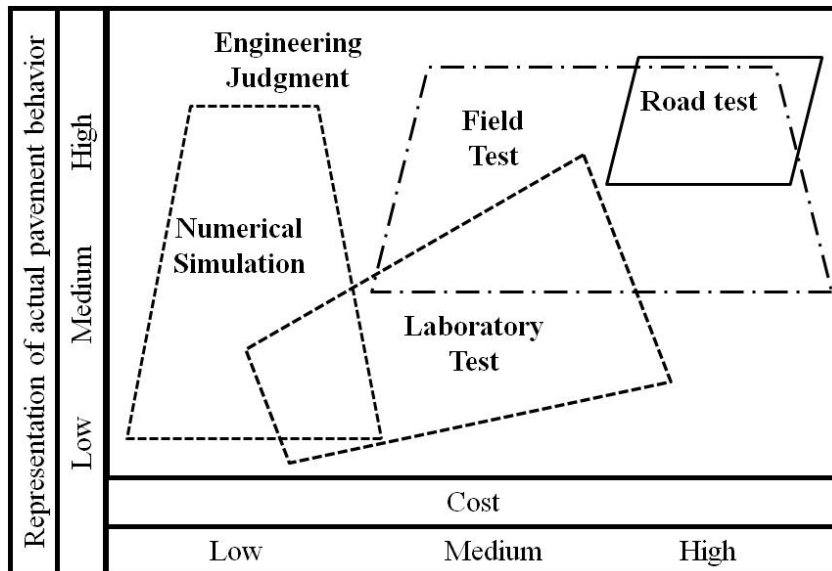


Figure 2. Mechanisms of geosynthetic reinforcement

1.2 RESEARCH METHODOLOGIES FOR GEOSYNTHETIC-REINFORCED PAVEMENTS

Since the 1970s, a large number of investigations have been conducted to assess the performance benefits of geosynthetic-reinforced pavement based on laboratory tests, full-scale tests, and numerical simulations (Zornberg 2011). These three methodologies afford distinct perspectives on pavement performance data, as illustrated in Figure 3.



Zornberg and Gupta 2010

Figure 3. The relationship among diverse facets of pavement design

The quality of pavement performance data on the vertical axis is assumed based on the cost and the applied method for the collection of data.

Full-scale tests consist of field studies and accelerated pavement tests, which mimic certain pavement behavior but come at a relatively high cost. Consequently, the number of full-scale studies conducted has been limited (Ingle and Bhosale 2017).

This research team’s literature review focused on laboratory studies of geogrids because a large number of laboratory studies on geogrids are available given their relatively low cost, which also results in a comprehensive database for performance evaluation of geogrids.

Many factors can affect the structural benefits of geogrids, including geogrid stiffness and geometry, geogrid location and/or depth, asphalt surface quality and thickness, base aggregate thickness, and subgrade stiffness. As such, existing laboratory studies focused on investigating the different factors. The various laboratory tests used consisted of the cyclic triaxial test, the plate load test, the pullout test, the modified pavement analyzer test, the bending stiffness test, and the pullout stiffness test. This review concentrated on investigations including laboratory-scale experiments using stationary cyclic plate loads.

Based on the database compiled, the researchers analyzed the effects of different geogrid factors on the performance benefits of flexible pavements. A granular equivalent (GE) factor was used as a measure of the performance benefits of geogrids in the pavement system.

The GE factor was initially developed and utilized by the Minnesota Department of Transportation (MnDOT) to design the thickness of surface and base materials for flexible pavement systems (Fredrickson et al. 1970, Siekmeier and Casanova 2016, Siekmeier 2018). The concept of GE is similar to the structural number (SN) defined in the American Association of State Highway and Transportation

Officials (AASHTO) pavement design procedure to quantify the structural capacity of the material layers in the overall pavement system (AASHTO 1993).

MnDOT defined that one inch of Class 5 aggregate base material has a GE of 1 and GE values of other materials can be determined based on comparisons with Class 5 aggregate base material. For example, if a triaxial geogrid base reinforcement has GE of 2, it means the structural strength of the base aggregate reinforced with the triaxial geogrid is equivalent to a 2-in. Class 5 aggregate base in the pavement system. Based on the database of laboratory test results compiled, in this research, the team developed a predictive model for the GE factor of geogrids to include various geogrid factors.

1.3 SMALL- AND LARGE-SCALE LABORATORY TESTS

Small- and large-scale cyclic load testing facilities have been used to investigate factors affecting the performance benefits of geosynthetic base reinforcement. These factors include the location of the reinforcement layer within the aggregate base course layer, the thickness of the base course layer, the strength/stiffness of the subgrade layer, and the engineering properties and geometry of the reinforcement.

Test sections have generally included laboratory-reinforced and unreinforced pavement sections established in a test box or tank. Cyclic loadings are applied to simulate construction and the designed traffic loads. The performance response is evaluated with the magnitude of rutting as a function of cyclic loading.

These testing methods have been promoted worldwide to measure the performance of geosynthetic-reinforced pavement. Some of the new small- and large-scale laboratory studies with their test configurations, geosynthetic properties and locations, and layer thicknesses and properties are presented in Table 1.

Table 1. Test configurations, geosynthetic properties and locations, and layer thicknesses and properties

Source	Tank dimensions (m)	Geosynthetic type and description	Geogrid location	HMA thickness (cm)	Base or Subbase thickness (cm)	Subgrade material properties
Haas et al. 1988	4.5×1.8 ×0.9	Light-duty biaxial geogrid	Asphalt/base interface, base/subgrade interface, and middle of the base layer	7.62 to 10.16	Different thicknesses of granular bases for each series	Fine-grained sand subgrade (SP)
Al-Qadi et al. 1994	3.1×1.8 ×2.1	Geotextile and geogrid in two test sections and a biaxial geogrid in the third section	Base/subgrade interface	7	15	Weak silty-sand subgrade with CBR = 4% and well-graded gravel base course

Source	Tank dimensions (m)	Geosynthetic type and description	Geogrid location	HMA thickness (cm)	Base or Subbase thickness (cm)	Subgrade material properties
Perkins 2001b	2×2 ×1.5	Geotextile and light-/ heavy-duty biaxial geogrids	Base/subgrade interface, 10 and 4 cm above the base/subgrade interface	7.5	30, 37.5, and 20	Clay subgrade with CBR = 1.5% and silty-sand subgrade with CBR = 15%
Ling and Liu 2001	0.6×0.2 ×0.5	Biaxial and uniaxial geogrids	Asphalt/subgrade interface	4 to 6	Sections without base (subgrade 30 cm)	Ottawa sand subgrade
Perkins 2001b	2×2 × 1.5	Geotextile and light-/ heavy-duty biaxial geogrids	Base/subgrade interface	7.5	30	Weak subgrade with CBR = 1.5%, base material with GW-GM
Leng and Gabr 2002	1.5×1.5×1 .35	Biaxial geogrid	Base/subgrade interface	0 (unpaved)	15 and 25	Clay-sand subgrade with CBR = 4%, base material with GW
Abu-Farsakh and Chen 2011	2×2×1.7	Biaxial and triaxial geogrids	Base/subgrade interface, middle of the base layer, upper one-third of the base layer	5.2	30.5	Weak subgrade with silty clay and CBR = 0.5%
Qian et al. 2013	2×2.2×2	Triaxial geogrids (light-, medium-, and heavy-duty)	Base/subgrade interface	0 (unpaved)	15, 23, and 30 (base material CBR = 20%)	Weak subgrade with CBR = 2%
Abu-Farsakh et al. 2016	2×2×1.7	Triaxial geogrid, geotextile	15.2 cm below asphalt/base interface, plus base/subgrade interface	7.6	25.4, 30.5 and 45.7	Very wet plus high plasticity clay to serve as the weak natural subgrade soil
Ghafoori and Sharbaf 2016	1.8 m diameter, 2.1 m height	Light-duty biaxial/ triaxial geogrids	Mid-depth of thick aggregate base and subgrade/base interface of thin base	7.6	30.5 and 40.6	Silty-clay subgrade (SC-SM) and base materials (GP-GM).
Nair and Latha 2016	0.75× 0.75×0.62	Geotextile, two types of biaxial geogrids	Subbase-subgrade interface	0 (unpaved)	–	Low plasticity clay with un-soaked CBR = 19%
Gu et al. 2017	2.4 m diameter, 1.80 m height	Triaxial geogrid	Base/subgrade interface for a thin base and mid-depth of a base for thick base	15	15 and 25	Sandy soil

Source	Tank dimensions (m)	Geosynthetic type and description	Geogrid location	HMA thickness (cm)	Base or Subbase thickness (cm)	Subgrade material properties
Ibrahim et al. 2017	1×0.35 ×0.55	Uniaxial geogrid	Base-subgrade interface, one-third of the height of the base layer	5	15	30 cm clay subgrade
Mahaffay et al. 2019	1.8×1.8 ×1.8	Four geogrids (one triaxial, three biaxial) and one woven geotextile	Base/subbase interface, subbase/subgrade interface	12.7	17.8	SP and SW subgrade with CBR = 3%, base with GP-GM and GW-GM materials, plus subbase with CBR = 15%
Robinson et al. 2019	1.8×1.8 ×1.8	Three biaxial and one triaxial geogrid and one woven geotextile	Subbase/subgrade interface, base/subbase interface		13	18 cm base with CBR = 80% to 100% and 30 cm subbase with CBR = 15% to 50%

CBR=California bearing ratio

The information in this table illustrates that most of the researchers have investigated geogrids of differing stiffness and aperture shape (biaxial or triaxial). Nonetheless, the effect of geogrid confinement depends on other specifications such as rib shape, aperture size, junction strength, stiffness of the ribs, and properties of aggregates (Perkins et al. 2004, Zornberg and Gupta 2010). Generally, the optimal position of the geosynthetics in the pavement structure relies on the base course layer thickness plus the magnitude of the dynamic load.

Moghaddas-Nejad and Small (1996) implied that, for a thin (e.g., 40 mm) aggregate base course layer and a very weak subgrade layer, the optimal location is at the interface between the aggregate base course layer and subgrade (at the zone of neutral elastic tensile strain (between 0.05% and 0.2%) below the load center). Haas et al. (1988) indicated that, for a 250 mm thick aggregate base layer, the best position is also at the interface.

In most cases, load amplitude for the research was based on equivalent single-axle loads (ESALs) as recommended by AASHTO (1993) and in the Guide for Mechanistic-Empirical Design of New and Rehabilitated Pavement Structures (MEPDG for short) (ARA, Inc. 2004, Mallela et al. 2009), while applying half a single-axle wheel load of 40 kN. Also, dual tire pressure contact loading was converted by many researchers to an equal area for a single axisymmetric load in laboratory cyclic plate load tests. The wheel contact pressure was modeled as 550 kPa in a circular area with a diameter of 30.4 cm, so the gross contact pressure area for the load was 726 cm².

Furthermore, test box sizes utilized by various investigators varied from 300 x 300 x 300 cm to 45 x 25 m x 15 cm. Due to the confining effects provided by box boundaries, pavement sections did not simulate certain situations of the unconfined asphalt layer in the field condition, which is a limitation of laboratory-scale tests.

Studies performed on the geosynthetic reinforcement benefits for the subgrade layer strength showed that the benefits of the reinforcement were higher for weak subgrade layers than for stiffer ones. Cancelli and Montanelli (1999) showed that the permanent surface deformation between reinforced and unreinforced sections increases by decreasing the subgrade stiffness and the California bearing ratio (CBR) value. Perkins and Cuelho (1999) revealed that geogrids afforded better development for weak subgrade layers (a CBR value of 1.5) as well.

The summary of major findings from various investigators are summarized in Table 2, where it is shown that most of the investigators evaluated the effects of geosynthetic reinforcement in terms of the distribution of vertical stress at the subgrade level and surface deformation by assuming permanent deformation (i.e., rutting depth) of 19 to 25 mm for pavement as a performance index.

Table 2. Summary of major findings in the studies related to sensors

Source	Sensor types	Findings
Haas et al. 1988	Five dial gauges (LVDTs) on the asphalt surface; foil-type strain gauges on the mesh at several positions with increasing radial distance from the load center; in some selected tests, pressure cells located 3.81 cm below the top of the subgrade layer	Geogrid reinforcement can increase the number of cyclic load cycles enforced by a factor of 3 (for a failure rutting criterion of 2 cm). Reduction of the base thickness with 25% to 50% by reinforcement. Optimal location of geogrid reinforcement throughout the granular base layer found to rely on the granular base thickness and subgrade strength. Geogrid can be located at the base/subgrade interface in thin thickness base sections, and also near the midpoint position of thicker base thicknesses.
Al-Qadi et al. 1994	LVDTs at the top of the surface and one load cell at the subgrade/base interface	Geosynthetics can substantially improve the performance of a pavement section constructed on a weak subgrade soil. The mechanisms of the reinforcing geogrids and geotextiles are different. Geotextiles can provide substantial separation between the subgrade and aggregate layers.
Perkins 2001b	Sensors measuring enforced pavement load, deflection of the surface of the asphalt, tensile strain in the asphalt, stress, and strain in the base and subgrade and strain on the geosynthetic, temperature, and moisture content	Notable enhancement in pavement performance as surface rutting, especially for weak subgrades (CBR = 1.5%), but little improvement for stiffer subgrades (CBR = 20%). Higher TBR for geogrid with greater stiffness and located at the middle position of the thick base thickness. Sections with two layers of geogrids have better performance than sections with geotextile. Better distribution of stress was found on tops of subgrades for reinforced sections. Reinforcement provided at least a 20% reduction in aggregate base thickness.
Ling and Liu 2001	Five strain gauges, and settlement along the asphalt surface measured with 3 LVDTs	Geosynthetic reinforcement can increase the stiffness and bearing capacity of the asphalt pavement. Under cyclic loading, the life of the AC layer was lengthened with geosynthetic reinforcement (and enhancement was more notable for dynamic loading when compared to static loading). Stiffness of the geogrid plus its interlocking with the AC supplied the restraining effect.

Source	Sensor types	Findings
Perkins 2001b	Sensors measuring enforced pavement load, asphalt surface deflection, tensile strain in the asphalt, stress, and strain in the aggregate base/ subgrade and strain on the geosynthetic, temperature, and moisture content, including pore-water pressure	Initial pore-water pressure depends on the amount of compaction energy impacted in the construction layers, time of construction, and time between construction and loading. Results of a relatively short period between pore pressure and loading showed rapid development of rutting, and results for a long time showed a lower rate of rutting. Set up time (16 days to 2 months) should be assumed in design.
Leng and Gabr 2002	LVDT, pressure cells	Enhancement in stress distribution because of geosynthetics at the base/subgrade soil interface is designated by a decrease in measured maximum stress (under the center of the loaded area) and measurement of more uniform stress distribution on the subgrade soil layer. Greater modulus of geogrid afforded a better load-spreading effect compared to a lower modulus geogrid. Enhancement in plastic surface deformation was linked to two aspects: decrease in vertical deformation of subgrade layer and decrease in lateral spreading of base course.
Abu-Farsakh and Chen 2011	Sensors for checking stress distribution, vertical strain, and developed pore-water pressure in the subgrade, plus the strain distribution along geogrids	Better performance was realized when the geogrid layer was located at the upper one-third of the thick aggregate base layer than that when the geogrid was located at the base/subgrade interface or the middle of the aggregate base layer.
Qian et al. 2013	Sensors for measuring surface deformations plus vertical stresses at the base/subgrade interface, earth pressure cells	Decreased stress distribution angle and modulus ratio of aggregate base course to subgrade with an increase of load cycles. However, stress distribution angle increased when increasing base course thickness.
Abu-Farsakh et al. 2016	Sensors for measuring stress distribution, permanent vertical strain, and developed pore-water pressure in the subgrade layer, strain distribution along geogrids, development of pore-water pressures	Geosynthetics located at base/subgrade interface position act more as weak subgrade stabilization; resilient modulus value of aggregate base course layer can be increased with geosynthetic reinforcement, and, for geosynthetics functioning as subgrade stabilization alone, resilient modulus of subgrade can be almost doubled.

Source	Sensor types	Findings
Ghafoori and Sharbaf 2016	Pressure cells, foil strain gauges installed on the ribs of geogrids, and LVDTs located on top of the loading system	Vertical pressure at the center of the subgrade/base interface decreased by an average of 18% and 24% for biaxial and triaxial geogrid-reinforced sections, respectively. Application of geogrid increased the number of loads by a factor of 1.5 to 7 according to the test section and geogrid type, given the rutting depth experienced with different loading applications. Application of geogrid resulted in reduction of the base thickness from 11 to 44%.
Nair and Latha 2016	Pressure cells at the subbase/subgrade interface, LVDTs on the top of the surface	At greater deformations, the reinforced systems enhanced fewer permanent deformations and more elastic deformations compared to unreinforced systems. Reinforced sections showed higher load resistance and indicated fewer plastic deformations compared to unreinforced sections.
Gu et al. 2017	Strain gauges for geosynthetics, pressure cells, accelerometers, strain gauges (LVDTs) for AC	Inclusion of geogrid at the center of the aggregate base course slightly decreased tensile strain beneath the AC, which is beneficial in prolonging the fatigue life of the flexible pavement, but, at the base/subgrade interface, is not efficient in extending the fatigue life of the flexible pavement. Geogrid reinforcement can raise the resilient modulus of the aggregate base course for design purposes.
Ibrahim et al. 2017	LVDTs on top of the surface, strain gauges monitored at three positions in the base	Ideal position of the geogrid was found to be within 33 to 50% of the aggregate base course layer height as measured from beneath the base layer. Locating geogrid at the base/subgrade interface can be good in decreasing compressive strains (rutting) but not in lessening tensile strain at the bottom of the AC layer (fatigue).
Mahaffay et al. 2019	Six LVDTs, three pressure cells at different locations	Using geosynthetic for airport pavement structure provides a performance benefit per TBR values and in reducing base course thickness as well. Geosynthetics at the subbase/subgrade interface in thicker airport pavements provide lower performance benefit compared to geosynthetics at the base course/subbase interface.
Robinson et al. 2019	Pressure cells; six LVDTs on the surface of the asphalt layer and one LVDT located on the load plate	Some level of permanent deformation (e.g., 2.5 cm) can be appropriate to employ in reinforcing benefits when inclusion of geosynthetics occurs at the subgrade/subbase interface. Only modest evidence indicated that locating geosynthetics closer to the surface than the subgrade/subbase interface would be desirable for thick airfield pavements overall.

AC=asphalt concrete, CBR=California bearing ratio, LVDT=linear variable differential transformer, TBR=traffic benefit ratio

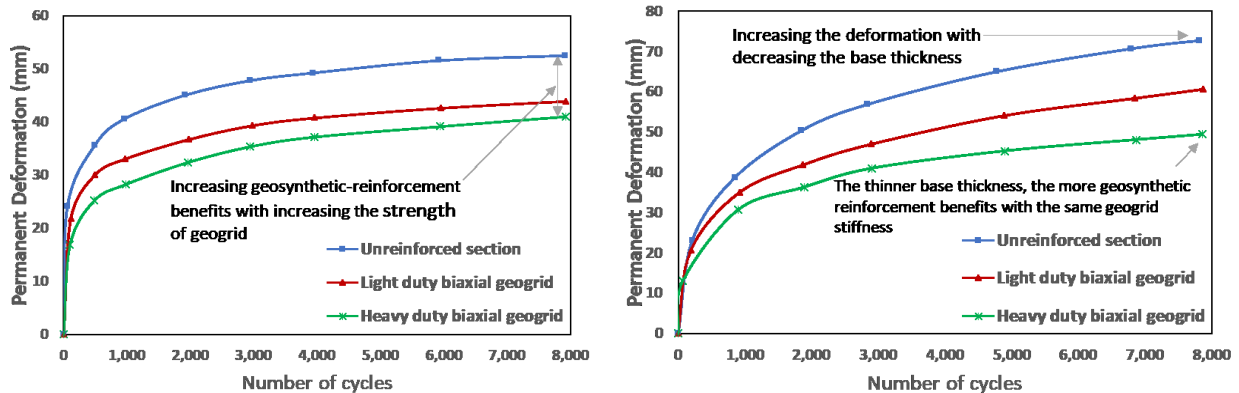
1.3.1 Analysis of Results in the Laboratory Test Database

Based on the literature review for laboratory tests, geogrid base reinforcement benefits are based on several factors, such as the location of the geogrid layer within the aggregate base course layer, engineering properties and geometries of the geogrids, asphalt surface and base course quality and thickness, and strength/stiffness of the subgrade layer. The results of these investigations illustrated that reinforcement was able to promote and extend the service lives for reinforced sections while decreasing the permanent deformation (rutting) in reinforced sections.

The increase in the service life of a pavement structure has been commonly defined by the application of the traffic benefit ratio (TBR). The TBR is described as the ratio of the number of load cycles to achieve a particular rutting depth in the reinforced section over an unreinforced section with the exact same corresponding thickness, loading characteristics, and material properties. Also, the results of these investigations showed that the required aggregate base course thickness for a given design could be decreased when a geogrid was included. This reduction in the base course thickness is commonly described by the base course reduction (BCR) factor, which is defined as the reinforced base thickness over the unreinforced base thickness for a given traffic level.

1.3.1.1 Base Course Thickness

The performance benefits of geogrids generally decrease with a rise in the thickness of the aggregate base course and become negligible when the aggregate base course is very thick. For instance, Figure 4 shows the permanent surface deformation versus the number of cycles for a 25.4 cm and 15.2 cm base thickness and different strength and geometry of the geogrid in the same locations of the sections.



(a) 25.4 cm base course thickness

(b) 15.2 cm base course thickness

Modified from Leng and Gabr 2002

Figure 4. Permanent rutting deformation development using light- and heavy-duty biaxial geogrids in different base course thicknesses

For a 15.2 cm base course thickness, using a light-duty biaxial geogrid can reduce about 10 mm of rutting depth compared to the unreinforced section, so the reduction for heavy-duty biaxial geogrids is about 20 mm. For a 25.4 cm base course thickness, using a light-duty biaxial geogrid could reduce about

6 mm rutting depth compared to the unreinforced section with the reduction for heavy-duty biaxial geogrids being about 10 mm (Leng and Gabr 2002).

The use of geogrids reduces the vertical stresses at the top of the subgrade layer due to the lateral confinement effects of geogrids, which reduces the permanent deformation of the pavement structure. The increase in geogrid stiffness causes an important reduction of permanent deformation, as well as strains and stresses. Figure 5 shows the maximum vertical stresses at the interface position between the subgrade and aggregate base course layer for three base course thicknesses of 15, 23, and 30 cm.

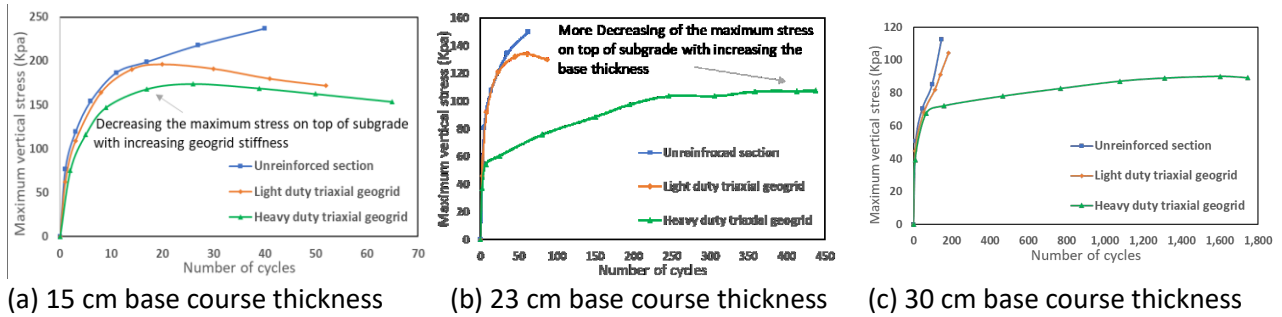
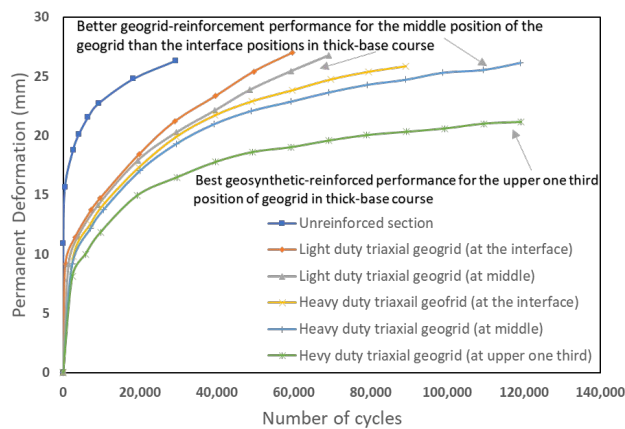


Figure 5. Maximum vertical stresses at the interface between subgrade and the aggregate base course layer for different thicknesses of base courses

1.3.1.2 Locations of Geogrids in Pavement Foundations

The position of geogrids within the aggregate base layer under the pavement is critical to its reinforcement capability. Figure 6 shows the permanent surface deformation versus the number of cycles for different strengths and geometries of geogrids located at different locations.



Modified from Abu-Farsakh and Chen 2011

Figure 6. Permanent surface deformation for different strength and geometry of geogrid located at different locations of sections

The ideal position of the geogrid depends on many aspects, such as the strength of the subgrade layer and the aggregate base course thickness. For a thin aggregate base course layer (e.g. less than 10 in),

locating the geogrid at the subgrade/base course interface position provides better performance. The geogrid should be located at the lower one-third of the aggregate base course layer for a thicker base course layer. However, limited benefits are forecasted when a single layer of geogrid is located at the middle/higher location within the aggregate base layer for a thick base course (Alimohammadi and Abu-Farsakh 2019, Abu-Farsakh and Chen 2012, Abu-Farsakh and Chen 2011). As shown in Figure 6, the TBR values are around 3 and 3.5 for light- and heavy-duty geogrid placed in the middle of the base course, respectively. The TBR values are around 3.8 and 4.6 for light- and heavy-duty geogrids at the interface position, respectively. The TBR is 7.2 for heavy-duty geogrid located at the lower one-third of the base course.

1.3.1.3 Geogrid Properties

Currently, the available data cannot provide a clear, quantitative relationship between the performance of geogrid base reinforcement and the geogrid properties, such as stability modulus, aperture geometry, junction strength, flexural stiffness, and tensile modulus (Luo et al. 2017). Research shows that these properties work together to identify the performance of the geogrid, so any single property cannot be sufficient to define the performance of the geogrid. However, research shows that the performance benefits of geosynthetic reinforcement increase by increasing the stiffness of the geosynthetics (from low to high stiffness) in the pavement (Alimohammadi and Abu-Farsakh 2019). As shown in Figure 7 (a), TBR values are around 2.1, 3.5, 3.8, and 4.6 for light- and heavy-duty biaxial geogrids and light- and heavy-duty triaxial geogrid, respectively (with 5.2 cm HMA and a 30.5 cm base).

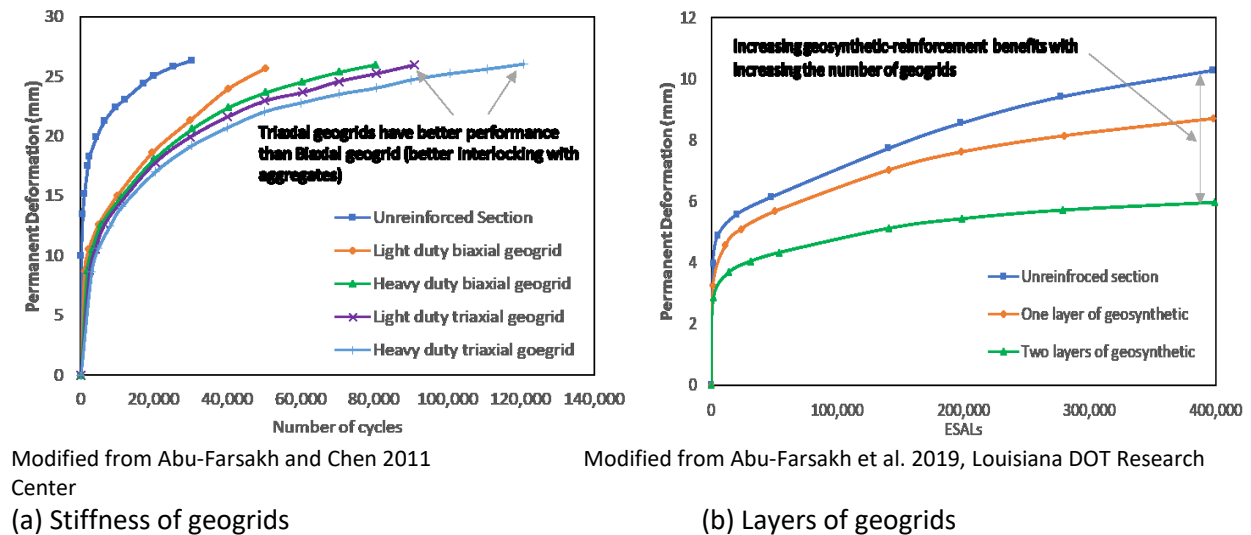


Figure 7. Permanent surface deformation for different stiffness of geogrid located at the base-subgrade interface and the effect of several geosynthetics layers

It has also been shown that using two or more layers of geosynthetics can result in more reinforcement benefits than a single layer of geosynthetics. Figure 7(b) shows the effect of several geosynthetic layers on permanent deformation.

The reinforcement layer is commonly located between the aggregate base course and the subgrade interface. Given the wide application of this technique, many experimental and analytical investigations have been performed to quantify and possibly assess the advances from geogrid base reinforcement of pavements. The findings propose that the application of geogrid reinforcement in flexible pavement has three main benefits: helping in construction of pavements, especially over soft/wet subgrades, improving or extending the pavement's designed service life and for a given service life, and decreasing the thickness of the pavement layer cross-sections (or basically the base course layer) (Ingle and Bhosale 2017, Perkins and Cuelho 1999, Cuelho and Perkins 2017).

1.4 REVIEW OF FULL-SCALE FIELD STUDIES

1.4.1 Quantifying Pavement Performance with Field Trials

Pavements are designed to deteriorate and fail after their design period or service life is reached in the field. This failure happens when the pavement condition declines below the performance criteria while the combined effects of dynamic loads and environmental factors cause the damage (Zornberg et al. 2008).

Since the initial use of geosynthetics in the reinforcement of flexible pavements, three different methodologies—field-scale tests, laboratory tests, and numerical simulations—have been used to assess the performance benefits of geosynthetic reinforcement on pavements (Zornberg 2011). The experimental techniques used in these studies include laboratory repeated load triaxial tests, laboratory cyclic plate load tests, field cyclic plate load tests, and full-scale field accelerated load tests (Sævarsdóttir 2014).

Field-scale tests, and especially accelerated performance testing (APT), can simulate the influences of long-term loading in a short time period in the field. APT is performed on full-scale road sections, during which the magnitude, location, and repetition of the loads, along with the environmental conditions, are controlled. In most cases, APT programs are conducted in conjunction with other laboratory testing programs.

1.4.2 Applications of Geosynthetic Reinforcement in Pavements

The benefits of the inclusion of geosynthetics within pavement layers as base reinforcement and subgrade stabilization have been widely recognized. Geosynthetics are usually classified into seven categories: geotextiles, geogrids, geomembranes, geonets, geofoam, geosynthetic clay liners, and geocomposites. Among these categories, geogrids and geotextiles are the most common products for pavement reinforcement applications. These products can usually be used at the subgrade-base course interface or within the base course layer of the pavement to beneficially increase the number of load repetitions to failure or to decrease the pavement layer thicknesses (Abu-Farsakh and Nazzal 2009, Saghebfar, Hossain and Lacina 2016, Alimohammadi and Abu-Farsakh 2019, Alimohammadi 2020).

The benefits of geosynthetic reinforcement on flexible pavements can be summarized as lateral restraint, separation, and a tensioned membrane effect of the geosynthetics. In reinforced sections,

when compared to an unreinforced section, the vertical stresses transferred through the geosynthetic-reinforced base layer can be reduced based on load spreading over a wider area on top of the subgrade layer. Also, geosynthetics can decrease shear stresses, thereby reducing subgrade stress. The tensioned membrane effect of geosynthetic reinforcement occurs in highly deformed pavements as well. Table 3 shows five applications of the geosynthetic reinforcement in pavements and other categories (Zornberg 2017).

Table 3. Summary of application benefits of geosynthetic reinforcement in pavements

Application	Objective	Mechanism	Functions of geosynthetic	Significance in pavement performance
Mitigation of reflective cracking in asphalt overlays	Postpone reflective cracking in asphalt overlays	Markdown of stress concentrations in asphalt overlays around cracks	Reinforcement, stiffening barrier separation	Decreases the effects of degradation in asphaltic surface layers caused by water invasion
Separation	Mix aggregate with subgrade soils	Lessen loss of aggregate particles into subgrade	Separation, filtration	Keeps the quality of the aggregate
Stabilization of base materials	Keep the modulus of the aggregate from degrading	Lateral restraint, which is associated with decreasing the time-dependent lateral displacements of unbound aggregate	Stiffening	Decreases lateral displacement of unbound aggregate materials, which promotes preserving aggregate confinement and keeps aggregate modulus; consequently, results in a similarly wide distribution of vertical loads and lower contact stresses of the base-subgrade
Stabilization of soft subgrade materials	Improve the bearing capacity of subgrade soils	Improvement of tension membrane-induced under wheel paths, and soil-geosynthetic interface shear transfer apart from the wheel path	Reinforcement, stiffening, filtration, separation	Diminishes vertical stresses on subgrade layer under the wheel paths and promotes the redistribution of shear/normal stresses apart from the wheel paths
Lateral drainage	Decrease addition of moisture within base/subgrade materials	Gravity-induced and suction-driven lateral drainage (for saturated and unsaturated soil conditions, respectively)	Drainage, filtration, separation	Decreases formation of positive pore-water pressures and reduces soil moisture content (for saturated and unsaturated soil conditions, respectively)

As noted in the first row of Table 3, one of the applications of geosynthetics is the mitigation of reflective cracks in asphalt overlays. The increased stresses from lateral movements generate reflective cracks that can be inoculated by placing a new pavement overlay, composing it liable to early failure promoted by moisture penetration. Geosynthetics can be used to reduce the progression of these reflective cracks by three main functions: promoting tensile forces at the vicinity of the crack tip,

reducing strains and stresses in the bituminous materials, and providing a layer that allows horizontal deformations so that large displacements can possibly progress without failure at the vicinity of the existing cracks. Application of geosynthetics can accomplish reinforcement at the interface of an existing pavement surface and a new overlay (Zornberg 2017).

In the second row of the table, separation is one of the significant benefits of the application of geosynthetics in the pavement layers. Aggregates tend to lose their desired properties due to traffic loads, because fine particles from the subgrade layer migrate into the aggregate layer. This intermixing of the materials at the base/subgrade layer interface causes a reduction in the efficient base thickness/layer modulus, potentially leading to structural failure in the pavement. A geosynthetic layer located at the subgrade/base (or even within the base layer near to the interface) makes a separator layer that mitigates this intermixing (Propex 2019).

The third application, in the third row of the table, is the stabilization of base materials. In other words, geosynthetics can be used to enhance the stiffness of the aggregate layer materials. Geosynthetics can be used in base/subgrade stabilization when they are placed at the base-subgrade interface position as well as in the aggregate base layer thickness. When using geogrids for stabilizing the aggregate layer, the aperture sizes of geogrid and base material particle sizes should be properly selected (recommended as more than 1.3 maximum dimensions of aggregated for the aperture sizes for example, according to references) (ASTM 2008, Palmeira and Góngora 2016). For geotextile reinforcement, proper interface frictional effectiveness should be provided. The greater modulus of the geosynthetic-stabilized aggregate, the wider distribution of vertical loads and the smaller vertical stresses acting at the aggregate/subgrade interface (Zornberg 2017).

The fourth application of geosynthetic reinforcement in the table is subgrade stabilization, which can be defined as developing the bearing capacity of the soft subgrade soils and all other functions of the geosynthetics, such as reinforcement, separation, stiffening, and filtration, which are also involved in this application. Generally, the geosynthetic performs as a tensioned membrane and includes a concave shape, so the tension develops a vertical component that directly resists against the applied vertical load (Koerner 1997).

Finally, geosynthetic reinforcement can provide lateral drainage applications, as described in the last row of the table. Moisture in the base and subgrade layers can be harmful. Moisture trapped under and within the pavement layers can heighten the distresses of the pavement due to increasing pore pressures and softening of the subgrade soil stiffness. Geosynthetics with drainage capabilities can drain the entrapped water and decrease the pore pressure in pavement (Zornberg 2017).

1.4.3 Literature Review of Geosynthetic-Reinforced Field Tests

In the last decade, extensive research studies on geosynthetics in pavement applications have been conducted. A variety of experimental techniques have been used in these studies, including laboratory repeated triaxial load tests, laboratory cyclic plate load tests, field cyclic plate load tests, and full-scale field accelerated load tests. The experimental studies confirm the benefits of geosynthetics in improving the performance of pavements in terms of extending their service lives and reducing permanent surface

deformation. The test configurations, special features, and loading details of field cyclic plate load tests and full-scale field accelerated load test studies are detailed in Table 4.

Table 4. Test configurations and special features of field test studies

Source	Field test dimensions	Field test specification	Loading
Webster 1993	Four traffic lanes with each lane containing four test items	Lanes 1 and 2 were designed to measure potential of geogrids for base reinforcement and lanes 3 and 4 to determine the comparative performance of the various types of geogrids.	13.6-ton single-wheel-assembly test cart; FWD with 400 mm height to produce a force up to 11.4 ton.
Perkins 2002	Four test sections, CRREL FERF/HVS 9.91 m × 3.18 m	Four full-scale test sections constructed/loaded with an HVS and smaller-scale test sections used to evaluate base reduction factors.	40 kN cyclic load applied to a stationary plate; HVS.
Maxwell et al. 2005	21 m section along US 45 in Wisconsin. incorporated with three test sub-sections	Two types of geogrids with different stiffnesses and a woven geotextile at the subgrade/base interface.	FWD seating load of 22 kN, the observed load sequence 22, 40, 62, 80, and 90 kN was completed.
Zornberg et al. 2008	32 test sections constructed and located in Leon County of the Bryan district, Texas	Well and poorly-performing geosynthetic-reinforced and unreinforced sections. Eight reinforcement plans were expected. Field monitoring was conducted.	FWD: done every 91.5m with four different load levels (2.7, 3.6, 4.9, 6.8 ton); RDD done using two static load levels of 3.6 ton.
Hossain and Schmidt 2009	4.8 km test section on VA 743 with 40 mm layer of HMA, a 165 mm layer of HMA, and 300 mm graded aggregate base	Two testing sections, with one for control, and a 142 Kg tensile strength geotextile was located between the aggregate base and subgrade in one lane of the section and aligned with the traffic direction.	DCP: 8 kg mass and a drop height of 575 mm, and FWD.
Tang et al. 2014	Six test sections constructed over soft soil subgrade with 24 m long and 4 m wide dimension for each test section	Two unreinforced sections, with one section constructed over an embankment of 30 cm thick sand reinforced with non-woven geotextile. Two other sections reinforced by triaxial geogrids at the aggregate/subgrade interface.	ALF used to apply cyclic moving wheel loads on each test lane section. A nominal speed of 16.8km/h or 350 passes per hour, which applied a 43.3 KN axle load, representing half of the standard axle load, the 80 KN single-axle load was used as well.
Rajagopal et al. 2014	200 m long road section treated with 150 mm thick geocell layer on an experimental basis	Two sections of highway under construction near Chennai were selected, and the road was reinforced with two different types of geogrid (stiff and flexible).	Cyclic load and monotonically load with plate load tests.

Source	Field test dimensions	Field test specification	Loading
Mousavi 2016	Three test sections with comparable subgrade conditions by using different subgrade stabilization measures	Used different subgrade stabilization measures, with select fill material and geosynthetic reinforcement (Geogrid BX1200 and Geotextile HP570) and an almost thin ABC.	Field loading performed by using 1,000 passes of a loaded construction truck.
Hanandeh et al. 2016	Six test sections in which each lane section was 24 m long and 4 m wide	Two control sections, with one section constructed over a non-woven geotextile-wrapped sand embankment; two sections reinforced with triaxial geogrid.	The ALF applied a nominal speed of 16.8 km/h. The tests were designed to apply a maximum load of 44 kN for the first 110,000 passes, followed by a maximum load of 54 kN for additional 100,000 passes and a maximum load of 64 kN for the last 100,000 passes until reaching 19 mm rut depth.
Siekmeier and Casanova 2016	Case study of roads in Iowa	FWD testing conducted at approximately one-eighth mile intervals.	FWD tests using 4-ton pressure.
Cuelho and Perkins 2017	17 test sections 15.3 m long; 14 sections containing geosynthetic reinforcement and three constructed without reinforcement	Compared related practical performance of geosynthetics used for subgrade stabilization. Post-trafficking excavation used to evaluate damage to geosynthetics.	Traffic loads using three-axle 20.6 metric ton dump truck with 620 kPa tire pressure in one direction at 5 mph (8 kph).

ABC=aggregate base course, ALF=accelerated loading facility, CRREL=Cold Regions Research & Engineering Laboratory, DCP=dynamic cone penetrometer, FERF=Frost Effects Research Facility, FWD=falling weight deflectometer, HMA=hot-mix asphalt, HVS= heavy vehicle simulator, RDD=rolling dynamic deflectometer

1.4.4 Factors Affecting Geosynthetic Reinforcement Benefits

The results of the experimental studies show that geosynthetic reinforcement benefits depend on several factors. These factors include strength/stiffness of subgrade layer, base course thickness, HMA thickness, location of reinforcement layer within the base course layer, and geometric and engineering properties of the geosynthetics. Generally, the location of the reinforcement layer depends on the thickness of the base course layer and the magnitude of the applied load (Perkins and Ismeik 1997). Table 5 shows geosynthetic types, properties, and the locations used in the research studies.

Table 5. Properties of geosynthetics and locations in the tests of various researchers

Source	Geosynthetic type	Geosynthetic properties	Geogrid location
Webster 1993	Two general types of geogrids	Three products having a sheet-type structure with a polypropylene polymer composition; remaining three products were coated polyester with a woven structure	Subgrade surface; in two sections, geogrid located in the middle of the base course layer
Perkins 2002	Five sets of geogrids and two sets of geotextiles, with a total of eight types	Geogrids, polypropylene with welded grid, extruded multi-layer, biaxial types, and woven geotextile	Base/subgrade interface; 100 mm and 40 mm above base/subgrade interface
Maxwell et al. 2005	Woven geotextile and two different geogrids	Two different geogrids, both essentially flexible, and a geotextile	Base/subgrade- interface
Zornberg et al. 2008	Biaxial geogrid; woven geotextile	Biaxial geogrids, woven geotextile	Interface between the subgrade and base course
Hossain and Schmidt 2009	Geotextile	142 Kg tensile strength fabric	300 ft aligned with the direction of traffic in the test lane and at the subgrade-base interface
Tang et al. 2014	Triaxial geogrid, high-strength geotextiles	Triaxial geogrid made with polypropylene and geotextile made from high-tenacity polypropylene filaments formed into weaves	Two sections reinforced by the triaxial geogrid and geotextile, placed at the base/subgrade interface, and, in one section, two layers of geogrid at the upper one-third of the aggregate base layer thickness
Rajagopal et al. 2014	Geogrids	Both geogrids of the biaxial type having tensile strengths in the same range	Geogrid layers located within the subbase layer at a depth of 200 mm below the surface
Mousavi 2016	Triaxial geogrid	Triaxial geogrid made with polypropylene	Base-subgrade interface
Hanandeh et al. 2016	Triaxial geogrid, high-strength geotextiles	Triaxial geogrid made with polypropylene and geotextile made from high-tenacity polypropylene filaments formed into weaves	Triaxial geogrid and woven geotextile reinforced for three sections, placed at the base/subgrade interface; in one section, two layers of geogrid used in the upper one-third of the aggregate base layer thickness
Siekmeier and Casanova 2016	Geotextile and geogrids	Biaxial	Base/subgrade interface and within the base layer at different positions

Source	Geosynthetic type	Geosynthetic properties	Geogrid location
Cuelho and Perkins 2017	Geogrids and geotextiles	Twelve geosynthetic products (welded geogrids, woven geogrids, and stronger, integrally-formed geogrid; geotextiles and weaker integrally-formed geogrid)	Base course-artificial subgrade interface

Many studies have been conducted to connect the reinforcement mechanism of pavement systems with their geometric and engineering properties. Some studies also investigated the influence of geogrid aperture sizes versus soil particle dimensions on frictional reinforcement efficiency.

Several geogrid studies demonstrate that the optimal transfer of shear stresses occurs when the minimum width of the geogrid aperture is less than the average particle size of the aggregate materials, D_{50} (Koerner 1997, Perkins 1999, Perkins et al. 2009a, Cuelho and Perkins 2017). Reinforcement stiffness has an important effect on the achieved reinforcement benefits. In general, studies demonstrate that geosynthetics with higher modulus afford better improvement to the stress distribution transferred to the subgrade and reduce the surface deformation compared to geogrids with lower modulus (Perkins 2001, Leng and Gabr 2002).

Also, some experimental studies have been performed on both single-layer and multi-layer geogrid-reinforced sections. For instance, Cancelli and Montanelli (1999) illustrated that multi-layer geogrids show lower deformation than the common single layer geogrid. Their test results indicated that geogrid layers were able to mobilize stresses, preventing local shear failure and deformations in reinforced sections. Table 6 shows layer properties and variables and factors in the manuscripts reviewed in this report.

Table 6. Layer properties and factors in the literature

Source	HMA thickness	Base (Subbase) type and thickness	(Subgrade) materials	Variables (investigated parameters)
Webster 1993	50.8 mm	305, 355, and 457 mm thick, (crushed limestone)	Heavy clay with average subgrade strength of CBR = 7.1 for one case and average CBR = 2.5 for the other cases	Base course thickness, subgrade CBR values, geogrid types, and locations
Perkins 2002	75 mm	300 mm thick, (crushed-stone base course obtained from a quarry in West Lebanon, Montana)	Clay with CBR = 1 and moisture content of 28%	Geosynthetic type and stiffness and locations, pore-water pressure; temperature
Maxwell et al. 2005	75 mm (with 1500 MPa stiffness)	450 mm (with 100 MPa stiffness)	Clay with 70 MPa stiffness	Geosynthetic type and stiffness, environmental variation, moisture content of the lower granular layers

Source	HMA thickness	Base (Subbase) type and thickness	(Subgrade) materials	Variables (investigated parameters)
Zornberg et al. 2008	The top cover of 25.4 mm	New base course layer of 178 mm, scarified existing base course layer of 254 mm, existing base course layer of 127 mm, silty gravel with sand	Gray clay soil excavated with a depth approximately 5 ft with high plasticity, high dry strength, no dilatancy, and high toughness	Geosynthetic types, lime and no lime treatment, environmental, construction, and site factors
Hossain and Schmidt 2009	38 mm topcoat and a 165 mm binder	305 mm of a graded aggregate base	One section elastic silt (MH) with CBR = 4.5, other section with sandy clay (CL) or sandy silt (ML) with CBR = 5	Geosynthetic type and stiffness and locations
Tang et al. 2014	–	254 and 457 mm crushed limestone in the base course	Native subgrade soil with heavy clay (C.H.)	Geosynthetic type and stiffness and locations, base aggregate thickness, embankment layer
Rajagopal et al. 2014	–	200 mm granular aggregates	Black cotton soil undergoing severe swelling and shrinking with CBR = 4 and 8	Geosynthetic types and different construction methods, subgrade stiffness
Mousavi 2016	50 mm	230 mm granular aggregates	Natural Piedmont residual soils classified as A-4, plus soft low-plasticity soils located at the top 80 cm and classified as A-7-5 and stiff high plasticity materials	Subgrade CBR values, load magnitude and repetitions on surface deformation
Hanandeh et al. 2016	19 mm	254 and 457 mm crushed limestone in the base course	Native subgrade soil with heavy clay (C.H.)	Geosynthetic type stiffness and locations, embankment layer, base aggregate thickness
Siekmeier and Casanova 2016	76, 101, 114, 127, 140, 152, and 178 mm	152, 229, 254, 305, and 457 mm and subbase layer for some sections	Different R-values, from 19 to 50	25 FWD drops at approximately 15.24 m intervals
Cuelho and Perkins 2017	–	277, 414, and 632 mm base thickness (crushed aggregates and classified as GP-GC and CBR approximately 20)	Natural overburden material classified as lean, sandy clay (CL), CBR = 1.79	Base course thickness, geosynthetic type, and stiffness

CBR=California bearing ratio, FWD=falling weight deflectometer

1.4.5 Comparison of the Results for Geosynthetic Reinforcement in Flexible Pavements

Many researchers have addressed the benefits of using geosynthetic reinforcement in flexible pavements during the last three decades in conducting laboratory testing, full-scale (large-scale) testing, and numerical modeling. The results of these studies illustrate that the reinforcement mechanism can extend the service lives of reinforced sections and reduce the permanent deformation (rutting) in these sections. This increase in the service life of the pavement structure is commonly defined as the TBR

factor. (As stated previously, the TBR factor is identified as the ratio of the number of repetitions of the load for reinforced over unreinforced sections to achieve a particular rut depth with identical thickness, material properties, and loading properties.)

The results of these investigations show that the required base course thickness might be decreased when geogrids are placed in their design, which are usually defined by the BCR factor. Again, the BCR factor is defined as the reinforced base thickness divided by the unreinforced base thickness for a given traffic level. Table 7 shows a summary of the major findings in the studies related to this project.

Table 7. Summary of major findings in the literature related to instrumentation

Source	Instrumentation	Criteria	Findings
Webster 1993	Four sets of multi-depth reflectometers, MDD, which is an LVDT deflection measuring device	Traffic continued on test item until 76 mm of rutting occurred or each item in the traffic lane reached 25.4 mm of rutting	Geogrid performance is a function of the location depth of geosynthetics; for subgrade strengths greater than CBR = 1.5, geogrid reinforcement had the best performance when placed between the base course layer and subgrade. Mechanism of geogrid reinforcement consisted of grid interlock with the aggregate base material, subgrade confinement, and, to some extent, a tensioned membrane effect.
Perkins 2002	Pore pressure transducers, foil strain gauges, soil stress cells	TBR, performance behavior, rutting behavior, dynamic response behavior	Results showed the geosynthetic reinforcement benefits on subgrade stabilization and base reinforcement. Pore-water pressure also reduced geosynthetic performance and increased deformations. Temperature can cause delamination between binder and courses in AC cracking.
Maxwell et al. 2005	Strain gages, FWD tests and equipment	Larger deflections in the spring and smallest deflections in winter obtained through test sections	Total deflections were always smaller for reinforced sections compared to unreinforced sections. Smaller deflections were measured in sections that were thicker or reinforced with less extensible geosynthetics; greater deflections were typical during spring due to warm and wet conditions.
Zornberg et al. 2008	LVDTs and earth pressure cells	Permanent deformation and surface rutting	Application of geosynthetics can improve the strength/stiffness of the pavement system. Results of monotonically and cyclic load tests were close to each other.
Hossain and Schmidt 2009	FWD testing, RDD testing and related equipment, moisture sensor	Pavement performance: deflection under testing	Structural damage not observed in the pavement in the year and half of service; however, moisture led to the phenomena of differential volume change as the cause of longitudinal cracking. Better performance of geosynthetic reinforced pavements identified in terms of reducing permanent deformation, and geogrid reinforcement provided benefits by stabilizing pavement over subgrade with clays of high plasticity. Junction strength was the most critical factor controlling confined stiffness of geogrids. Reasons related to low performance of one geosynthetic can be related to its low junction strength, high manufacturing variability, high sensitivity to installation damage, and low friction coefficient.

Source	Instrumentation	Criteria	Findings
Tang et al. 2014	DCP, FWD and equipment	Deformation from loading	Service life prolonged up to 16% with geotextile reinforcement after eight months of traffic. Geotextiles can reduce permanent deformation about 20% for less permeable, densely graded aggregates above subgrades with CBR \leq 3. For stiff soils with CBR = 9, neither contamination nor slipping observed with geotextile reinforcement. However, comparison was inconclusive given geotextile slipping and uneven contamination.
Rajagopal et al. 2014	LVDTs, potentiometers, strain gauges, thermocouples, reflectometer, earth pressure cells, and piezometers at the top of the subgrade layer	Permanent deformation and surface rutting	Sections with geotextile showed less permanent deformation than sections with geogrids. Majority of permanent surface deformation attributed to aggregate layer instead of soft subgrade soil layer. No marked change of aggregate layer moduli before/after loading detected from non-destructive LWD and Gg tests.
Mousavi 2016	DCP, FWD and equipment, pressure cells	Permanent deformation, surface rutting and vertical stress	Rut depth values increased with number of truck passes until they reached a relatively constant value within 1,000 truck passes, and the variation of the tests have a direct effect on the results. Vertical stress values measured near the interface of the subgrade for the geosynthetic-reinforced sections decreased with traffic.
Hanandeh et al. 2016	Two earth pressure cells, piezometers, spring-loaded LVDTs, potentiometers, Gg, LFWD, DCP, and PSPA	Rutting behavior 19 and 25.5 mm at the top surface	Adjusted TBR can increase to 2.12, with a rut depth of 19 mm for a 458 mm thick base layer on weak subgrade soil with two layers of geogrid reinforcement. Double layer of geosynthetics can enhance performance of the base layer more than one layer. Geosynthetics are capable of providing appreciable benefits in decreasing permanent deformation rather than the resilient properties of the subgrade layer.
Siekmeier and Casanova 2016	FWD equipment	FWD data during spring thaw	Layer of geogrid provides an average increase in GE of 5.3 in. and an additional 2.2 in. of GE compared to a geocell. Geogrids at a depth of 203 mm in a 254 mm reclaim layer provide an increase of 1.3 in. of GE compared to those at a depth of 152 mm. No apparent difference in effective GE between geogrid or type V geotextile fabric at the total depth of 508 mm. Type V geotextile fabric provides an approximate increase in GE of 2.3 in. compared to geocell. Type V geotextile fabric at a depth of 355 mm compared to 610 mm provides an apparent increase in GE of 2.7 in. 25.4 mm of bituminous surfacing provides an increase in GE ranging from 2.0 in. to 5.3 in. 100 mm of stabilized full-depth reclamation provides an increase in GE ranging from 1.7 in. to 7.6 in.

Source	Instrumentation	Criteria	Findings
Cuelho and Perkins 2017	LVDTs, resistance strain gages, pore-water pressure gages, LWD, DCP, in-field CBR, and nuclear densimeter tests	Rutting behavior 19 mm at the top of the surface	Longitudinal ruts can be the primary indicator of performance, intrinsic factors that influence performance may be due to the strength/stiffness of junctions and by the tensile strength in the cross-machine direction (by linear regression). Woven and non-woven geotextile performs well in separation. Rutted areas were where most of the damage from ribs were found, and no noticeable damage was found for geotextiles. For most geosynthetics, their strengths at 2% strain increased, and ultimate strengths that decreased the pore-water pressure did not show a clear trend in affecting performance of geosynthetics. The Giroud and Han design method underpredicted the depth of the base material needed to support the loads applied.

AC=asphalt concrete, CBR=California bearing ratio, DCP= dynamic cone penetrometer, GE=granular equivalent, Gg=geogauge, LFWD=light falling weight deflectometer, LVDT=linear variable differential transformer, LWD=lightweight deflectometer, MDD=multi-depth deflectometer, PSPA=portable seismic property analyzer, TBR=traffic benefit ratio)

Mitchell et al. (1979) performed a full-scale test on unpaved roads reinforced by the inclusion of non-woven geotextiles and geomembranes in the sections. The results of rutting distress showed that geosynthetic reinforcement can reduce the required base thickness. The researchers also confirmed that the effects of geosynthetic reinforcement are more important when the strength of the subgrade is low.

Webster (1993) conducted tests on six road sections, including the control section, one geogrid-reinforced section, and three geotextile-reinforced sections. All sections had a 100 mm base course thickness with a poorly-graded sand subgrade (CBR = 10). The results for the geotextile-reinforced sections showed that the reinforced sections did not perform better than the control section, probably due to the lateral movement of aggregates at the aggregate-geotextile interface, which limits the reinforcement effect of geotextiles.

Another paved road, in Bedford County, Virginia, was investigated in 1994 to measure pavement response to cyclic loading (Al-Qadi et al. 1994). The sections contained three sections of geotextiles, three sections of geogrids, and three unreinforced control sections. The results for the pavement sections were monitored for more than three years. The results for the geotextile-reinforced sections showed lower vertical stress at the top of the subgrade and less rutting depth compared to geogrid-reinforced and unreinforced sections.

Perkins and Cuelho (1999) found that geosynthetic reinforcement of test sections with 75 mm of asphalt and 200 mm to 375 mm base material thickness provided important benefits when the subgrade had a CBR of 1.5 or less, and many benefits were noted when the subgrade had a CBR of 20 or more.

Perkins (2002) initiated a project to provide a better analysis of the effect of traffic loading and geosynthetic reinforcement type. Four different full-scale test sections were developed and tested with heavy vehicle simulator (HVS) equipment. The test was implemented based on a previous test by Perkins and Cuelho (1999), wherein, three types of geosynthetics were identical, including eight types of

geosynthetics total. Additional test sections utilized the previous test box to examine the influence of aggregate type and thickness reduction of the base course incorporated with different types of reinforcement to show the effects of geosynthetic/aggregate shear interaction specifications on the reinforcement benefit.

The results showed unreinforced test sections with rounded aggregate (maximum particle size of 38 mm) had lower performance than unreinforced sections with crushed aggregate (maximum particle size of 19 mm). The inverse result was true for reinforced sections, which did not correspond to the results from direct shear tests, while it can be concluded that the direct shear test may be useful in defining the reduction factor for interface shear.

The TBR (extension of life) was defined by back-calculation using the ASSHTO Guide for Design of Pavement Structures (AASHTO 1993) with base course thickness reduction from previous test results, and with the verification of service life comparisons between building sections with reduced thickness and unreinforced ones. Perkins (2002) showed the 1993 ASSHTO guide was too conservative, except for the condition where aggregate was excessively thin (less than 150 mm in thickness). The pore-water pressure had a significant impact on the pavement during loading, with its magnitude during pavement loading being highly dependent on its initial value, and on the set-up time of the subgrade, with the threshold greater than 16 days of set-up time identified. The pore-water pressure under adjacent sections can negatively affect TBR and performance behavior, showing the need for additional comparative research to develop design methods that incorporate pore-water pressure.

A field investigation on geosynthetic-stabilized subgrade was conducted by Cuelho and Perkins (2017). For this study, 12 test sections, 10 reinforced and 2 unreinforced, with a thin base layer, were constructed at a Montana Department of Transportation (MDT) facility on poor subgrade material. A fully loaded three-axle dump truck was used to apply loads on sections. Loading was applied in a single direction on each test section until it reached an average of 100 mm of permanent deformation.

This research showed that tensile strength at 2% and 5% in the cross-machine direction of geogrids plays an important role in the stabilization of weak subgrade soils. Analysis of displacement of the geosynthetics found that, by applying wheel load pulses, the rutting bowl began to form on the side of the vehicle toward the edge of the test sections, and geosynthetic begin to move toward the rutted areas. The authors believed that the primary reinforcement mechanism of geosynthetics changes from the lateral restraint of the base course to the membrane effect.

A rapid rate of rutting was observed in some test sections. These were sections with a shallow depth of gravel base course having a high percentage of rounded particles. The base course was not able to carry the heavy loads imparted by the test vehicle. The mode of failure of these test sections was a shear failure in the subgrade and involved tensile rupture of several geogrid products and a pullout of one geotextile product.

A follow-up study by Cuelho and Perkins (2017) was initiated to determine which properties of geosynthetics play a significant role in subgrade stabilization. In this study, new test sections with a thicker base course were constructed to further investigate the performance of geosynthetics under less

severe conditions. Statistical analysis of test results revealed that junction strength and stiffness of the geogrids, wide-width strength, and cyclic stiffness in the cross-machine direction correlate reasonably well with rut performance. The results of the rutting analysis indicated that the woven geotextile performed the best. Using the woven geotextile resulted in a TBR of 11 and a base course reduction of 26.9%. The non-woven geotextile, although the weakest product in terms of tensile strength, performed better than many of the geogrid products.

Siekmeier and Casanova (2016) performed a study to investigate and better understand and assess the structural benefit of geosynthetic reinforcement on both short-term and long-term performance of flexible pavements. During the spring of 2013, FWD tests were conducted on two trunk highways in the MnDOT Bemidji District to compare geosynthetic-reinforced roadways with unreinforced sections. The testing occurred on MN 11 and MN 72 in Lake of the Woods, Koochiching, and Beltrami counties and was completed within the first week following a complete thaw.

A total of 29 different pavement sections with varying lengths and years of construction were selected for testing. The shortest continuous segment was 400 m in length, and they proposed to use 400 m as the baseline segment in each test section. Within this baseline segment in each test section, they collected data for 25 FWD drops at approximately 15.24 m intervals. MnDOT provided information on all different pavement sections for the variables, including length and year of construction, layer thicknesses, geosynthetics used, and traffic volume. Outside the baseline segments, FWD testing was conducted at approximately 200 m intervals to allow for advanced spatial analysis into variability.

The researchers found that geogrids provided an increase in the GE factor of several millimeters in some situations. The results showed that a layer of geogrid provides an average increase in GE of 135 mm, and geogrids at a depth of 203 mm in a 254 mm reclaim layer provides an increase of 33 mm of GE compared to that at a depth of 152 mm. There was no apparent difference in effective GE between geogrids or type V geotextile fabric at the total depth of 508 mm. Type V geotextile fabric at a depth of 355 mm compared to 610 mm provided an apparent increase in GE of 70 mm. It was concluded that geogrids generally reduce pavement deflection.

1.5 SUMMARY DISCUSSION OF FACTORS AFFECTING GEOSYNTHETIC REINFORCEMENT

As discussed previously, several factors, including strength/stiffness of the subgrade layer, base course thickness, HMA thickness, location of the reinforcement layer within the base course layer, the geometric and engineering properties of the geosynthetic's affect on the geosynthetic reinforcement of the flexible pavement, and often all of the variables' affect on the geosynthetic performance are interdependent and act simultaneously. A brief discussion of these factors based on the different investigation findings presented in this section follows.

- **Strength/stiffness of the subgrade layer:** As the subgrade layer strength goes down, geosynthetics are more beneficial (Abu-Farsakh et al. 2016). The reinforcement provides important benefits when the subgrade has a CBR of 1.5 or less, and many benefits are noted when the subgrade has a CBR of 20 or more (Perkins and Cuelho 1999). Geosynthetic reinforcement can reduce permanent deformation about 20% for subgrades with a CBR of 3 and lower (Hossain and Schmidt 2009).

- **Base course thickness:** Geosynthetic reinforcing can reduce base course thickness for a given traffic level as defined by the BCR factor and the average base course thickness reduction of 27% for pavement depends on other factors as well (Cuelho and Perkins 2017), but, usually, the BCR factor for assessing the decreasing the base thickness ranges from 11% to 44% for pavements with geosynthetic reinforcement (Ghafoori and Sharbaf 2016). A layer of geogrid provides an average benefit using BCR at 135 mm; however, there is no apparent difference in BCR between geogrid or geotextile fabric at a depth of 500 mm or more in pavement (Siekmeier and Casanova 2016a).
- **HMA thickness:** Depending on the traffic level, increasing the thickness of the HMA layer can decrease the benefits of the geosynthetic reinforcement; however, this increase can also result in decreases for the required base course for the same traffic repetitions. Some studies show that increasing the bituminous surfacing layer by 25 mm can provide decreases in the required base course thickness from 50 mm to 130 mm in the pavement foundation (Siekmeier and Casanova 2016a).
- **Location of reinforcement layer:** Although the results are conflicting regarding the optimal location of geosynthetics in the pavement layers, most studies placed reinforcement at the bottom of the base course layer. Generally, the optimal location of the reinforcement layer depends on the thickness of the base course layer and the magnitude of the traffic loads (Perkins and Ismeik 1997); however, for subgrade strengths greater than CBR = 1.5, the geogrid reinforcement has the best performance when placed between the base course layer and the subgrade (Webster 1993). For thin aggregate base course layers (e.g., 40 mm) and very weak subgrade layers, the optimal location is at the interface between the aggregate base course layer and the subgrade (Moghaddas-Nejad and Small 1996). For a 250 mm thick aggregate base layer, the best position is also at the interface (Haas et al. 1988). However, some studies suggest that, for heavy loads and thicker aggregate base course layers (more than 250 mm), the optimal position is in the middle of the aggregate base course layer. For very heavy loads, studies show that placing geosynthetics at the range of 350 mm at the bottom of the thick aggregate base course layer is better than placing them in the middle of the aggregate base course layer (Zornberg and Gupta 2010).
- **Geometric and engineering properties of the geosynthetic (strength and stiffness):** In general, studies demonstrate that geosynthetics with higher modulus provided better improvement to the stress distribution transferred to the subgrade and reduce the surface deformation compared to geogrids with lower modulus (Perkins 2001, Leng and Gabr 2002). Also, multi-layer geogrids show lower deformation than the common single layer geogrids (Cancelli and Montannelli 1999). A double layer of geosynthetics can also enhance the performance of the base layer more than one layer of geosynthetics. The optimal transfer of shear stresses occurs when the minimum width of the geogrid aperture is less than the average particle size of the aggregate materials, D_{50} (Koerner 1997, Perkins 1999, Perkins et al. 2009a, Cuelho and Perkins 2017) so it is recommended that the aperture sizes of geogrids and base material particle sizes should properly be selected (more than 1.3 times the maximum dimensions of the aggregate for the geogrid aperture sizes).

CHAPTER 2: LABORATORY TESTS AND RELATED LAB DATA

2.1 IAMS EQUIPMENT

The integrated mobile accelerated test system (IMAS), shown in Figure 8, was used to perform the laboratory tests for this project.



Figure 8. Integrated mobile accelerated test system for laboratory tests

2.2 TEST SECTIONS, CONFIGURATIONS, SENSORS, AND PROCEDURES FOR PERFORMING THE TESTS

The IMAS apparatus was developed by David White of Ingios Geotechnics, Inc. to mimic field loading conditions of roadway systems in a large-scale laboratory system, wherein the conditions can be more easily controlled. The IMAS performs a cyclic load test with a large number of load cycles, which simulates vehicle-loading conditions on a pavement foundation. The IMAS can help determine the resilient modulus, deflection, and permanent deformation of the pavement over time so that the service life of the pavement system and the long-term performance of the pavement structure can be evaluated.

The IMAS has a square base container, where the depth is 3 ft and the length is 5 ft. Boundary effects and simulation of the stiffness of the natural soils are controlled through the use of rigid walls and a foam layer. The load plate system and hydraulic actuator are above the test specimen in the center of the device to provide the repeated loading during the test. All the sensors are connected to the data acquisition system, and the results can be recorded during the test for up to one million cycles.

This section and the next section of the report describe the test sections, configurations, sensors, and procedures for performing the tests.

2.2.1 Test Sections

Factors that can affect GE values of geogrids include geogrid stiffness, geogrid aperture, and rib shape, aperture and rib sizes, the geogrid location/depth, HMA thicknesses, base aggregate quality, stiffness, thicknesses, and subgrade stiffness.

Figure 9 shows the test sections studied using the IMAS device and finite element analyses.



Note: GE values of sections #0, #1, #2, #4, #5, #7, #12, and #15 are determined based laboratory tests. GE values of sections #3, #6, #8, #9, #10, #11, #13, #14, and #16 are computed based on numerical simulations.

GE values of sections #0, #1, #2, #4, #5, #7, #12, and #15, are determined based on laboratory tests. GE values of sections #3, #6, #8, #9, #10, #11, #13, #14, and #16 are computed based on numerical simulations.

Figure 9. IMAS laboratory test sections and finite element model sections

Tests were conducted on eight IMAS test sections to evaluate the reinforced base course behavior using different types of geogrids and with different locations, named as follows: GE0, GE1, GE2, GE4, GE5, GE7, GE12, and GE15. GE0 was the control section, and no geogrid was installed in this section. Biaxial geogrids were used in GE1, GE2, and GE5, and triaxial geogrids were used in GE4, GE7, GE12, and GE15. For GE1, GE2, GE4, and GE12, the geogrids were placed at the interface between the base course layer

and the subgrade layer; for GE5 and GE7, the geogrids were installed at the middle of the base course layer. Both light-duty and heavy-duty geogrid products were used in the test sections. The details for the test sections are shown in the previous Figure 9.

The main parameters studied were geogrid type (biaxial or triaxial), geogrid stiffness (“light” duty or “heavy” duty), geogrid location/depth, and aggregate base thickness. Seventeen sections (or combinations) were studied using a combination of experimental testing (using the IMAS) and finite element modeling. The IMAS sections were used to calibrate the finite element models. Again, section #0 was a control section (with no geogrid) and the remaining sections (#1 to #16) were experimental sections stabilized with geogrid.

In summary, IMAS experimental laboratory tests were performed on eight sections (sections #0, #1, #2, #4, #5, #7, #12, and #15). This determined eight GE values (with control section #0 having just GE gain). The finite element method (FEM) models were later calibrated based on the results of these eight sections.

Then, the calibrated FEM models were used to determine GE values for the remaining nine sections: #3, #6, #8, #9, #10, #11, #13, #14, and #16. These results were later verified using full-scale field-testing pavement sections.

2.2.2 Test and Sensor Configurations

The research team developed the IMAS configuration shown in Figure 10.

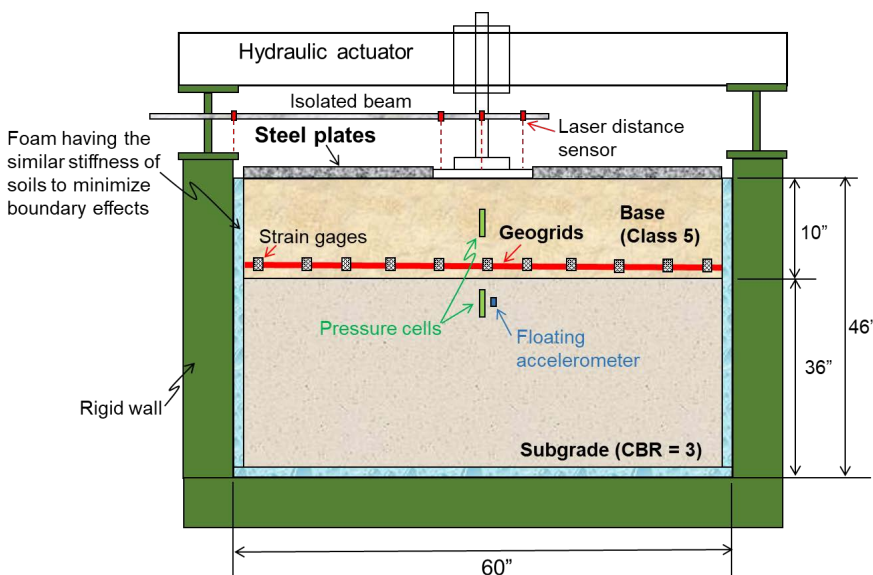


Figure 10. Test configuration in IMAS device

The thickness of the subgrade layer is about 20 in. The rigid wall of the IMAS box may cause boundary effects; therefore, foam blocks were installed between the rigid walls and the soil materials. This foam layer has a similar stiffness of soils between rigid walls and soils to minimize any boundary effects.

Strain gauges were installed on the geogrids to measure strain, which indicates how much the geogrid is mobilized under loading. Linear variable differential transformers (LVDTs) were installed on top of the HMA surface (using steel plates to simulate loading in the field) to measure the deformation basin. LVDTs were also installed at the bottom of the Class 5 aggregate layer to measure the deformation basin of subgrade soils. Pressure cells were installed at the bottom Class 5 layer to measure force distribution in the pavement foundation and confirm the benefit of geogrids on the distribution of vertical stress on the top of the subgrade.

2.2.3 Loading Pattern

For each test, the load was provided in the IMAS using a 12-in. diameter loading plate sitting above the center of each test section. For each test section, to simulate real traffic loading, 100 different loading shape patterns were assumed and randomly selected during loading. Although the loading pattern was random, the distribution followed the same standard for each test section.

A total of 100,000 cycles loading were performed for each section with a cyclic load pulse time of 0.15 seconds and a dwell time of 0.85 seconds. Each complete test took about 17 hours to conduct. Table 8 provides detailed information on the loading pattern showing the magnitude, number of cycles, distribution, and load and dwell time. Ten loading levels were implemented in the tests, as shown in Table 8.

Table 8. Ten loading distribution levels in IMAS tests

No.	Max load (lb)	Min load (lb)	Cyclic stress (psi)	Distribution (%)	Cycles (no.)
1	513	226	2.5	5	5,000
2	1,013	226	7	8	8,000
3	1,526	226	11.5	15	15,000
4	2,039	226	16	22	22,000
5	2,539	226	20.5	16	16,000
6	3,052	226	25	12	12,000
7	3,565	226	29.5	9	9,000
8	4,073	226	34	6	6,000
9	4,586	226	38.5	5	5,000
10	5,086	226	43	2	2,000

Instead of adding loads incrementally, the IMAS was programmed to randomly select loads from 10 loading levels, following a normal distribution, as shown in Table 8. This better simulated realistic traffic loading with a mix of light and heavy vehicles. Figure 11 illustrates the normal distribution of the loading pattern as well.

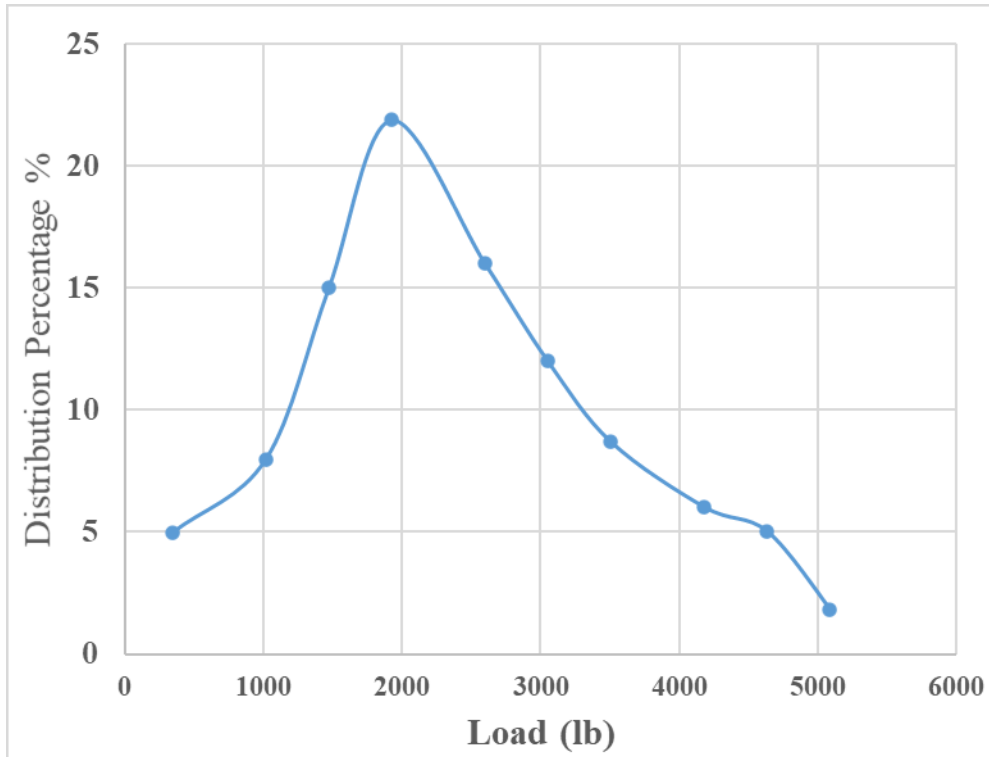


Figure 11. Distribution of loading pattern

2.2.4 Geogrids, Aggregates, and Subgrade Soils

2.2.4.1 Geogrids

The following Tensar geogrids were used in the laboratory tests: light-duty Tensar BX1100 Biaxial, heavy-duty Tensar BX1200 Biaxial, light-duty Tensar TX130s Triaxial, and heavy-duty Tensar TX7 Triaxial. The properties of these geogrids are shown in Appendix A. It should be noted that biaxial geogrids have different sizes and strength in each direction while the strength for triaxial geogrids is equal for each direction. Figure 12 illustrates the machine direction and cross-machine direction for biaxial geogrids.

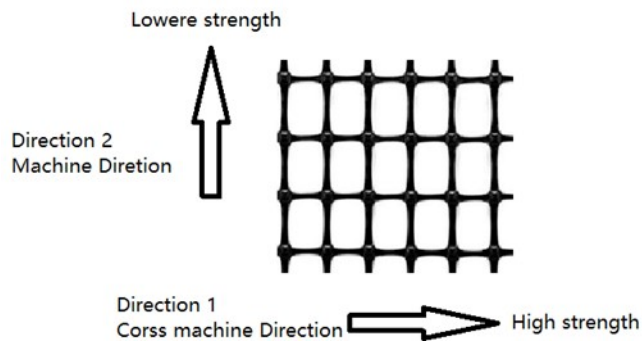


Figure 12. Biaxial geogrid directions

2.2.4.2 Base Course Material Properties

Class 5 aggregates, which are typically used in Minnesota for the base course of pavement construction projects, were used for the aggregate base layer in the laboratory. The results of index property tests on the materials used are shown in Appendix B. Comparison to the MnDOT specification for Class 5 aggregates is shown on the grain-size distribution curve in Appendix C.

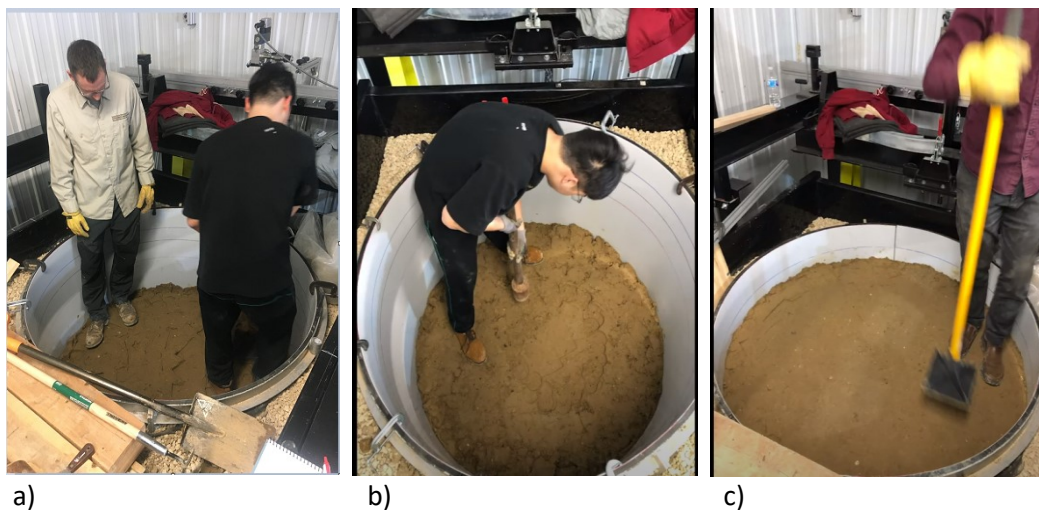
2.2.4.3 Subgrade Soil Properties

The subgrade soil used had a CBR = 3, which is representative of common subgrade soil conditions in Minnesota. Ingios Geotechnics, Inc. performed index property tests on the subgrade soils. The detailed report is shown in Appendix C. From Appendix C, it is shown that the soil was classified as A-7-6(2) and sandy lean clay (CL) according to AASHTO and the Unified Soil Classification System (USCS) methods, respectively, with liquid limit and plastic limit values of 30 and 22, respectively, and a plastic index value of 8. To achieve CBR = 3, the subgrade was prepared at a target moisture content of 16.6% (see Appendix C).

2.3 TEST PREPARATION AND SENSOR SETUP

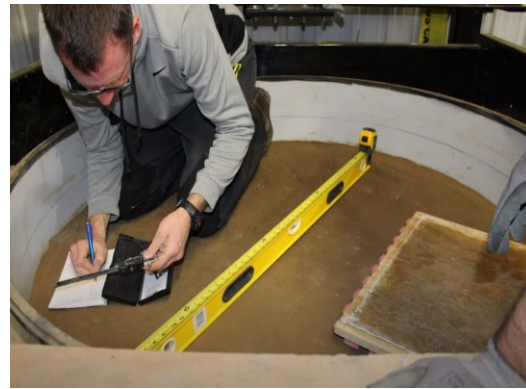
2.3.1 Subgrade Preparation

The subgrade soil was added layer by layer, each having less than 15 in. loose height, to reach a uniform compacted condition. A 50-lb drop hammer, which is a compaction soil hammer, was used to provide the compaction after adding each layer. To keep the surface flat, a tamper was also used after each compaction. Finally, after cleaning the surface, a surveyor's spirit level instrument was used to measure and level the surface. The subgrade preparation steps are illustrated in Figure 13.





d)



e)

Figure 13. Subgrade preparation procedures: a) add soil layer, b) compact soil with a hammer, c) level the soil layer with a tamper, d) add soil, layer by layer, and compact each layer, and e) perform measurement and final leveling of subgrade surface

2.3.2 Base Layer Preparation

After subgrade preparation, the geogrid was placed at the subgrade surface in some sections. Then, the aggregates were placed above the geogrid layer. A rake was used to level the surface. After leveling the surface, a compactor was used to provide the compaction on the base layer for three minutes. The plate compactor used in the compaction step and its specifications, along with compaction details, are presented in this section as well. The base preparation steps are illustrated in Figure 14.



a)



b)

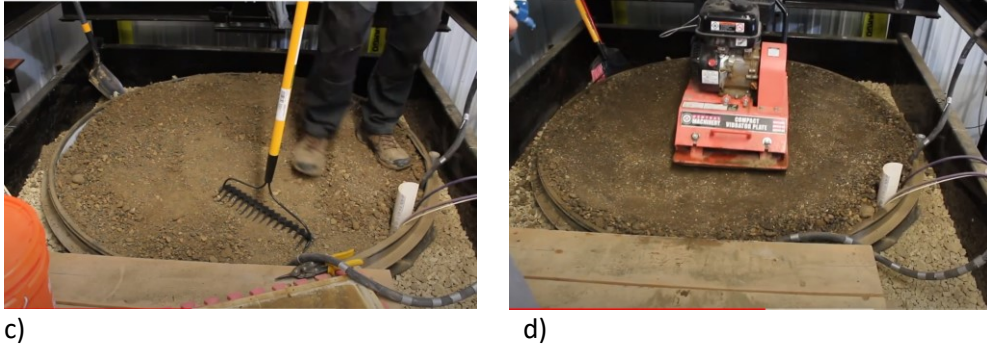


Figure 14. Base layer preparation steps: a) place the geogrid, b) add aggregate on top of the geogrid, c) level and prepare the aggregate surface layer, and d) compact the aggregate layer

To make sure the geogrid obtains the maximum involvement and interlocking with the aggregates at the interface, a 1 in. thick layer of aggregate was placed at the top of the subgrade surface. Then, the geogrid was placed at the top of this thin layer, and base materials were then placed and compacted. Figure 15 illustrates the concept and steps to place the geogrid at the top of the subgrade layer.

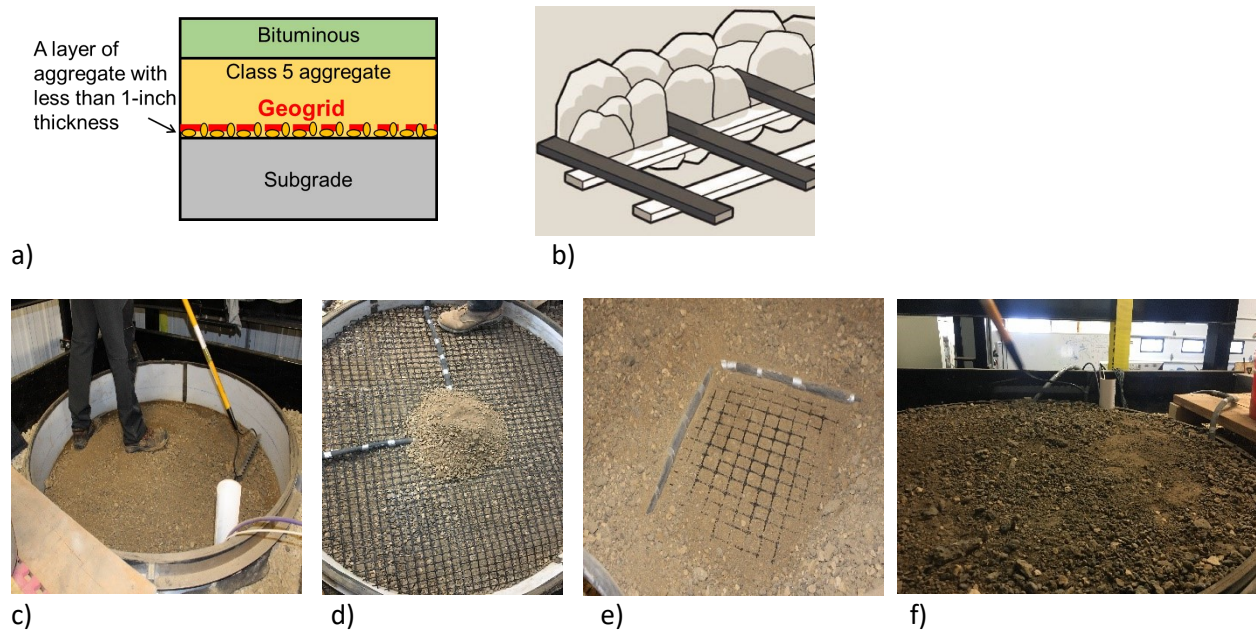


Figure 15. Application of 1 in. aggregate layer through the geogrid at the interface: a) aggregate layer placed with less than 1 in. thickness, b) aggregates entrapped in the geogrid apertures, c) thin layer of aggregate spread on top of the surface, d) geogrid placed on top of thin aggregate, e) aggregate added and spread across and through the top of the geogrid, and f) base materials placed on top, leveled, and prepared for compaction

To compact the base layer, a 6.5 HP plate compactor was used for three minutes after placing the 10-in. of base materials and adding adequate moisture to compact the base layer. Table 9 provides the specifications for the compactor.

Table 9. Specifications of the plate compactor

SKUs	69738,66571,69086
Certification	EPA
Brand	Central Machinery
Engine Brand	Predator®
Horsepower (hp)	6.5
Engine displacement (cc)	179cc
Speed (max)	5500 VPM
Plate length (in.)	16-1/2in.
Plate width (in.)	22 in.
Product Height	35-3/8 in.
Product Length	34-1/2 in.
Product Width	15-1/4in.
Product Weight	176.00 lb
Shipping Weight	176.60 lb
Travel speed (ft/min)	0-82
Vibration frequency (VPM)	5500
CA Residents	Warning Prop 65 Info

A tamper was used to level the final surface of the base layer for each test section. Figure 16 shows the steps that were followed to compact the base layer.



a)



b)



c)



d)



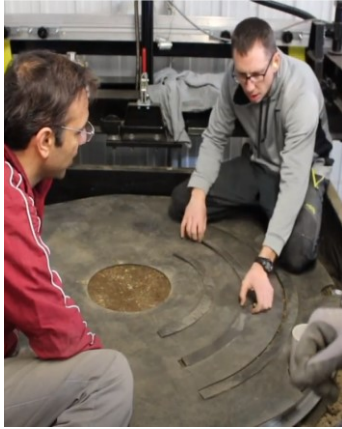
e)

Figure 16. Steps to compact the base layer: a) compactor used, b) prepare the compactor, c) level the aggregate surface, d) compact the base layer, and e) level the surface after compaction

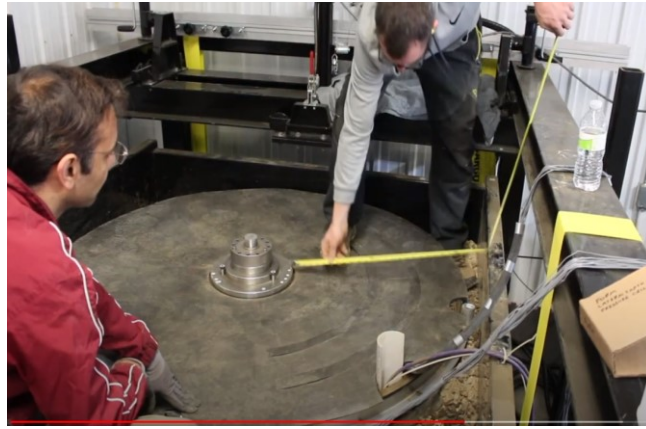
Dynamic cone penetrometer (DCP) tests were performed for quality control in each section, with the results shown in Appendix C, and Proctor and sand cone test results are shown in Appendix D.

2.3.3 Surface Layer Preparation

It would be difficult to pave an asphalt surface for the laboratory tests using the IMAS. Therefore, the asphalt layer was simulated using steel plates, which provided an equivalent weight of the real asphalt surface. The normal asphalt surface layer was replaced with a double layer of steel with the loading plate set in the middle of the container. Then, a thin foam layer was placed on top of the base layer to provide friction and protection with the double layer of steel set around the loading plate. Each steel layer has seven triangular pieces of the pie to cover the flat circular surface of the base material. The final step was to connect all the sensors to the data acquisition system. These surface preparation steps are illustrated in Figure 17.



a)



b)



c)



d)



e)

Figure 17. Surface layer preparation steps: a) place a plastic cover layer on top of the aggregate, b) adjust the loading plate on the center of the aggregate layer, c) place the steel layer on top of the plastic cover layer, d) adjust the sensors, and e) set up the strain gauge data acquisition system

Installation of the steel surface plates are illustrated in Figure 18.



Figure 18. Steel surface plate installation: a) set first layer of steel plates and b) set the second layer of steel plates

2.3.4 Sensors and Sensor Set-Up Procedure: Selection of the Instrumentation

A great amount of information is needed to help compare and evaluate the behavior of the reinforced base course using different types of geogrids and determine the optimal location to place the geogrids. To compare pavement system performance between each test section, measurements of permanent deformation, stress at both the subgrade and base layer, and strain behavior on the geogrid rib in different directions were recorded. These measurements were used to help understand the mechanism(s) for each geogrid reinforced system.

Three instruments were selected based on the literature review, the data type, and the cost. A laser LVDT was used to measure the deformation developing on the pavement (via the steel surface in the laboratory), strain gauges were used to measure the strain behavior in the geogrid ribs, and a pressure cell was used to record the pressure. The instruments are shown in Figure 19.

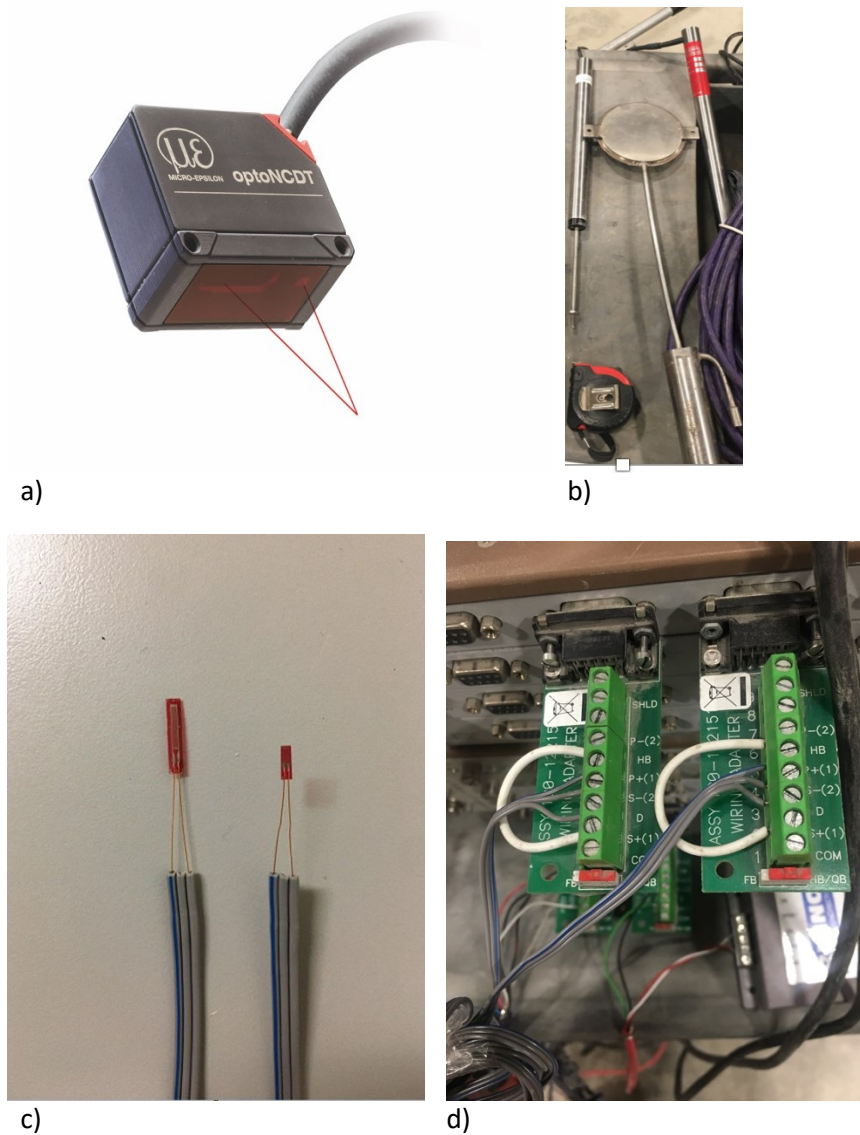


Figure 19. Instrumentation: a) laser surface deformation sensor, b) pressure cell sensor, c) two types of strain gauges for biaxial and triaxial geogrids, and d) strain gauge data acquisition system

To measure the load mobilization and strain behavior of the geogrid in each test section, strain gauges were installed on the top surface of the geogrid in each section. For both triaxial and biaxial geogrids, the strain gauges were placed in two directions. For biaxial geogrids, the aperture is rectangular, direction 1 is set at the short side and direction 2 is set at the long side, and the angle between them is 90°. For triaxial geogrids, since the aperture shape is in an isosceles triangle pattern, direction 1 and direction 2 are selected randomly because they have the same size and length on the geogrid as well as at the junction. The pressure cells were located at the center of the layer below the loading plate and covered by sand, as shown in Figure 20.



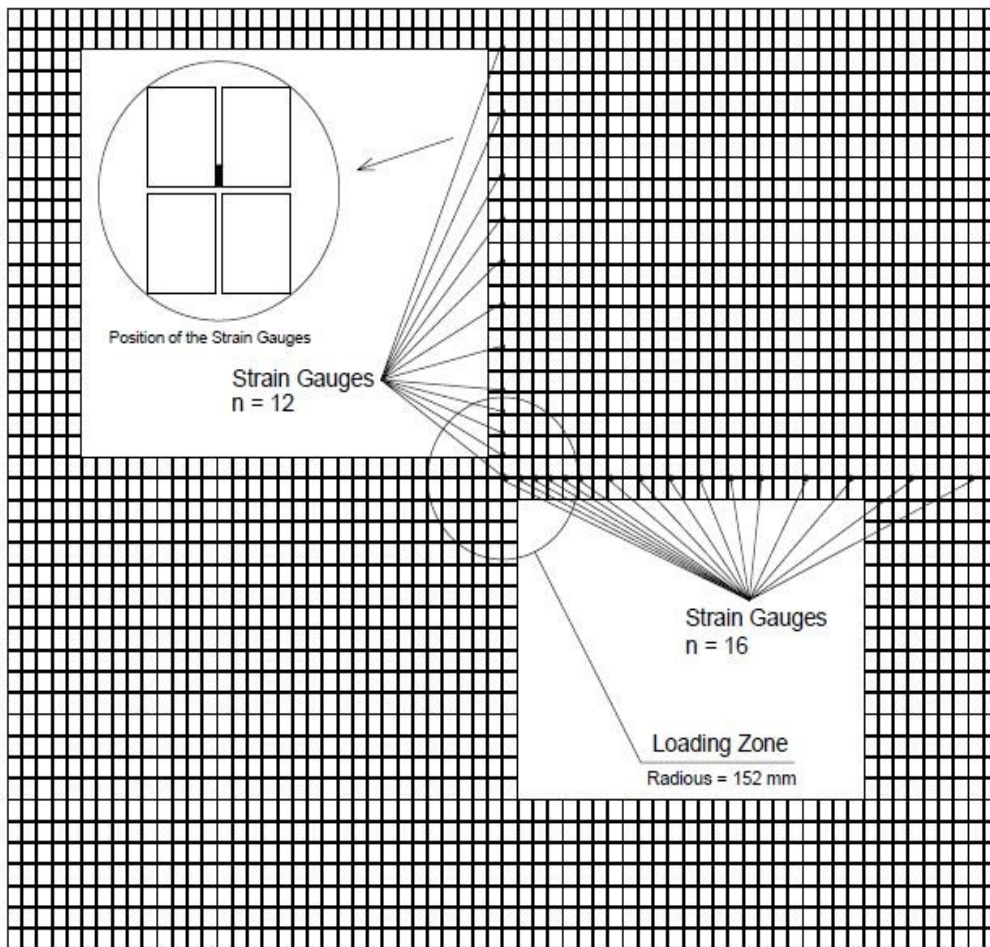
a)



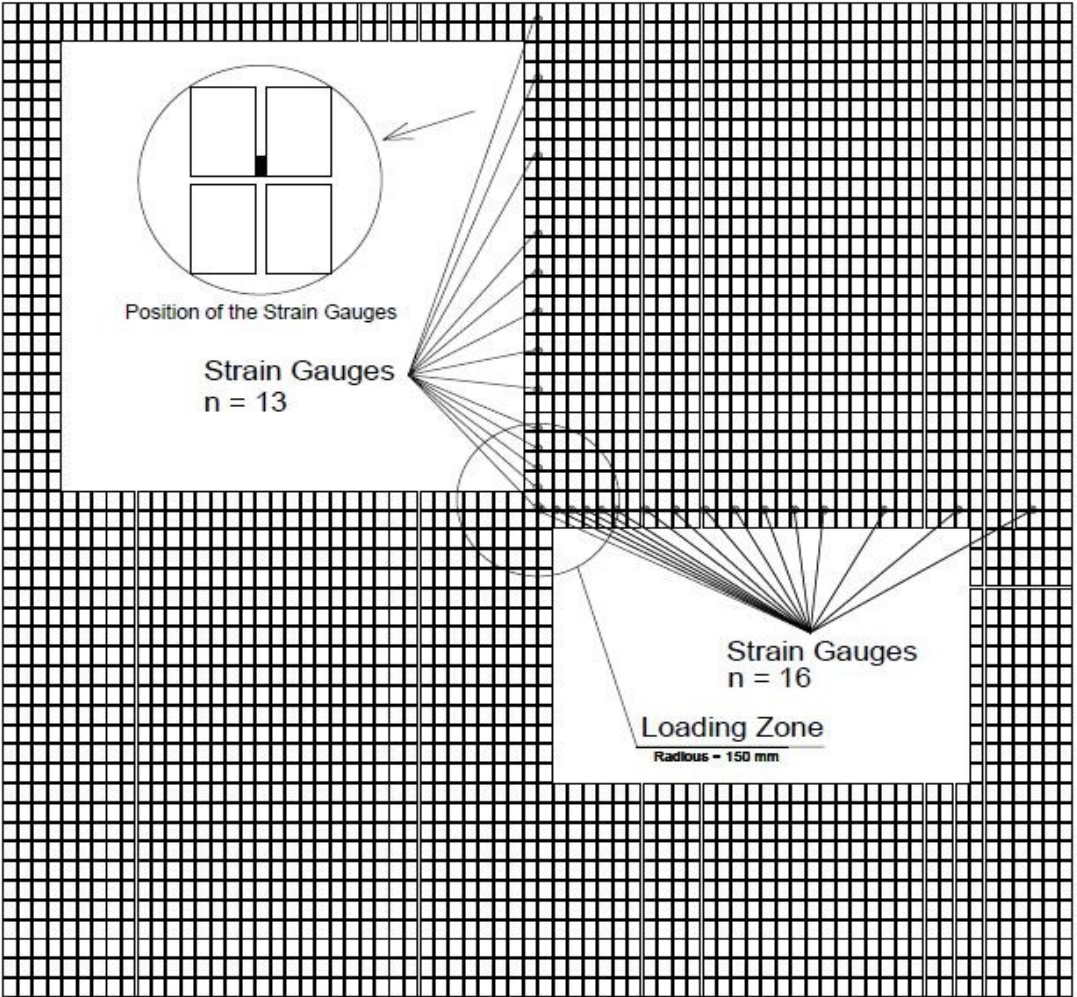
b)

Figure 20. Installation of earth pressure cells: a) place the pressure cell and b) cover the pressure cell with sand

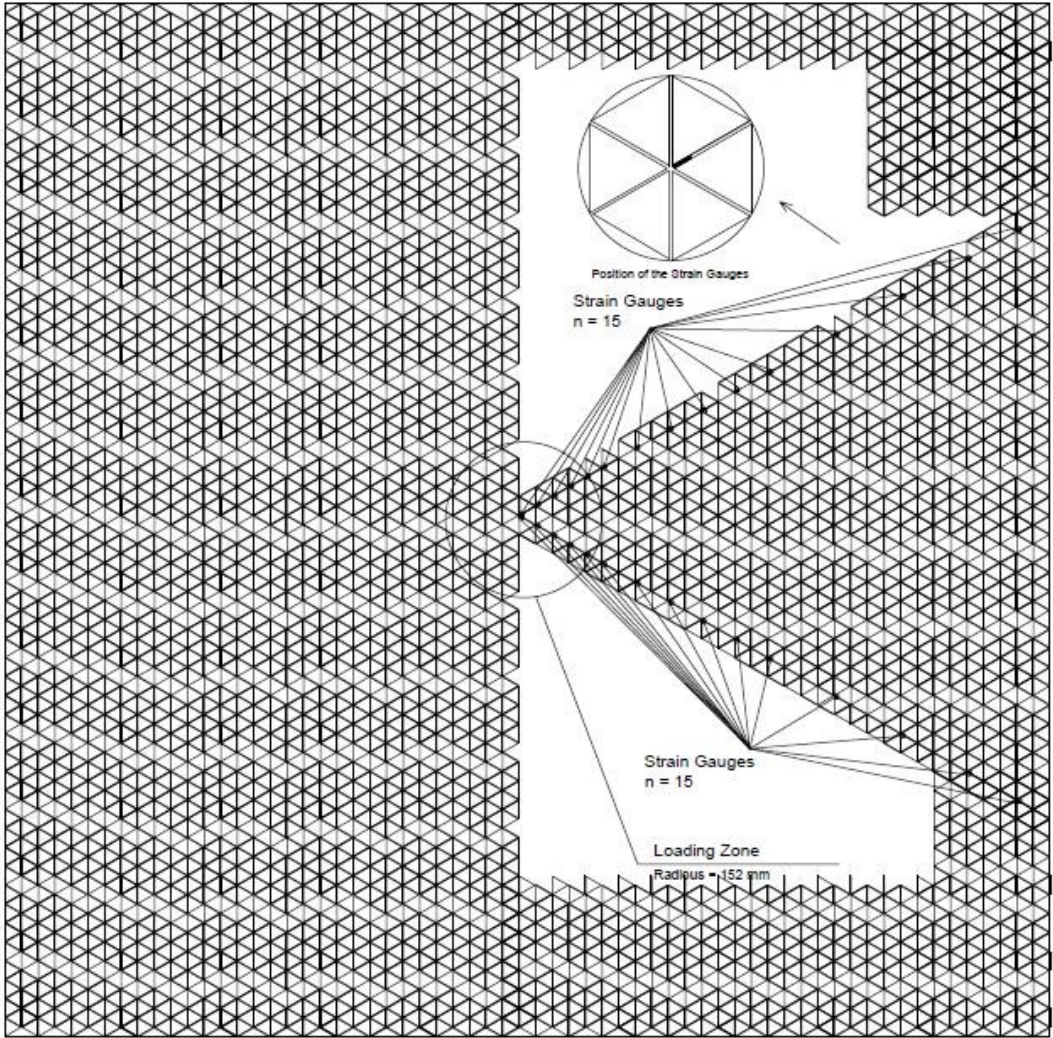
The sand can protect the sensor during loading and compaction of the base material. Figure 21 shows the layout for the strain gauges on the biaxial and triaxial geogrid.



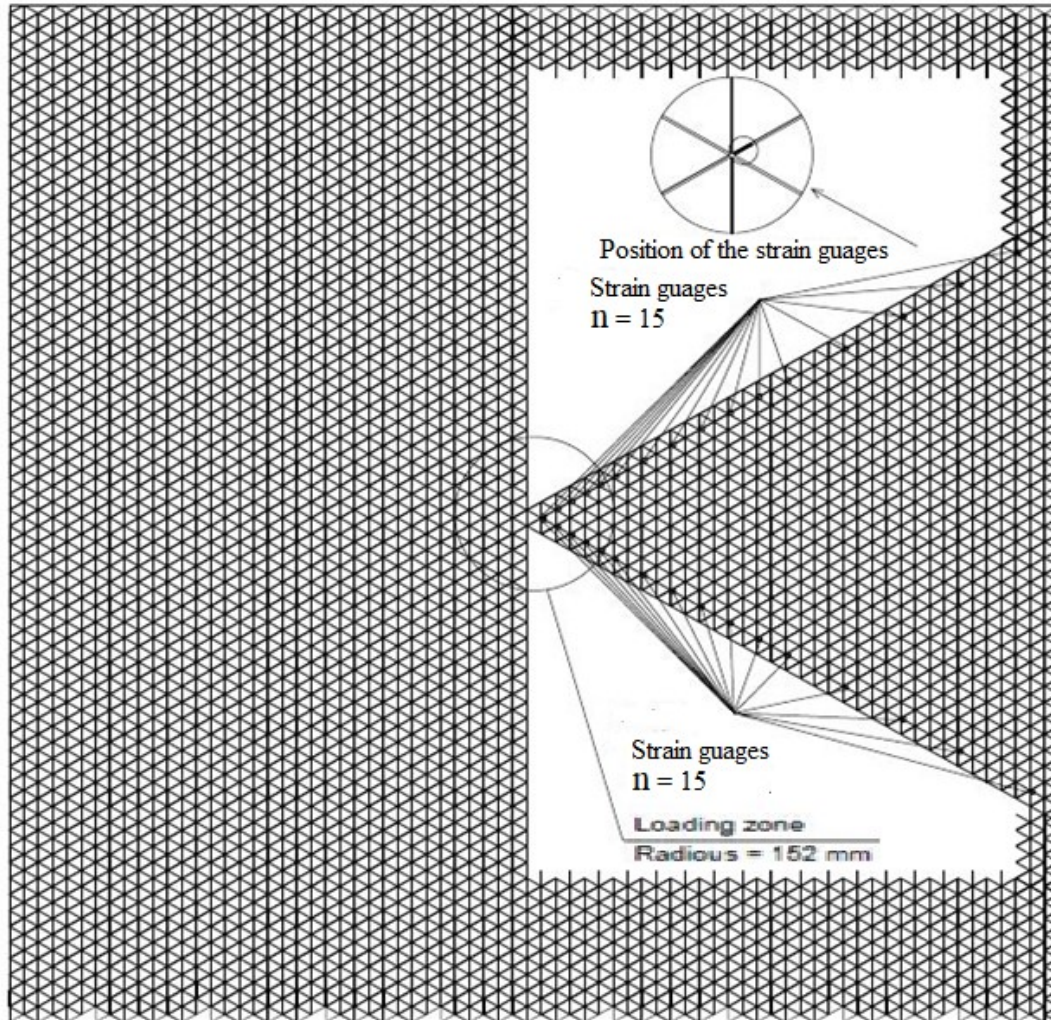
a)



b)



c)



d)

Figure 21. Position of strain gauges for: a) high duty biaxial, b) light-duty biaxial, c) high duty triaxial, and d) light-duty triaxial

2.3.5 Setting Up Strain Gauges on Geogrids

The procedure to install strain gauges on geogrids consisted of 17 steps: 1) prepare strain gauges and required materials, 2) cut the geogrids, 3) stabilize the geogrids on the foam with nails, 4) brush and mark the strain gauge positions on the geogrid, 5) clean the surface of the geogrid with alcohol, 6) apply the primer, 7) apply the glue to attach the strain gauges on the geogrid, 8) apply the topcoat liquid on the strain gauges, 9) apply the plastic foam for protection of strain gauges during the compaction process, 10) add foam tape as protection, 11) set the strain gauges in two directions, 12) test the strain gauges with an ohm meter, 13) protect the strain gauge wires by passing them through a plastic tube, 14) prepare the subgrade and install sensors, 15) set the geogrids in their positions, 16) verify the response of the sensors in the laboratory, and 17) set up the data logger software. Figure 22 illustrates some of the main parts of installing and setting up the strain gauges on each of the geogrids.

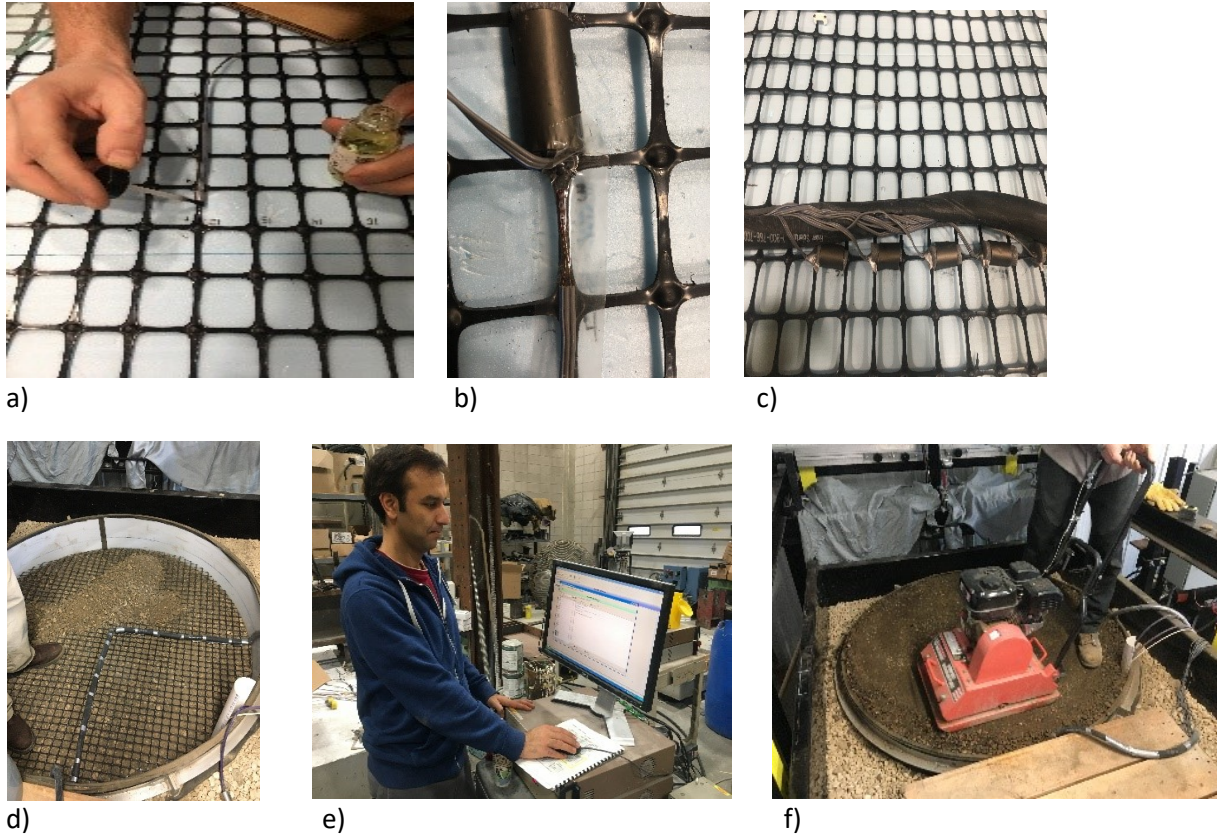


Figure 22. Key setup steps for strain gauge installation on geogrids: a) apply the topcoat liquid on the strain gauges, b) add foam tape as protection, c) protect strain gauge wires by passing them through a plastic tube, d) set the geogrids in their positions, e) set up the data logger software, and f) compact the base layer with the plate compactor for 3 minutes and simultaneously record the strain gauge and sensor results to measure the effect of compaction on mobilization of the geogrid

After this, the researchers could place the additional aggregate over the geogrids, install other sensors, tamp and level the test section, and compact the base layer using the plate compactor for three minutes. Results from the strain gauges and sensors were recorded to measure the effects of compaction on mobilization of the geogrids during compaction.

2.4 RESULTS

2.4.1 Summary Plots

This section presents the data collected in the laboratory using the IMAS device. All the pressure cell data and strain data were plotted versus the cycles of loading for each test section. For the pressure cells, the data were collected every 0.005 seconds; for the strain gauges, the data were recorded every 0.1 second. The loading data were recorded every 0.6 second. The load was sufficiently steady so that the recorded values could be compared to the other data sets as well. All the pressure cell data and strain data were plotted for the whole 100,000 cycles. To look at the details, five time intervals with a 500-second duration were selected so that a small range of data could be reviewed and analyzed. These five intervals were 0–500 seconds, where the test started; 2,000–2,500 seconds, where the slope of the

data plot was changing; 30,000–30,500 seconds, in the middle point of the tests; 45,000–45,500 seconds, in the third quarter of the tests; and 60,000–60,500 seconds, which was the end of the testing. For each test, both the overall data and the specific time interval data were compared and analyzed to evaluate the benefits of geogrid reinforcement.

2.4.1.1 Strain Gauge Results – Compaction Stage

Figure 23 and Figure 24 illustrate the strain gauge results of biaxial and triaxial geogrids for reinforced sections under the compaction loading steps of the tests.

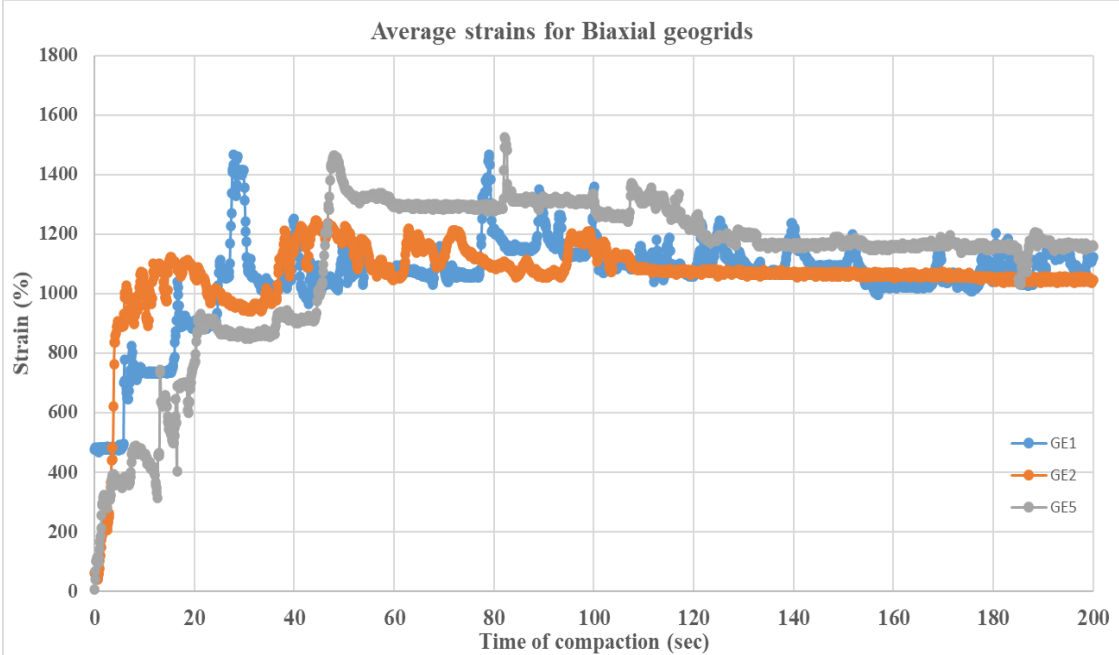


Figure 23. Average strains in the compaction part for biaxial geogrids

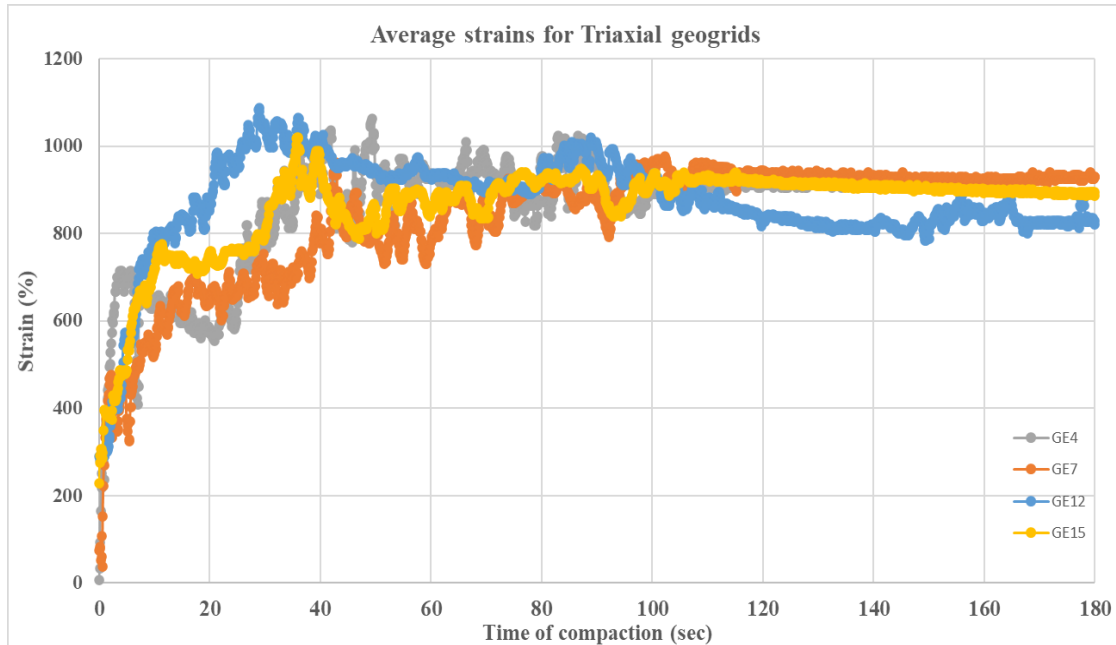


Figure 24. Average strains in the compaction part for triaxial geogrids

From the results, it is obvious that, during application of the compaction loads, the results from strain gauges in the biaxial geogrids showed fluctuation and reached higher values than with the triaxial geogrids, which gradually increased to the maximum strain value. Also, the residual strain in triaxial geogrids was less than that with biaxial geogrids.

2.4.1.2 Strain Gauge Results – Loading Part

Figures 25 through 38 illustrate the strain gauge results of biaxial and triaxial geogrids for the reinforced sections of GE1, GE2, GE4, GE5, GE7, GE12, and GE 15 in both directions under loading.

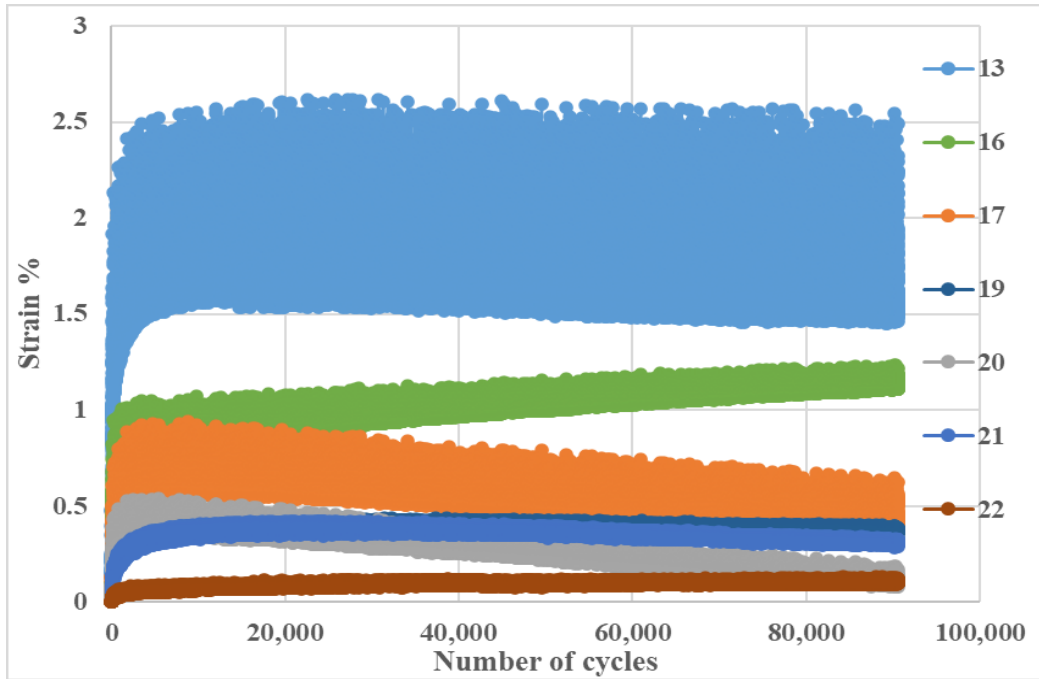


Figure 25. GE1 strain gauge in direction 1

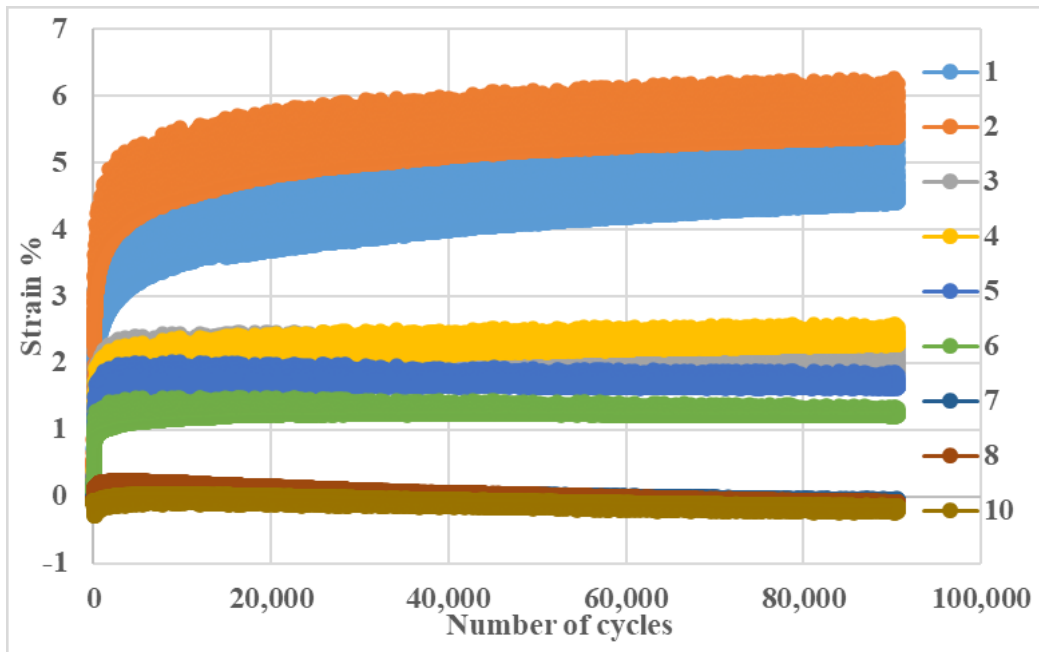


Figure 26. GE1 strain gauge in direction 2

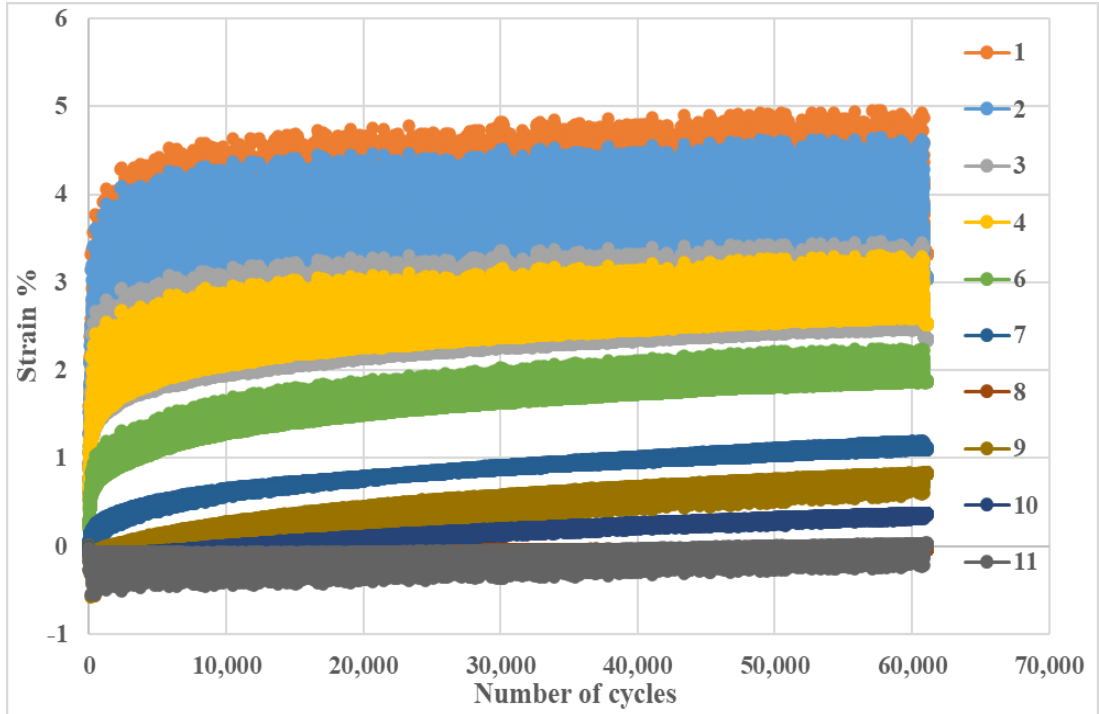


Figure 27. GE2 strain gauge in direction 1

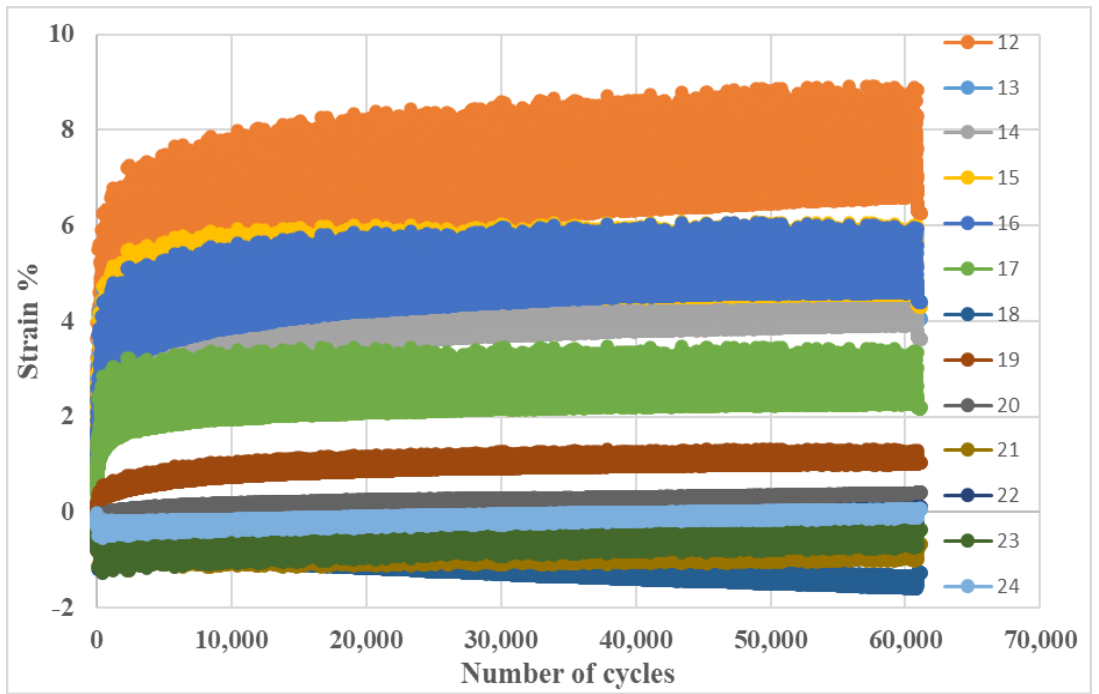


Figure 28. GE2 strain gauge in direction 2

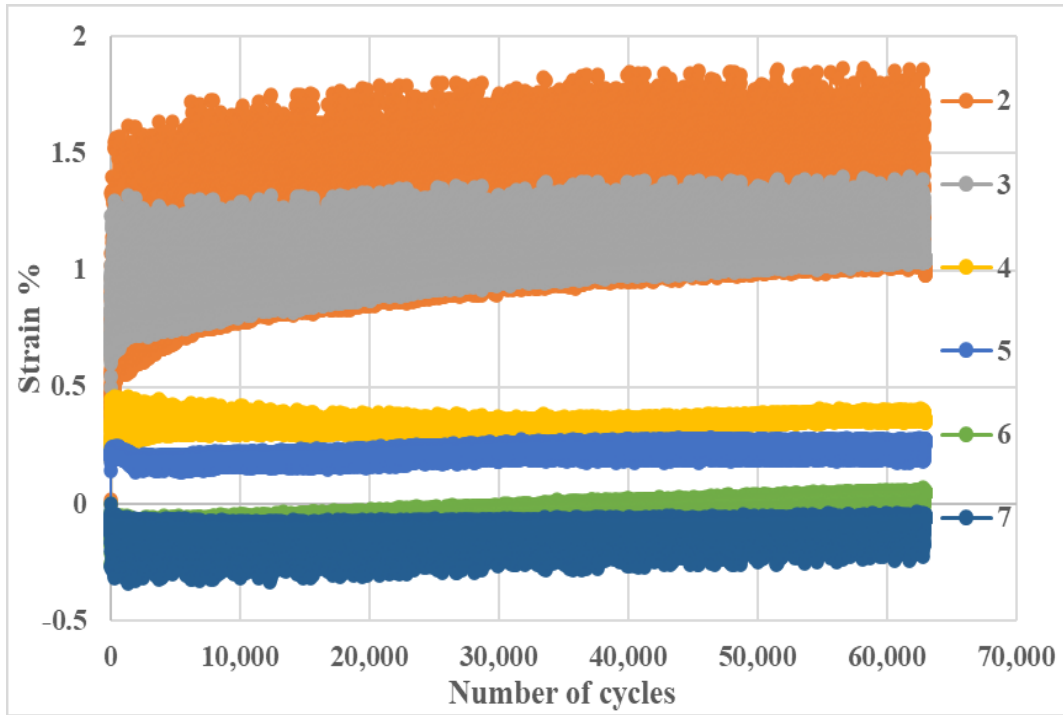


Figure 29. GE4 strain gauge in direction 1

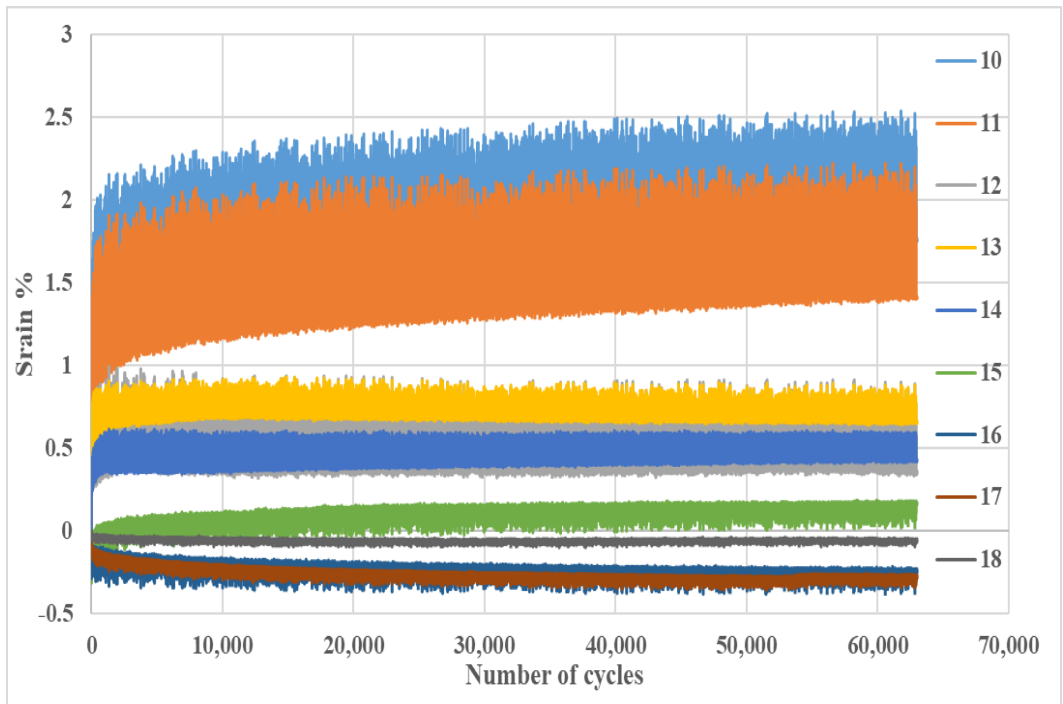


Figure 30. GE4 strain gauge in direction 2

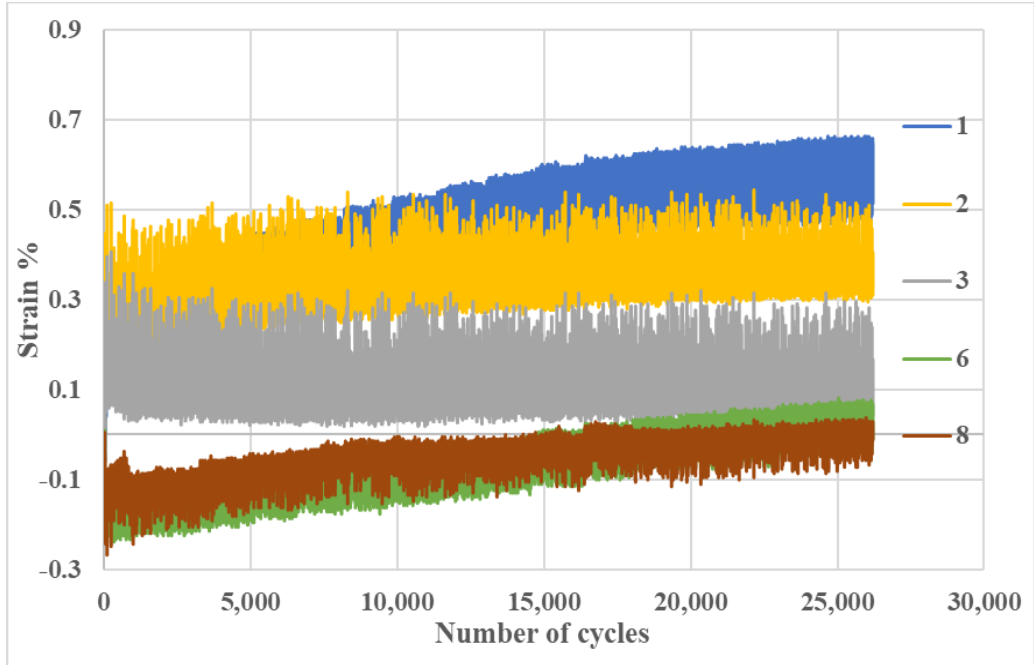


Figure 31. GE5 strain gauge in direction 1

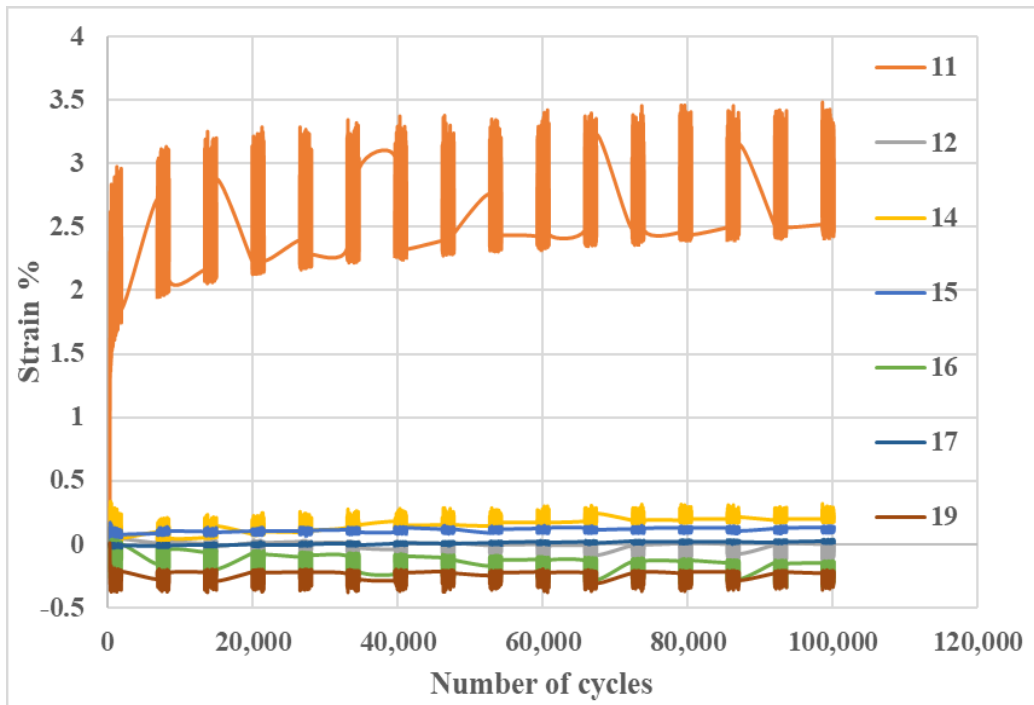


Figure 32. GE5 strain gauge in direction 2

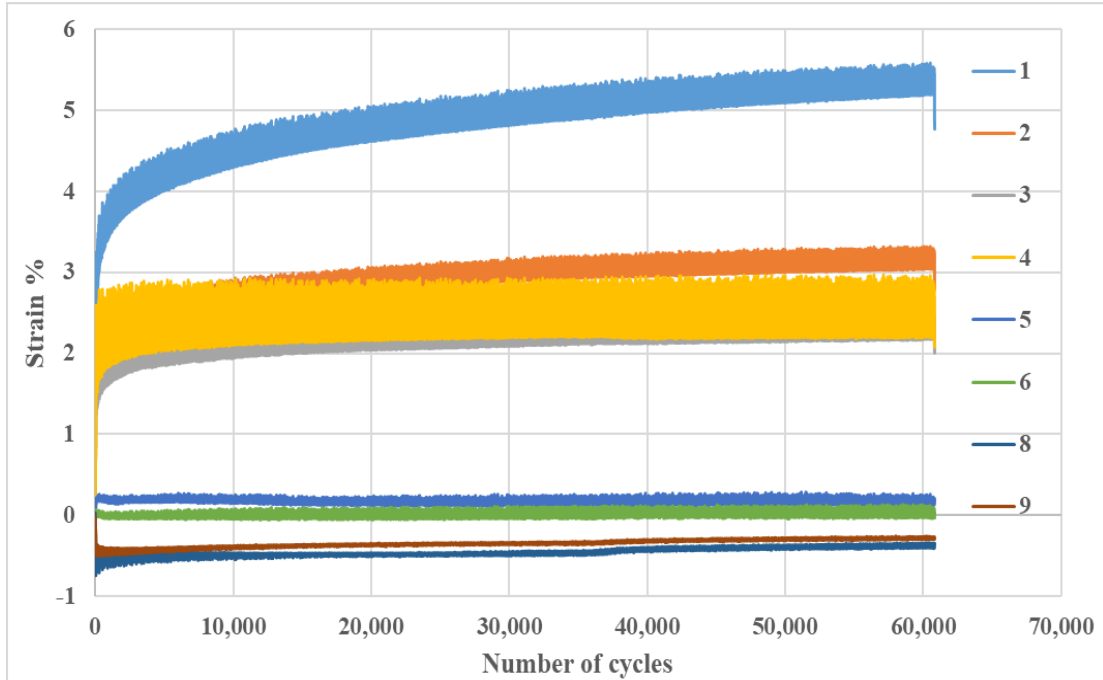


Figure 33. GE7 strain gauge in direction 1

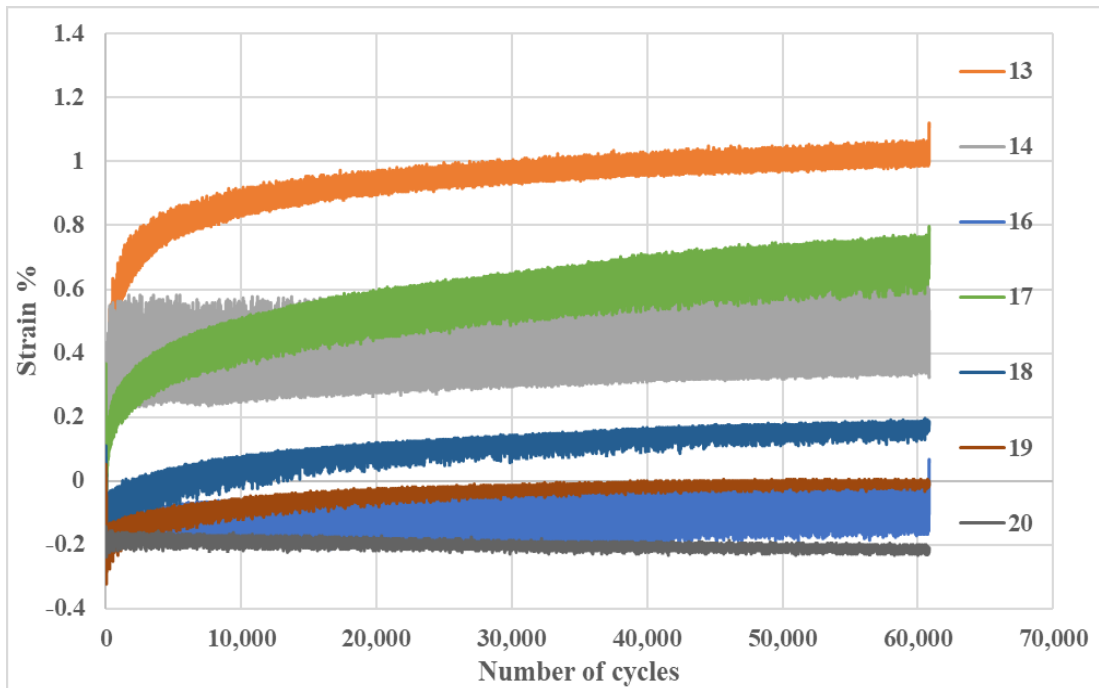


Figure 34. GE7 strain gauge in direction 2

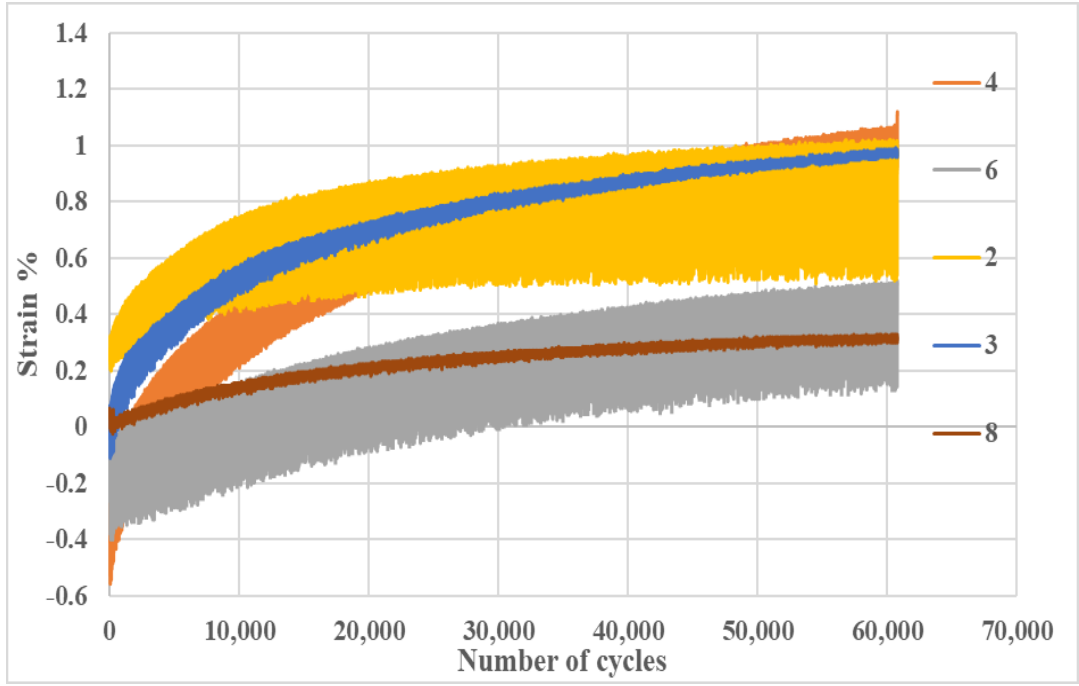


Figure 35. GE12 strain gauge in direction 1

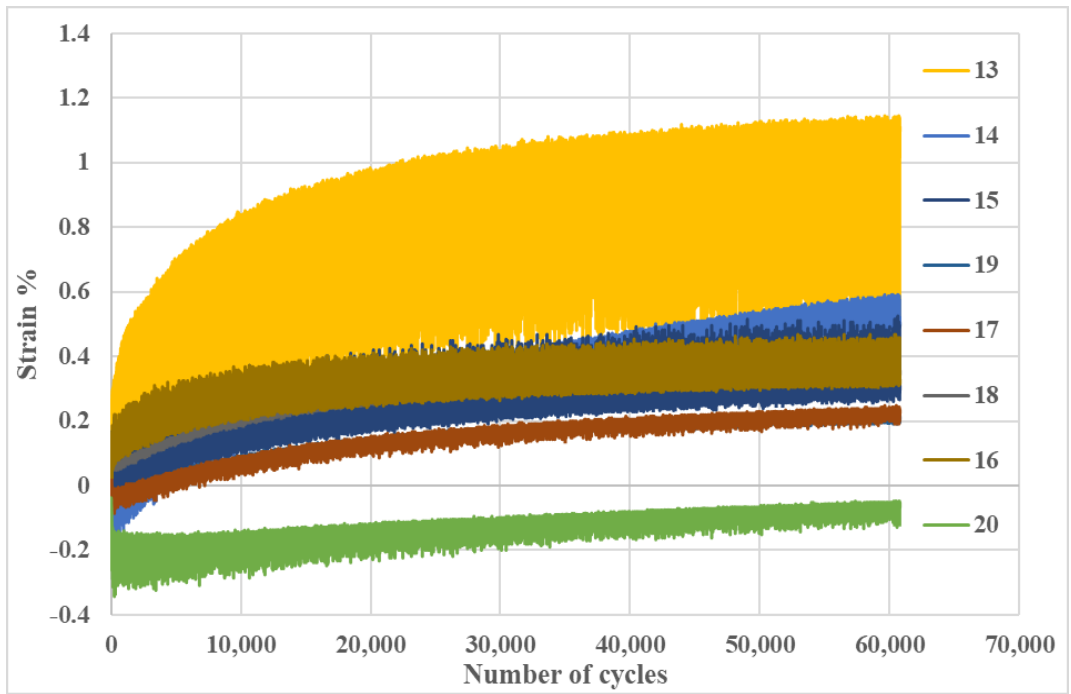


Figure 36. GE12 strain gauge in direction 2

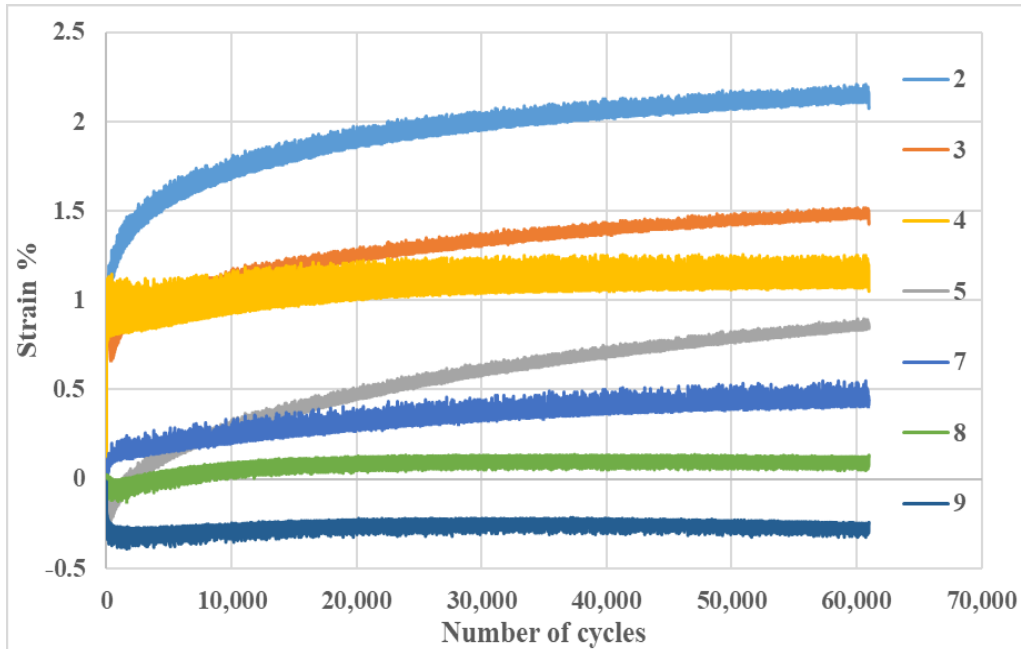


Figure 37. GE15 strain gauge in direction 1

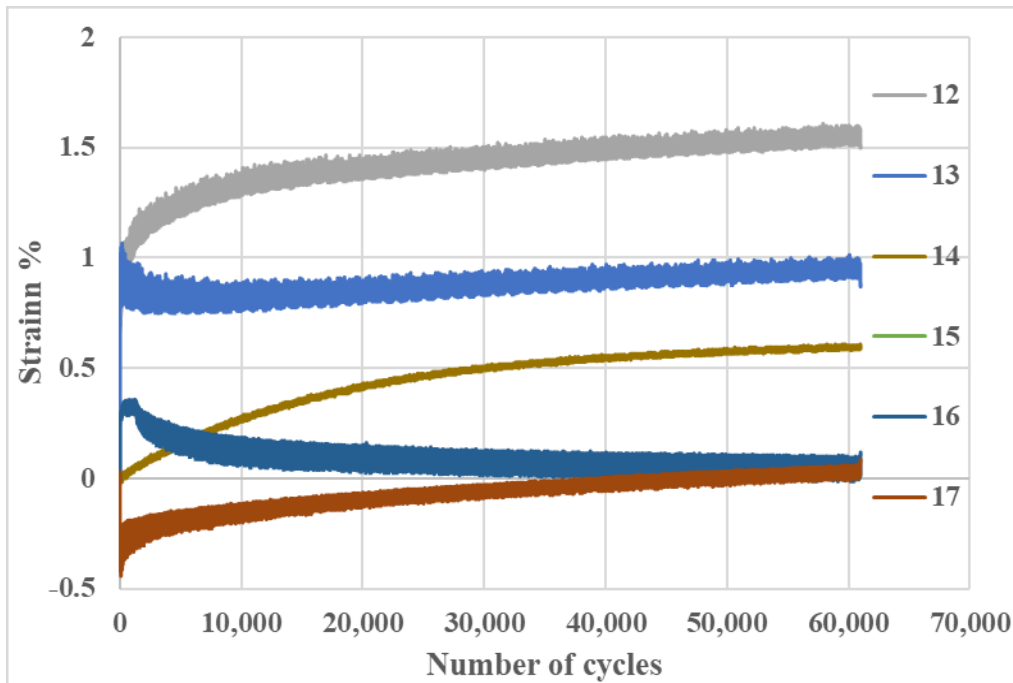


Figure 38. GE15 strain gauge in direction 2

As illustrated in the previous Figure 21, the strain gauges were set up in both direction for the biaxial and triaxial geogrids. The number of strain gauges were set up in each direction were not equal because of the inequality of the grid sizes in direction 1 and direction 2 in biaxial geogrids. Also,, some results from some of the strain gauges were out of scale, so those results were eliminated in the figures.

Strain gauge No. 1 was located under the loading plate and the numbers assigned for the other strain gauges were sequential from there until the end of each direction. In other words, the lowest number in each direction on the vertical axis on the right in each chart is the strain gauge located at the center of the geogrid part under the loading plate and, as the numbers goes up, the strain gauge location was farther from the center; the last number was for the geogrid located at the corner of the geogrid in each direction.

From the results, it can be seen that, during application of the cyclic loads, the strain gauge results are significantly higher under the loading plate than farther away from it. Some strain gauges showed negative values means compression in the results. This might be due to the sensitivity of the strain gauges, and these negative values occurred mainly for the strain gauges that were set up at the corners of the geogrids. This was interpreted to mean that, due to the loading, tension deformation takes place at the center of the tank and uplift occurs at the corner of the tank. Also, for section GE5 in Figure 32, the strain gauges in direction 2 were missing data from the data logger for some gap times while performing and recording the test data; however, all the information from strain gauges for this direction in this section are presented in the figure.

2.4.1.3 Permanent Deformation Results

Figure 39 illustrates the permanent deformation results for the triaxial and biaxial geogrids.

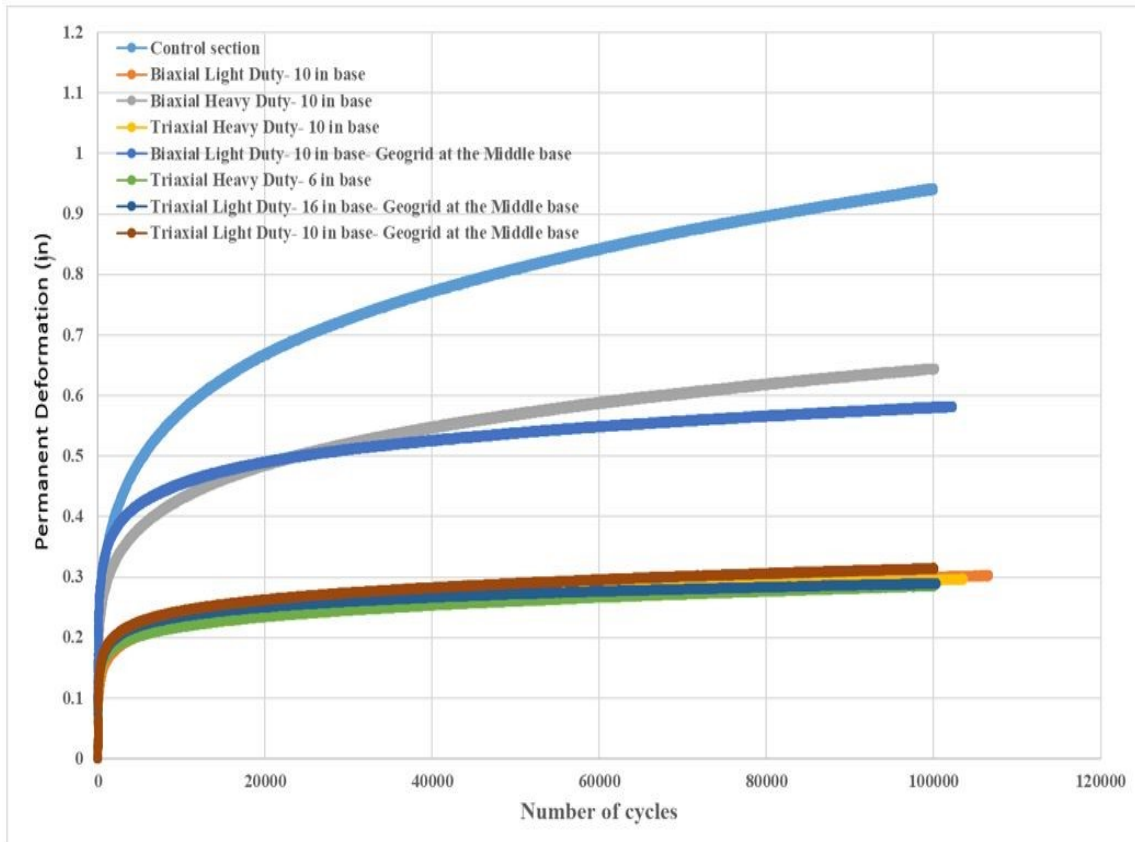


Figure 39. Permanent deformation results of triaxial and biaxial geogrids

The increase in the service life of the pavement structure has been commonly defined by the application of the TBR. The TBR is described as the ratio of the number of load cycles to achieve a particular rutting depth in the reinforced section over an unreinforced section with exact corresponding thickness, loading characteristics, and material properties. From the results, it is obvious that the triaxial geogrids performed much better than the biaxial geogrids in reducing the permanent deformation of the sections for the same cyclic load numbers.

2.4.1.4 Pressure Cell Results

Two pressure cells were used for each test with one located on top of the subgrade and the other located on top of the geogrid in the base aggregate layer to measure the values of the pressure developing in both the aggregate and subgrade layers. Figures 40 through 47 show comparisons of the values for the two earth pressure cells (EPC) in all eight of the test sections.

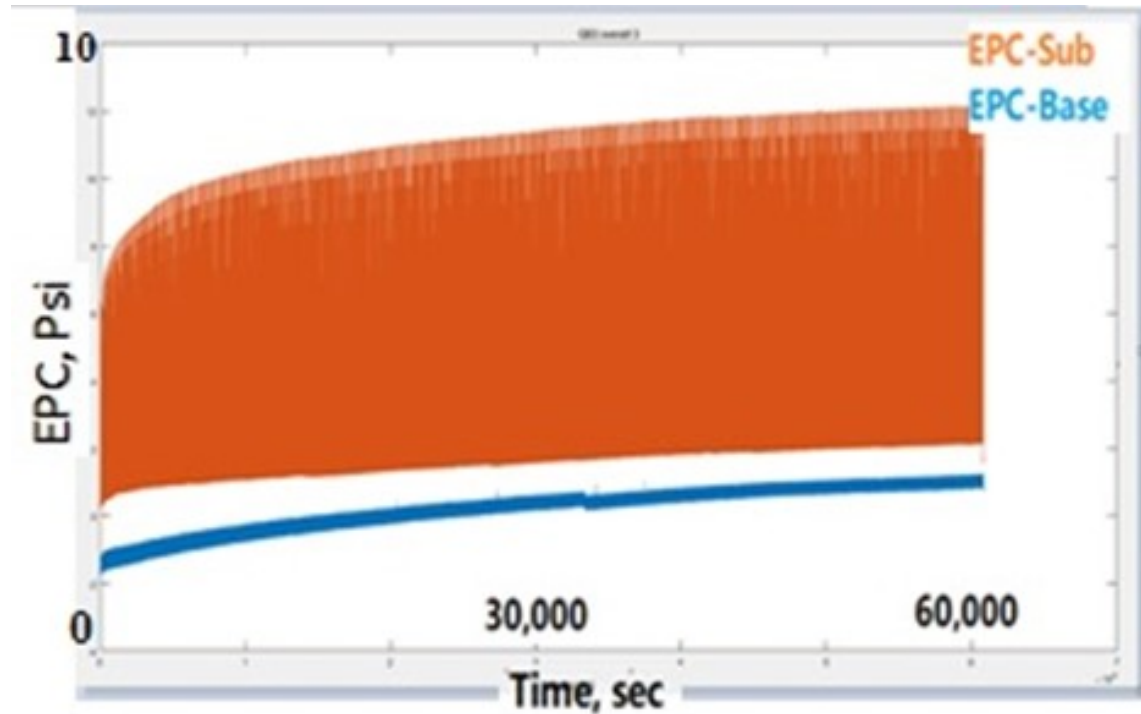


Figure 40. Pressure cell results for section GE0

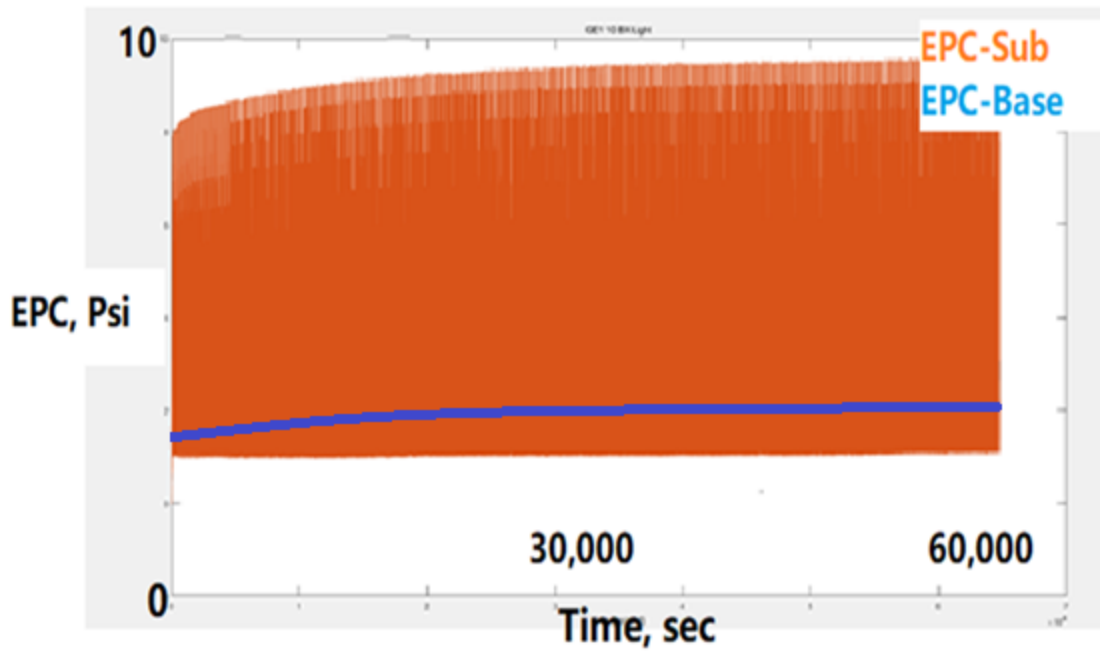


Figure 41. Pressure cell results for section GE1

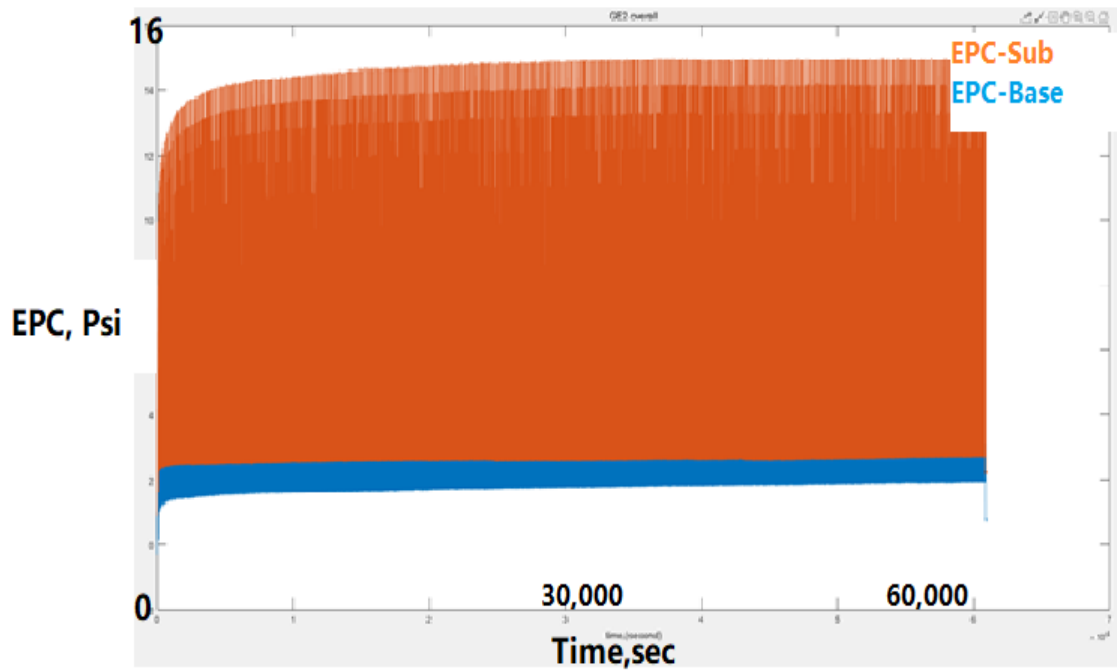


Figure 42. Pressure cell results for section GE2

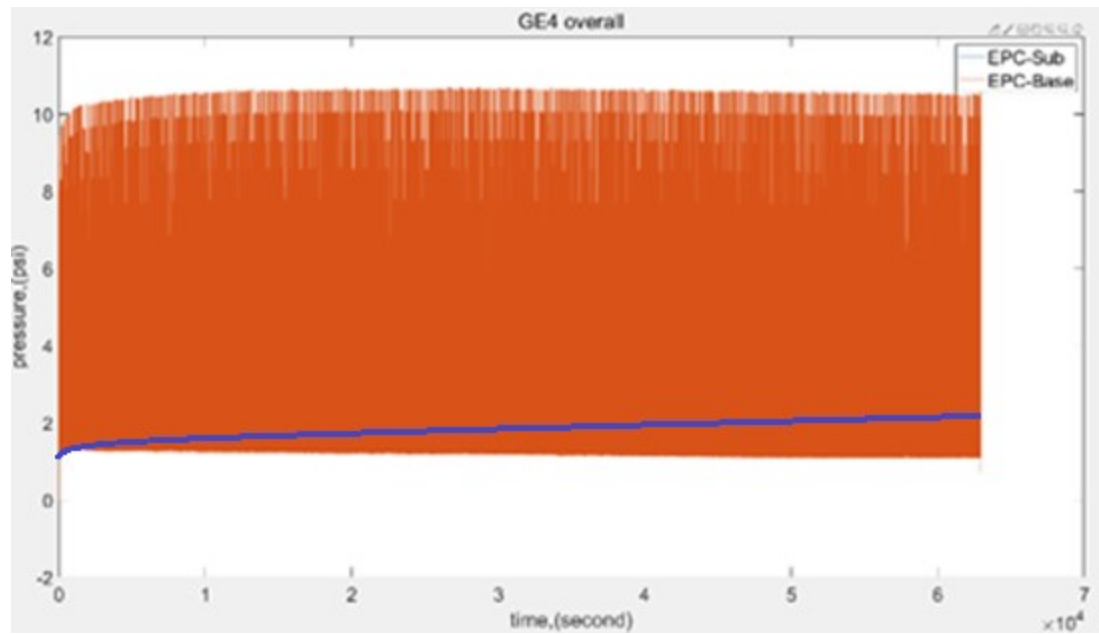


Figure 43. Pressure cell results for section GE4

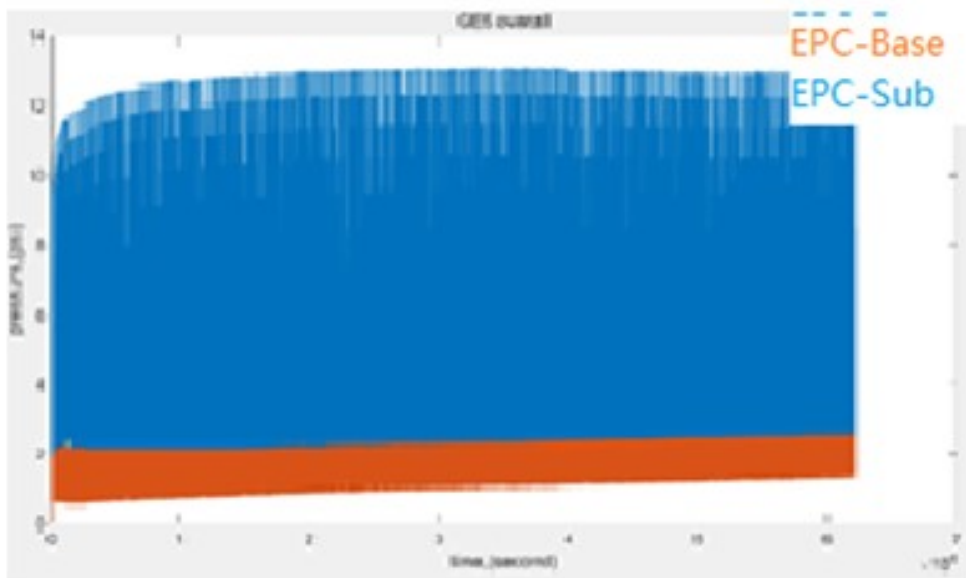


Figure 44. Pressure cell results for section GE5

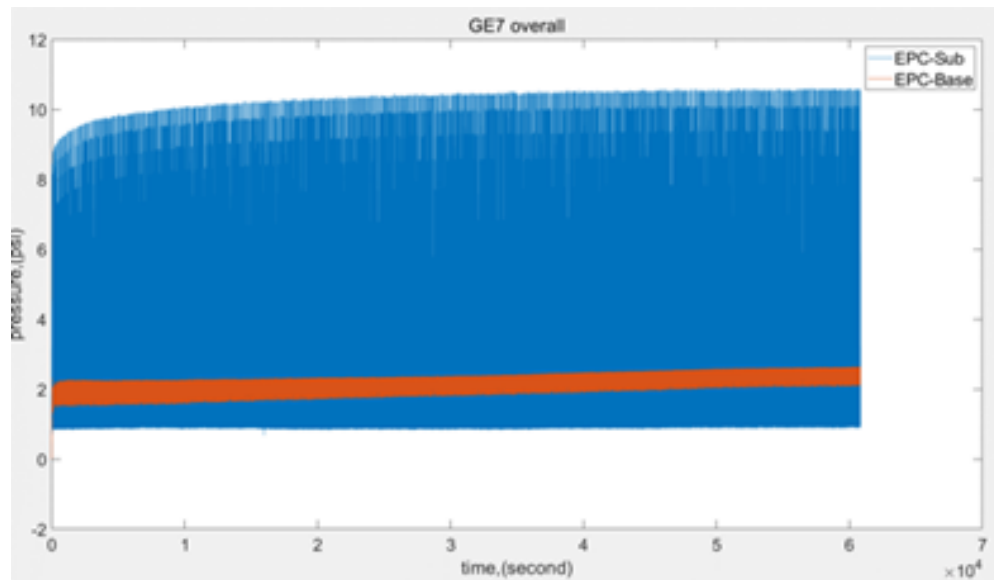


Figure 45. Pressure cell results for section GE7

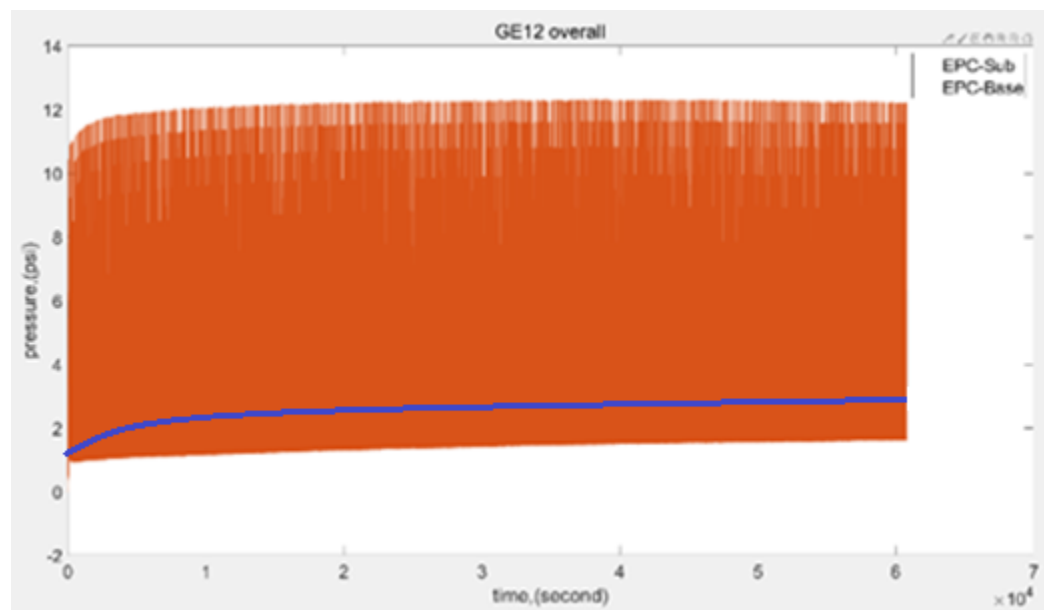


Figure 46. Pressure cell results for section GE12

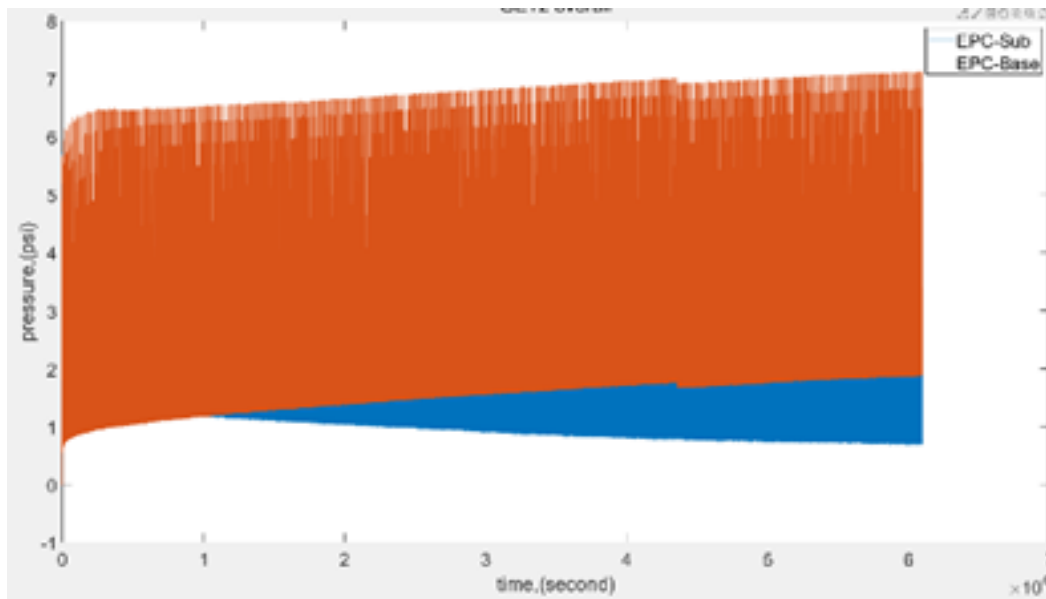


Figure 47. Pressure cell results for section GE15

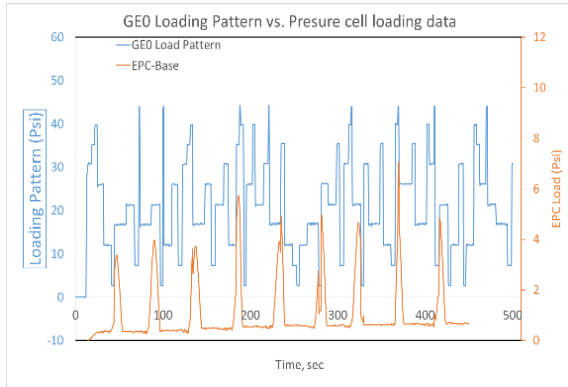
These charts show that the test sections with heavy-duty geogrids always had higher pressure cell data readings than those with light-duty geogrids. These results show that the heavy-duty geogrids can provide more confinement than light-duty geogrids and can therefore provide better performance for pavement sections. For all the overall earth pressure cell results, except for GE4 and GE7 in Figure 43 and Figure 45, respectively, the test sections had similar trends: the earth pressure cell data values increased as loading occurred, both in the subgrade layer and the base course layer, but the increasing rate and magnitude were higher in the base course layer than the subgrade layer.

2.5 DETAILED RESULTS

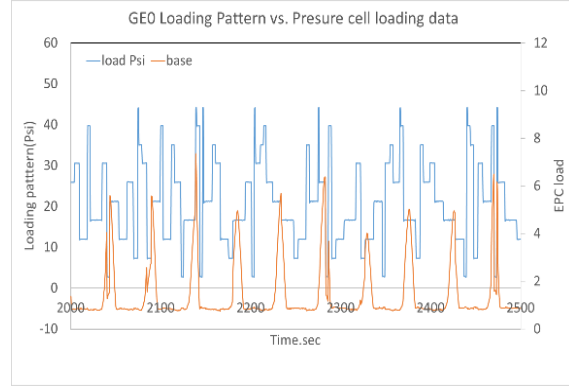
2.5.1 Loading Pattern vs. Earth Pressure Cell Data

For the pressure cells, data were collected every 0.005 second, and loading data were recorded every 0.6 second. The load was sufficiently steady so that the recorded values could be compared to the pressure cell data sets as well. All the pressure cell data were plotted for the whole 100,000 cycles. To look at the details, five time intervals with a 500-second duration were selected so that a small range of data could be reviewed and analyzed. These five intervals were 0–500 seconds, where the test started; 2,000–2,500 seconds, where the slope of the data plot was changing; 30,000–30,500 seconds, in the middle point of the tests; 45,000–45,500 seconds, in the third quarter of the tests; and 60,000–60,500 seconds, which was the end of the tests.

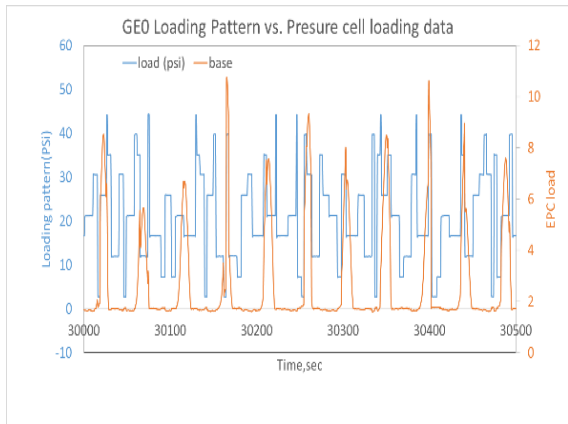
Figures 48 through 55 represent the loading versus earth pressure cell (EPC) result graphs for all five selected time intervals. All the results show the consistent trend of loading and pressure in all sections at the five time intervals.



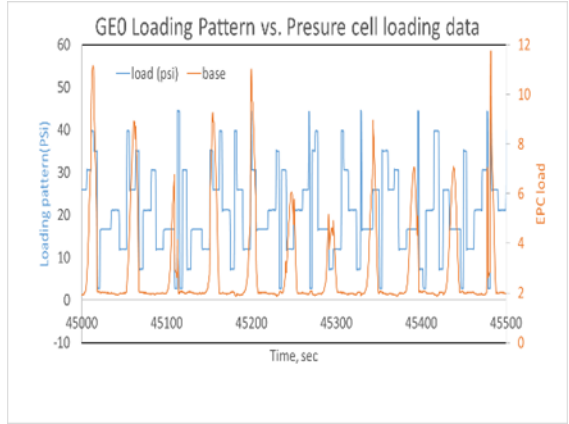
a)



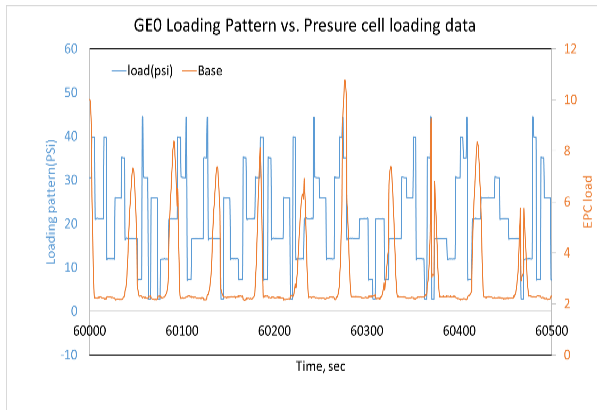
b)



c)

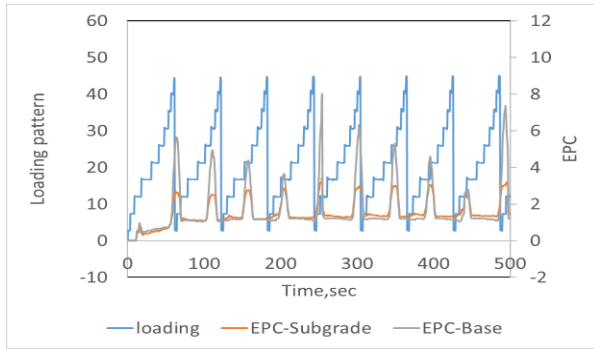


d)

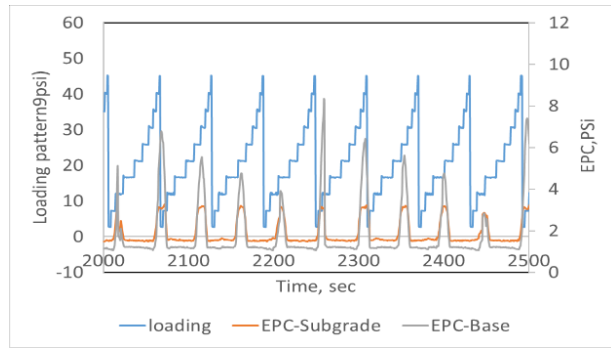


e)

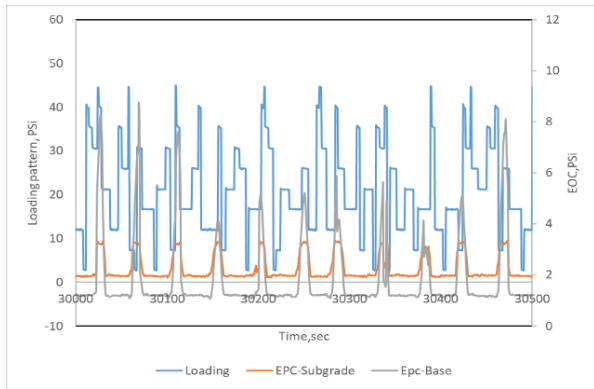
Figure 48. GEO section loading vs. EPC results for time intervals: a) 0–500 sec, b) 2,000–2,500 sec, c) 30,000–30,500 sec, d) 45,000–45,500 sec, and e) 60,000–60,500 sec



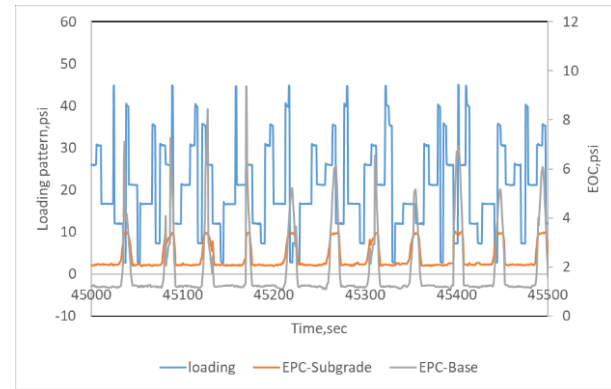
a)



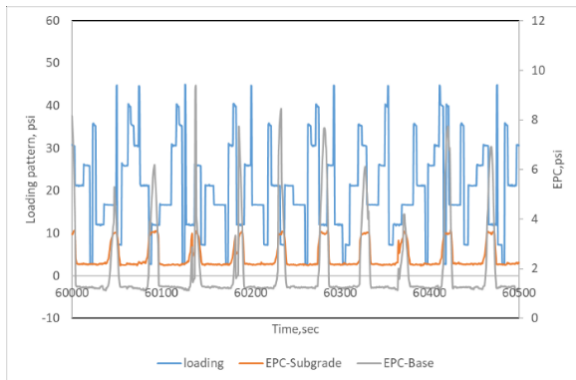
b)



c)

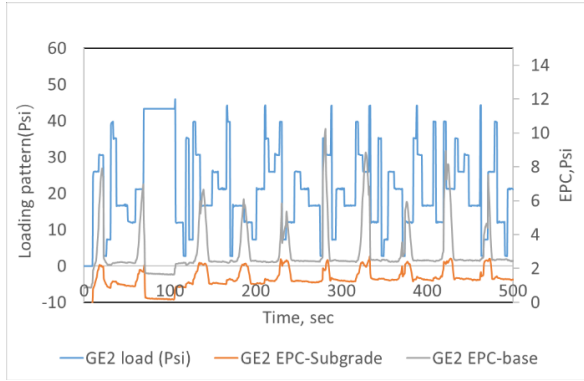


d)

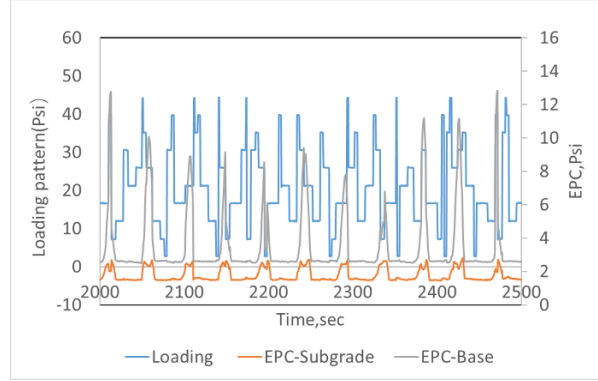


e)

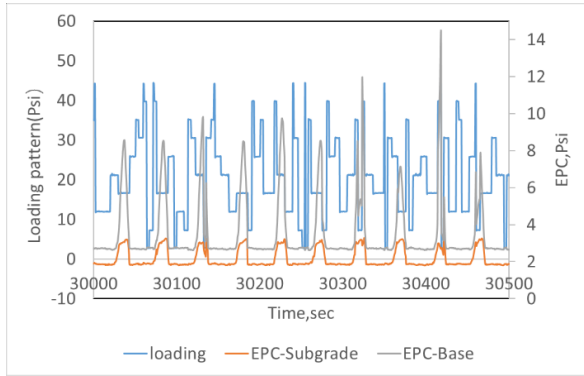
Figure 49. GE1 section loading vs. EPC results for time intervals: a) 0–500 sec, b) 2,000–2,500 sec, c) 30,000–30,500 sec, d) 45,000–45,500 sec, and e) 60,000–60,500 sec



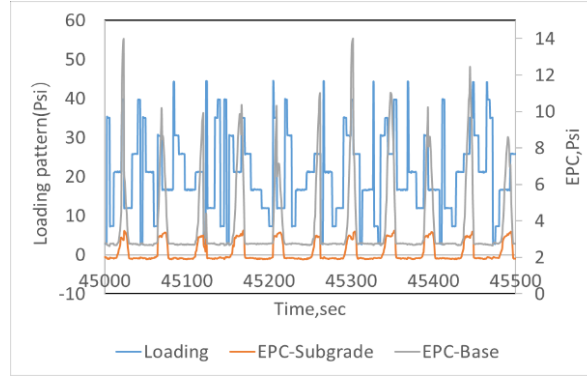
a)



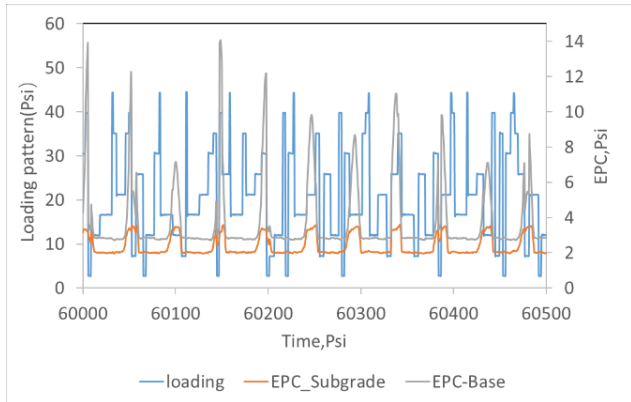
b)



c)

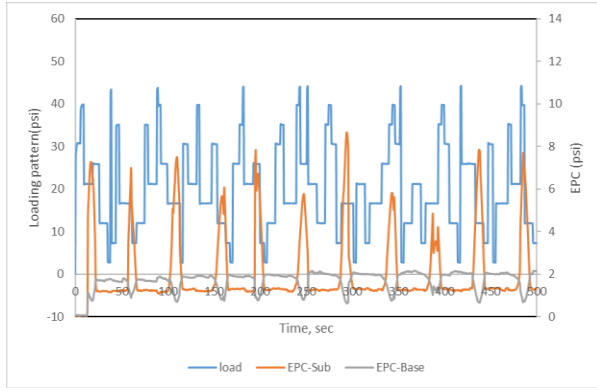


d)

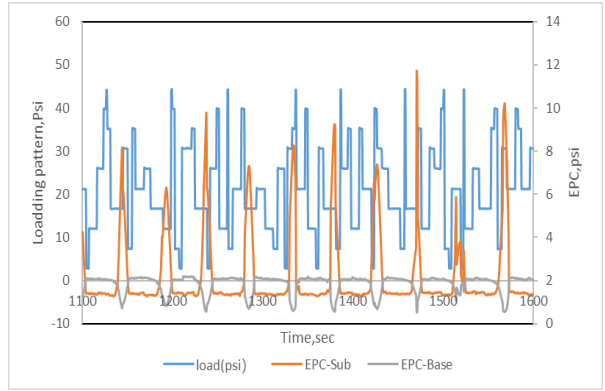


e)

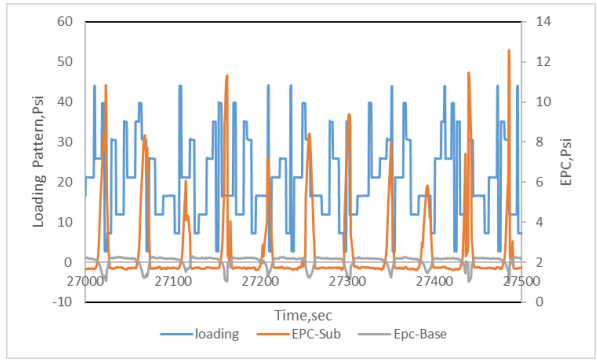
Figure 50. GE2 section loading vs. EPC results for time intervals: a) 0–500 sec, b) 2,000–2,500 sec, c) 30,000–30,500 sec, d) 45,000–45,500 sec, and e) 60,000–60,500 sec



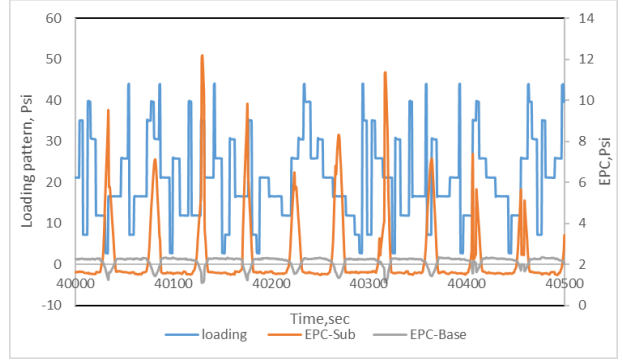
a)



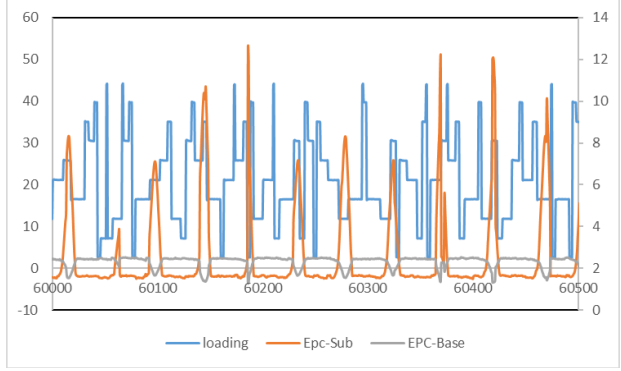
b)



c)

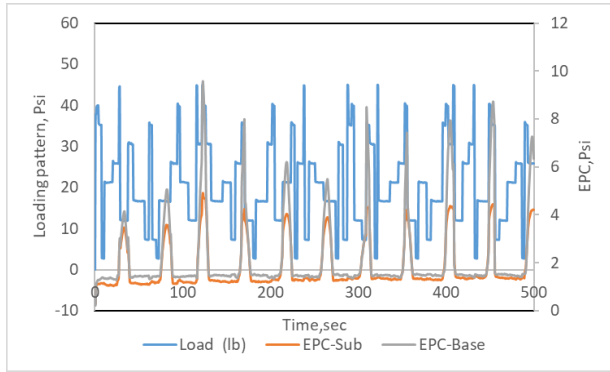


d)

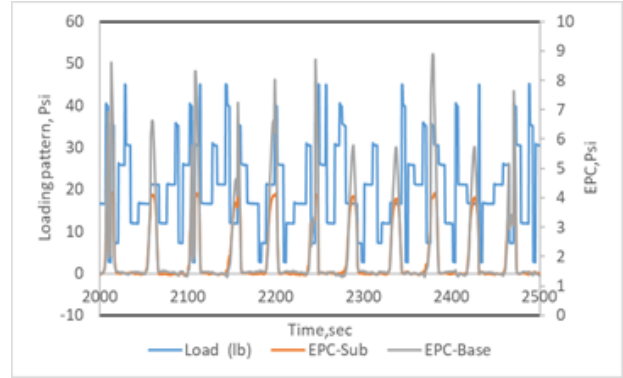


e)

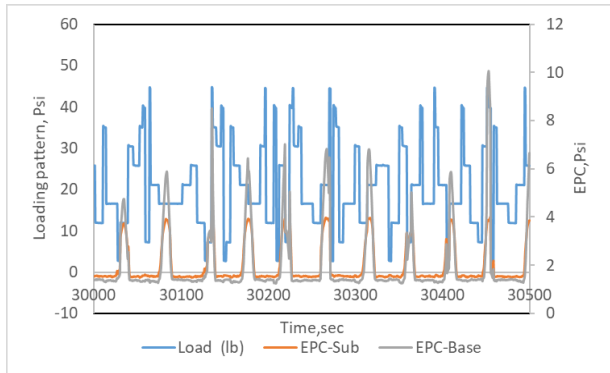
Figure 51. GE5 section loading vs. EPC results for time intervals: a) 0–500 sec, b) 2,000–2,500 sec, c) 30,000–30,500 sec, d) 45,000–45,500 sec, and e) 60,000–60,500 sec



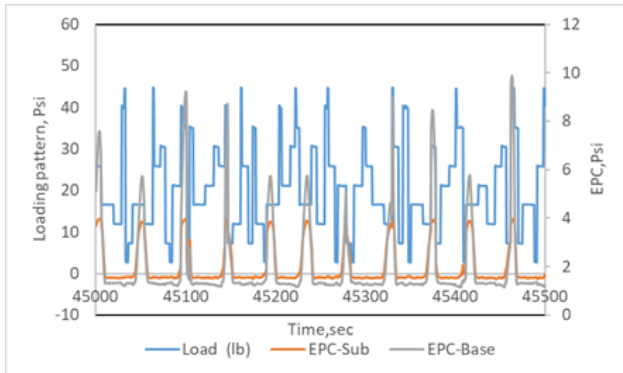
a)



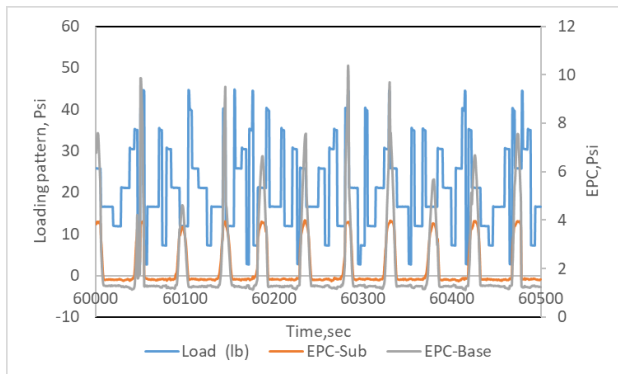
b)



c)

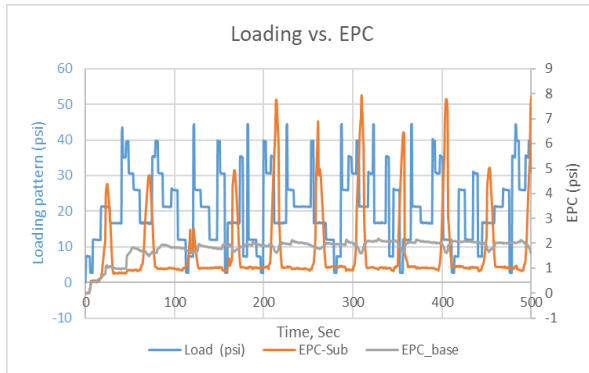


d)

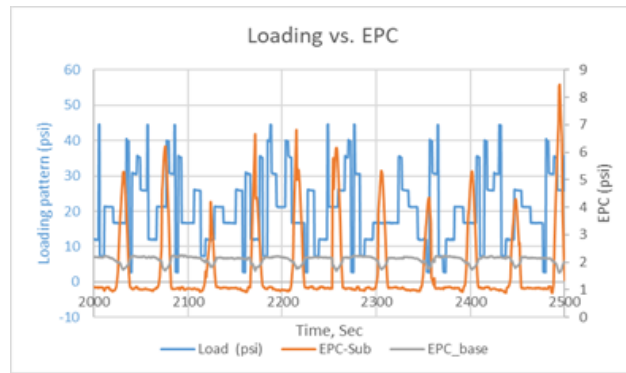


e)

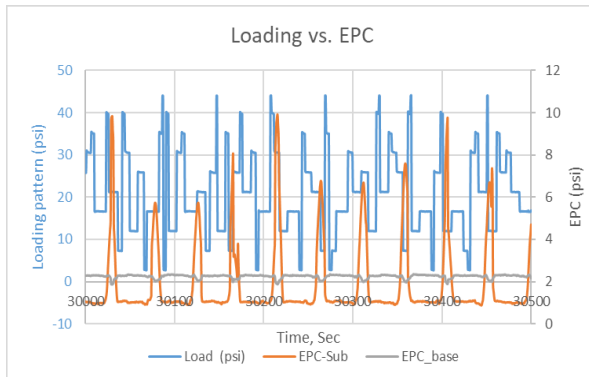
Figure 52. GE4 section loading vs. EPC results for time intervals: a) 0–500 sec, b) 2,000–2,500 sec, c) 30,000–30,500 sec, d) 45,000–45,500 sec, and e) 60,000–60,500 sec



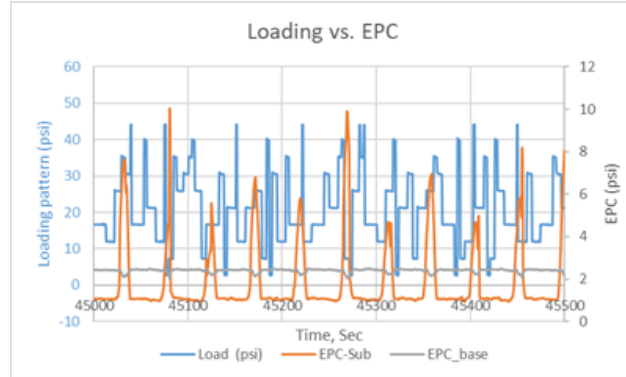
a)



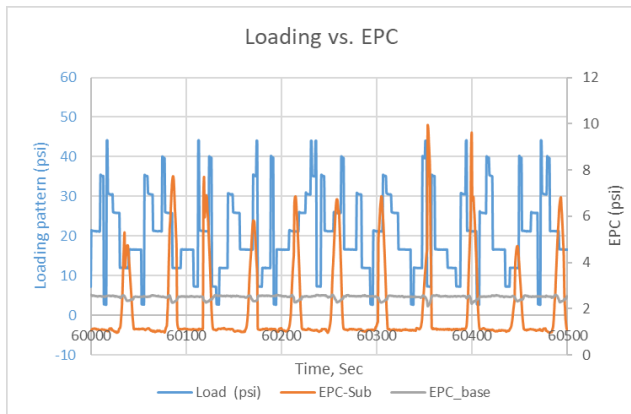
b)



c)

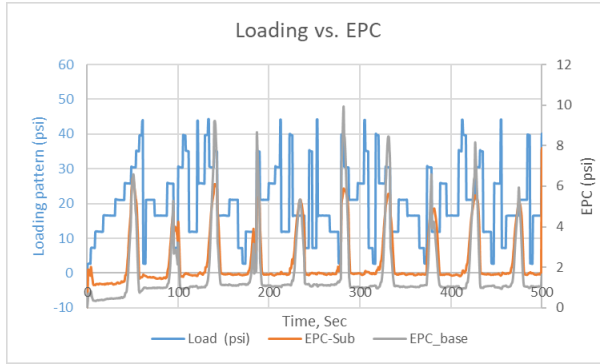


d)

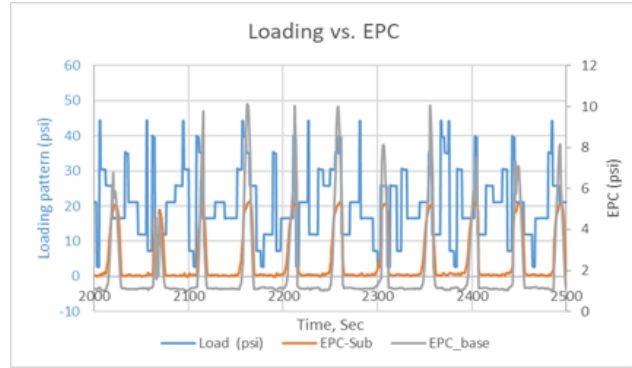


e)

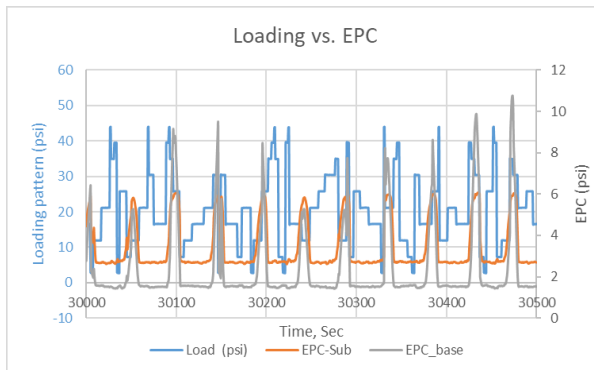
Figure 53. GE7 section loading vs. EPC results for time intervals: a) 0–500 sec, b) 2,000–2,500 sec, c) 30,000–30,500 sec, d) 45,000–45,500 sec, and e) 60,000–60,500 sec



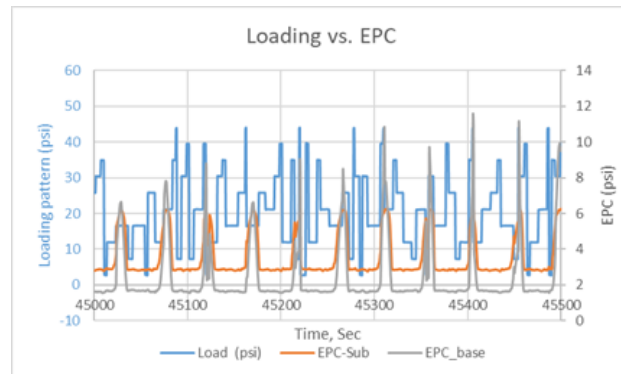
a)



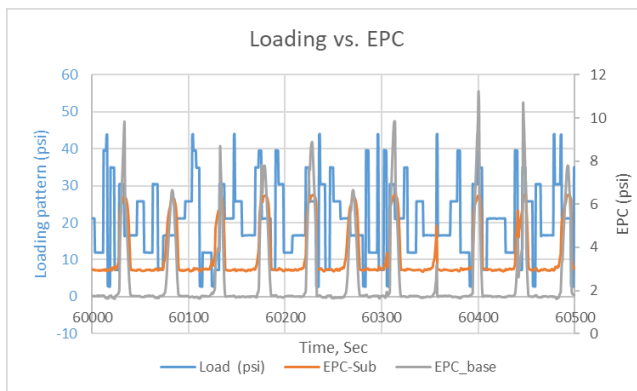
b)



c)

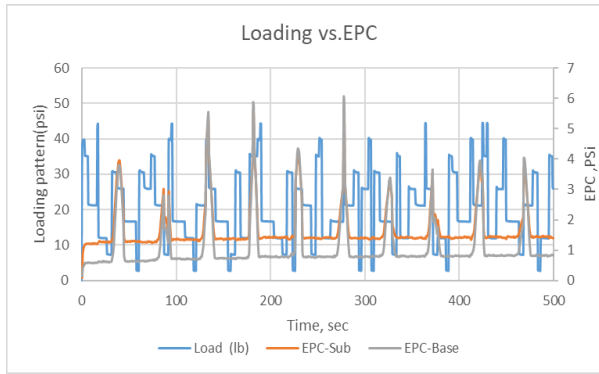


d)

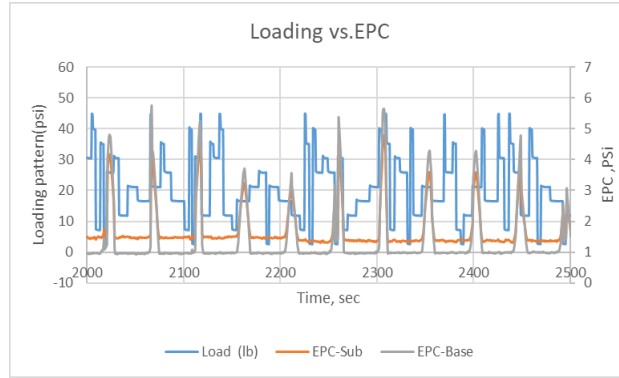


e)

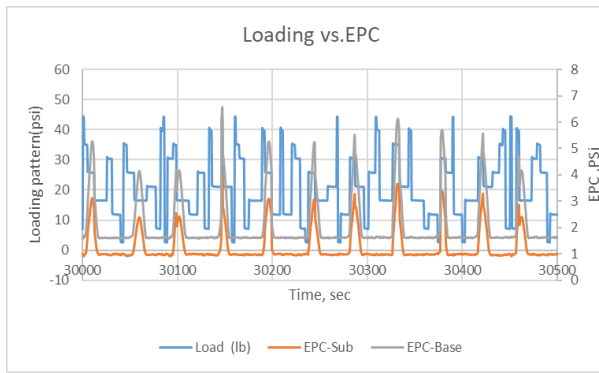
Figure 54. GE12 section loading vs. EPC results for time intervals: a) 0–500 sec, b) 2,000–2,500 sec, c) 30,000–30,500 sec, d) 45,000–45,500 sec, and e) 60,000–60,500 sec



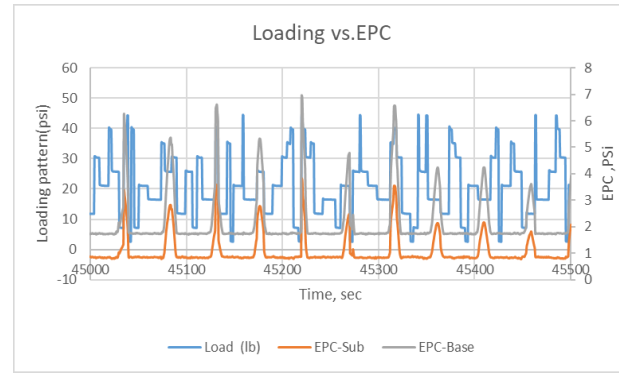
a)



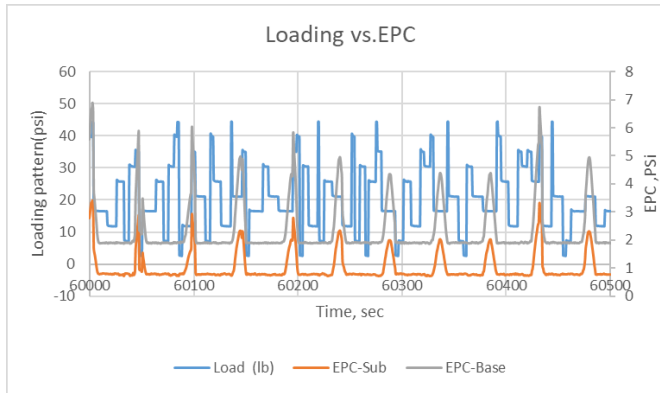
b)



c)



d)



e)

Figure 55. GE15 section loading vs. EPC results for time intervals: a) 0–500 sec, b) 2,000–2,500 sec, c) 30,000–30,500 sec, d) 45,000–45,500 sec, and e) 60,000–60,500 sec

2.5.2 Loading Pattern vs. Strain

For the strain gauges, the data were recorded every 0.1 second, and the loading data were recorded every 0.6 second. The load was sufficiently steady so that the recorded values could be compared to the strain gauge data sets as well. All the strain data were plotted for the whole 100,000 cycles. To look at the details, again five time intervals with a 500-second duration were selected so that a small range of data could be reviewed and analyzed.

Again, these five intervals were 0–500 seconds, where the test started; 2,000–2,500 seconds, where the slope of the data plot is changing; 30,000–30,500 seconds, in the middle point of the tests; 45,000–45,500 seconds, in the third quarter of the tests; and 60,000–60,500 seconds, which was the end of the tests. Figures 56 through 69 show the loading versus strain gauge results for all five selected time intervals and both directions of the geogrids in the sections.

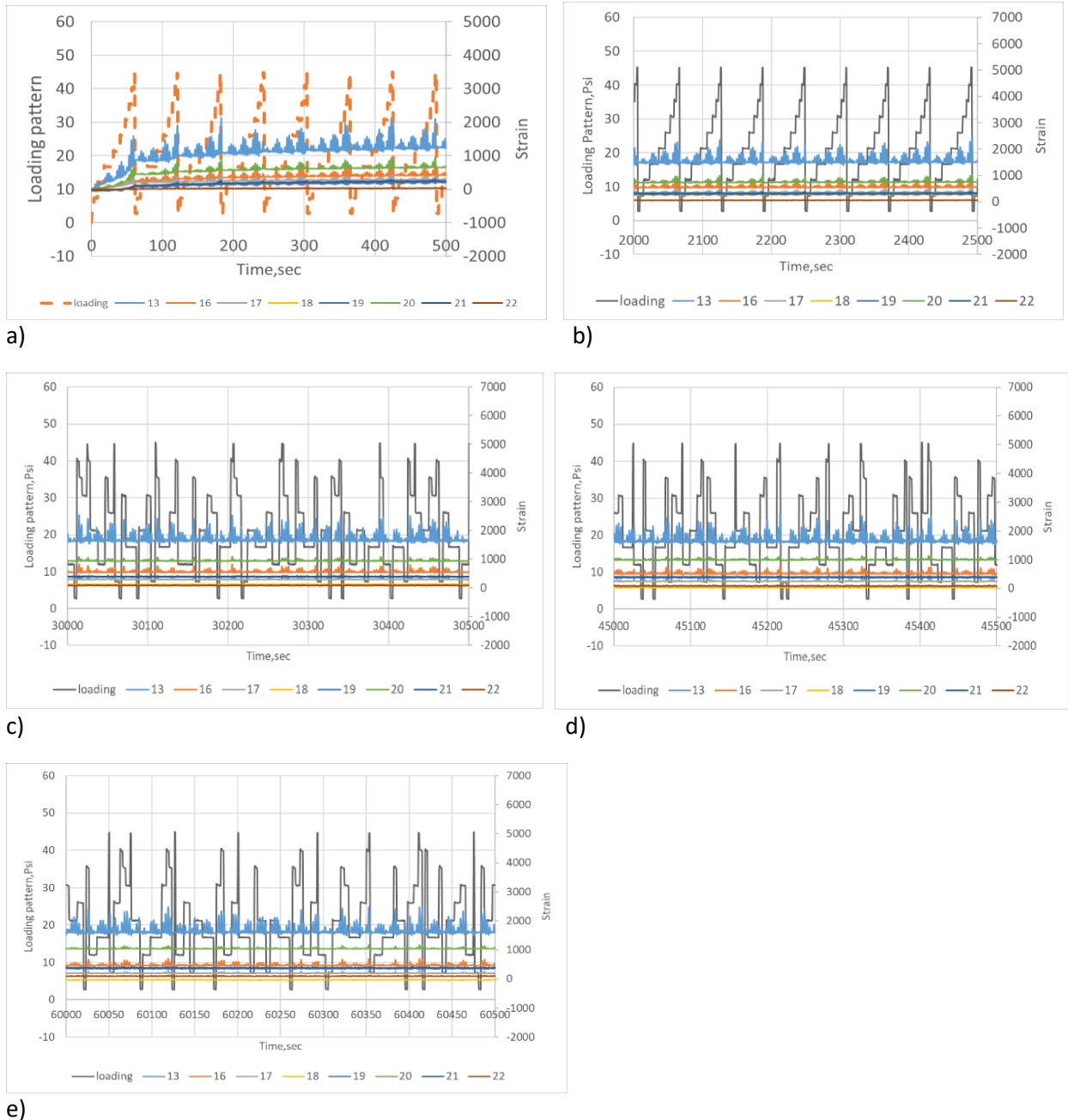
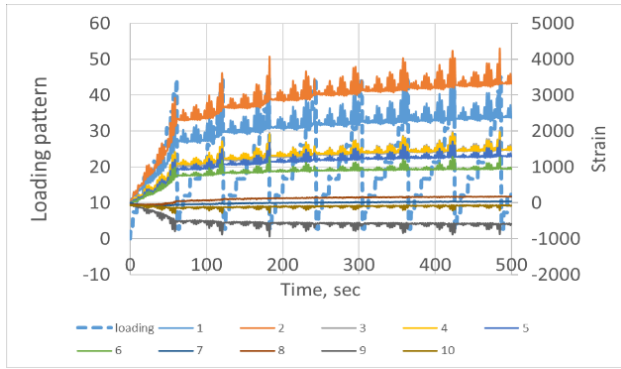
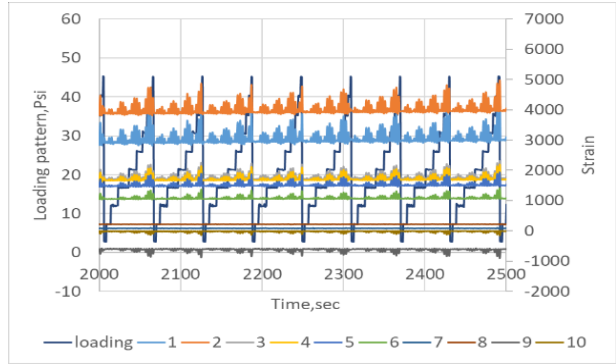


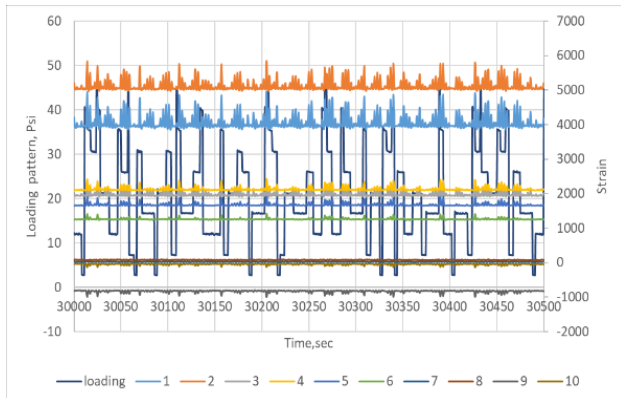
Figure 56. GE1 section loading vs. strain for direction 1 in time intervals: a) 0–500 sec, b) 2,000–2,500 sec, c) 30,000–30,500 sec, d) 45,000–45,500 sec, and e) 60,000–60,500 sec



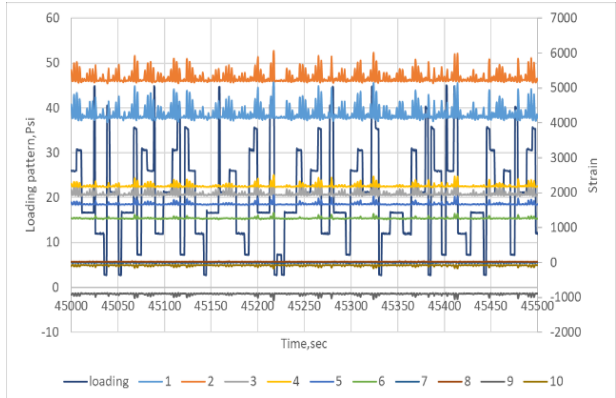
a)



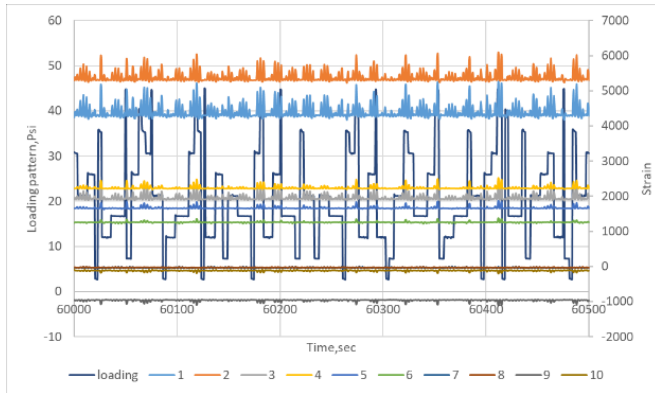
b)



c)

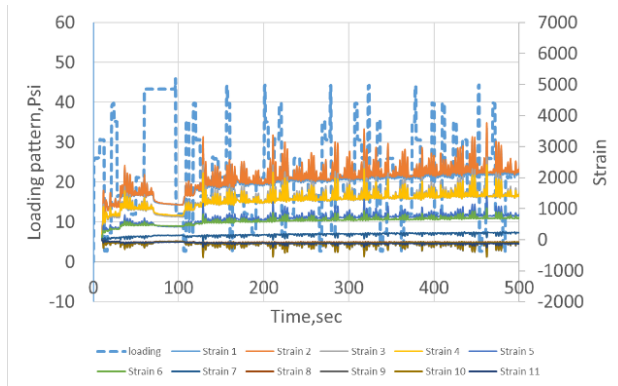


d)

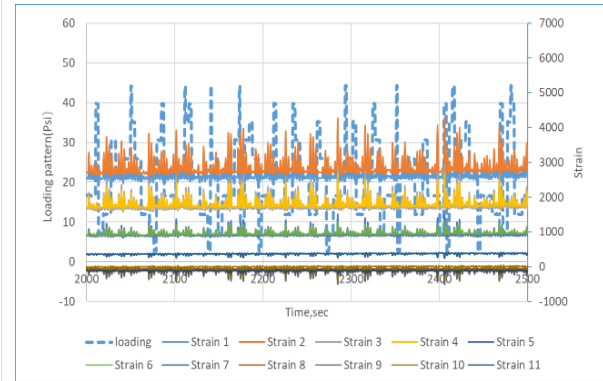


e)

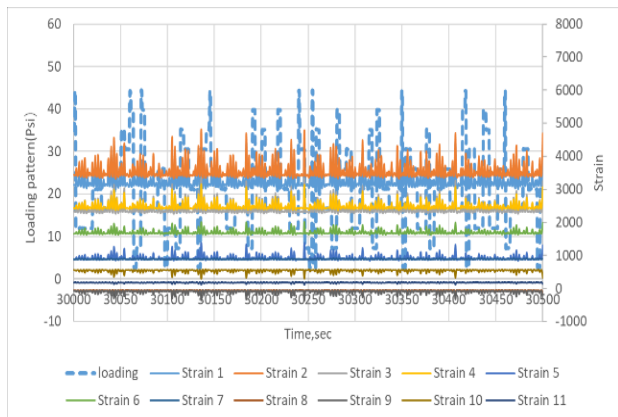
Figure 57. GE1 section loading vs. strain for direction 2 in time intervals: a) 0–500 sec, b) 2,000–2,500 sec, c) 30,000–30,500 sec, d) 45,000–45,500 sec, and e) 60,000–60,500 sec



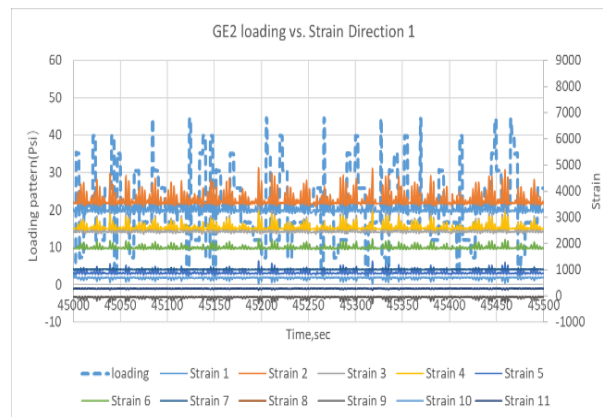
a)



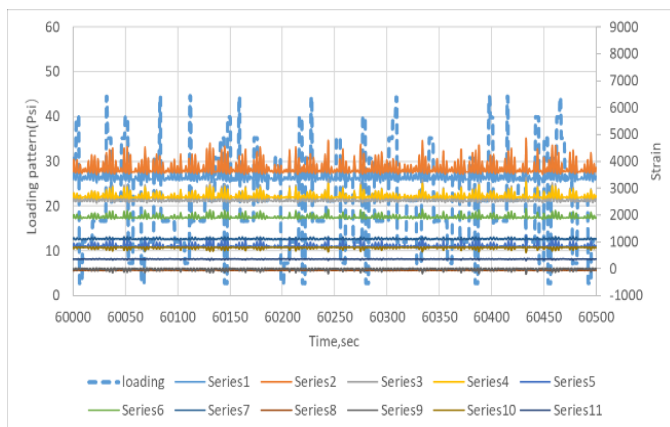
b)



c)

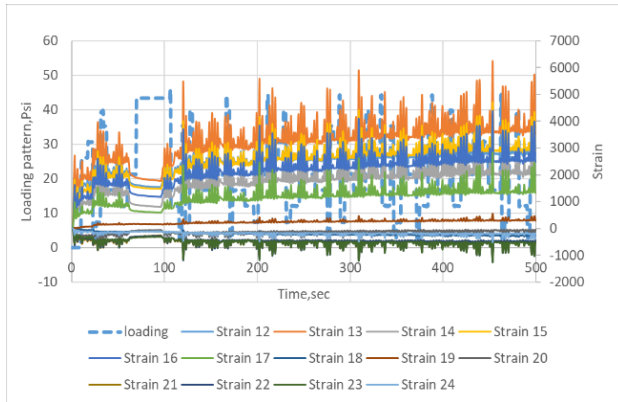


d)

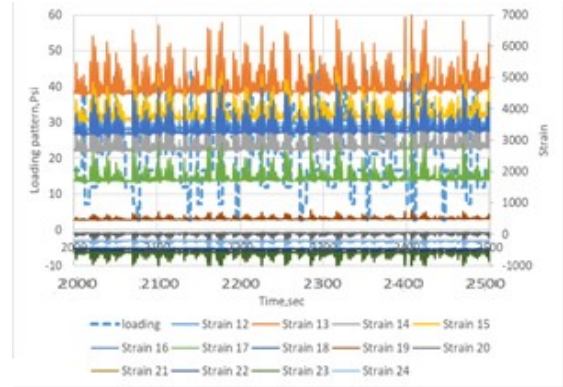


e)

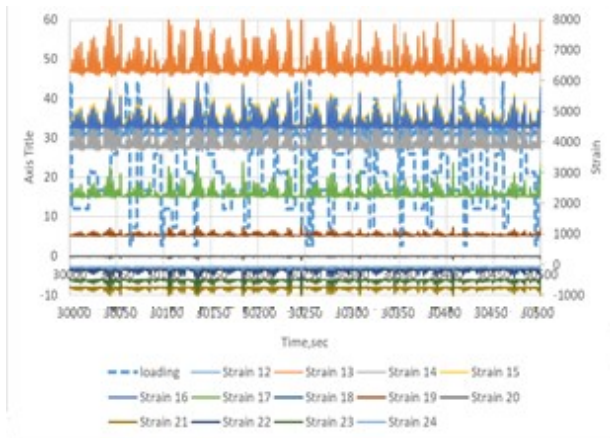
Figure 58. GE2 section loading vs. strain for direction 1 in time intervals: a) 0–500 sec, b) 2,000–2,500 sec, c) 30,000–30,500 sec, d) 45,000–45,500 sec, and e) 60,000–60,500 sec



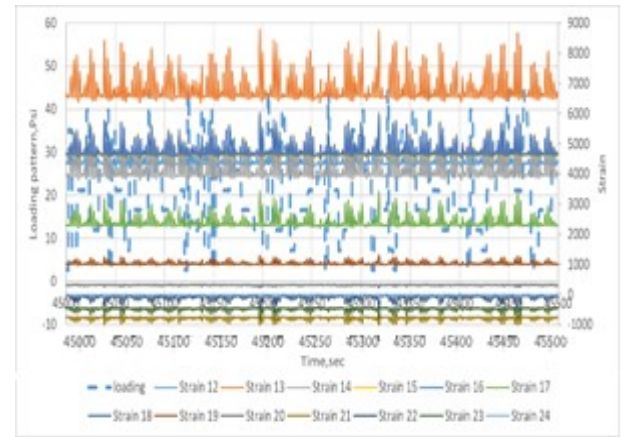
a)



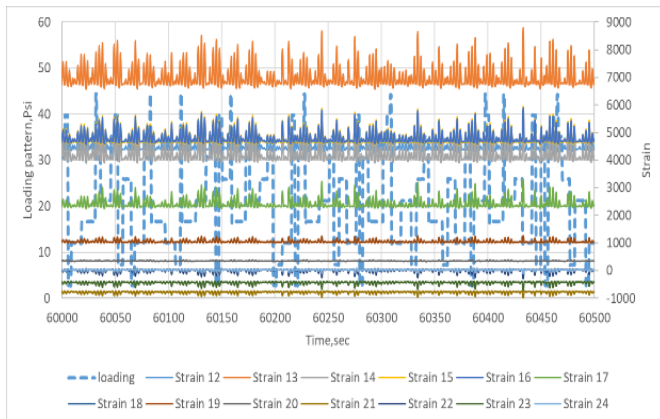
b)



c)

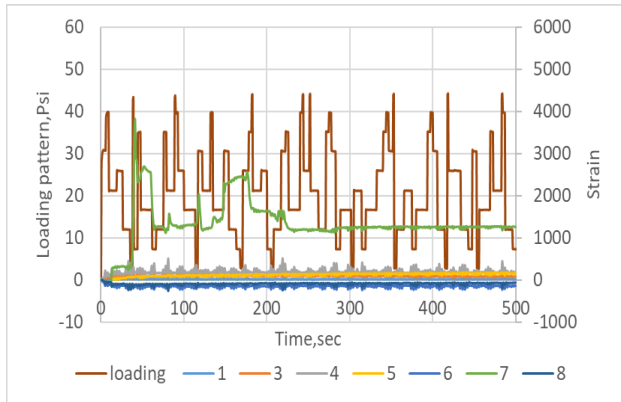


d)

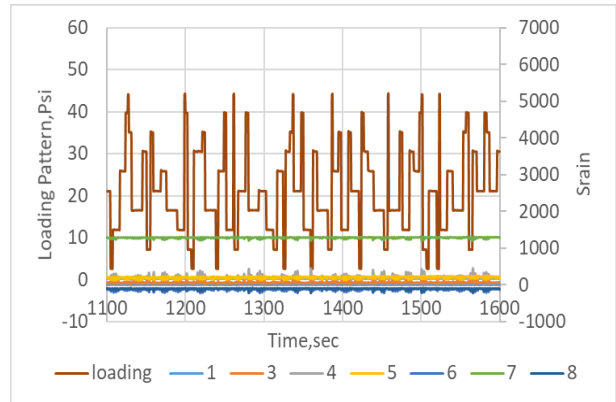


e)

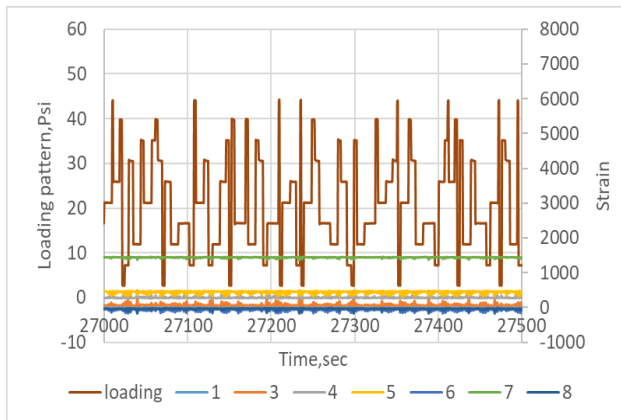
Figure 59. GE2 section loading vs. strain for direction 2 in time intervals: a) 0–500 sec, b) 2,000–2,500 sec, c) 30,000–30,500 sec, d) 45,000–45,500 sec, and e) 60,000–60,500 sec



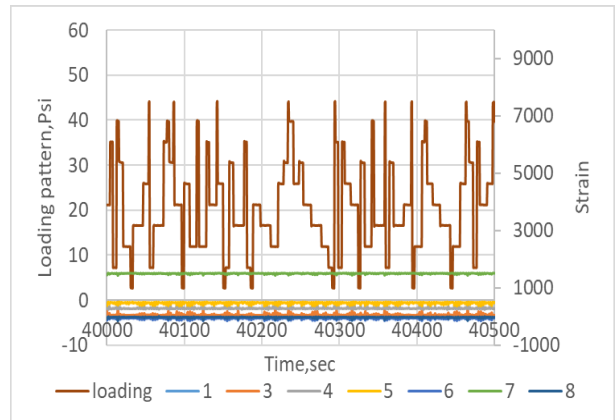
a)



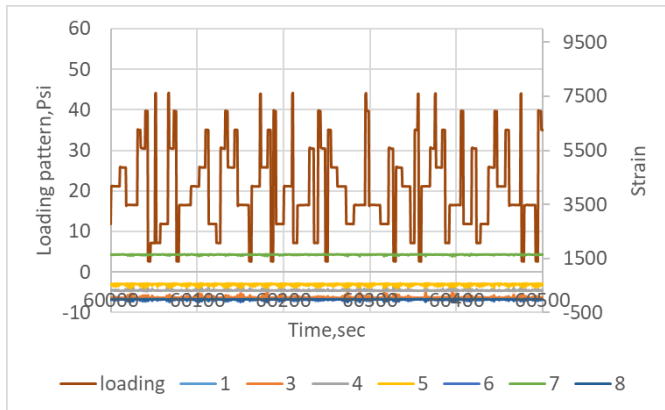
b)



c)

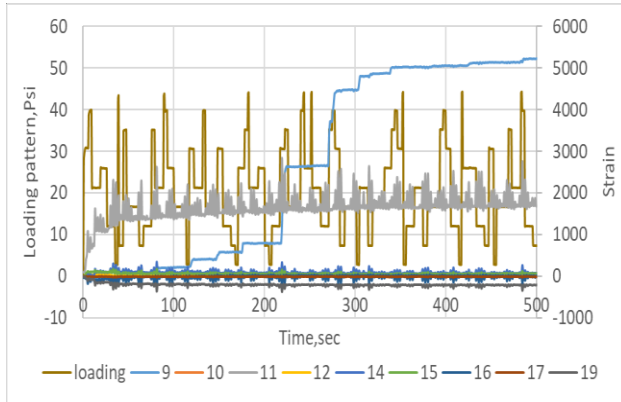


d)

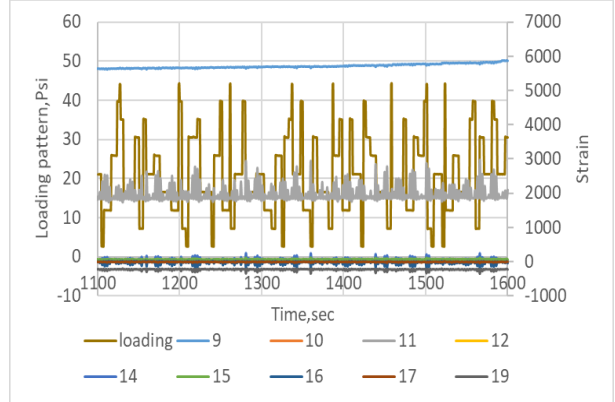


e)

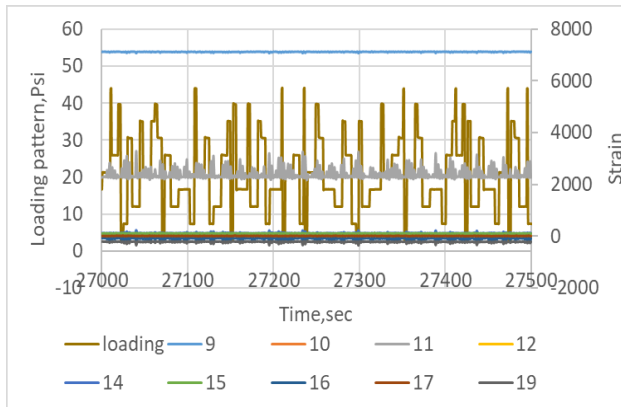
Figure 60. GE5 section loading vs. strain for direction 1 in time intervals: a) 0–500 sec, b) 2,000–2,500 sec, c) 30,000–30,500 sec, d) 45,000–45,500 sec, and e) 60,000–60,500 sec



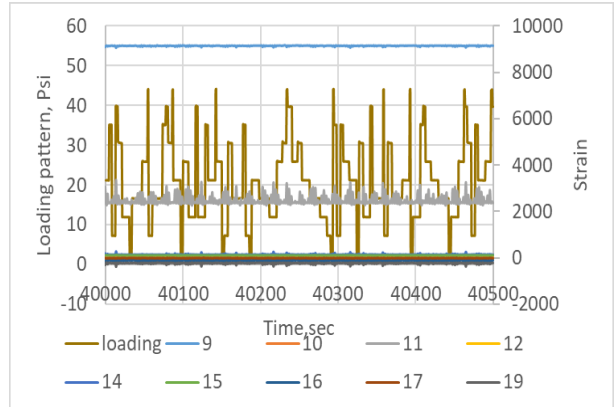
a)



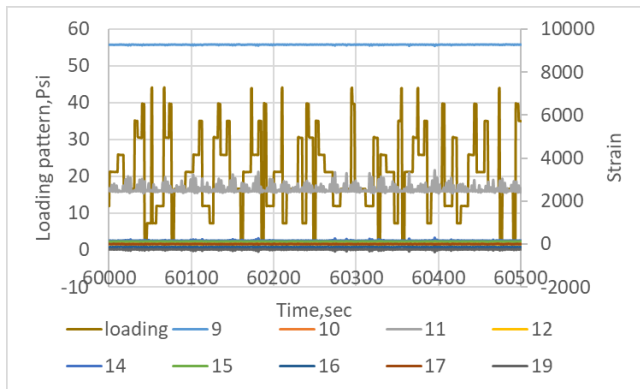
b)



c)

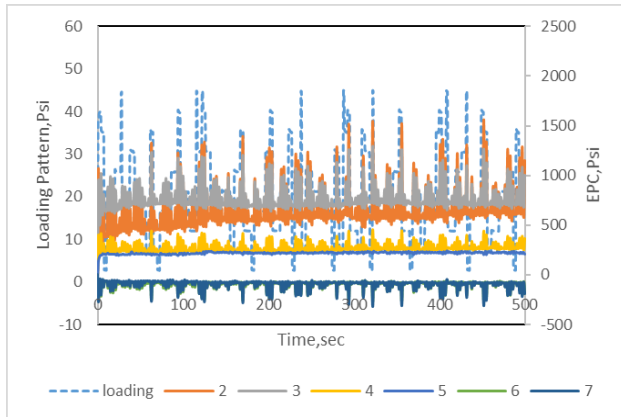


d)

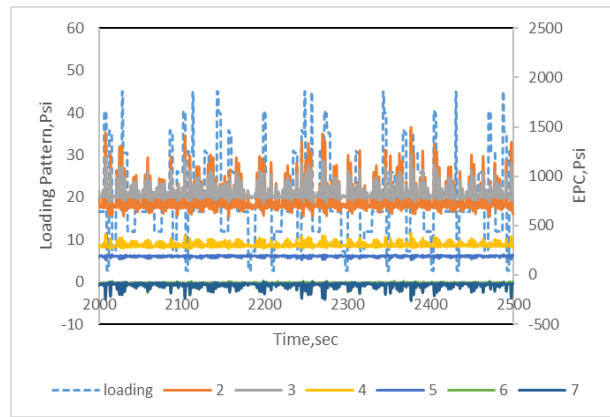


e)

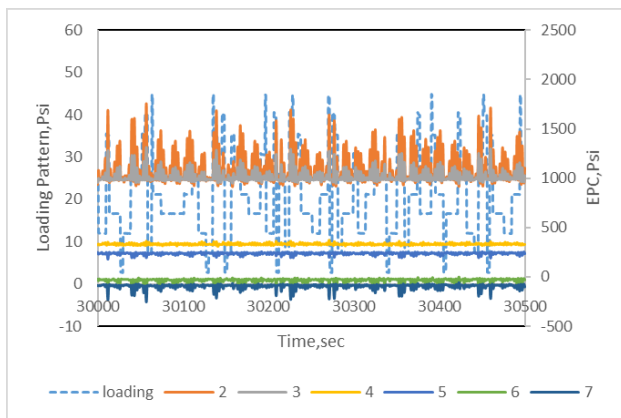
Figure 61. GE5 section loading vs. strain for direction 2 in time intervals: a) 0–500 sec, b) 2,000–2,500 sec, c) 30,000–30,500 sec, d) 45,000–45,500 sec, and e) 60,000–60,500 sec



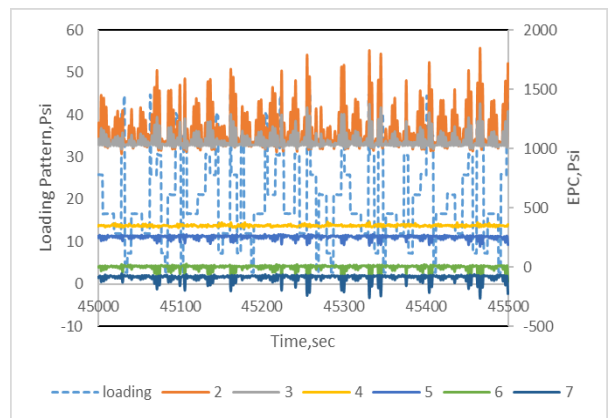
a)



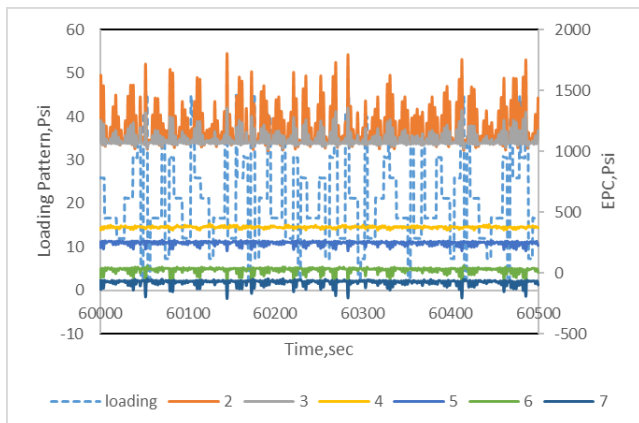
b)



c)

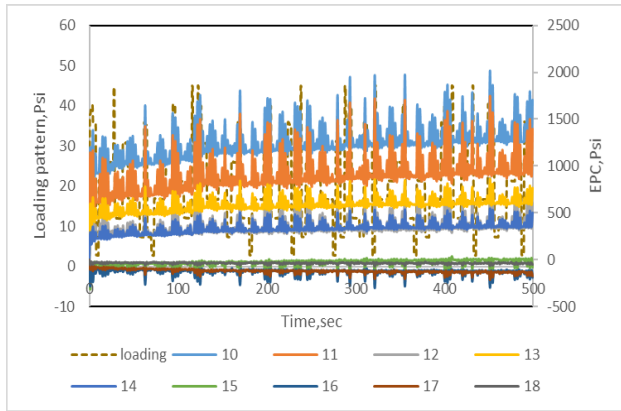


d)

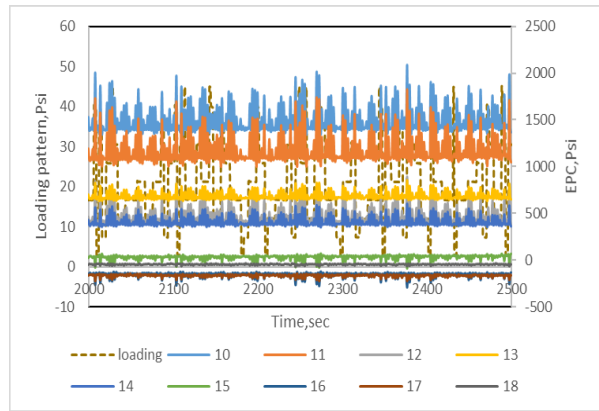


e)

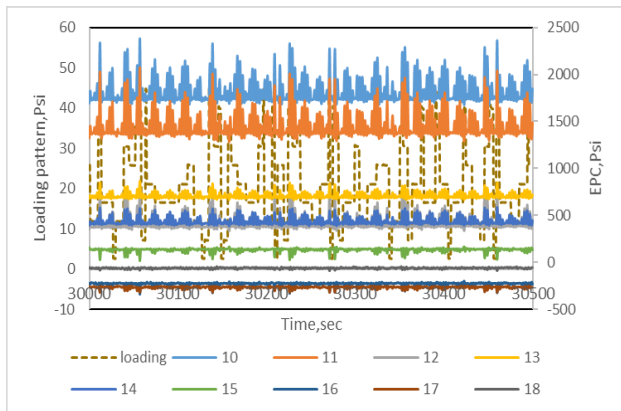
Figure 62. GE4 section loading vs. strain for direction 1 in time intervals: a) 0–500 sec, b) 2,000–2,500 sec, c) 30,000–30,500 sec, d) 45,000–45,500 sec, and e) 60,000–60,500 sec



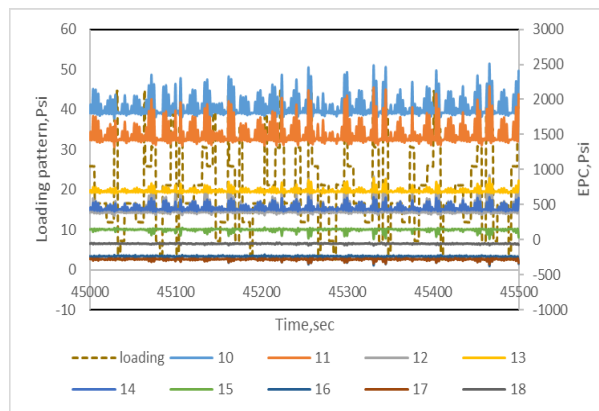
a)



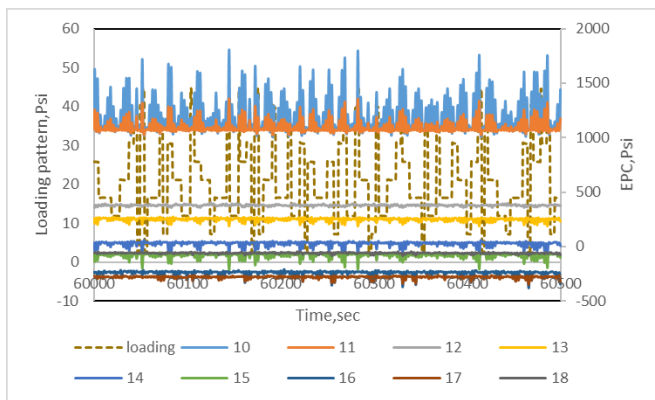
b)



c)

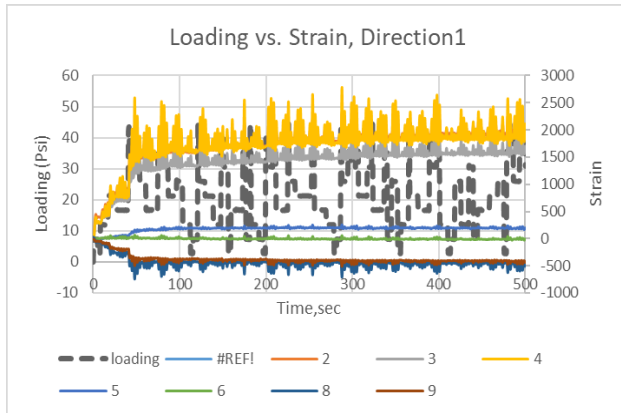


d)

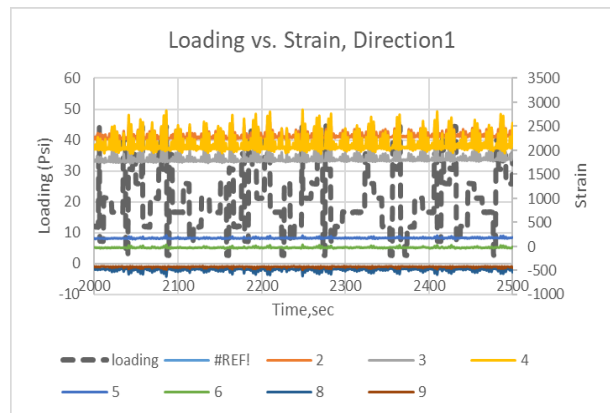


e)

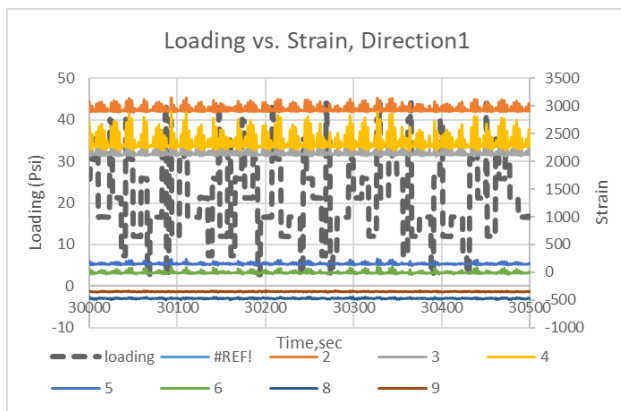
Figure 63. GE4 section loading vs. strain for direction 2 in time intervals: a) 0–500 sec, b) 2,000–2,500 sec, c) 30,000–30,500 sec, d) 45,000–45,500 sec, and e) 60,000–60,500 sec



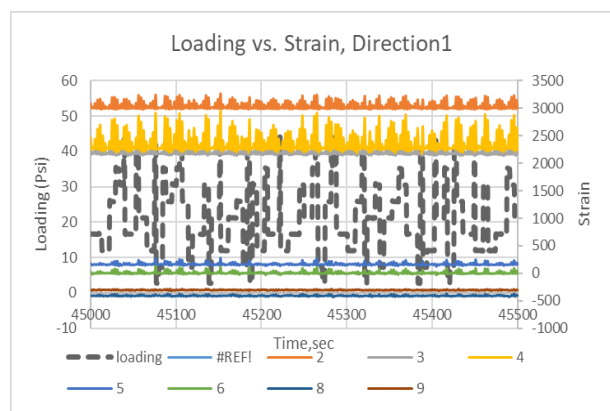
a)



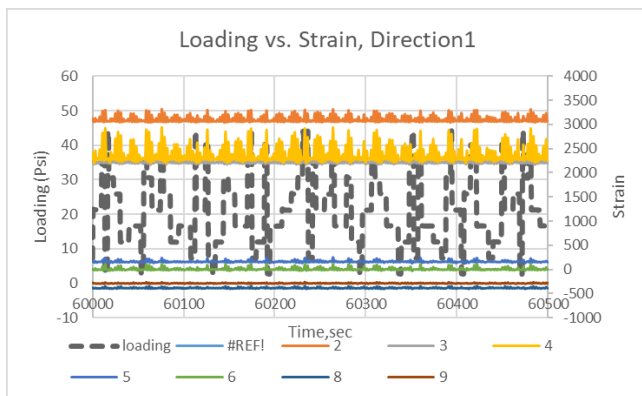
b)



c)

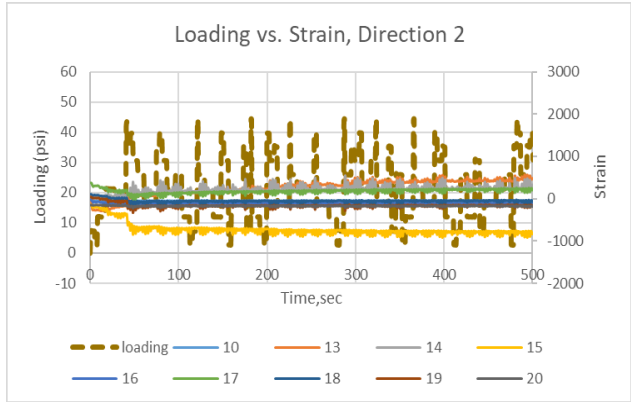


d)

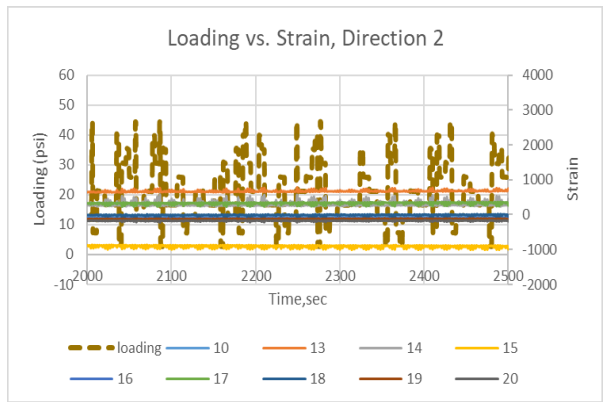


e)

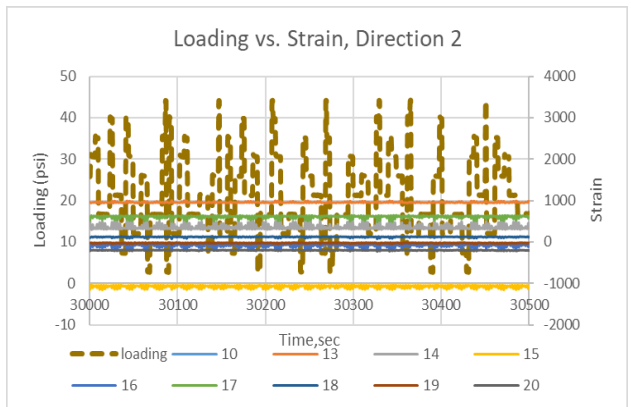
Figure 64. GE7 section loading vs. strain for direction 1 in time intervals: a) 0–500 sec, b) 2,000–2,500 sec, c) 30,000–30,500 sec, d) 45,000–45,500 sec, and e) 60,000–60,500 sec



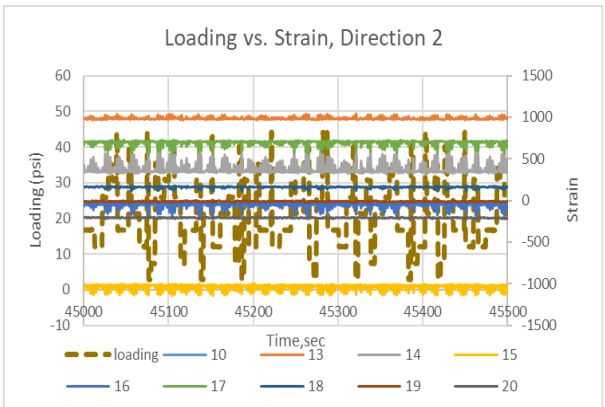
a)



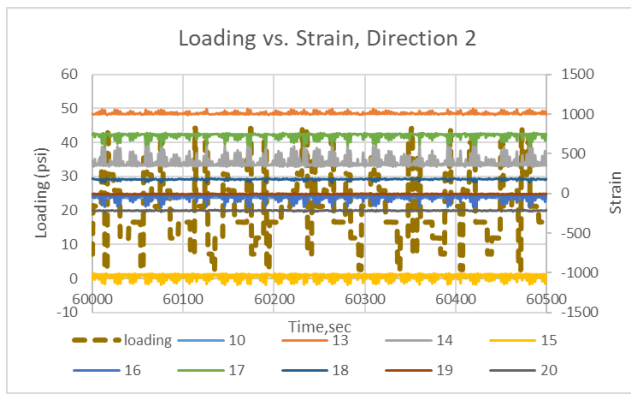
b)



c)

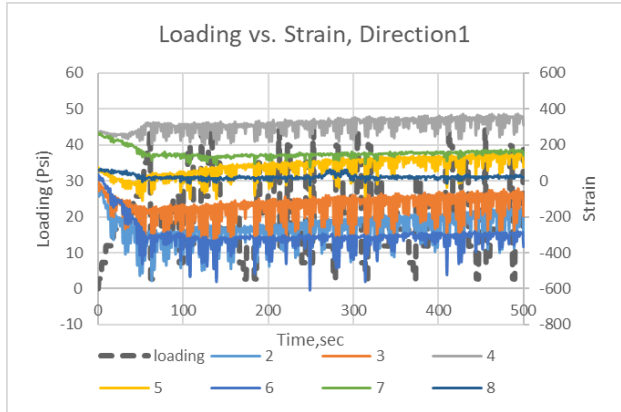


d)

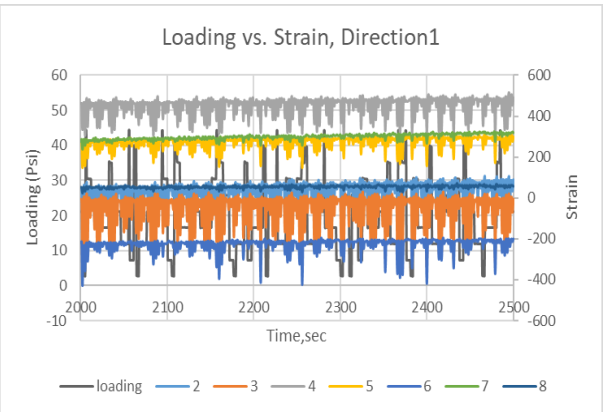


e)

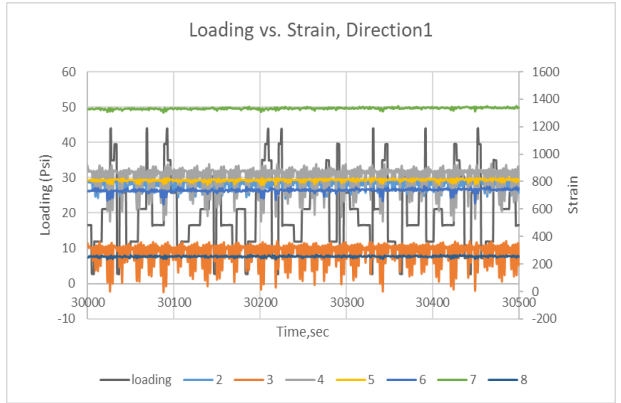
Figure 65. GE7 section loading vs. strain for direction 2 in time intervals: a) 0–500 sec, b) 2,000–2,500 sec, c) 30,000–30,500 sec, d) 45,000–45,500 sec, and e) 60,000–60,500 sec



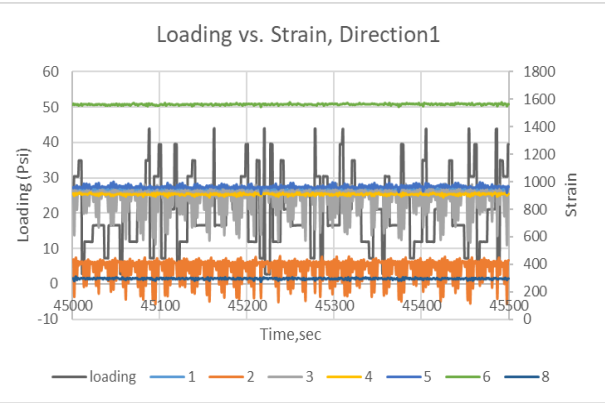
a)



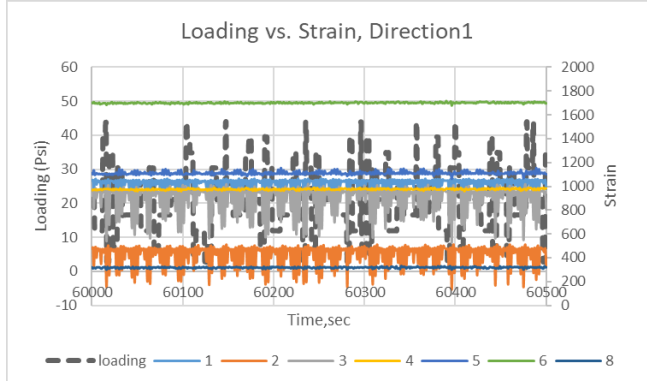
b)



c)

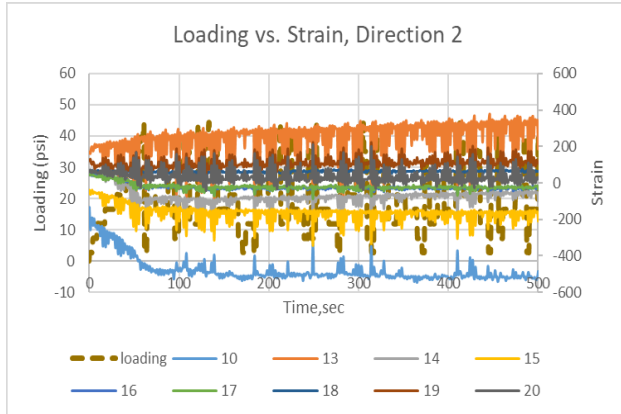


d)

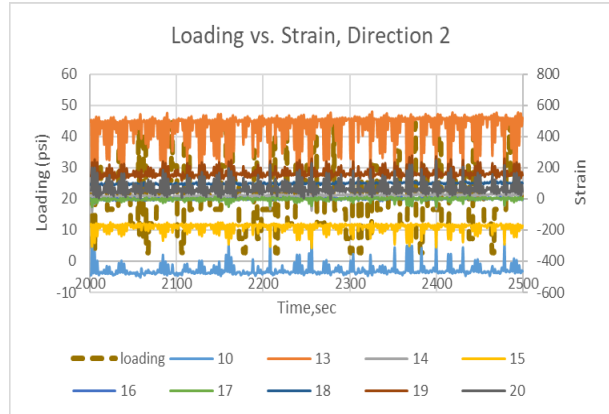


e)

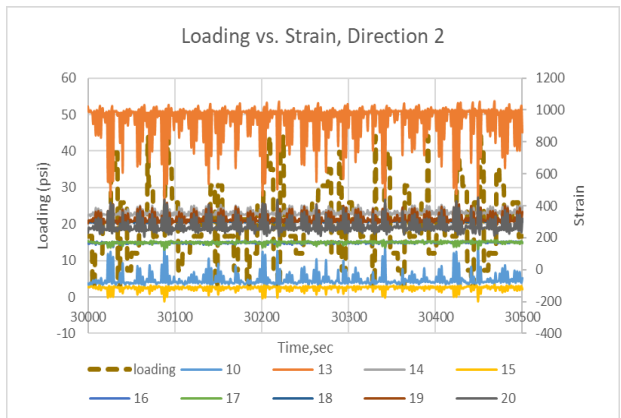
Figure 66. GE12 section loading vs. strain for direction 1 in time intervals: a) 0–500 sec, b) 2,000–2,500 sec, c) 30,000–30,500 sec, d) 45,000–45,500 sec, and e) 60,000–60,500 sec



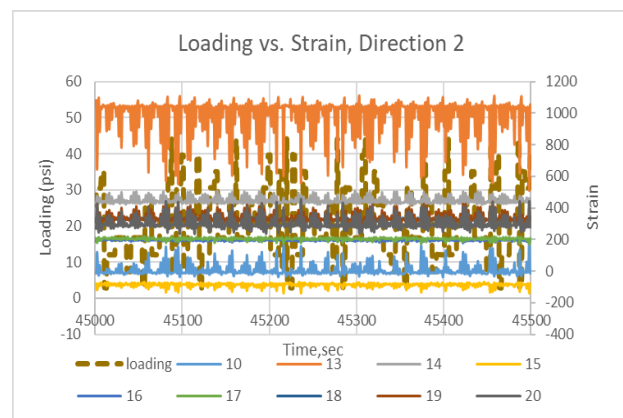
a)



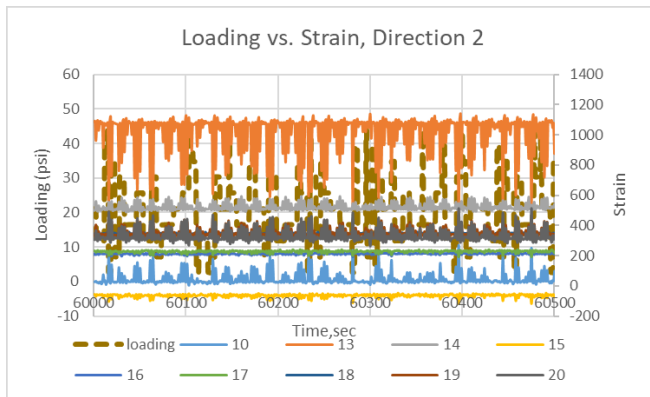
b)



c)

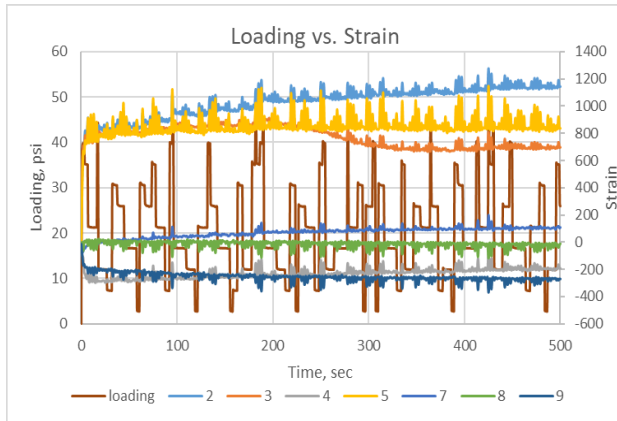


d)

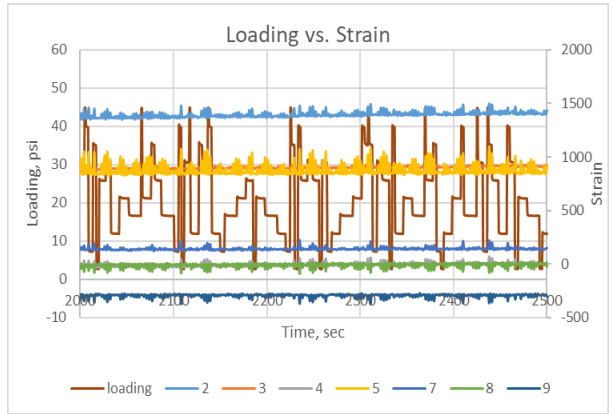


e)

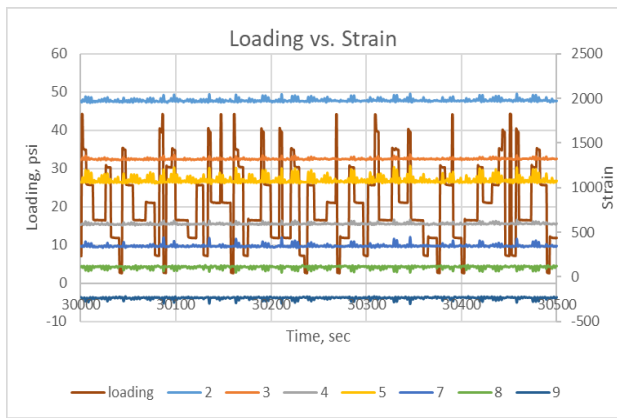
Figure 67. GE12 section loading vs. strain for direction 2 in time intervals: a) 0–500 sec, b) 2,000–2,500 sec, c) 30,000–30,500 sec, d) 45,000–45,500 sec, and e) 60,000–60,500 sec



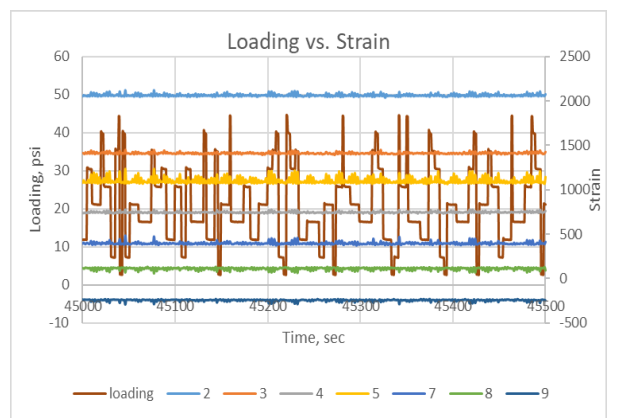
a)



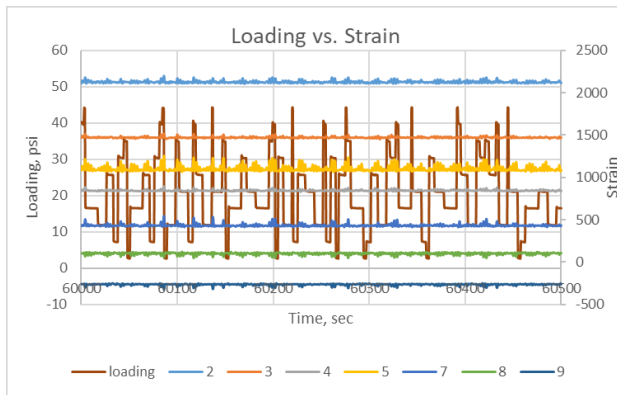
b)



c)

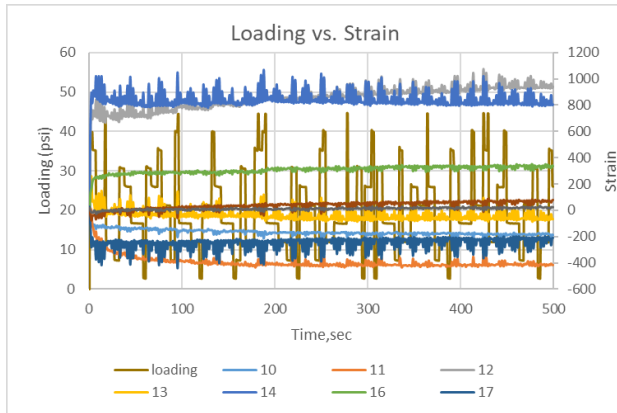


d)

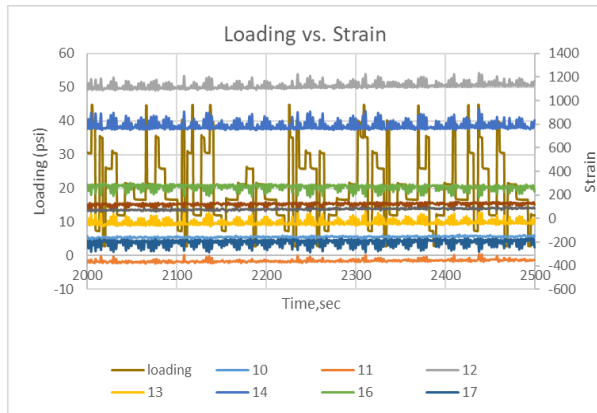


e)

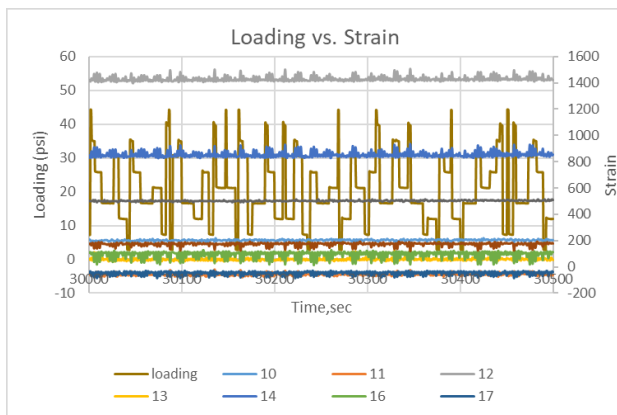
Figure 68. GE15 section loading vs. strain for direction 1 in time intervals: a) 0–500 sec, b) 2,000–2,500 sec, c) 30,000–30,500 sec, d) 45,000–45,500 sec, and e) 60,000–60,500 sec



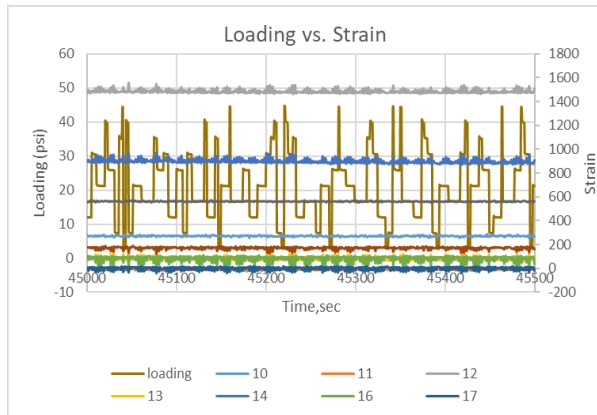
a)



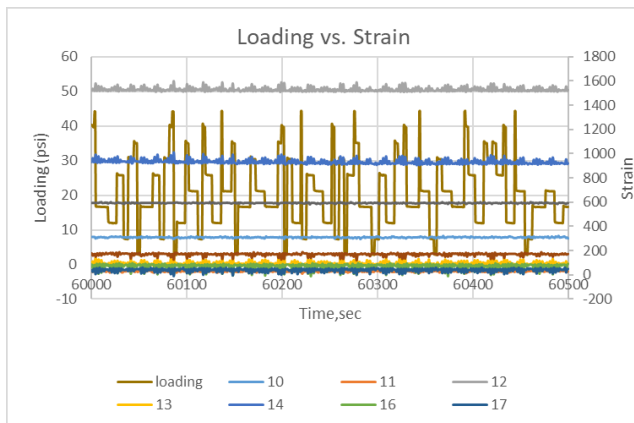
b)



c)



d)



e)

Figure 69. GE15 section loading vs. strain for direction 2 in time intervals: a) 0–500 sec, b) 2,000–2,500 sec, c) 30,000–30,500 sec, d) 45,000–45,500 sec, and e) 60,000–60,500 sec

The scale of strain in all of the charts is in microstrain. It can be seen from the results that, for the triaxial geogrids, the strain results are similar in each direction; however, for biaxial geogrids, the strain is always higher in direction 2 than in direction 1.

CHAPTER 3: FIELD TESTS AND RELATED FIELD DATA

3.1 FIELD TEST SECTION PLAN AND CONSTRUCTION

The research team partnered with Ingios Geotechnics, Inc. to conduct field automated plate load tests (APLTs). This field test equipment can quantify the underlying layer mechanistic properties with a special sensor kit that measures the pavement deflection basin. The results for cyclic deformation, permanent deformation, elastic modulus, stiffness, resilient modulus, cyclic stresses, and the number of cycles are calculated in real-time and reported immediately. These results were used to evaluate GE and geogrid gain factors. The details, procedures, and results of the field tests are included in this chapter.

3.2 INTRODUCTION

Ingios conducted APLTs on test sections on the South Riverfront Drive project in Mankato, Minnesota. Testing was performed on July 31 and August 1, 2020. In situ testing included cyclic APLTs on the compacted aggregate base layer to determine composite, base layer, and subgrade layer resilient modulus (M_r) values. DCP tests were performed to determine penetration resistance and a CBR profile from the DCP tests at each test location. Tests were conducted at eight test points selected by the Iowa State University research team, with one test location in each of the eight sections. An additional test was conducted in an area next to a utility manhole in Section #5.

Figure 70 shows the test sections studied using the APLT device and finite element analyses.

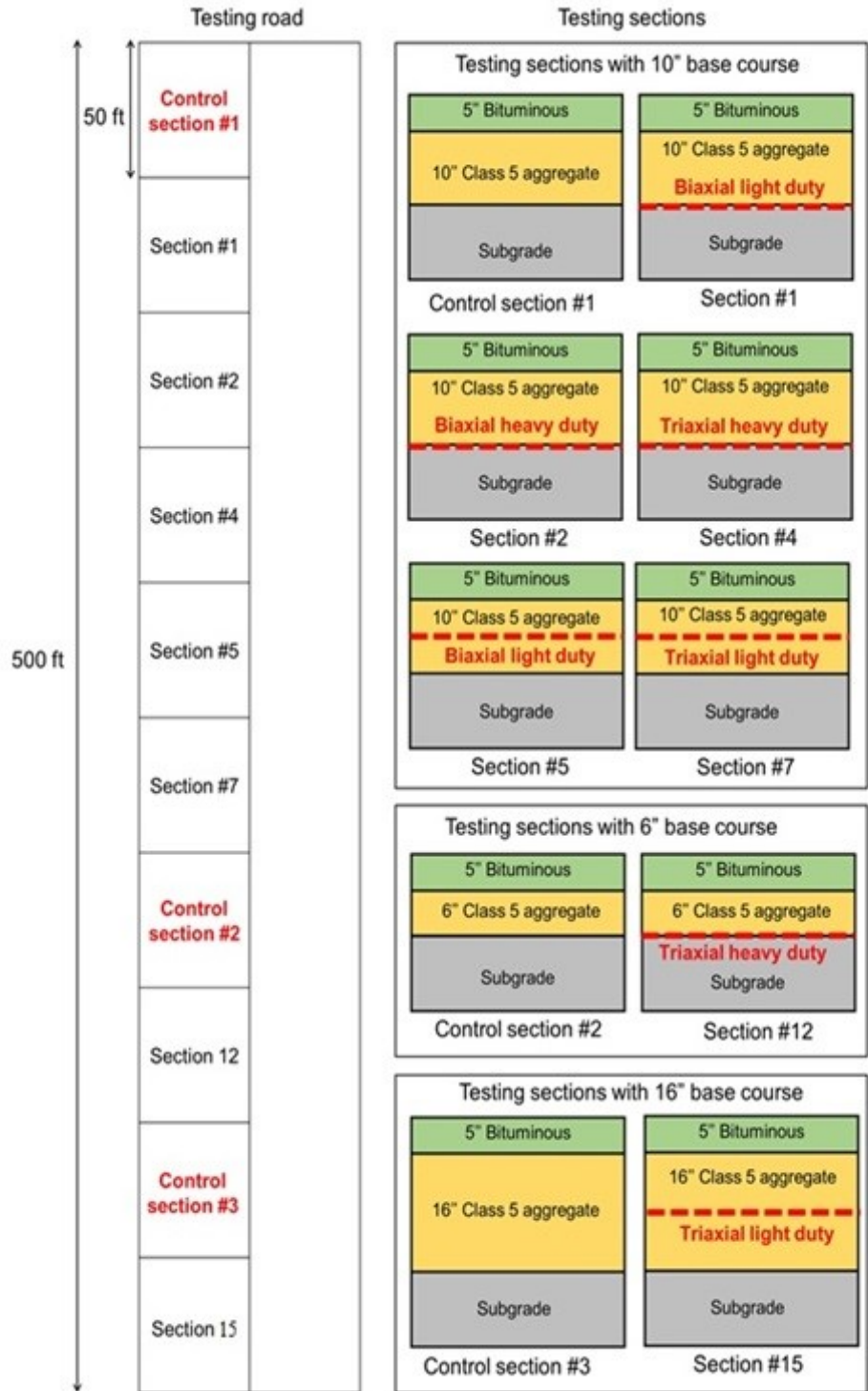


Figure 70. Field test sections

Ten test sections were studied to evaluate unreinforced and reinforced base course behavior using different types of geogrids in different locations: Control section 1, Section 1, Section 2, Section 4, Section 5, Section 7, Control section 2, Section 12, Control section 3, and Section 15. The three control sections were used in the field tests and generally designated as Control section 1, 2, and 3, with no

geogrids in these sections. Biaxial geogrids were used in Section 1, 2, and 5, and triaxial geogrids were used in Section 4, 7, 12, and 15. For Section 1, 2, 4, and 12, the geogrid products were placed at the interface between the base course layer and the subgrade layer; for Section 5 and 7, the geogrid was placed at the middle of the base course layer. Both light-duty and heavy-duty geogrid products were used in the test sections with the details for the test sections shown in the previous Figure 70.

The main parameters studied were geogrid type (biaxial or triaxial), geogrid stiffness (“light” duty or “heavy” duty), geogrid location/depth, and aggregate base thickness. Seventeen sections (combinations) were studied using a combination of experimental testing (APLTs) and finite element modeling.

The test section cross-section details were as follows:

- Control section 1: 10 in. Class 5 aggregate base over subgrade
- Section 1: 10 in. Class 5 aggregate base stabilized over subgrade with biaxial light-duty geogrid at subgrade/aggregate base interface
- Section 2: 10 in. Class 5 aggregate base stabilized over subgrade with biaxial heavy-duty geogrid at subgrade/aggregate base interface
- Section 4: 10 in. Class 5 aggregate base stabilized over subgrade with triaxial heavy-duty geogrid at subgrade/aggregate base interface
- Section 5: 10 in. Class 5 aggregate base stabilized over subgrade with biaxial light-duty geogrid embedded at mid-depth within the aggregate base layer
- Section 7: 10 in. Class 5 aggregate base stabilized over subgrade with triaxial light-duty geogrid embedded at mid-depth within the aggregate base layer
- Control section 2: 6 in. Class 5 aggregate base over subgrade
- Section 12: 6 in. Class 5 aggregate base stabilized over subgrade with biaxial light-duty geogrid at subgrade/aggregate base interface

The aggregate base material used on this project consisted of recycled asphalt pavement (RAP) classified as the MnDOT Class 5 aggregate base. Based on the research team’s field observations during construction, the subgrade near the surface also consisted of RAP. Per discussions with the contractor, the elevation profile in the test sections was constructed by first cutting the subgrade level and then backfilling with several inches of RAP and recompacting it.

1,400 cycle APLTs were conducted in each of the test sections except Control section 3 and Section 15, which were not tested by Ingios. Deflection basin measurements were obtained at three positions extending away from the plate (2r, 3r, and 4r). Results from the cyclic APLTs conducted at six different stress levels were used to determine the in situ “universal” model (AASHTO 2015). The k_1^* , k_2^* , and k_3^* model parameters for the composite (M_r -Comp) and stabilized aggregate base (M_r -Base) and subgrade layers (M_r -Subgrade) were determined for each test point. Summaries of each individual test result are provided in the Summary Plots section of this chapter.

Each cyclic stress increment was analyzed to characterize whether the behavior reached a near-linear elastic condition at the end of each stress increment. The layered analysis performed in determining M_r -Base and M_r -Subgrade was based on Odemark’s method of equivalent thickness (Tranquist 2019) and

Boussinesq's elastic solution for linear-elastic materials. The top aggregate base layer thickness was assumed as the nominal thickness per the section design. The applied cyclic stresses at the subgrade/base layer interface were calculated using the KENLAYER elastic layer analysis program (Huang 1993).

The following assumptions were made in calculating the M_r values:

- Shape factor, $f = 8/3$ for a rigid plate on granular material.
- Poisson's ratio, $\nu = 0.40$ for aggregate base material and 0.40 for subgrade material.
- Plate bending correction, $F_{\text{Bending}} = 1$ (No correction). The 12 in. diameter plate used in this study was 1 in. thick and had a 6 in. diameter steel loading pedestal centered on the plate.
- Future saturation correction, $F_{\text{Saturation}} = 1$ (No correction). Laboratory testing is needed to determine this correction factor; otherwise, field saturation is required in situ.

3.3 GEOGRID, AGGREGATES, AND SUBGRADE SOILS

3.3.1 Geogrids

The following Tensar geogrids were used in the field tests: light-duty Tensar BX1100 Biaxial, heavy-duty Tensar BX1200 Biaxial, light-duty Tensar TX130s Triaxial, and heavy-duty Tensar TX7 Triaxial. The properties of these geogrids are shown in Appendix A. It should be noted that biaxial geogrids have different sizes and strength in each direction while the strength for triaxial geogrids is equal for each direction, while the strength for triaxial geogrids is equal for each direction.

3.3.2 Base Course Material Properties

Class 5 aggregates, which contain virgin aggregates and a certain percentage of recycled aggregate and are typically used in Minnesota for the base course of pavement construction projects, were used for the aggregate base layer. The results of index property tests on the materials used are shown in Appendix E.

3.4 PROJECT LOCATION AND TEST LOCATIONS

Figure 71 shows the project location in Mankato, Minnesota, and Figures 72 and 73 show the field location in Mankato and test sections, respectively.

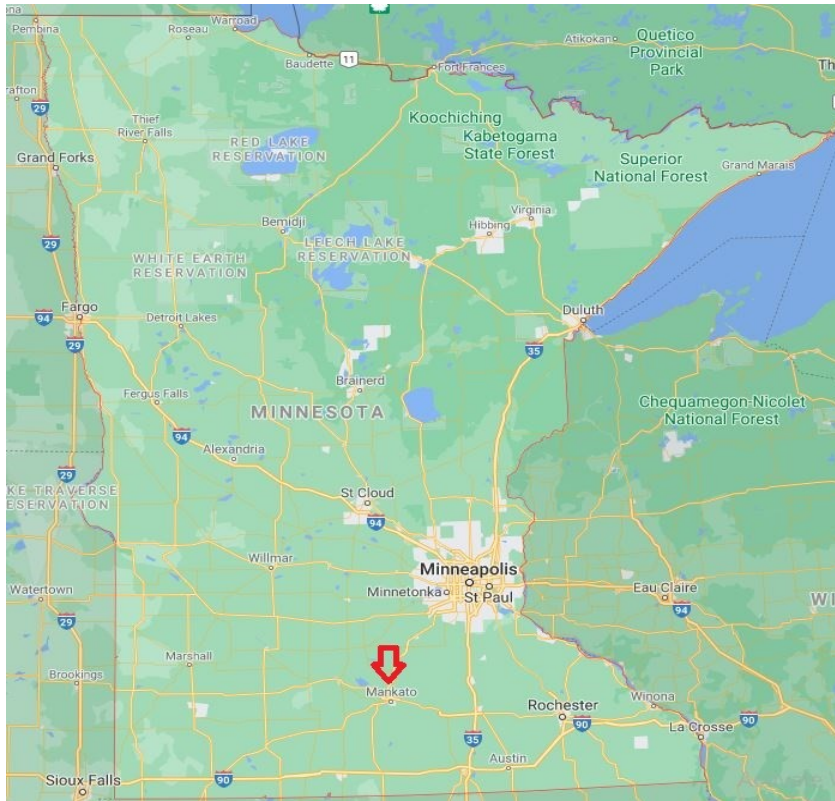


Figure 71. Project location in Mankato

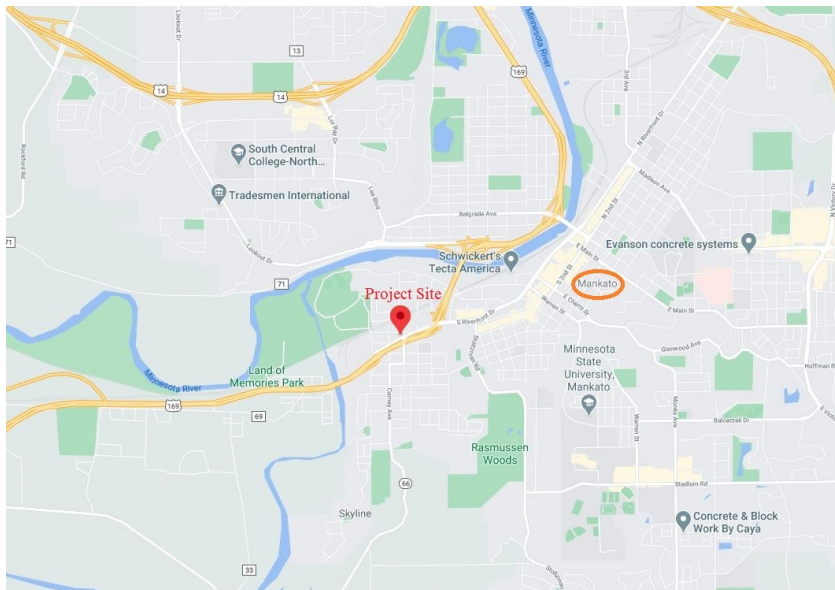


Figure 72. Field location in Mankato

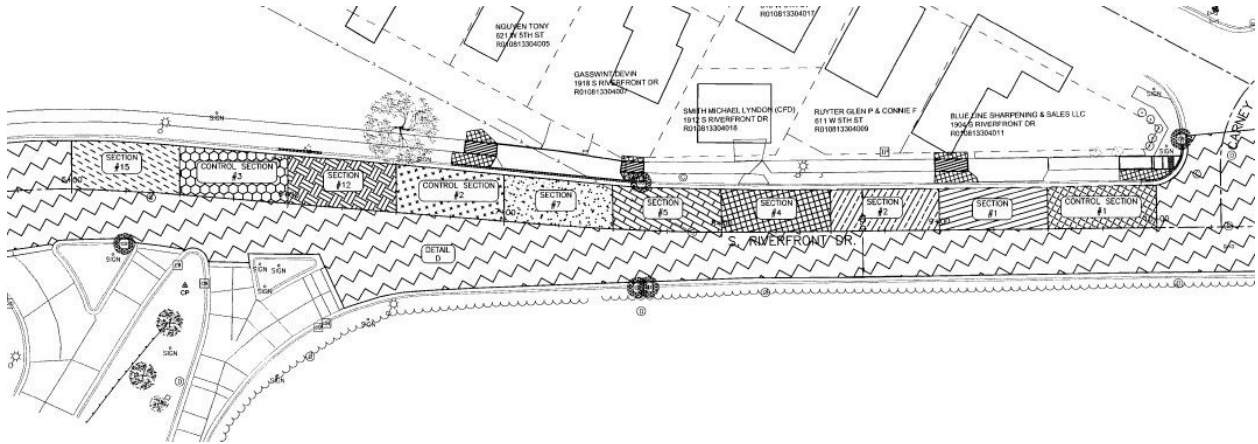


Figure 73. Field test sections in Mankato

3.5 SITE CONDITIONS AND IMAGES

Figure 74 shows the site conditions and construction procedure for the base and subgrade, along with placement of the geogrids in the construction process. Additional details on field test locations, test results, and images are included in Appendices E through H.



a)



b)



c)



d)



e)



f)



g)



h)



i)

Figure 74. a, b, and c) site condition and geogrid placement for construction, d) subgrade compaction around manhole in the road, e) compacted subgrade around the manhole, and f, g, h, and i) construction procedure for base and subgrade

3.6 AUTOMATED PLATE LOAD TESTING

Figure 75 shows the APLT equipment and the tests performed in the field.



a)



b)



c)



d)



e)

Figure 75. a and b) APLT equipment and truck, c and d) APLT loading actuator structure and sensors, and e) APLT equipment

3.7 PERFORMED QC/QA TESTS IN THE FIELD

During construction of the road sections, a series of quality assurance and quality control (QA/QC) geotechnical tests were performed on each test section. These tests included light falling weight deflectometer (LFWD) tests on top of the subgrade layers, DCP tests on top of the base layers, and sand cone compaction tests on top of the base layers.

Ingios also conducted intelligent compaction tests on top of the subgrade and base layers, which were beyond the scope of the project. This information is available upon request from Ingios Geotechnics, Inc. The remainder of this section provides details on the tests performed in the field.

3.7.1 Light Falling Weight Deflectometer Tests on Top of the Subgrade Layers

Figure 76 shows the LFWD tests conducted on top of the subgrade layers in the field. Additional details on the Proctor tests, LFWD tests, and sand cone tests are included in Appendix F.



a)



b)



c)

Figure 76. LFWD test on top of the subgrade layer in the field

3.7.2 Intelligent Compaction on Top of Subgrade and Base Layers

Figure 77 shows the intelligent compaction testing conducted by Ingios on top of the subgrade and base layers in the field.



a)



b)

Figure 77. Intelligent compaction on top of subgrade and base layers in the field

3.7.3 Dynamic Cone Penetrometer Tests on Top of Base layer

Figure 78 shows DCP tests conducted on top of the base layers in the field. Additional details on the DCP test results are included in Appendix G.

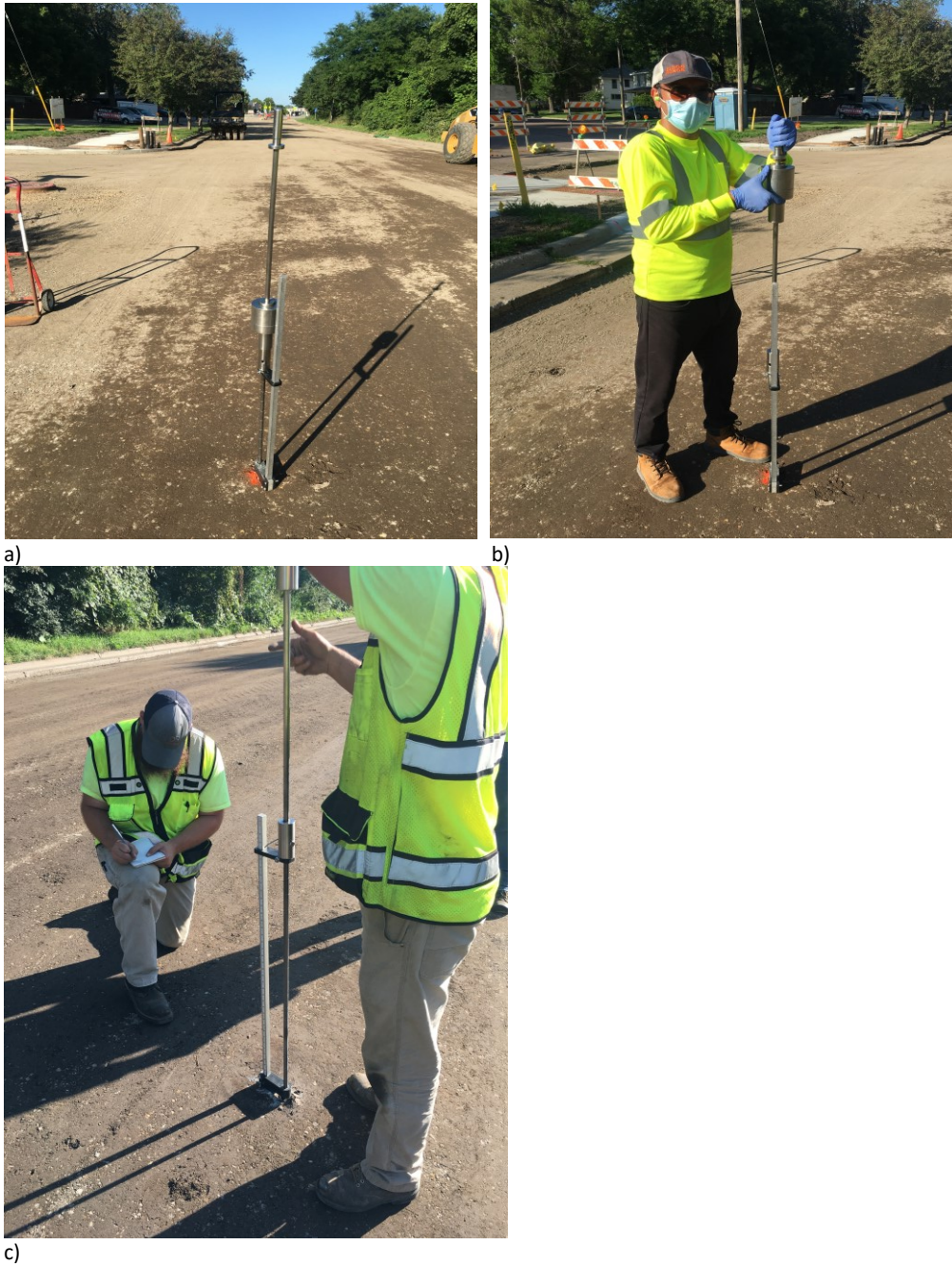


Figure 78. DCP tests on top of the base layer in the field

3.7.4 Sand Cone Compaction Test on Base layer

Figure 79 shows the sand cone compaction tests conducted on the base layer in the field.



a)



b)

Figure 79. Sand cone compaction test on base layer in the field

3.8 SUMMARY PLOTS

Figures 80 through 110 detail the test results for all test sections in the field.

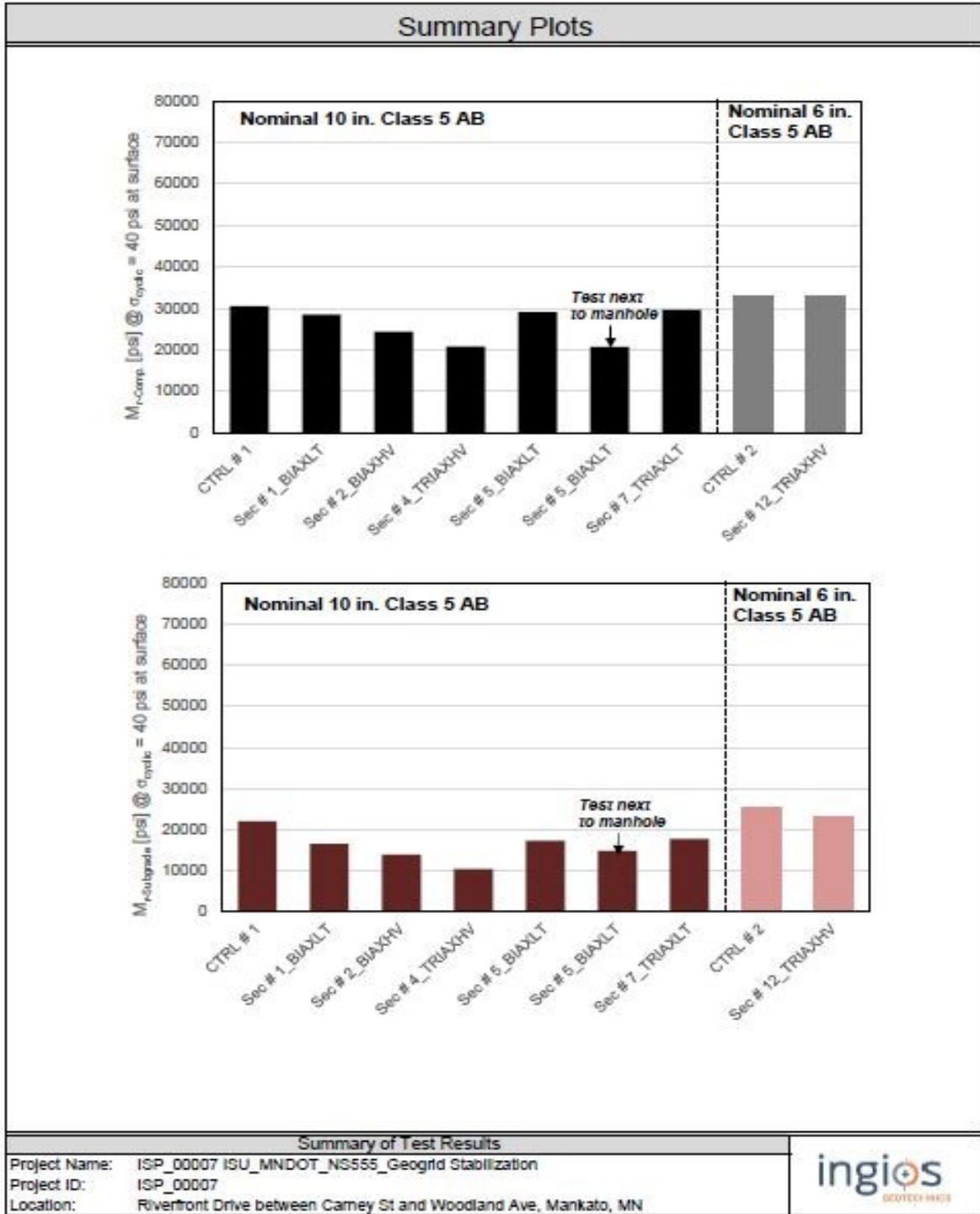


Figure 80. Resilient modulus of aggregate base materials for all test sections in the field

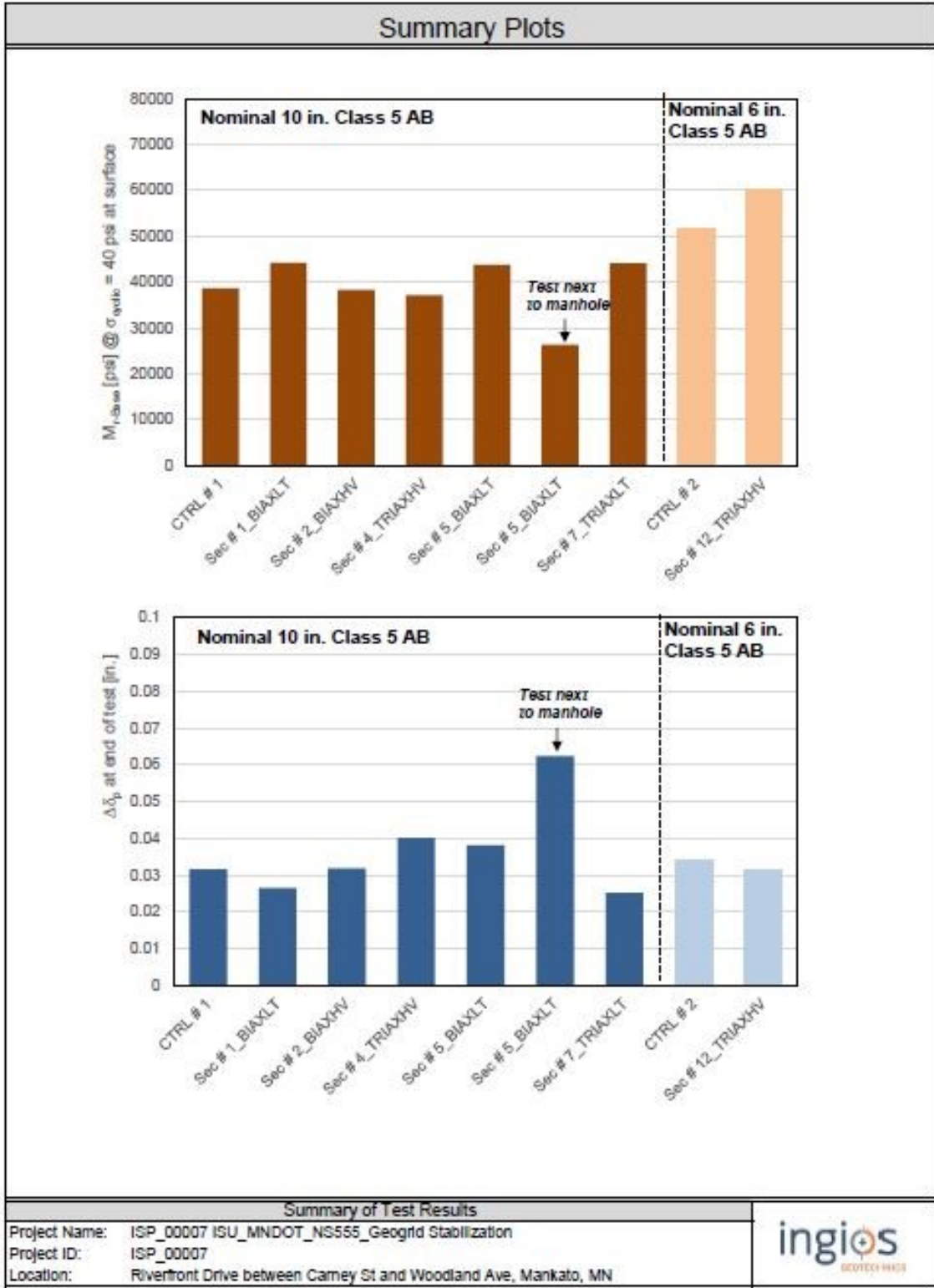
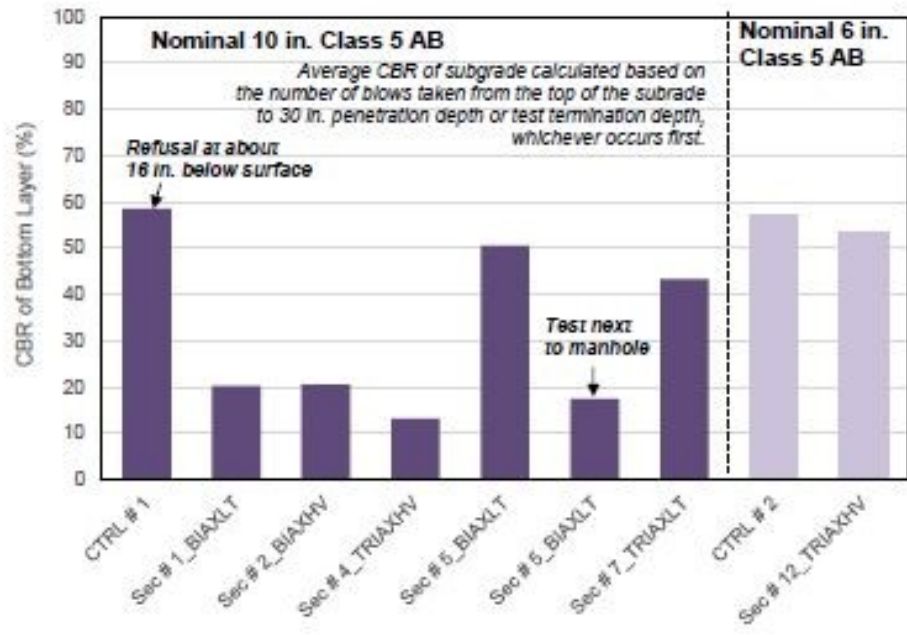
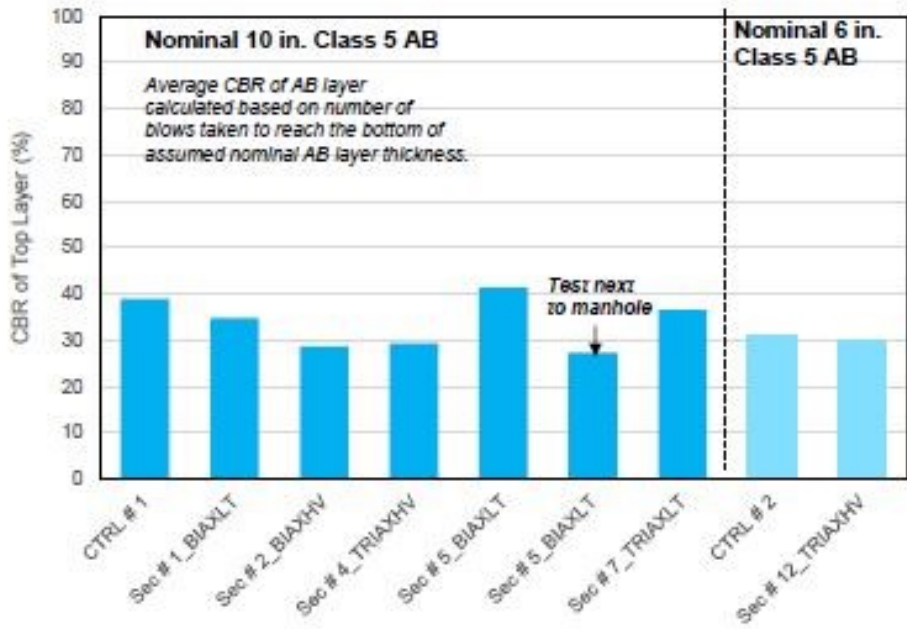


Figure 81. Base resilient modulus of all test sections in the field

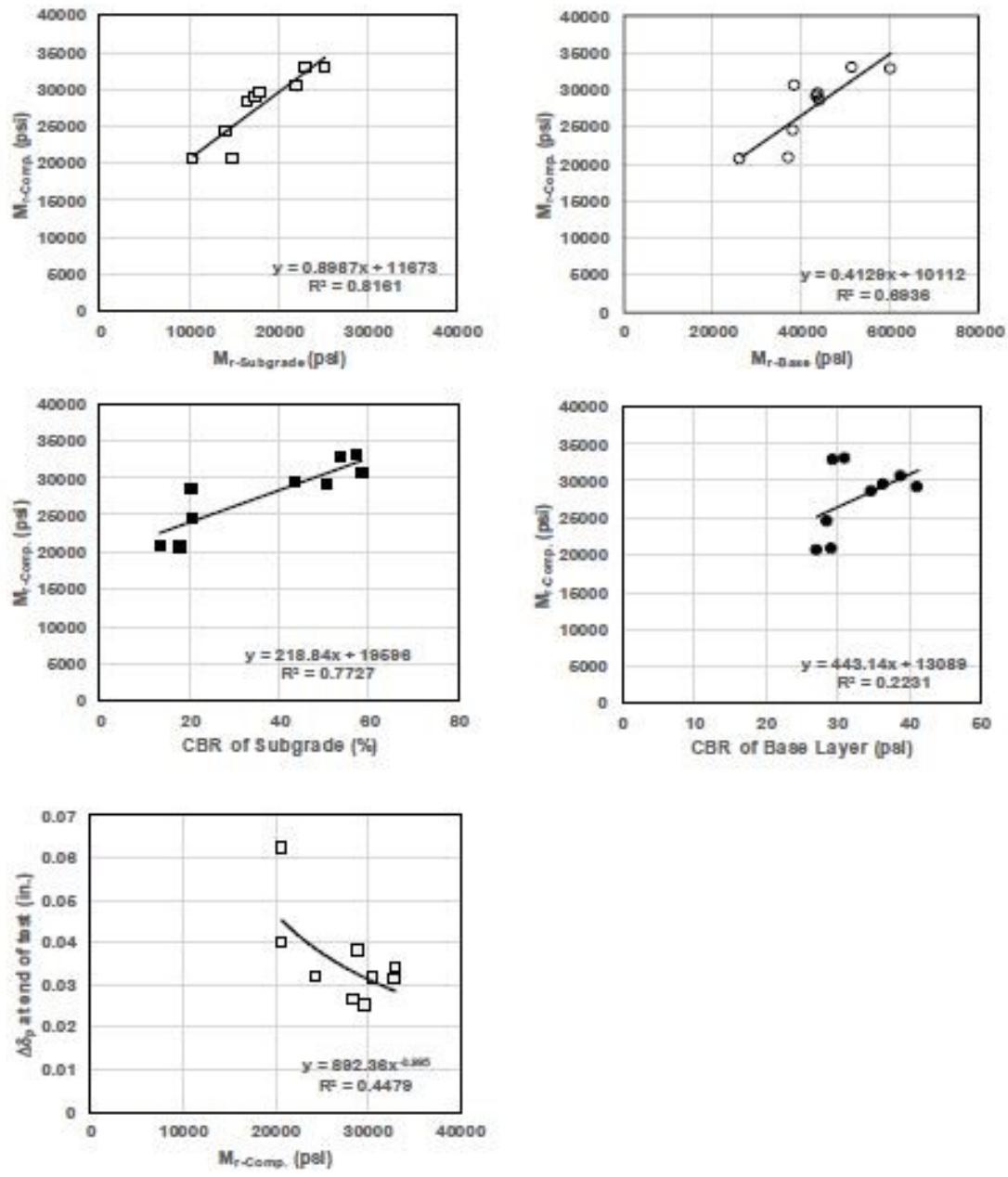
Summary Plots



Summary of Test Results	
Project Name: ISP_00007 ISU_MNDOT_NS555_Geogrid Stabilization	
Project ID: ISP_00007	
Location: Riverfront Drive between Carney St and Woodland Ave, Mankato, MN	

Figure 82. CBR results at top layer of all test sections in the field

Summary Plots



Summary of Test Results	
Project Name: ISP_00007 ISU_MNDOT_NS555_Geogrid Stabilization	
Project ID: ISP_00007	
Location: Riverfront Drive between Carney St and Woodland Ave, Mankato, MN	

Figure 83. Summary of test results for all test sections in the field

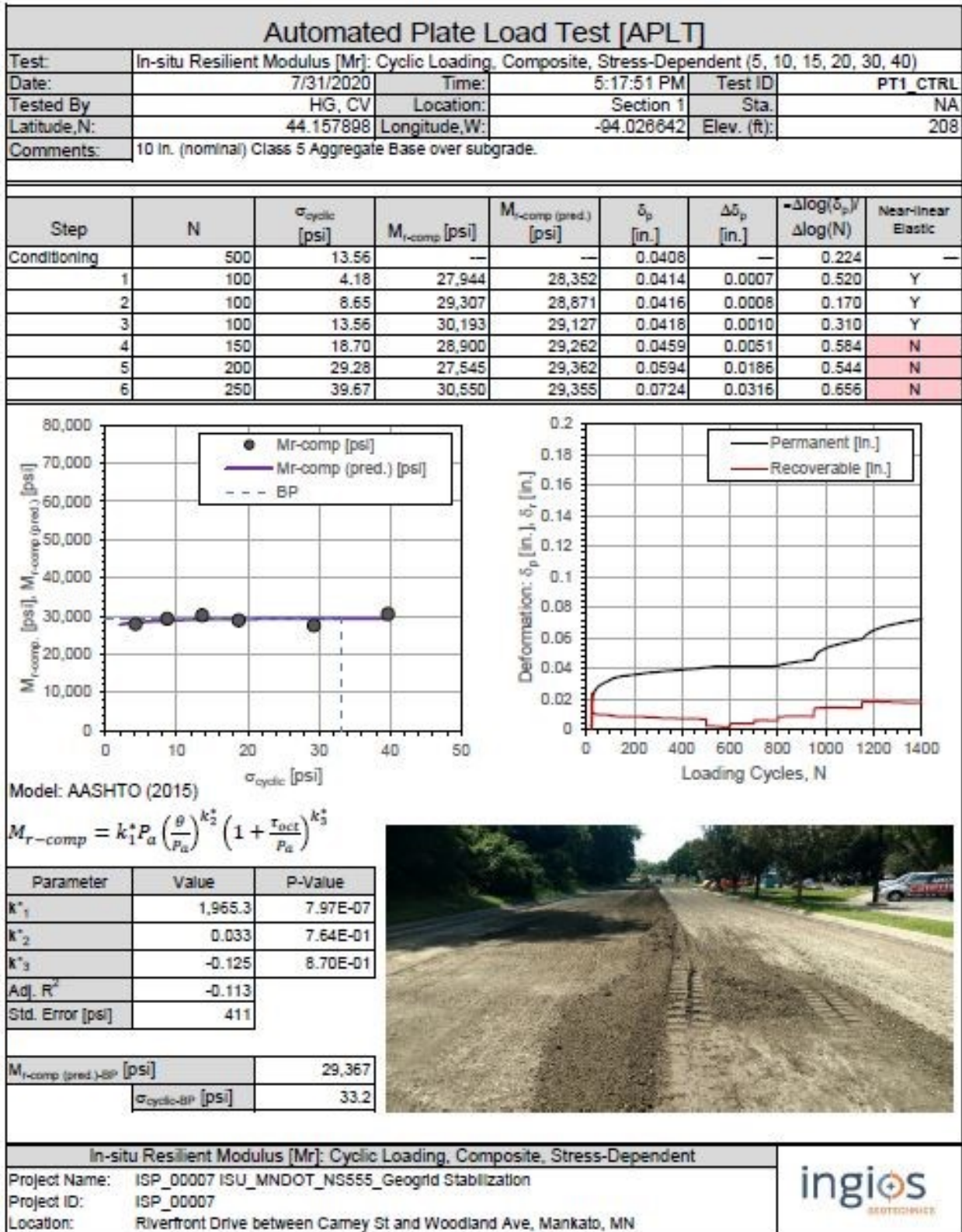


Figure 84. APLT results for Section 1, page 1 of 6

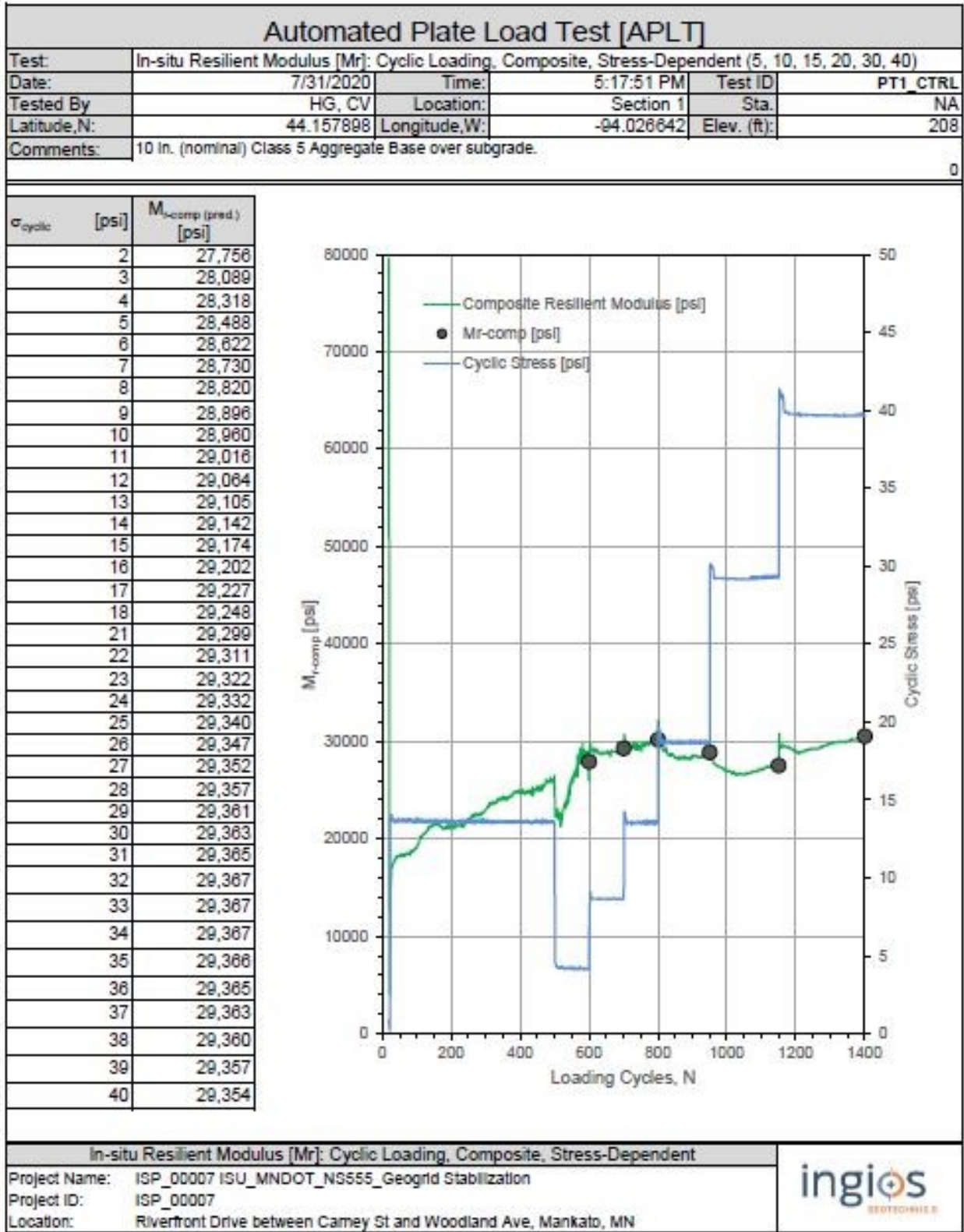


Figure 85. APLT results for Section 1, page 2 of 6

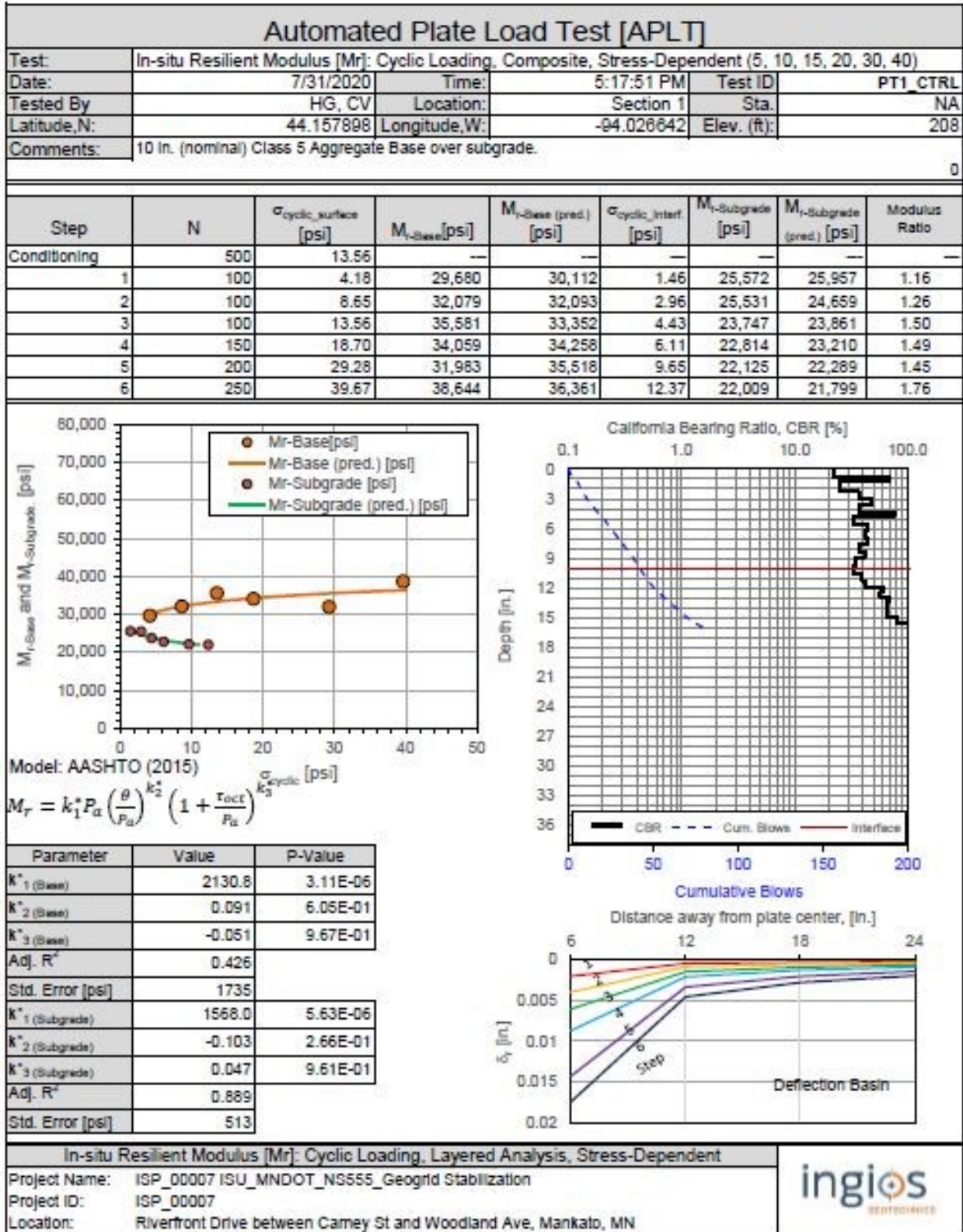


Figure 86. APLT results for Section 1, page 3 of 6

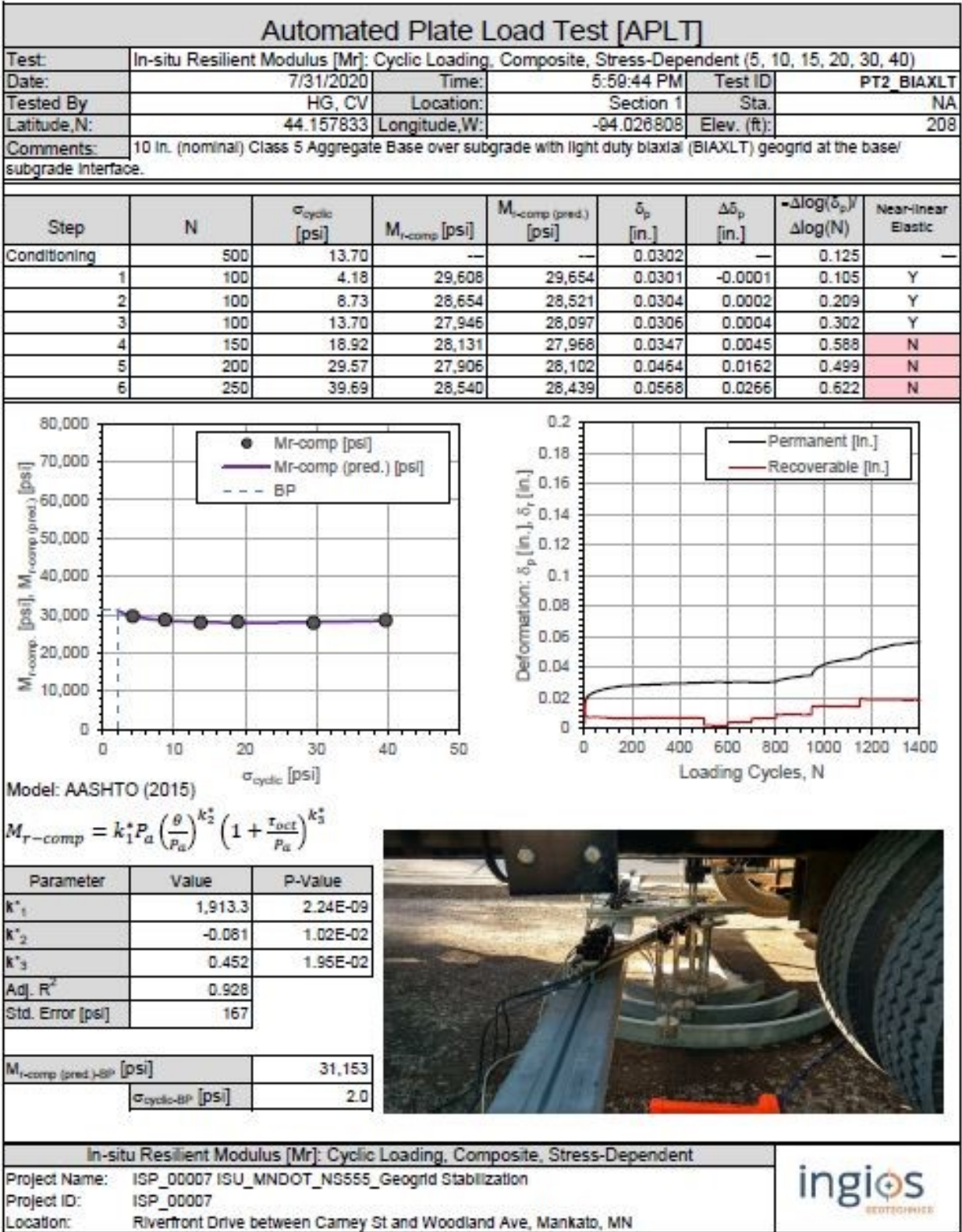


Figure 87. APLT results for Section 1, page 4 of 6

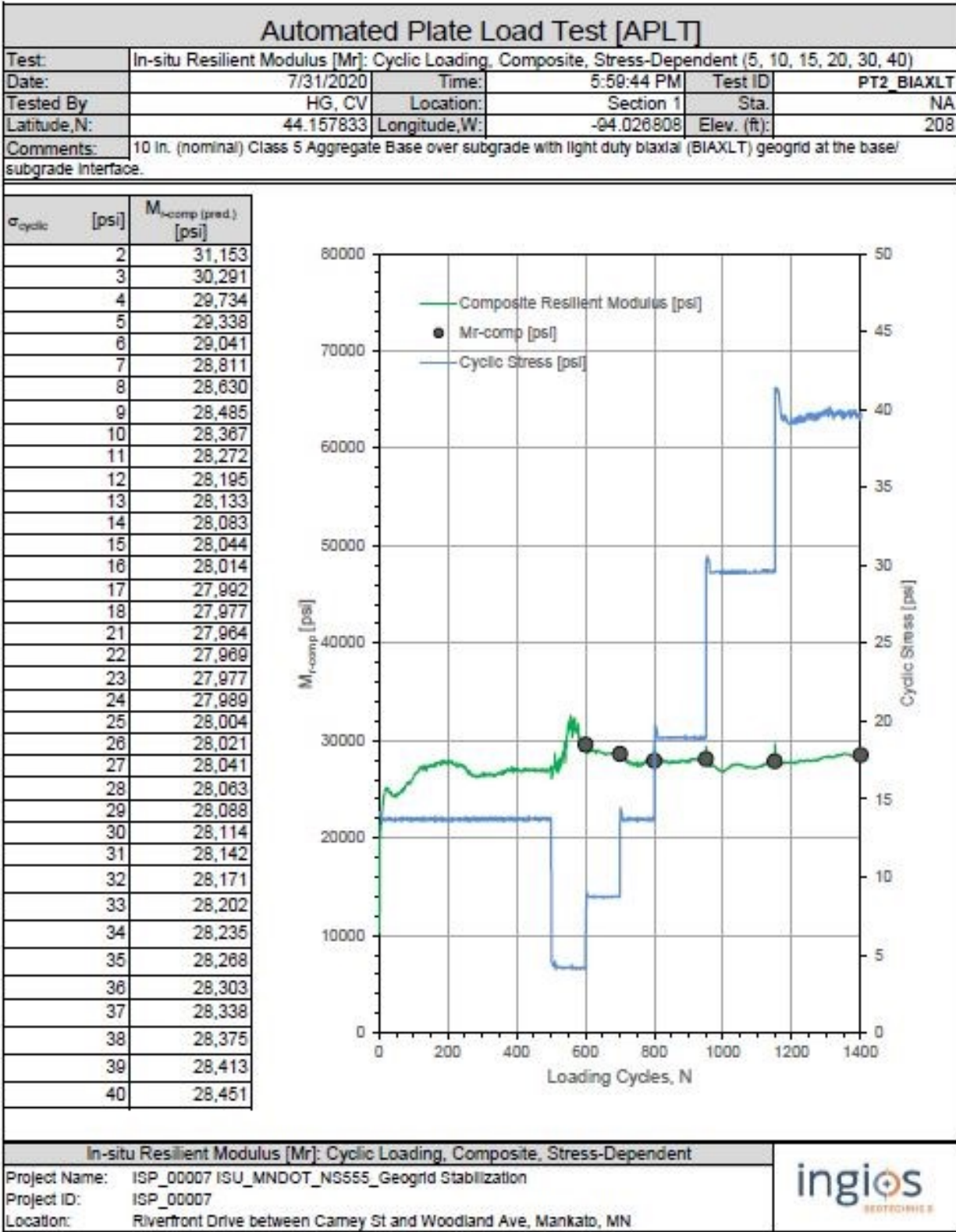


Figure 88. APLT results for Section 1, page 5 of 6

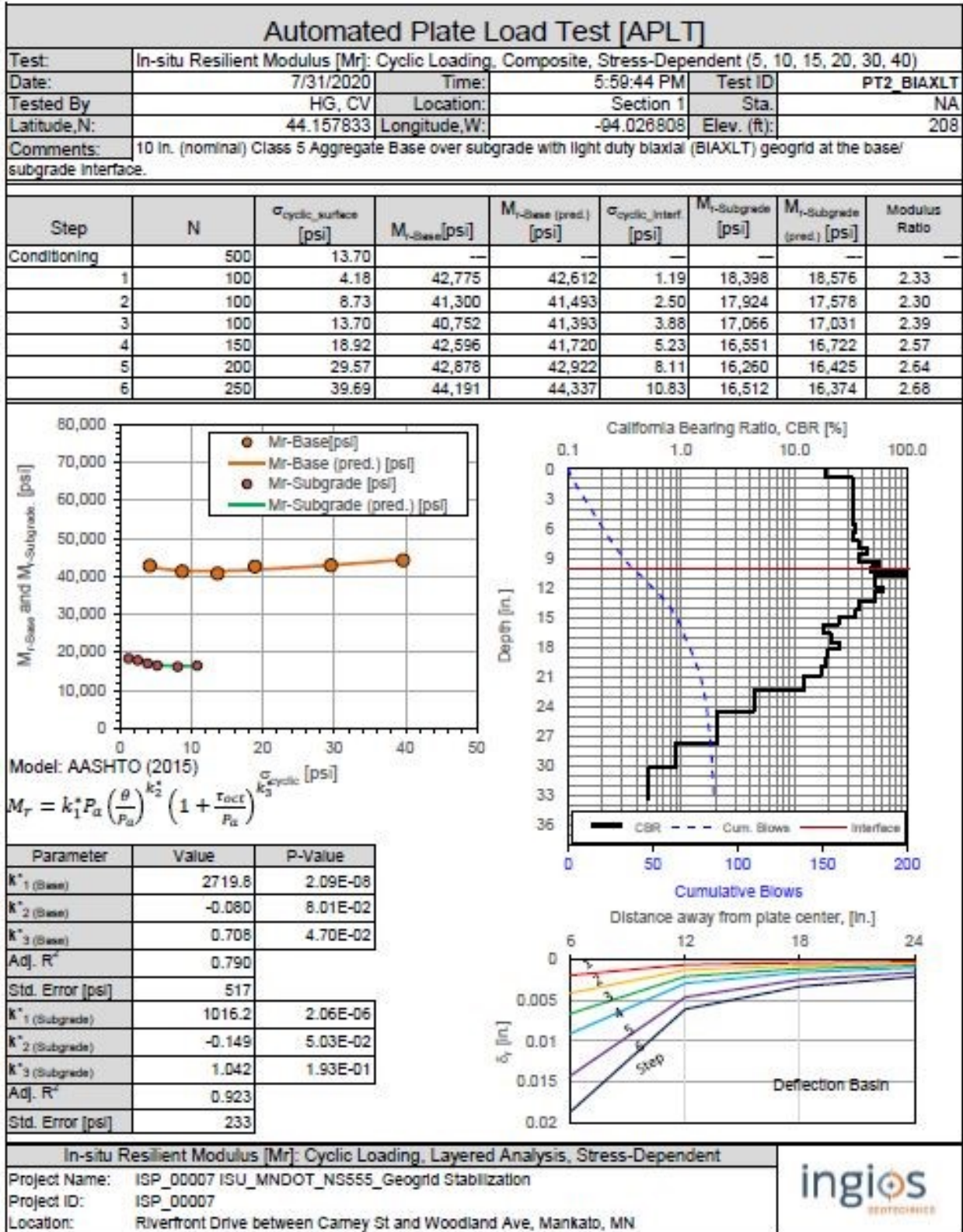


Figure 89. APLT results for Section 1, page 6 of 6

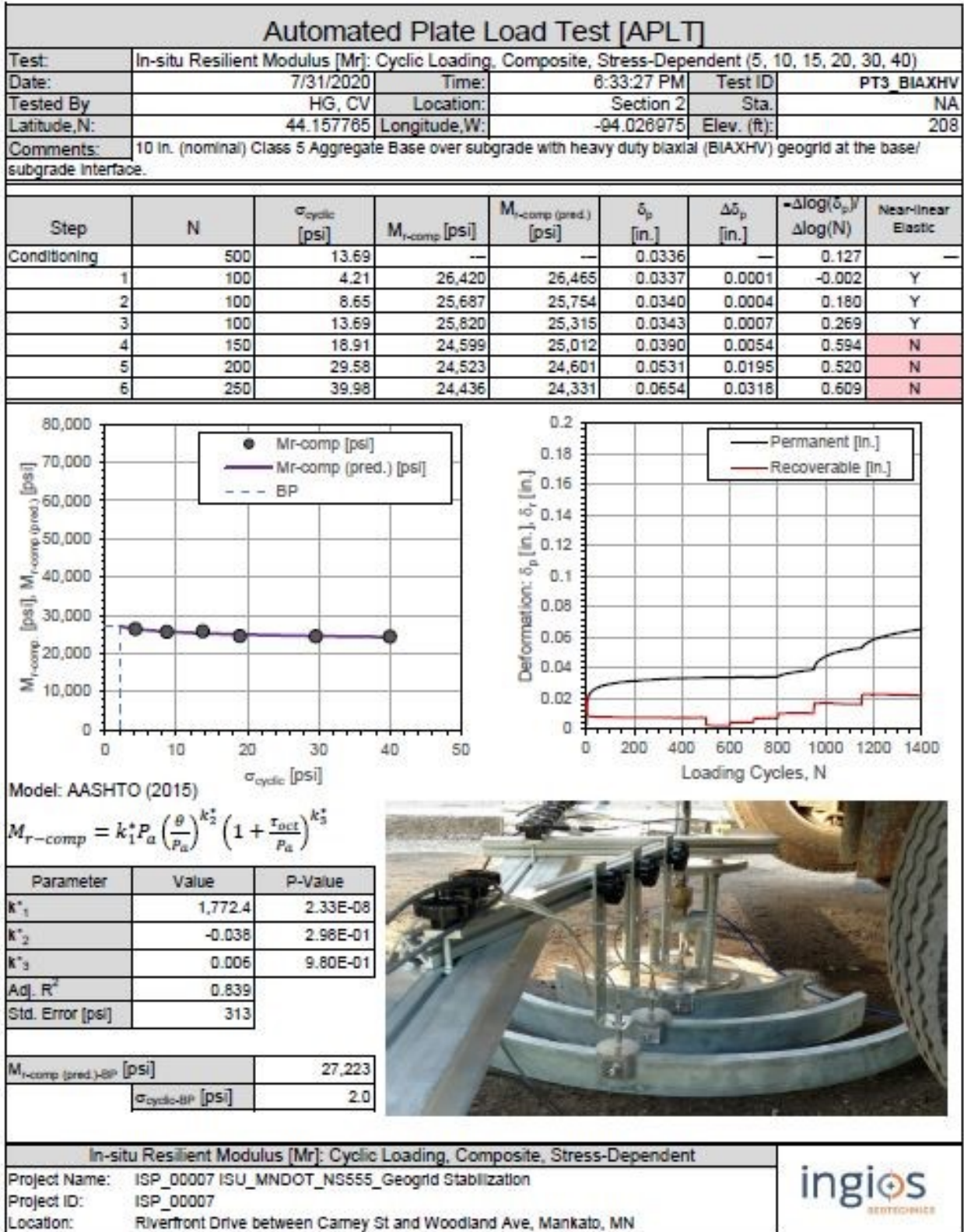


Figure 90. APLT results for Section 2, page 1 of 3

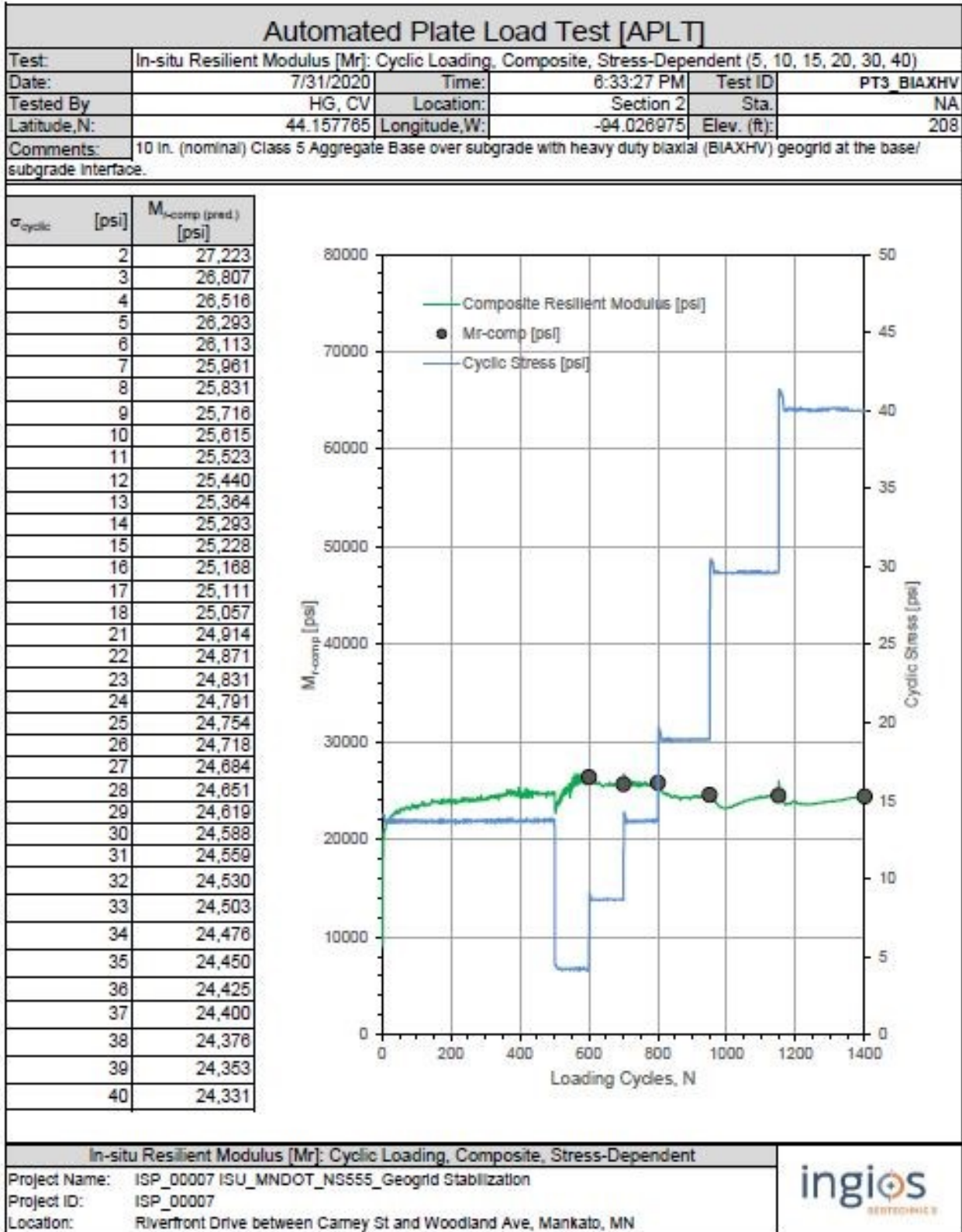


Figure 91. APLT results for Section 2, page 2 of 3

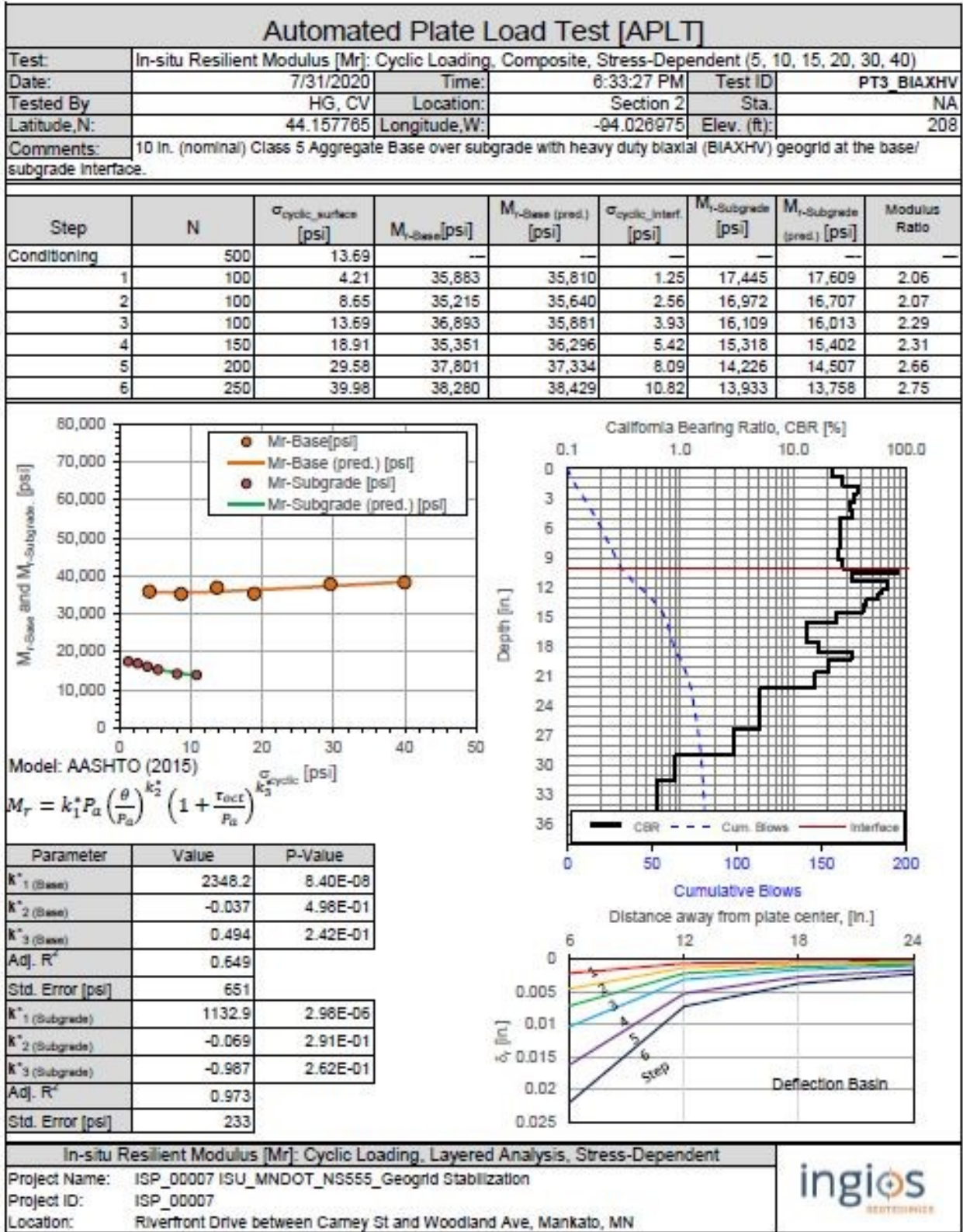


Figure 92. APLT results for Section 2, page 3 of 3

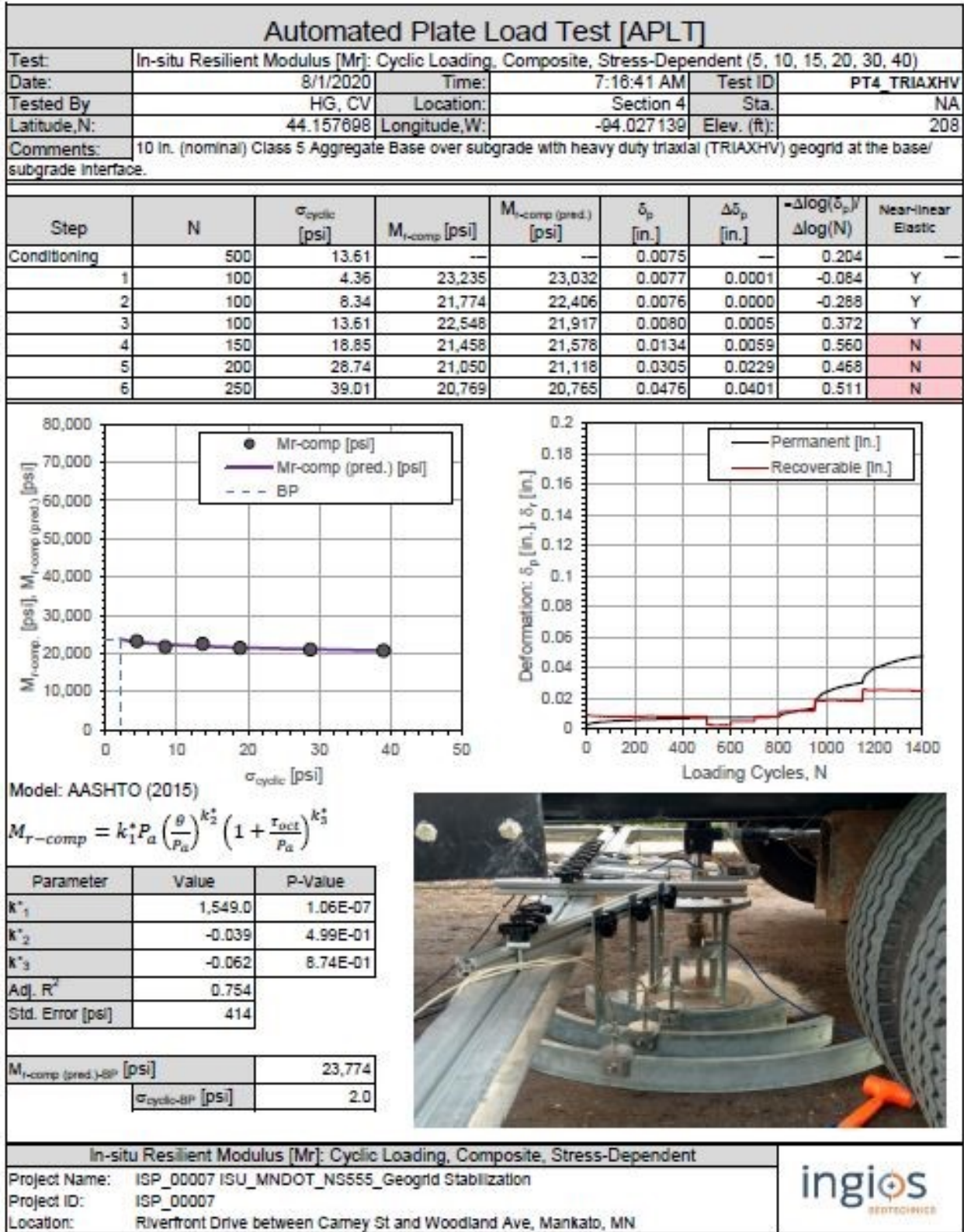


Figure 93. APLT results for Section 4, page 1 of 3

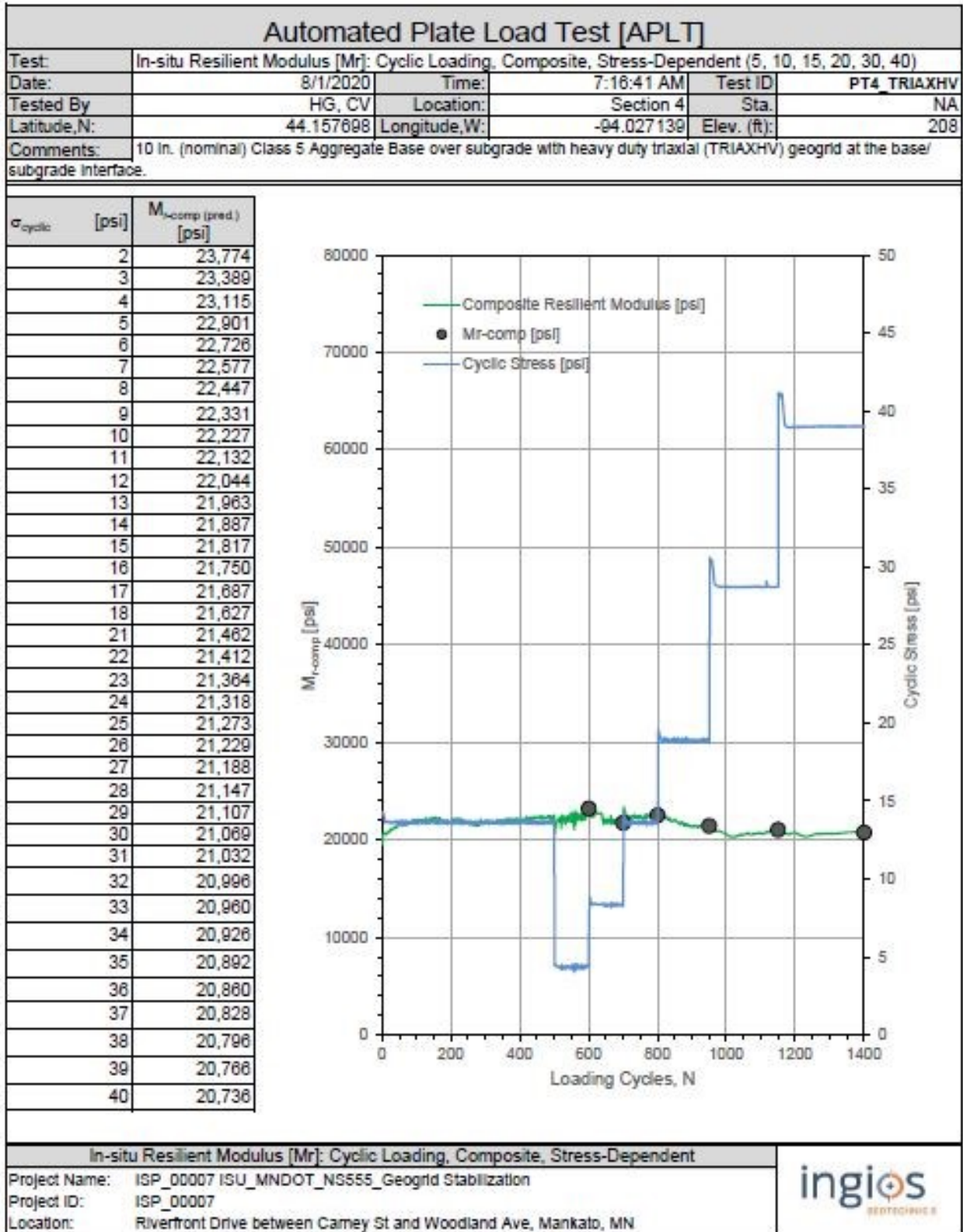


Figure 94. APLT results for Section 4, page 2 of 3

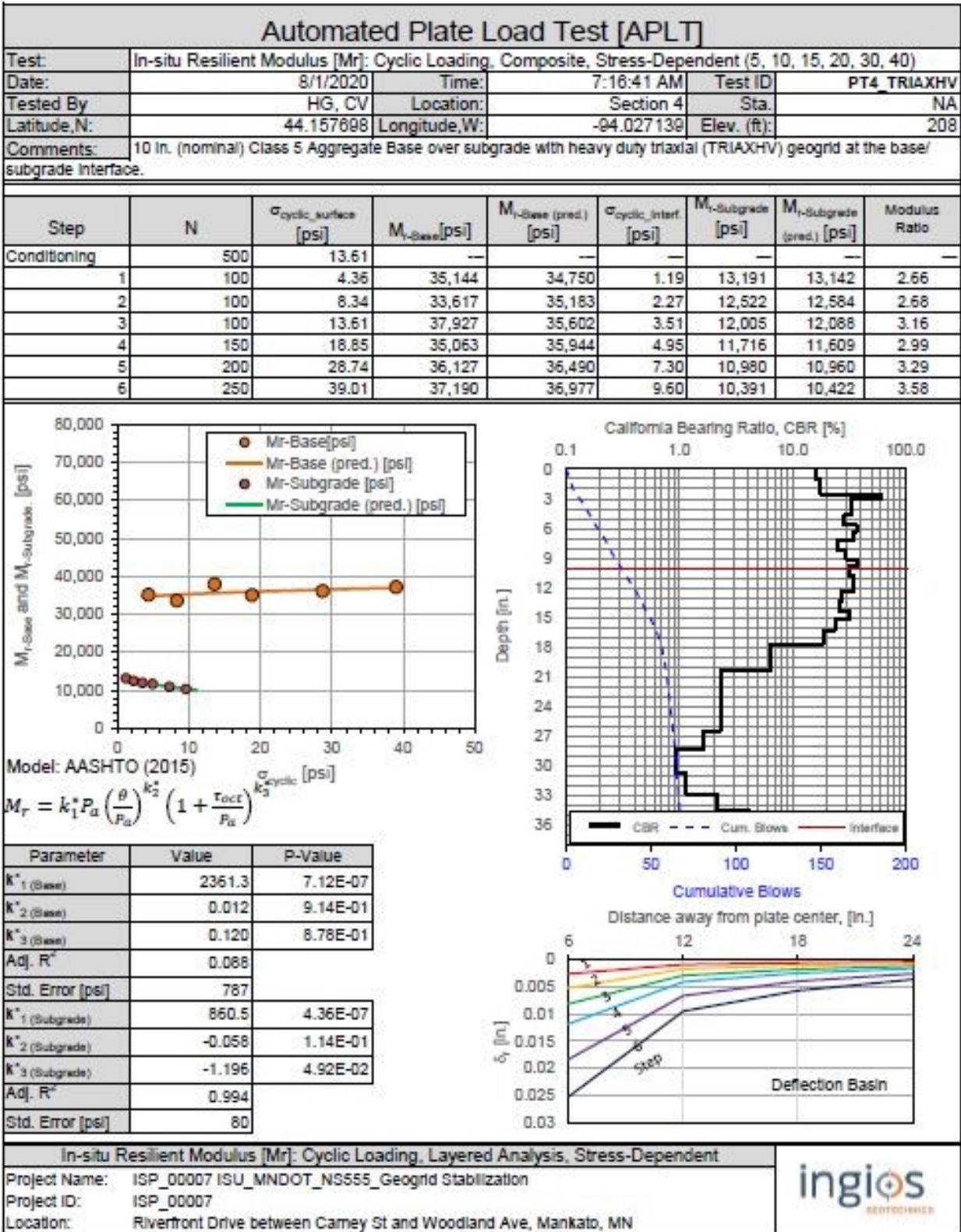


Figure 95. APLT results for Section 4, page 3 of 3

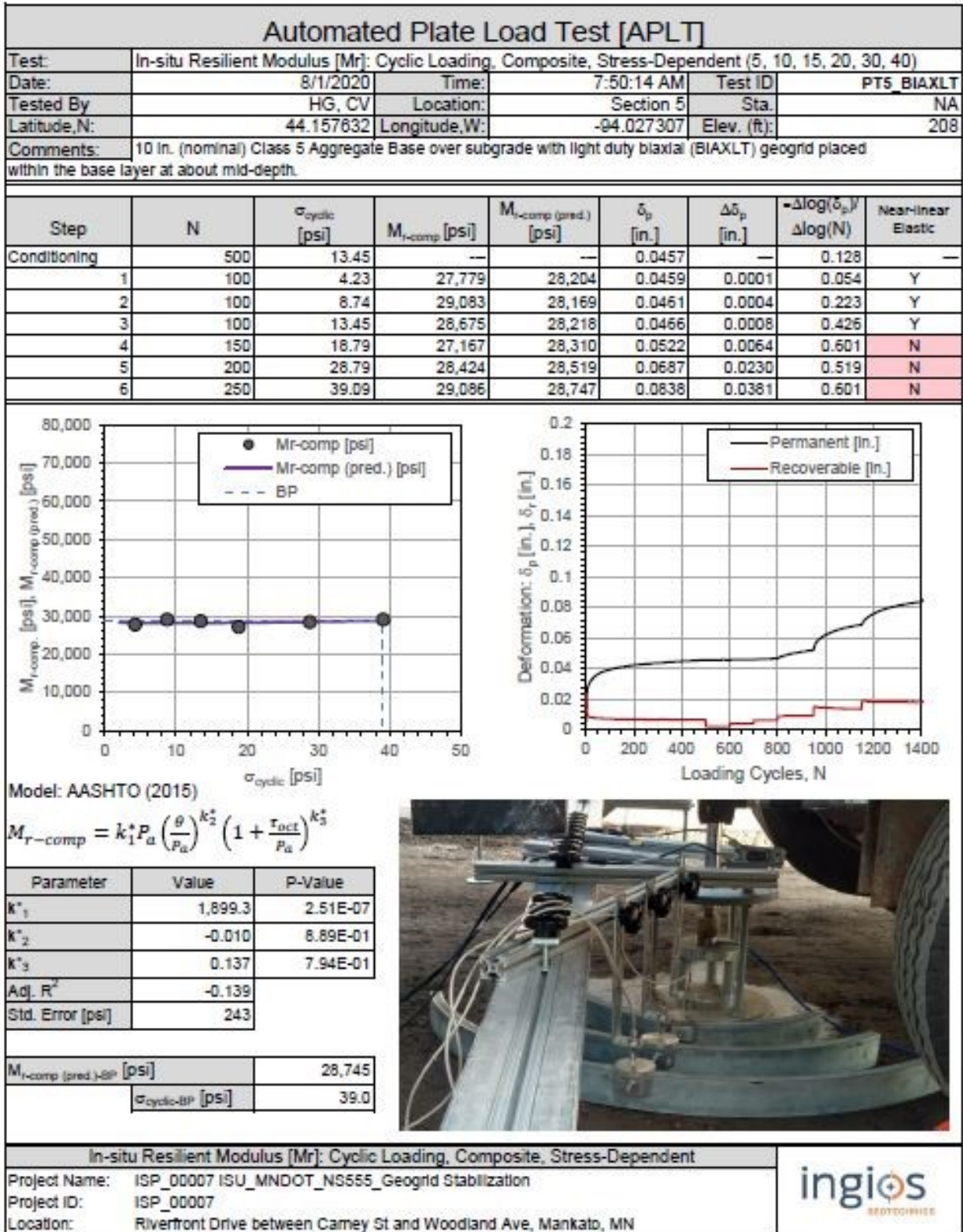


Figure 96. APLT results for Section 5, page 1 of 3

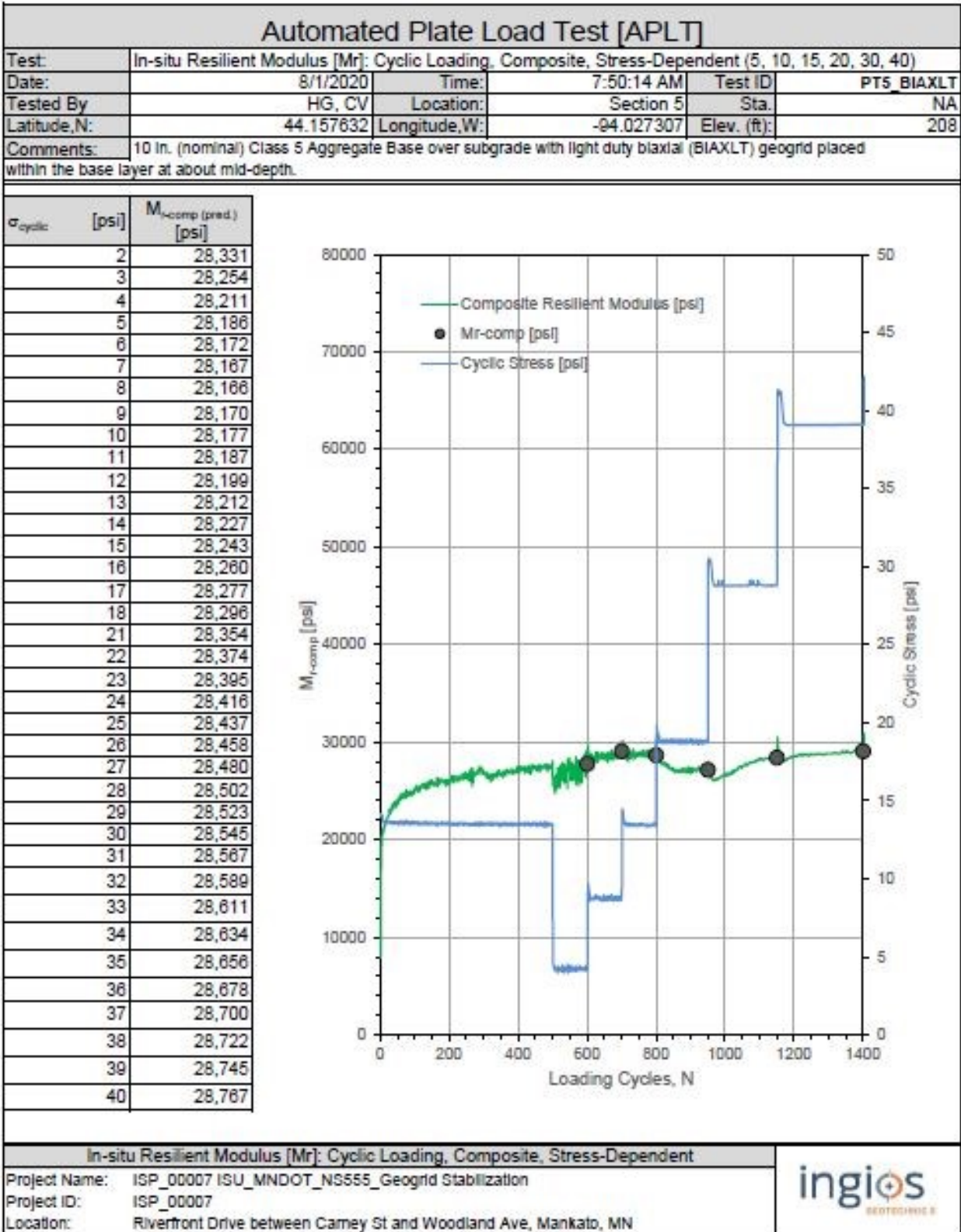


Figure 97. APLT results for Section 5, page 2 of 3

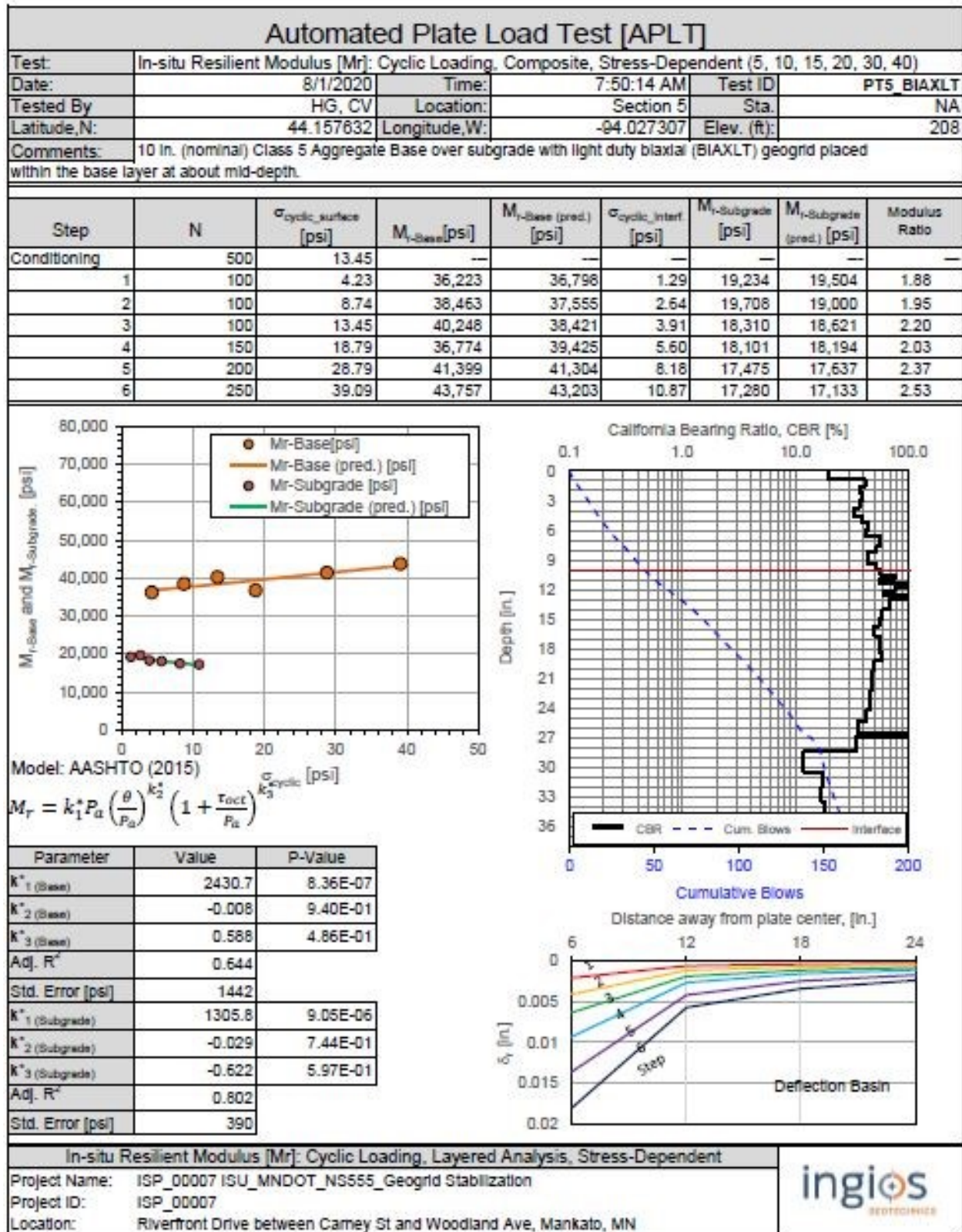


Figure 98. APLT results for Section 5, page 3 of 3

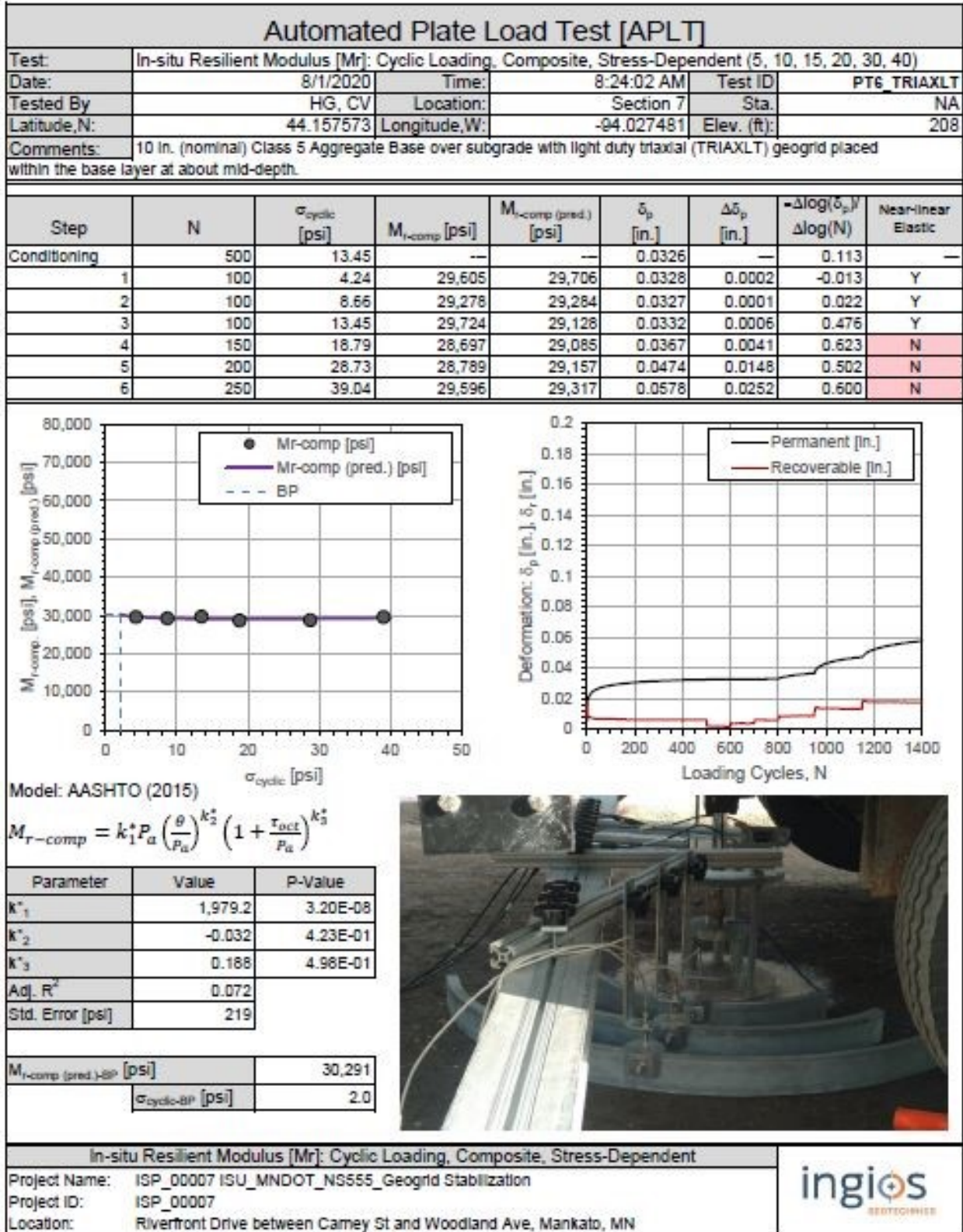


Figure 99. APLT results for Section 7, page 1 of 3

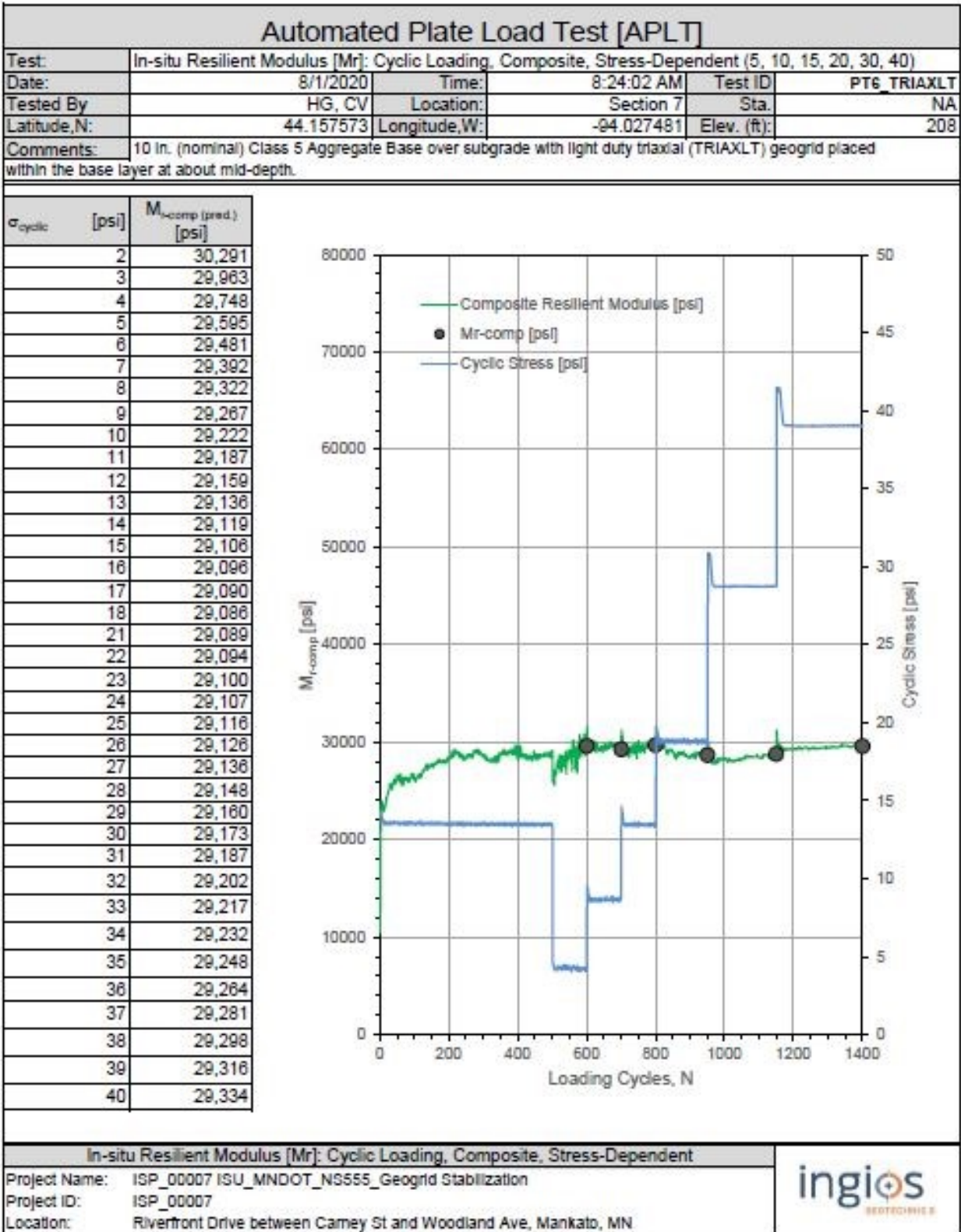


Figure 100. APLT results for Section 7, page 2 of 3

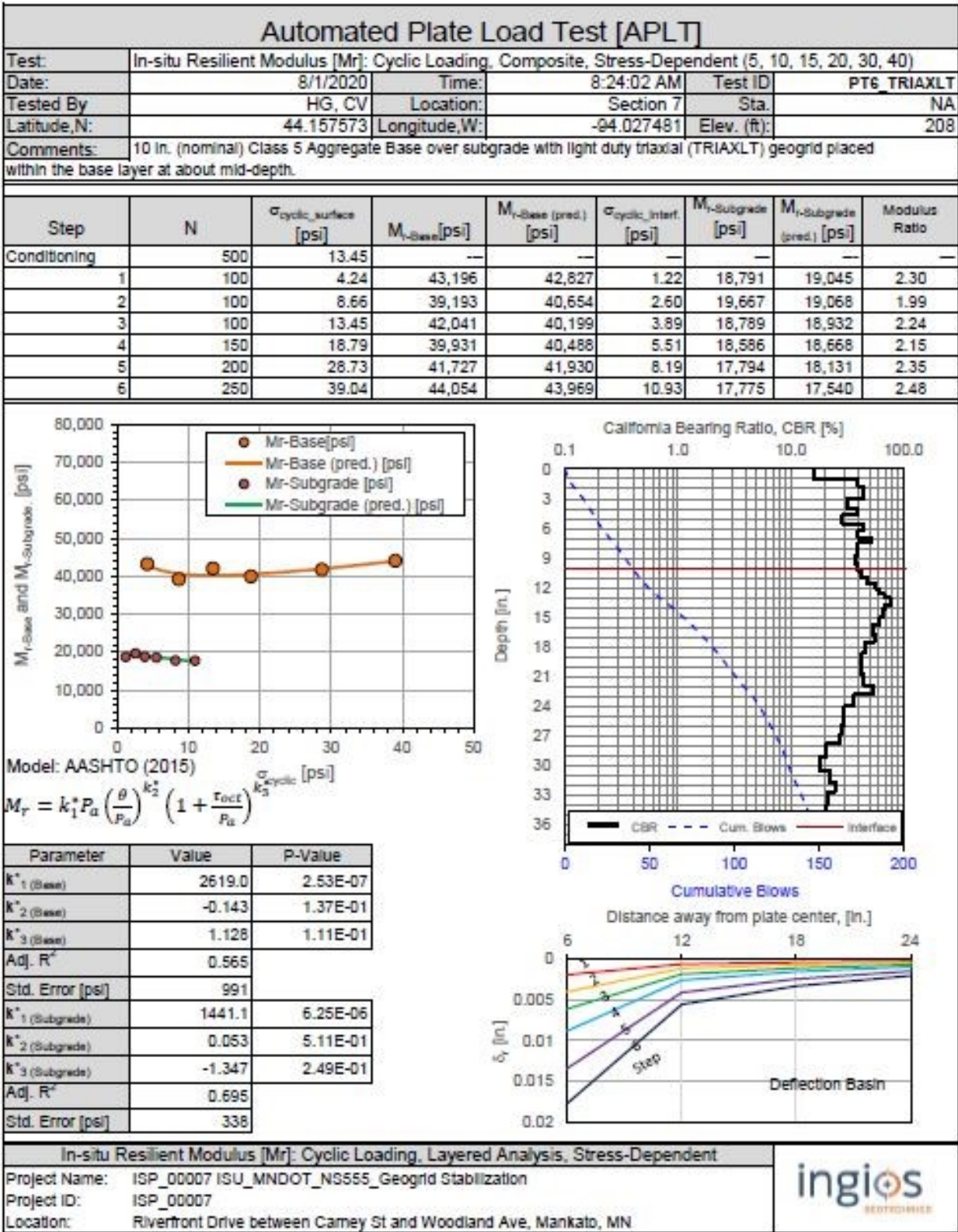


Figure 101. APLT results for Section 7, page 3 of 3

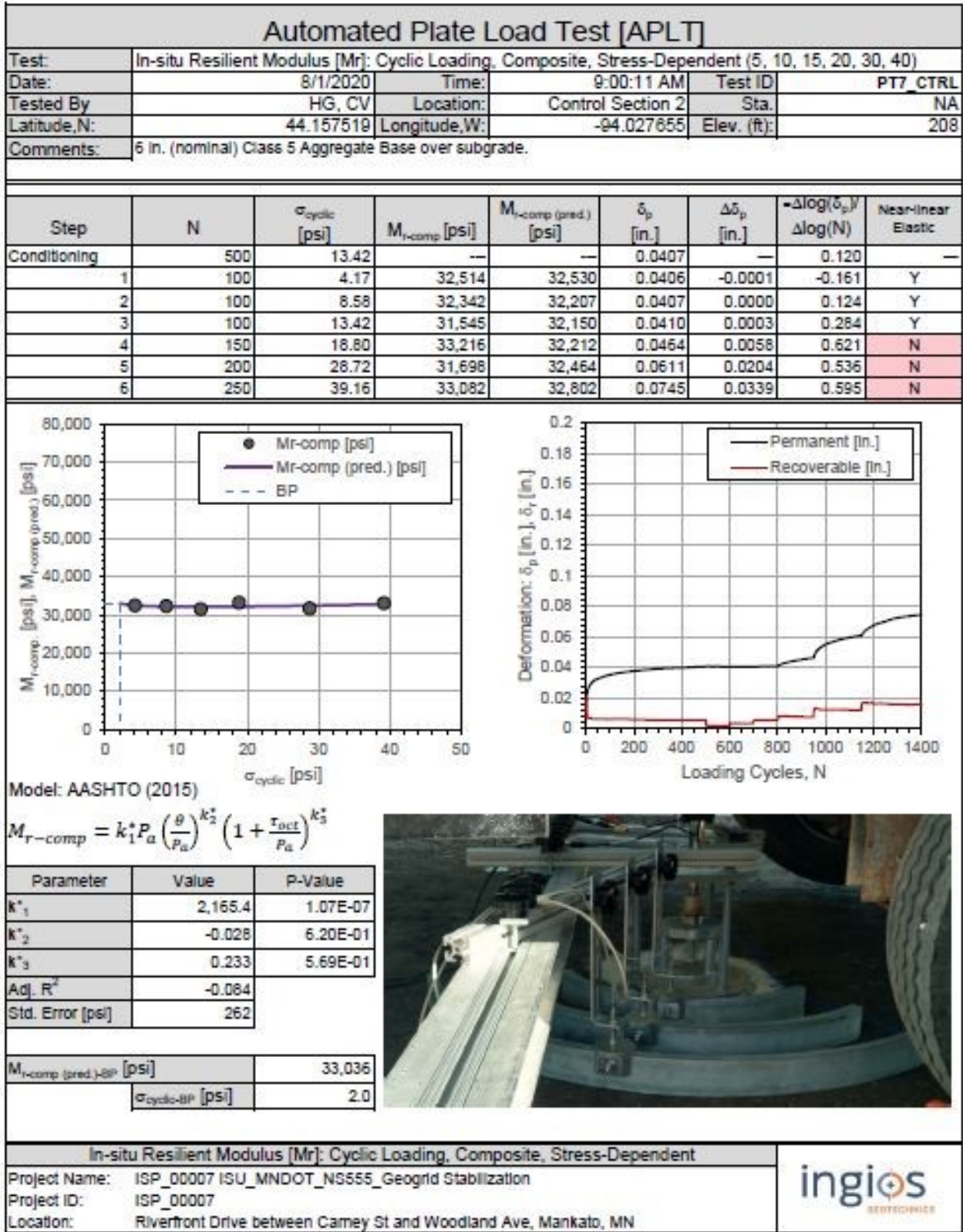


Figure 102. APLT results for Control section 2, page 1 of 3

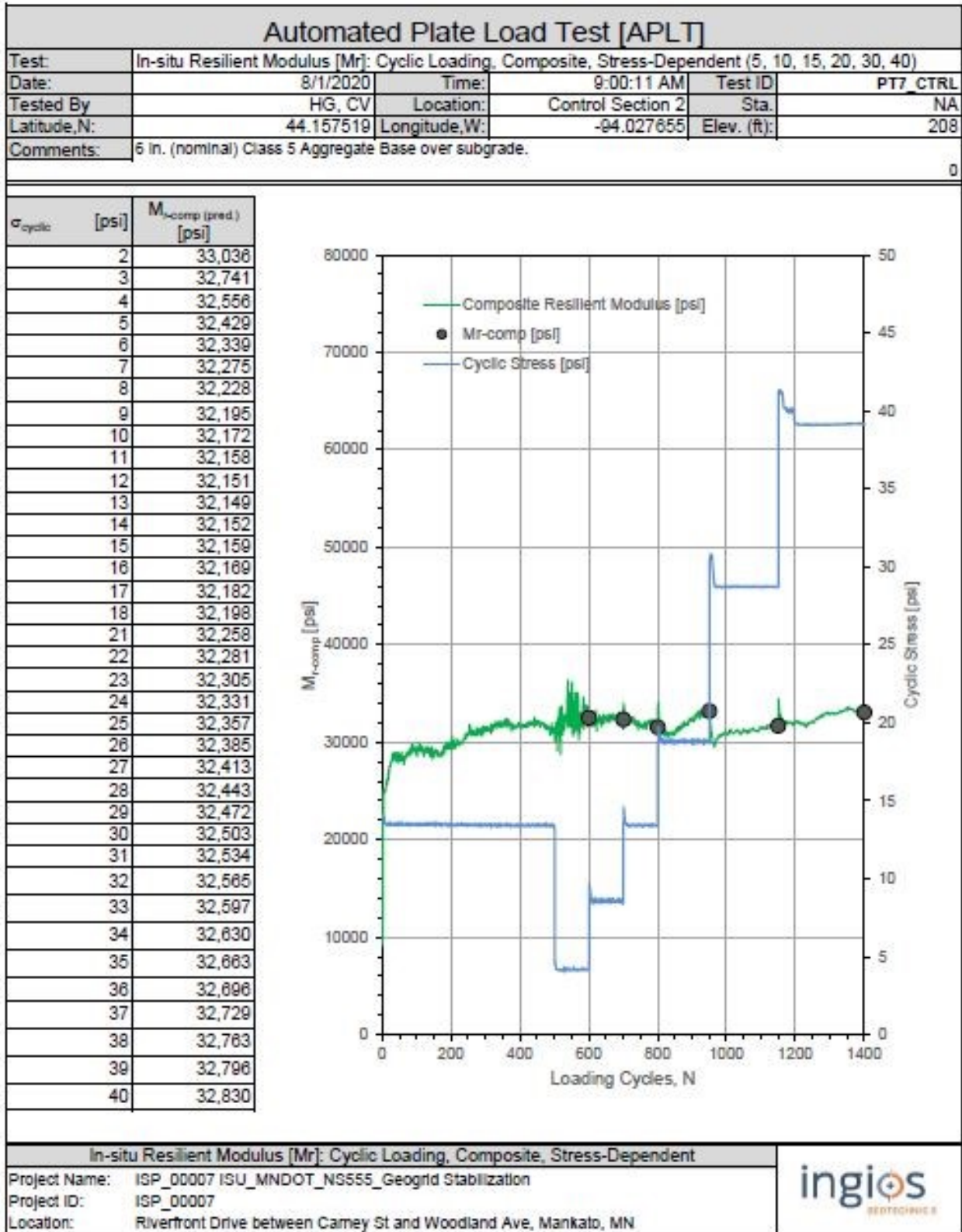


Figure 103. APLT results for Control section 2, page 2 of 3

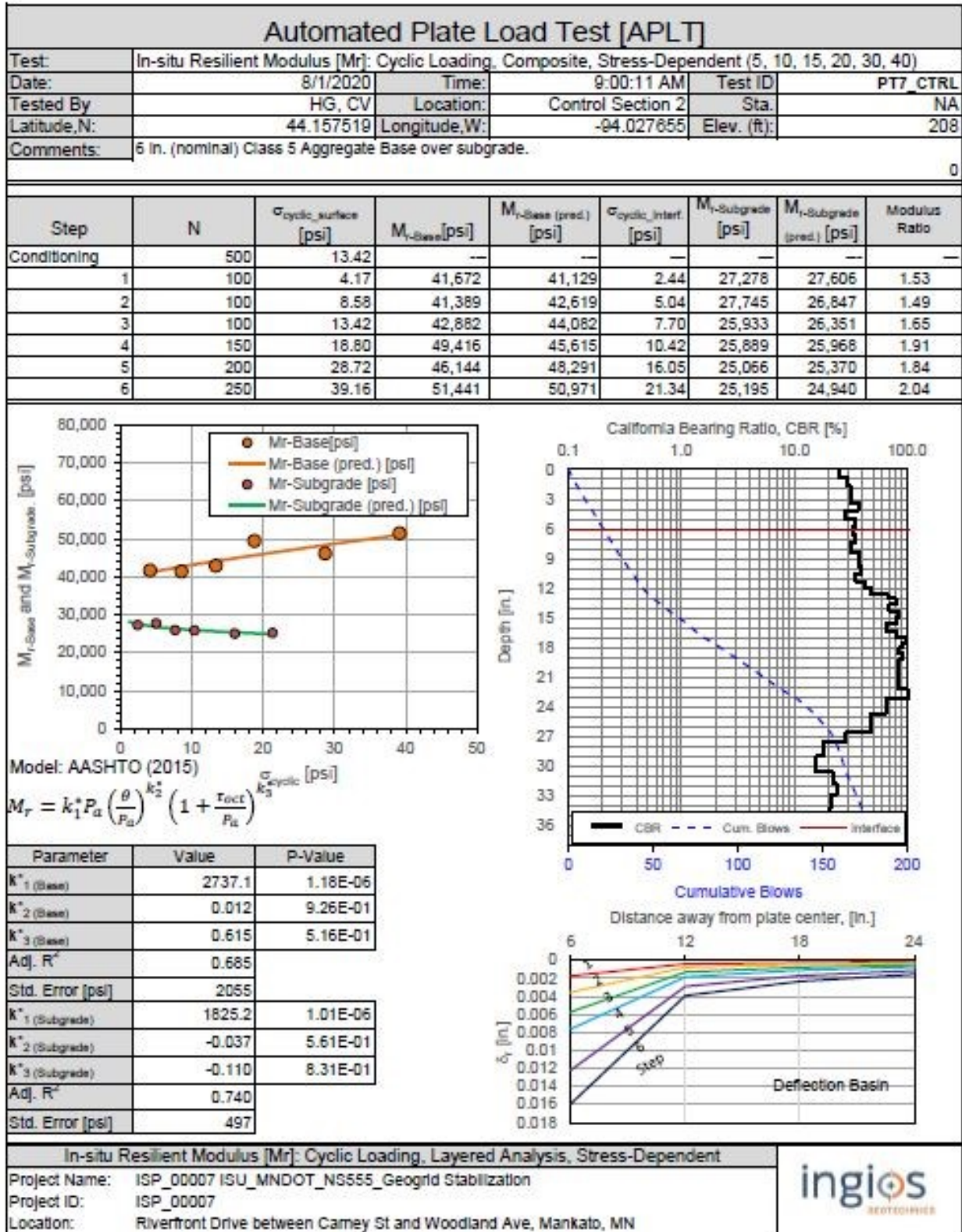


Figure 104. APLT results for Control section 2, page 3 of 3

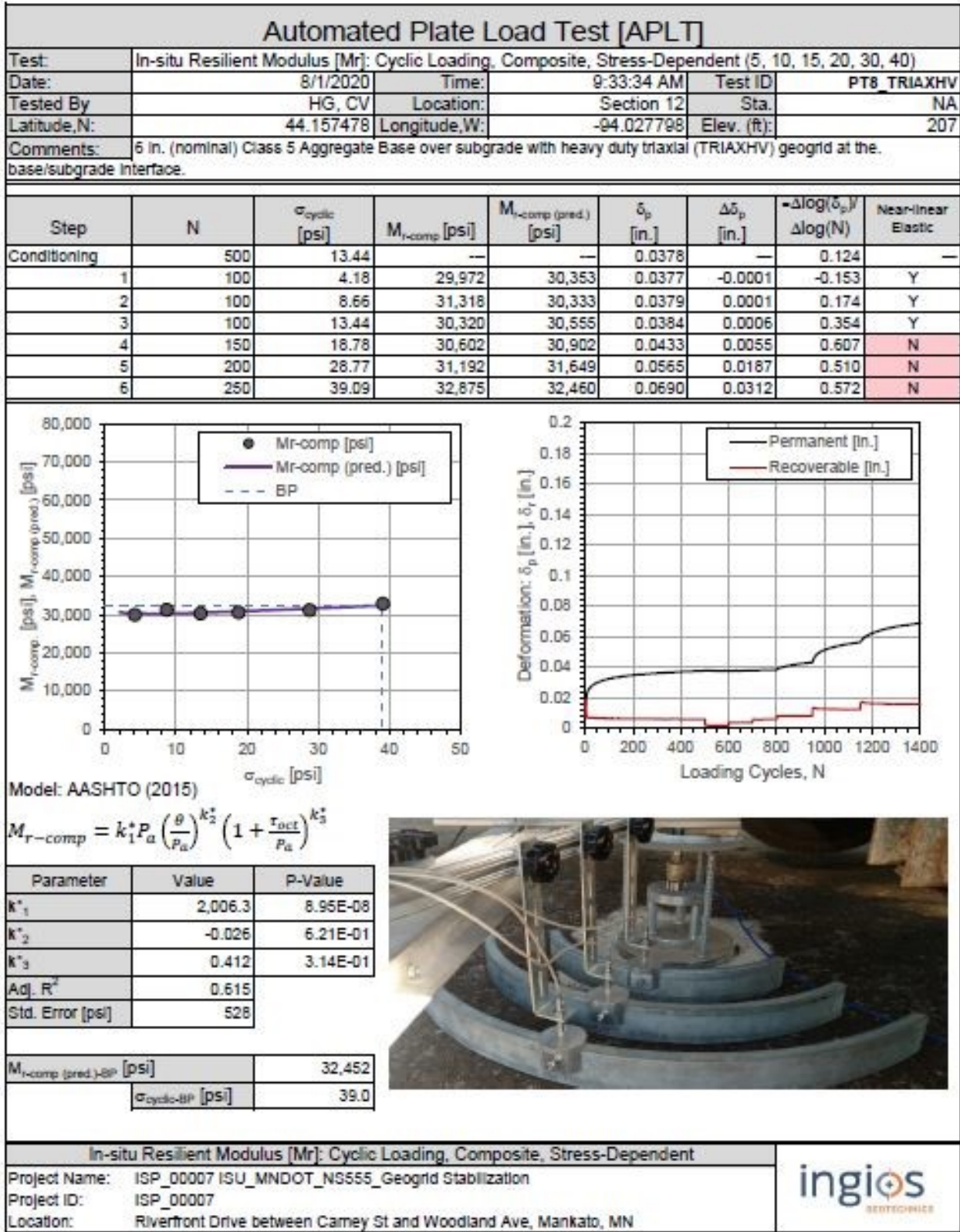


Figure 105. APLT results for Section 5, page 1 of 6

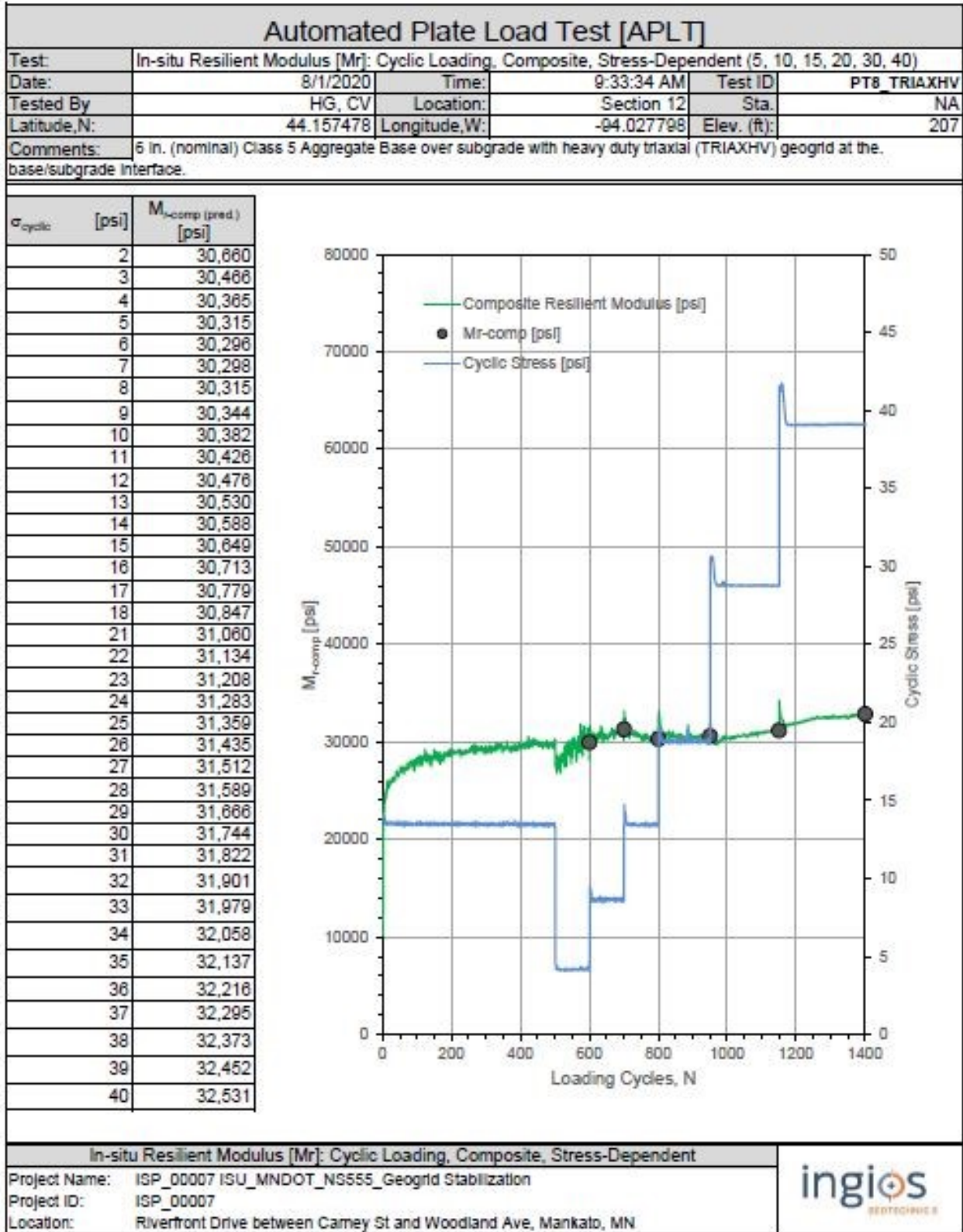


Figure 106. APLT results for Section 5, page 2 of 6

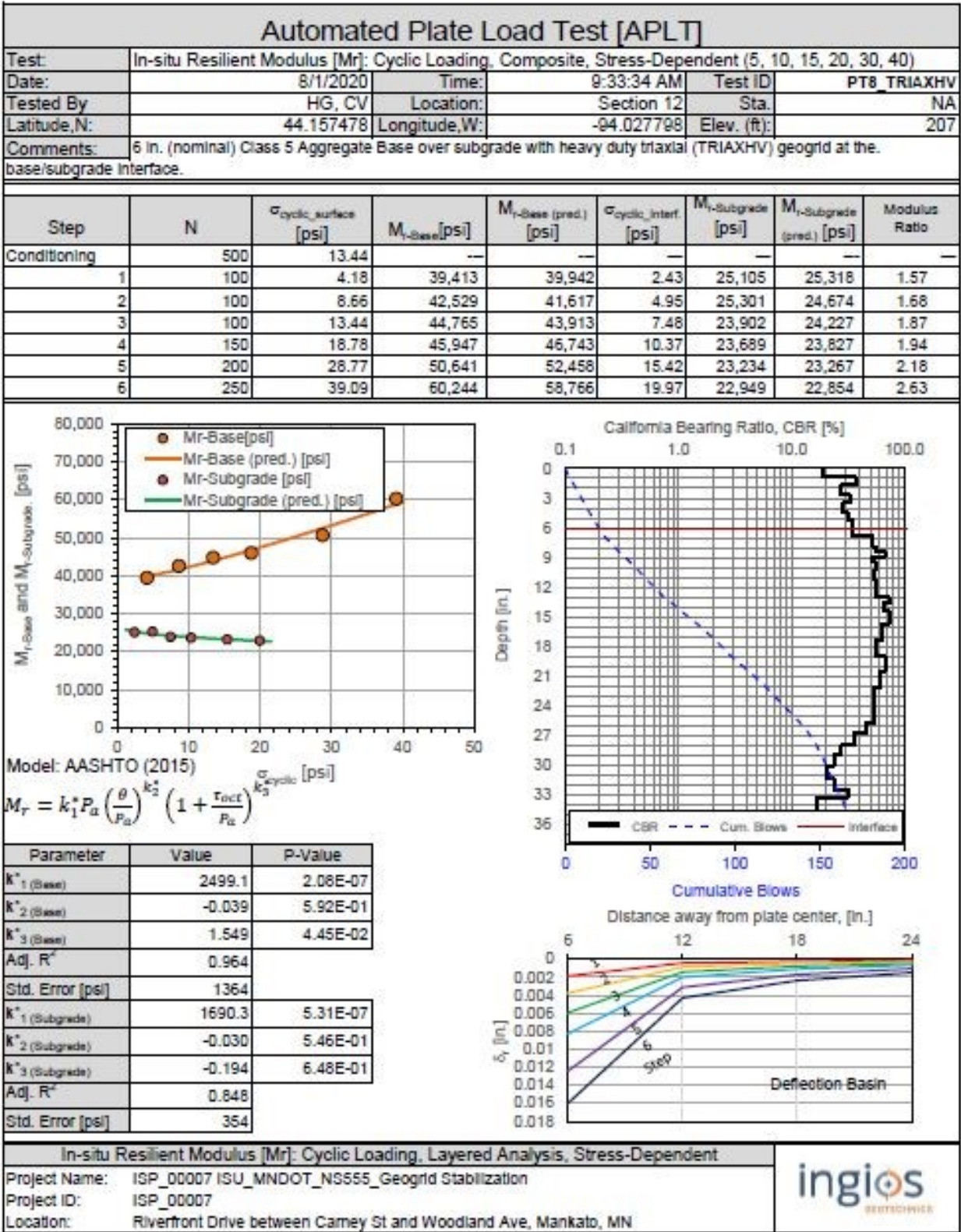


Figure 107. APLT results for Section 5, page 3 of 6

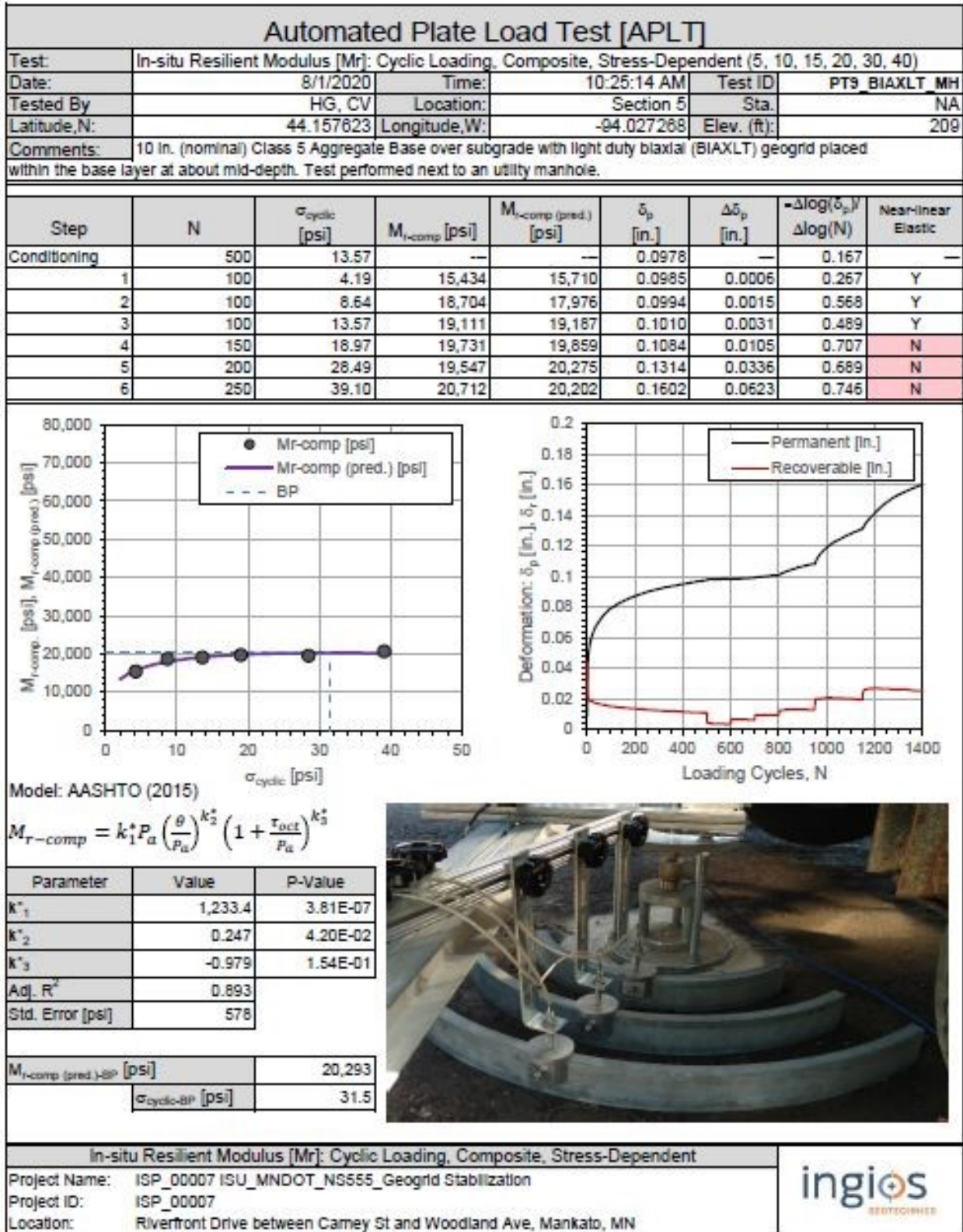


Figure 108. APLT results for Section 5, page 4 of 6

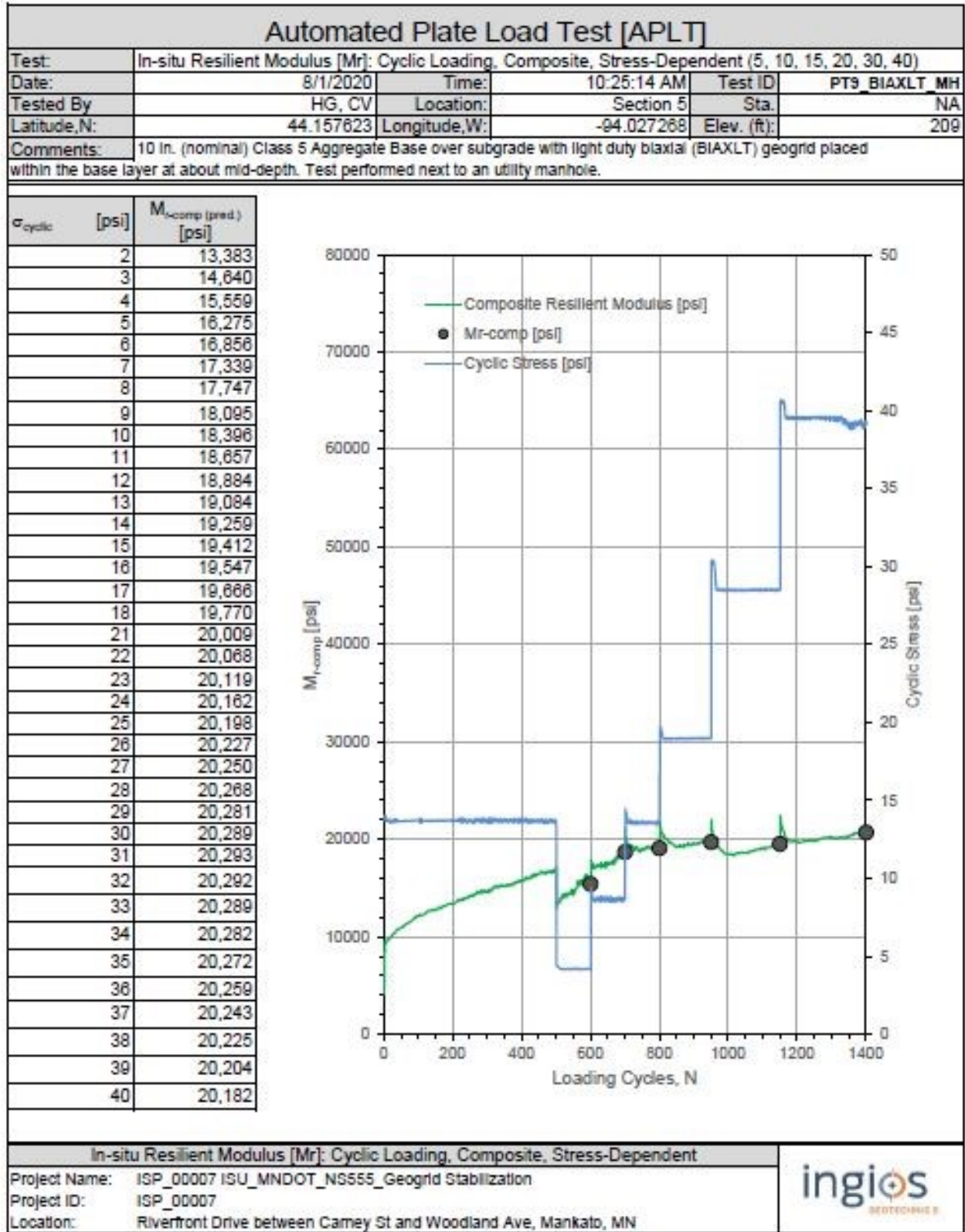


Figure 109. APLT results for Section 5, page 5 of 6

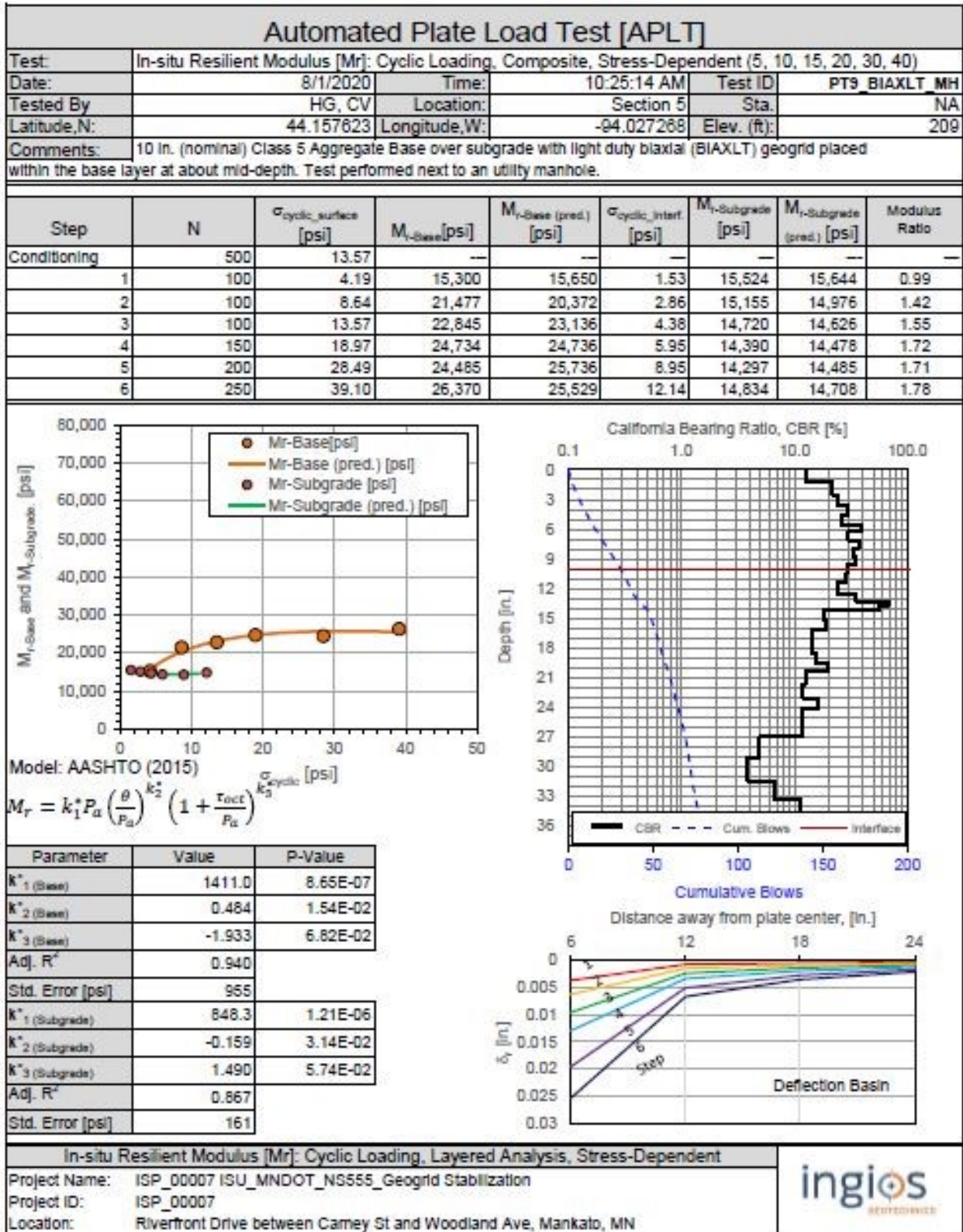


Figure 110. APLT results for Section 5, page 6 of 6

CHAPTER 4: GEOGRID DESIGN CRITERIA

4.1 REVIEW OF GEOSYNTHETIC FLEXIBLE PAVEMENT DESIGN METHODS

4.1.1 Introduction

In pavement applications, geosynthetics have been a satisfactory solution to reinforce the base layer. However, the lack of knowledge of design methodologies including geosynthetics have been considered an obstacle in pavement foundation design. The current design that each manufacturer defines provides the requirements for their materials per the specific conditions of each project.

The current procedures have not allowed the benefits of geosynthetic technology to be widely employed in pavement design, while the effective application of geosynthetics promotes their abilities and does provide preliminary designs for defining technical requirements according to each type of product. Because of this process, it is left to the methodologies of pavement and foundation design engineers to use geosynthetics as pavement reinforcement during construction.

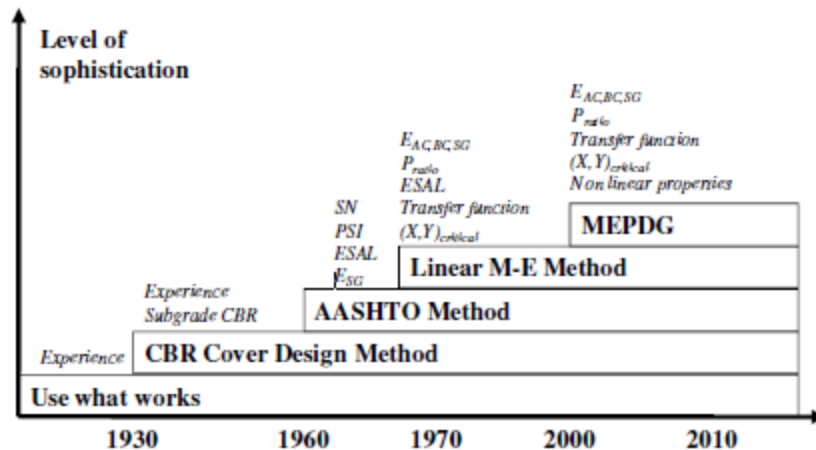
In this chapter, the available reinforced base layer design methods were investigated. The research team looked into the various methods for base course reduction and prolonging the service lives of pavement structures. This work focused on the description of each of the design processes, the AASHTO 1993 method, and methodologies using geogrid construction procedures that have been studied for years.

4.1.2 Historical Reinforced Pavement Design Methods

The design of geosynthetics in flexible pavement are discussed in many previous publications (Lukanen 1980, AASHTO 1993, Holtz et al. 1998, Berg et al. 2000, Perkins 2002, Leng and Gabr 2002, Abu-Farsakh et al. 2016). AASHTO has published several procedural publications on the use of geosynthetics for reinforcement of bases in flexible pavement structures. The first method is covered in AASHTO PP 46 (2001); the second method is covered in AASHTO R 50 (2009) from the Federal Highway Administration (FHWA) Geosynthetics Design and Construction Guidelines (Holtz et al. 1998); and the third method is covered in AASHTO R 50-09 (2014), which was an updated version for the most current method at the time.

All of the published procedures used the AASHTO 1993 methodology to incorporate the use of geosynthetics by including the structural contribution of placing reinforcement at the base-subgrade interface. Berg et al. (2000) and AASHTO (2001) proposed that additional support documents be developed by AASHTO.

Figure 111 depicts the historical pavement design methods.



Reck 2009

Figure 111. Historical pavement design methods

While Holtz et al. (1998) concentrated on placement procedures and damage during construction, this project report highlights the benefits of using geosynthetics in pavement structures and recommends some design criteria procedures for the reinforcing base layer (based on Hanandeh 2016). In this chapter, a brief description of the current methods of geosynthetic reinforcement design for flexible pavements is presented.

4.1.3 Geogrid Design Basics

The BCR is used to reduce the required thickness of the unreinforced base course directly. It is recommended that agencies with limited experience with geosynthetic reinforcement primarily use the reinforcement to improve the service life of pavement structures and limit reduction of the structural section until more experience is gained (Berg et al. 2000).

The design steps for use of geosynthetic base reinforcement for flexible pavements are outlined below. For details refer to Berg et al. (2000). Initial assessment of geosynthetic applicability requires evaluation of factors such as subgrade strength, aggregate thickness required for the unreinforced section, characteristics of base-subbase materials, seasonal variations in moisture levels, reinforcing mechanisms, and the value added by geosynthetic reinforcement. The design of unreinforced pavement section is based on evaluation of structural layers, type of material, and the thicknesses required for a pavement section without geosynthetics. Potential benefits of using geosynthetics reinforcement requires reviewing of available data to define potential and target benefits for the specific project. The conditions for which various geosynthetics products should be considered for this application are summarized in Table 10. Reinforcement benefits are defined using the TBR or BCR.

Table 10. Conditions for various geosynthetic products

Roadway Design Conditions		Geosynthetic Type					
Subgrade	Base/Subbase Thickness ¹ (mm)	Geotextile		Geogrid ²		GG-GT Composite	
		Nonwoven	Woven	Extruded	Knitted or Woven	Open-graded Base ³	Well Graded Base
Low (CBR < 3) (M _R < 30 MPa)	150 - 300	①	●	●	□	●	⑤
	> 300	①	①	◐	◐	◐	⑤
Firm to Very Stiff (3 ≤ CBR ≤ 8) (30 ≤ M _R ≤ 80)	150 - 300	⑥	◐	●	□	●	⑤
	> 300	⑥	⑥	◐ ⁷	□	□	⑤
Firmer (CBR > 8) (M _R > 80 MPa)	150 - 300	○	○	◐	□	□	⑤
	> 300	○	○	○	○	○	⑤

Source: Berg et al. 2000

When evaluating the influence and magnitude of the reinforcing effects, numerous variables appear to impact performance. The literature review shows the magnitude of pavement performance ranging from no improvement to a multiple order of magnitude increase in design life. A summary of the variables that lead to this performance range is presented in Table 11.

Table 11. Variables that influence the effect of reinforcement

Pavement Component	Variable	Range from Test Studies/Remarks	Condition where Reinforcement Appears to Provide Most Benefit	
Geosynthetic	Structure	Rigid (extruded) and flexible (knitted and woven) geogrids, woven and nonwoven geotextiles, geogrid-geotextile composites	See Table 4-1 and Table 4-2	
	Modulus (@2% and/or 5% strain)	100 kN/m to 750 kN/m	Higher modulus improves potential for performance	
	Location	Geogrid		Moderate load (≤ 80 kN axle load): Bottom of thin bases (≤ 250 mm), middle for thick (>300 mm) bases Heavy load (> 80 kN axle load): Bottom for thin bases (≤ 300 mm), middle for thick bases (> 350 mm)
		Geotextile		Bottom of base, on the subgrade
		Geogrid-geotextile composite		Bottom of open-graded base OGB
	Surface	Slick versus rough (firmer vs. soft)		Rough
	Geogrid Aperture	15 mm to 64 mm		> D ₅₀ of adjacent base/subbase ¹
Aperture Stiffness	Rigid to flexible		Rigid	
Subgrade Condition	Soil Type	SP, SM, CL, CH, ML, MH, Pt	No relation noted	
	Strength	CBR from 0.5 to 27: Low = CBR < 3, Firm to V. Stiff = 3 ≤ CBR ≤ 8, Firmer = CBR > 8	CBR < 8 (M _R < 80 MPa)	
Subbase	Thickness	0 to 300 mm	No subbase	
	Particle Angularity	Rounded to angular	Angular	

Pavement Component	Variable	Range from Test Studies/Remarks	Condition where Reinforcement Appears to Provide Most Benefit
Base	Thickness	40 mm to 640 mm	≤ 250 mm for moderate loads
	Gradation	Well graded to poorly graded	Well graded
	Angularity	Angular to subrounded	Angular
Pavement	Type	Asphalt, concrete, unpaved	Asphalt and unpaved
	Thickness	25 mm to 180 mm	75 mm

Source: Berg et al. 2000

The main goal for the pavement design is to protect the pavement layers over the subgrade to assure pavement performance life, considering the traffic loading and environmental conditions.

It is necessary to consider the sensitivity of soil moisture in both resistances as to possible changes in volume (swelling-shrinkage). Volume changes of an expansive subgrade soil type may cause serious damage to the structures that rely on it, for this reason when a pavement on this type of soil is constructed must be careful to prevent soil moisture variations and provide required the waterproofing of the structure. Another way to address the problem is by stabilizing the soil with some additive or lime.

Base layer aims, efforts to absorb loads transmitted by vehicles and evenly distribute these efforts to the subbase and through this the subgrade. Usually, basecoat crushed stone or crushed gravel or stabilized mixtures are used. The bases may be granular or be made of bituminous mixtures or mixtures stabilized with cement or another binder (Hanandeh 2016).

4.1.4 AASHTO and Manufacturer's Design Methodologies and Their Software Descriptions

The methodology presented is based on the version of the AASHTO 1993 flexible pavement design method. Which it has been modified to explain the structural contribution of the geosynthetics, according to the three different experimental program tests.

The modification of the AASHTO 1993 method by using two different of geosynthetics (geogrid and geotextile) was made based on field and laboratory tests. There are different design methodologies for flexible pavements including empirical methods. The empirical AASHTO method is a regression method based on empirical results obtained by the AASHO Road Test in the 50 states. The 1993 AASHTO methodology for flexible pavement is the methodology used as a starting point for the development of the including geogrids as reinforcement of base layer. This methodology has been modified to account for the contribution of using geosynthetics in the pavement. The results of three experimental tests were analyzed based on the two terms of extension the pavement life and reduction of base course thickness (Hanandeh 2016).

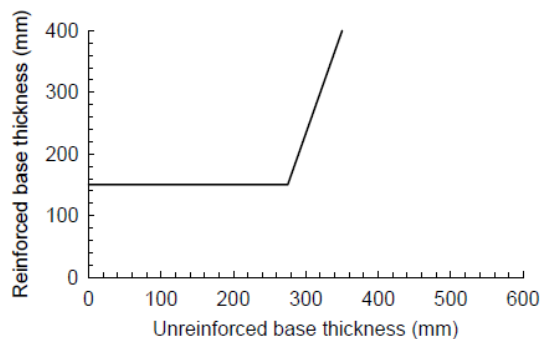
4.1.4.1 AASHTO Method for Flexible Pavement

The design method AASHTO, originally known as AASHO, was developed in the United States, based on a full-scale test conducted for two years from impairments who experience representing relations impairment - solicitation for all conditions tested.

From the 1986 version, the AASHTO method began introducing mechanistic concepts to adjust some parameters to different conditions which prevailed at the site of the original version.

The corresponding mathematical models also require a calibration to local conditions in the area where they are applied. The design equation model is based on the loss rate of serviceability (ΔPSI) during the service life of the pavement.

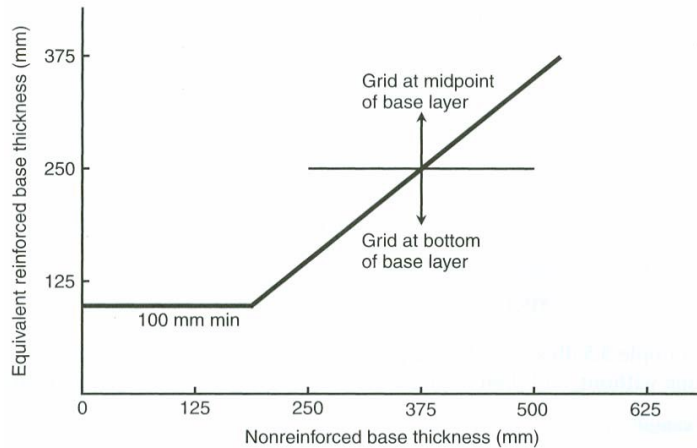
Cancelli and Montanelli (1999) performed their geosynthetics design model based AASHTO 1993 method by finding the layer coefficient ratio for the granular base layer. From the experiment results, the coefficient ratio was between 1.5 to 2 by use one layer of geogrid and different strength of soil subgrades. The values greater than 1.5 were calculated for subgrade CBR strengths less than three. The layer coefficient ratio value was used as a multiplication factor for the depth of the reinforced base in the equation used to calculate the structural number. This implies that for an equivalent structural number, the unreinforced base could be reduced by 33% to 50%. (Webster 1993) produced a design chart like that of Haas et al. (1988) by directly comparing and extrapolating test results for sections of equivalent base course thickness. The original design chart included the 50 mm thick asphalt concrete (AC) layer used in the experiments. The authors of this study for MnDOT modified the original chart by excluding the 50 mm thick AC layer, which resulted in the chart shown in Figure 112.



Adapted from Webster 1993

Figure 112. Flexible pavement design chart proposed

Penner (1985) created a new design chart for the base layer with geogrid reinforcement. He calculated the SN based on the AASHTO 1993 method and concluded that use of geogrid within the base layer can modify the AASHTO 1993 method. The chart he developed enables the conversion of a non-reinforced base course thickness into an equivalent thickness of a geogrid-reinforced layer, as seen in Figure 113.

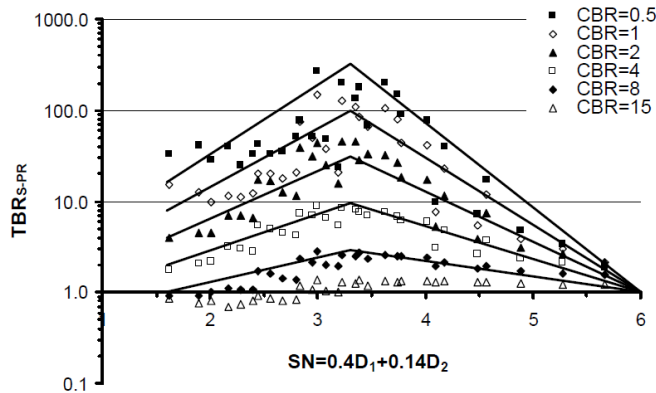


Penner 1985

Figure 113. Geogrid-reinforced base course for paved highway section using geogrids

Perkins (2002) employed the new pavement design method, mechanistic-empirical design (ARA 2004) for recommended a new design to incorporate the geosynthetics in the base course layer reinforcement. Also, they provide the advantage of incorporation the geosynthetic materials in base layer by specified three benefits. The first benefit increased the pavement life and the second benefit decreased the base course layers thickness, and the third benefit was installed geosynthetics in base course layer can in reduce the vertical stress and improve the stress distribution over weak subgrade soil.

They worked with the mechanistic approach to determining critical stresses at different pavement locations for the reinforced pavement section. Next then from damage model they obtained distress (rutting) for a different layer. Three finite element models were generated to mimic the following cases geosynthetics-reinforced pavement, pavement without geosynthetic reinforcement and pavement section with perfectly-reinforced pavement. The proposed finite model models were calibrated based on the results of cyclic plate loading test in the laboratory. The proposed finite element was employed to develop a design methodology based on the analysis of 465 pavement design problems. Applying the 1993 AASHTO pavement design method, the number of ESALs the pavement can support is calculated based on the AASHTO regression model (Hanandeh 2007). The TBR for the perfect-reinforced (PR) case is then estimated based on the Figure 114.



Perkins 2002

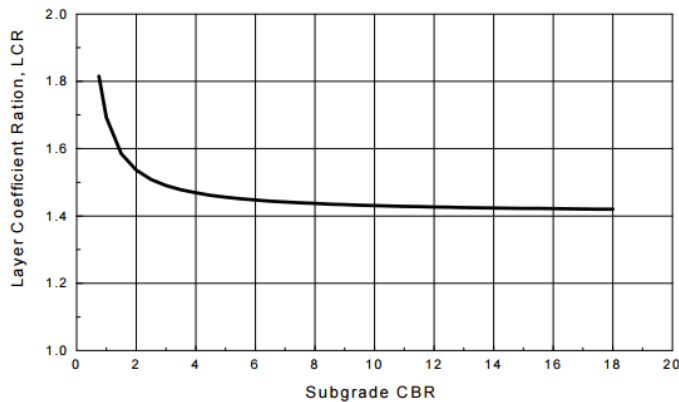
Figure 114. TRB versus SN for perfect reinforcement model

4.1.4.2 Tenax AASHTO Method Modified

The first step in this method is to calculate the structural number according to AASHTO methodology for the whole pavement layers. The structural contribution in equation (1) of using geosynthetics in a flexible pavement system can be quantified with increase the benefit of base course layer coefficient. Therefore, the AASHTO traditional equation to determine the SN is modified with a coefficient of enhancement layer (called LCR or the layer coefficient ratio).

$$SN = a_1 D_1 + a_2 (LCR) D_2 m_2 + a_3 D_3 m_3 \quad (1)$$

The LCR has a value greater than one. This value is determined based on the results of laboratory and field tests in flexible pavement with and without use of geogrids. By use Tenax chart the layer coefficient ratio can be determined as a function of CBR for subgrade soil in the Figure 115 and clearly shown that the higher value of CBR, the lower value of LCR.



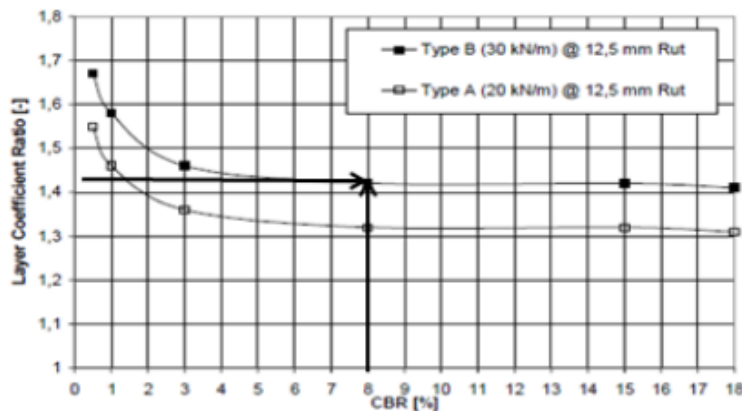
Cancelli and Montanneli 1999

Figure 115. Layer coefficient ratio vs. subgrade CBR

This chart was prepared from experimental cyclic loading test sections for a multilayer polypropylene extruded biaxial geogrid (Cancelli and Montanneli 1999).

Recalculation of the thickness of the base layer reinforced Based on the above Figure that determines the value of LCR, the value of LCR ranges between 1.4 and 1.8 depending on the CBR value. The reduction in base thickness is evaluated using a geogrid with equation (1), assuming no subbase layer. From the conclusions of the chart was designed where LCR ranged from 1.81 to 1.41 and was a function of subgrade CBR. The chart results showed an LCR of over 1.4 for subgrade CBR values greater than 8, which corresponded to a TBR of 4.5. The other full-scale test was constructed in an outdoor test lane with applied traffic loading (Cancelli and Montanneli 1999). The subgrade was clay for this test and installed at a CBR ranging from 1 to 8. The full-scale tests were interpreted by using (Berg and Associates 1992) and for the subgrade, at a CBR of 8 a TBR of 1.6 was obtained.

Using the graphical design of Figure 116, it is possible to calculate the thickness D_2 .



Cancelli and Montanneli 1999

Figure 116. Improvement graph layer coefficient vs CBR of the subgrade

The granular base of a flexible pavement. According to variables input (D_1 , a_1 , D_2 , a_2 , m_2) of a section without reinforcement is possible to determine the SN considering the CBR of the subgrade and incorporating the contribution of the geogrid related to the LCR. Subsequently, using equation (1) can determine the thickness D_2 (cost savings) for a pavement Flexible reinforced and equation (2) for as factor of the layer mixture (Hanandeh 2016).

4.1.4.3 Tencate Manufacture

Tencate used AASHTO 1993 to design reinforced base with geotextile. A project was performed for analysis pavements reinforced by geotextile using AASHTO 1993 pavement design. The method adjusts the structural number by combining a factor (M) to the structural layer equation of the base course layer including a geosynthetics. The values of M between 1.08 and 1.22.

The new updated for this method conducted by including a new factor named as geosynthetic structural coefficient (GSC) for the structural layer equation in AASHTO '93 design. The table shows the estimated base course reduction for different types of Mirafi products. This table correlates the BCR factors with the CBR of the subgrade. The values of BCR for RS580i geotextile ranged from 56% to 24% for CBR values ranging from 15 to 1 with varying BCR values for each geosynthetics within that CBR range. The equation shows the relationship between BCR and GSC. Also, GSC values ranging between 1.04 to 2.56.

$$GSC=LCR = \frac{1}{1-BCR} \quad (2)$$

Tensor suggested a new design method for geogrid-reinforced flexible pavement structure by analyzing and design the full-scale pavement testing results performed by the University of Alaska. Four test sections were constructed with a dimension of 50 mm of HMA on top of a base thickness varying from 152.4 mm to 457.2 mm. Two types of geogrids were installed in two of the test sections while one section had two layers of geogrid and one section served as the control. The applied load consisted of a single tire with a load of 20 kN in one direction and 9 kN in the reverse direction. The subgrade was clayey silt with a CBR ranging from 1.6% to 2.7%. The base course had an average CBR of 15%. Surface deformation (rutting) was measured as a function of the number of loading cycles. Based on these results, the TBR, defined as the number of cycles of load on a geogrid-reinforced section divided by the number of cycles on the control section for the same amount of deformation, were determined. The TBRs were plotted as function of the base thickness and the rutting failure criterion. For a final rutting of 25.4 mm, TBRs ranged from 2 to 3 for the light geogrid pattern and from 2 to 5 for the heavy geogrid pattern. The following steps can review the suggested design methodology:

Use the AASHTO 1993 design procedure to design the unreinforced pavement. Use of layer coefficients for the granular base and the HMA layer, required thicknesses, and design reliability. The number of ESALs (W_{18}) for the unreinforced pavement structure is based on the AASHTO regression model:

$$\log W_{18} = 9.36 \log(SN + 1) - 0.20 + \frac{\log[\Delta PSI / (4.2 - 1.5)]}{0.4 + 1094 / (SN + 1)^{5.19}} + 2.32 + \log M_R - 8.07 \quad (3)$$

Where W_{18} is the total number of 18-kip (80-kN) single-axle load applications before the resurfacing maintenance is required;

ΔPSI is the difference between the initial design serviceability index and the design terminal serviceability index ($\Delta PSI=1.5$ used in this study), and M_R is the subgrade resilient modulus (psi),

To determine the increase of pavement life for the reinforced case, the following is used:

$$(W_{18}) = \frac{W_{18}}{TBR} \quad (4)$$

The required structural number (SN_R) to carry $(W_{18})_R$ is first determined using the following equations. Then, the reduced aggregate base thickness can be determined as follows:

$$D_{2R} = \frac{SN_R - a_1 D_1}{a_2 m_2} \quad (5)$$

$$(D_{2R}) = \frac{W_{18}}{TBR} \quad (6)$$

Initial construction cost and a life-cycle cost analysis can be conducted to evaluate the cost-effectiveness of including the reinforcement (Hanandeh 2016).

4.1.4.4 Tensar Manufacturer

Tensar International Limited produced the SpectraPave4-PRO software. The software used AASHTO 1993. However, The AASHTO 1993 design methodologies for flexible pavements including empirical methods. The structural number is intended to conduct a specific number of traffic loads (ESALs) with levels of serviceability. This software just developed for Triax geogrid and the other geosynthetics products are not cover within SpectraPave4-PRO as shown in Figure 117.

The screenshot displays the 'Pavement Optimization Design Analysis - Data Input' window. It is divided into two main sections for material layer selection and a right-hand panel for design parameters.

Select Material Layers Used in Unstabilized Pavement Section

Layer Name	Material Description	Thickness (in)	Layer Coeff.	Drainage Factor
ACC1	Asphalt Wearing Course	3.00	0.420	
None				
None				
ABC	Aggregate Base Course	6.00	0.140	1.0
SBC	Subbase Course	6.00	0.080	1.0

Select Material Layers Used in Stabilized Pavement Section

Layer Name	Material Description	Thickness (in)	Layer Coeff.	Drainage Factor	TriAx Geogrid
ACC1	Asphalt Wearing Course	3.00	0.420		
None					
None					
MSL	Mechanically Stabilized Base Course	6.00	0.140	1.0	TX5
SBC	Subbase Course	6.00	0.080	1.0	

Geogrid Overlap for Base Course (ft)

Design Parameters (Right Panel):

- Target Traffic (ESALs): 100,000
- Reliability (%): 95
- Standard Normal Deviate: -1.645
- Standard Deviation: 0.49
- Subgrade Resilient Modulus (psi): 5000
- Serviceability: Initial 4.2, Terminal 2.0
- Buttons: Soft Subgrade Stabilization Analysis..., With Subgrade Stabilization, Without Subgrade Stabilization

Figure 117. SpectraPave4

It is obvious from full-scale and small-scale performance indicating research that a new method of flexible pavement design was required to provide the pavement engineer with an appropriate stiffness traffic improvement factor (TIF) for each triaxial geogrid-reinforced pavement section created within SpectraPave4-PRO. As such, SpectraPave4-PRO starts with the automatic generation of a stiffness (TIF) value that is appropriate for the pavement section considered in design. In the AASHTO 1993 empirical design formula, the predicted pavement life is a function of the SN, serviceability limits, and reliability. As such, pavement life using a Triaxial geogrid is calculated based on an enhanced SN. The mechanically stabilized layer (MSL) coefficient, or “a” value, of the TriAx geogrid-reinforced pavement section, is the key component of the enhanced SN value used within the AASHTO empirically based SN equation. The “a” value is representative of aggregate quality and degree of enhanced confinement achieved with a geogrid. Calibration of this “a” value has been done with an extensive catalog of pavement structures (thicknesses and material types), subgrade conditions, and TIF data. Complex algorithms that are based on the “a” value calibration have been created and programmed into SpectraPave4-PRO. The program automatically assigns the proper calibrated “a” value to the TriAx MSL for the user defined input conditions. Tensar International SpectraPave4-PRO v3Tensar TriAx Geogrid.

Tensar was calibrated TIF to an appropriately adjusted base layer coefficient for the MSL for include geogrid in the base. The TIF affiliated with the modified confinement influence. Layer coefficients presented in the AASHTO 1993 design manual for pavement materials are empirically derived correlations to material properties. The new adjusted layer coefficient includes the base aggregate and

the effect of enhanced pavement performance due to the inclusion of the geogrid, also, that producing a stiff composite of base layer and geogrid (Hanandeh 2016).

4.1.4.5 Introduction to MnPave Software for Flexible Pavements

MnPave is a computer program that combines known empirical relationships with a representation of the physics and mechanics behind flexible pavement behavior (MnDOT 1996). The mechanistic portions of the program rely on finding the tensile strain at the bottom of the asphalt layer, the compressive strain at the top of the subgrade, and the maximum principal stress in the middle of the aggregate base layer. Additional details are shown in Appendix J.

MnPave consists of three input modules: climate, traffic, and structure; and three design levels: Basic, Intermediate, and Advanced. The level is selected based on the amount and quality of information known about the material properties and traffic data. In the basic mode, only a general knowledge of the materials and traffic data are required. The intermediate level corresponds to the amount of data currently required for Mn/DOT projects. The advanced level requires the determination of modulus values for all materials over the expected operating range of moisture and temperature.

MnPave simulates traffic loads on a pavement using a layered elastic analysis (LEA) called WESLEA. It is a five-layer isotropic system program written in 1987 by Frans Van Cauwelaert at the Catholic Superior Industrial Institute Department of Civil Engineering in Belgium and modified in 1989 by Don R. Alexander at the U.S. Army Engineer Waterways Experiment Station in Vicksburg, Mississippi. All layers are assumed to be isotropic in all directions and infinite in the horizontal direction. The fifth layer is assumed to be semi-infinite in the vertical direction. Material inputs include layer thickness, modulus, Poisson's ratio, and an index indicating the degree of slip between layers. MnPave assumes zero slip at all layer interfaces. Other inputs include load and evaluation locations. Loads are characterized by pressure and radius. The LEA program calculates normal and shear stress, normal strain, and displacement at specified locations.

MnPave output includes the expected life of the pavement, which is calculated using a damage factor based on Miner's hypothesis. Reliability is estimated using Monte Carlo simulation. There is also a batch section for testing a range of layer thicknesses. In Research Mode (accessible from the "View" menu in the main MnPave window), output includes various pavement responses for each season. Figure 118 illustrate the MnPave window.

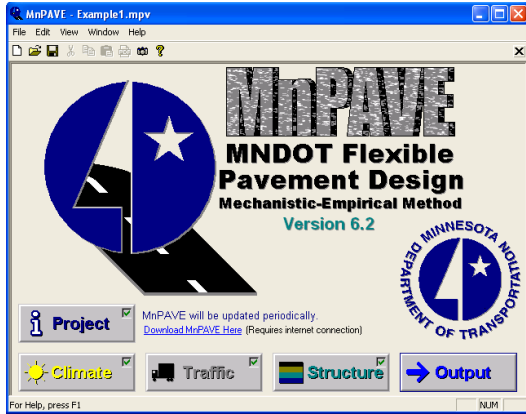


Figure 118. MnPave software

4.2 LABORATORY AND FIELD TESTS CONDUCTED AND THEIR BRIEF DESCRIPTIONS

In the laboratory tests that were conducted for this study, eight test sections were investigated to evaluate the reinforced base course behavior using different types of geogrids and under different locations. The tests were conducted in the laboratory of Ingios Geotechnics, Inc. in Northfield, Minnesota. The IMAS consists of a 5 ft wide and 3 ft deep rigid box and an automatic loading frame were used to apply the cyclic loads. Figure 119 shows the test sections that studied in both laboratory and field tests plus the sections that were calibrated and then investigated in this research by finite element approach. laboratory sections were consisting of section 0, section 1, section 2, section 4, section 5, section 7, section 12 and section 15 were illustrated in the Figure 119.



Note: GE values of sections #0, #1, #2, #4, #5, #7, #12, and #15 are determined based laboratory tests. GE values of sections #3, #6, #8, #9, #10, #11, #13, #14, and #16 are computed based on numerical simulations.

GE values of sections #0, #1, #2, #4, #5, #7, #12, and #15, are determined based on laboratory tests. GE values of sections #3, #6, #8, #9, #10, #11, #13, #14, and #16 are computed based on numerical simulations.

Figure 119. IMAS laboratory test sections and finite element model sections

In the performed field tests, APLTs were performed on test sections on the South Riverfront Drive project in Mankato, Minnesota. In situ testing included cyclic APLTs on the eight test points, with one test location in each of the eight sections. Field sections as well as laboratory sections were consisting of section 0, section 1, section 2, section 4, section 5, section 7, section 12 were illustrated in the Figure 119 plus an unreinforced section of section 12 to compare the results with relative reinforced section. The eight test configurations constructed by varying geogrid types (i.e., light-duty biaxial, heavy-duty biaxial, light-duty triaxial, and heavy-duty triaxial geogrids), geogrid locations in base course (i.e., at the interface between aggregate base course and subgrade or within the aggregate base course), and base aggregate thicknesses. The details for the test sections are shown in Figure 119. The IMAS for laboratory test and the APLT device used in field tests are resented in the Figure 120.

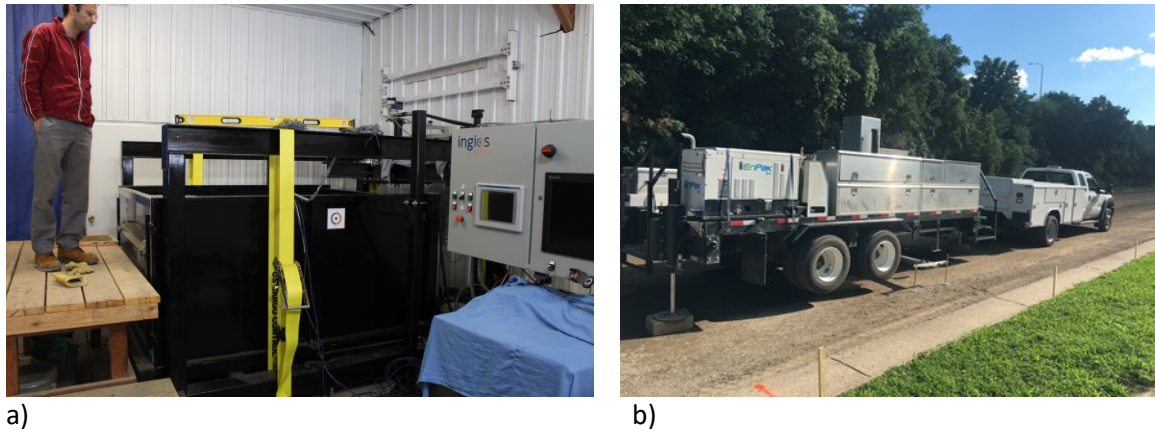


Figure 120. a) IMAS for laboratory test and b) automated plate load test device for field test

Finite element approach consists a total of seventeen sections which the IMAS sections were used to calibrate the finite element models. Then the calibrated FEM models were used to determine GE values of remaining sections. Section #0 is a control section (no geogrid) and the remaining sections (#1 to #16) are the sections were stabilized with geogrid. The value of section 0 is zero since it is unreinforced section. Each other seventeen sections provide a specific GE gain factor which represent the effects of relative variables studied in that section including geogrid stiffness and type, geogrid location, and base thickness. The specifications of the geogrids used in this research are included in Appendix A.

4.3 EVALUATION OF SHORT-TERM GE FACTORS FOR GEOGRID REINFORCED SECTIONS

The increase in the pavement structure's service life by geosynthetic reinforcement has been commonly defined by applying the TBR (Berg et al. 2000). The TBR is defined as the ratio of the number of load cycles on a reinforced section ($N_{Reinforced}$) over the number of load cycles on an unreinforced section ($N_{Unreinforced}$) to reach a defined failure state (rutting depth) by assuming the same geometry and material properties for both mentioned cases (Perkins et al. 2004).

$$TBR = \frac{N_{Reinforced}}{N_{Unreinforced}} \quad (7)$$

On the other hand, the GE factor is one of the MnDOT methods to characterize the pavement materials that enhanced their strength provided by geosynthetic reinforcement (MnDOT 1996). The GE factor can equate the structural performance of all layers of the pavement structure. The GE factor concept is similar to the AASHTO structural number concept (AASHTO 1993); however, local materials and conditions are assumed in the ratio between material factors and normalized to the performance of Class 5 and 6 aggregate base materials used in MnDOT. The mentioned class 5 and 6 aggregated could be classified as between the range of A-1 and A-2 according to AASHTO soil classification (AASHTO 1991). The total GE thickness in the pavement is defined by equation (8) as:

$$GE = a_1D_1 + a_2D_2 + a_3D_3 + \dots \quad (8)$$

Where GE is total aggregate thickness, D_1 is the thickness of asphalt layer (mm), D_2 is the thickness of base course layer (mm), D_3 is the thickness of subbase course layer (mm), and a_1, a_2, a_3 are the layer coefficients which for the base layer it defines as equation (9).

$$a_2 = 0.249 (\log Mr) - 0.977 \quad (9)$$

The benefits of geosynthetics can be incorporated by increasing the base plus subgrade materials' stiffness properties as their resilient modulus. When geosynthetic reinforcement is placed at the base and subgrade interface or within the base layer, it can reduce permanent surface deformations (Hanandeh et al. 2016, Saghebfar et al. 2016). In this method, the selection of the R-value is the critical responsibility of the engineers for design purposes. Any small changes in R-value markedly influence the structural specifications of pavements. Although R-values are difficult to evaluate due to reasons such as the limitations of this test, variations within the soil, classification, construction, and environmental conditions, some kind of judgment is necessary to enclose at design purposes. In current practice, the mean R-value minus one standard deviation is often selected as the design value as well. (MnDOT 1996)

In the research, to calculate GE factors from the performed field APLT test results, the following steps were conducted (Chiglo 2013, Alimohammadi et al. 2020c):

1. Adjust the center APLT deflection (μm) to the standard drop force of 4000 Kg (FWD4000) by the following equation:

$$\frac{4000 \text{ Kg}}{\text{Force of Drop (Kg)}} \times \text{Center deflection } (\mu\text{m}) = \text{FWD4000} \quad (10)$$

2. Convert the FWD deflection into equivalent Benkelman Beam deflections (B.B.) for Bituminous on Aggregate as

$$BB = 1.05 \times \text{FWD4000} + 5.0 \quad (11)$$

3. Convert the Benkelman Beam deflections (B.B.) into Benkelman Beam deflections at 26.6° Celsius.
4. Compute the standard deviation of all the B.B. of the detour segment.
5. Add twice the standard deviation of all B.B. to each BB26.6.

$$BBSD = BB_{26.6} + 2 \times \text{Standard Deviation of all BB} \quad (12)$$

6. Calculate GE according to the structural equation as follows:

$$\log_{10}(BBSD) = 2.728 - 0.0175 (G.E.) - 0.525 \log_{10}(R) \quad (13)$$

where: BBSD = Average peak spring Benkelman Beam deflection plus two standards deviations at 26.6° Celsius mat temperature, GE= Total Granular Equivalency, and R = Subgrade R-value

The TONN2010 software (MnDOT 2010), which is a software using by Minnesota Department of Transportation (MnDOT) follow the previous steps to evaluate roadway strength and overlay thickness calculating plus GE calculations, was used to evaluate the GE gain factor of each field test sections. Table 12 illustrates a summary of the test configurations and the results of the selected sections of performed investigation (Siekmeier and Casanova 2016a).

According to the steps explained above, the Total Granular Equivalent factors calculated from the field APLT test results for both unreinforced and geosynthetic reinforced sections, then the GE gain factor calculated by diminishing the Total Granular Equivalent for a reinforced section from the relative unreinforced section Total Granular Equivalent value and for each row separately.

The GE gain factor for geogrid reinforced calculated in this research is based on the test results and the method mentioned previously as illustrated in Table 12. As can be seen from Table 12, the range of GE gain factor from 36 to 152 mm for reinforced sections. These results indicated that the base layer's thickness could be decreased with the inclusion of geogrids (both triaxial and biaxial with light or heavy-duty stiffness) located at the interface of subgrade and or mid-depth of the base layer. From the results, it is obvious that the high-duty triaxial geogrid located at the middle of the base layer position has the best performance of geogrid reinforcement, among other sections with a base thickness of 254 mm. Results also represent that triaxial geogrids generally have better performance than biaxial geogrids in geosynthetic reinforcement.

Table 12. GE factors for geogrid-reinforced field test field sections

Section	Base thickness (mm)	Geogrid type	Strength of geogrid	Geogrid Position	Pavement's Temp (°C)	Seasonal effect	R value from M_r	Deflection (μm)	BB	Temp Adj	BB26.6	Total Granular Equivalent (mm)	GE gain factor (mm)	GE gain factor (in.)
Section 0	254	unreinforced	unreinforced	unreinforced	20.5	1.36	68	812	22.02	18	24.46	254	0	0
Section 1	254	Biaxial	Light-duty	interface	20.5	1.36	58	711	20.08	16.3	22.17	399	145	5.7
Section 2	254	Biaxial	Heavy-duty	interface	20.5	1.36	54	812	22.02	18	24.46	366	112	4.4
Section 4	254	Triaxial	Heavy-duty	interface	20.5	1.36	45	1010	26.36	21.3	28.93	335	81	3.18
Section 5	254	Biaxial	Light-duty	Middle	20.5	1.36	75*	965	19.74	16.0	21.8	290	36	1.41
Section 7	254	Triaxial	Light-duty	Middle	20.5	1.36	62	660	19.1	15.5	21.01	406	152	5.98
Control 2	152	unreinforced	unreinforced	unreinforced	20.5	1.36	72	863	23.27	18.8	25.61	198	0	0
Section 12	152	Triaxial	Light-duty	interface	20.5	1.36	69	787	21.67	17.6	23.89	267	69	2.71

* Adjusted R value calculated for this section according to $R_{\text{control 1}}/R_{\text{section 5}} = (68/62) = 1.09$ and then substitution of adjusted R value as $R_{\text{section 5}} = (68 \times 1.09) = 75$ in the calculations.

The results presented herein represent a selected number of measurements per sample group. Statistical determination of the minimum number of measurements requires knowledge of the coefficient of variation within a sample group and the difference between mean values of the selected sample groups. The determination of statistical input parameters needed for calculating statistical sample sizes was beyond this report's scope. As a result, these test results apply to the specific testing point locations. Due to the subgrade and base stiffness variability in the site, some unexpected results obtained, such as results for section 5; however, more experimental test with low site variability situation or finite element simulation by adapting calibrated results with the experimental sections can be performed to identify more beneficial results of geosynthetic reinforcement.

4.4 EVALUATING LONG-TERM GE FACTORS FOR GEOGRID REINFORCEMENT IN FLEXIBLE PAVEMENTS

The GE gain factor is one of the MnDOT methods to characterize the pavement materials, which enhanced their strength provided by geosynthetic reinforcement (MnDOT 1996) and applies to design the thicknesses of flexible pavement layers (Fredrickson et al. 1970, Siekmeier and Casanova 2016b, Siekmeier 2018). As the GE definition provided by MnDOT, one-inch Class 5 base aggregate material has a GE of 1 and consequently the GE values for other base materials can be evaluated according to the comparison with Class 5 materials. For instance, if using a biaxial geogrid reinforcement in pavement has GE value as 2, this means that the structural improvement of the reinforced base aggregate with the biaxial geogrid is equal to 2-in. Class 5 base aggregate in the pavement system (Alimohammadi et al. 2020a).

Two main methods are using by MnDOT to calculate GE gain factor in geosynthetic reinforcement of pavements. In the first method, the results of falling weight deflectometer (FWD) tests were converted to the equivalent Benkelman Beam (B.B.) deflections and then the GE gain factor was evaluated based on the results of the average peak spring Benkelman Beam deflection (Chiglo 2013, Siekmeier and Casanova 2016b). The details of this method and the steps which need to follow to calculate the GE gain factor from the results of FWD tests have mentioned in the previous related reference provided by the authors (Alimohammadi et al. 2020c). In the second method, which explained in this research, is based on the concept that the GE gain factor can equate the structural performance of all layers of the pavement structure. In this method, the GE gain factor concept is similar to the AASHTO structural number concept (AASHTO 1993); however, local materials and conditions are assumed in the ratio between material factors and normalized to the performance of Class 5 and 6 aggregate base materials used in MnDOT. The mentioned class 5 and 6 aggregated could be classified as between the range of A-1 and A-2 according to AASHTO soil classification (AASHTO 1991). The total GE thickness in the pavement is defined by equation (14) as:

$$GE = a_1D_1 + a_2D_2 + a_3D_3 + \dots \quad (14)$$

Where GE is total granular thickness, D_1 is the thickness of asphalt layer (mm), D_2 is the thickness of the aggregate base course (mm), D_3 is the thickness of the subbase layer (mm), and a_1, a_2, a_3 are the corresponding layer coefficients.

Using the concept of the mentioned GE method, a novel contribution applied in this research to calculated the GE gain factor based on the incorporation of the geosynthetic reinforcement benefits by adapting the ME Pavement Design (ARA, Inc. 2004). This approach is defined by modifying the base course resilient modulus (M_r) to incorporate the aggregate base course layer's developed strength by the geosynthetics. This approach concentrated on geosynthetic reinforcement effects on the base layer by assuming the reinforced section's same service life as that of the unreinforced section (Perkins 2001 2002, Perkins et al. 2009a). The entire rut depth-load cycle curve is used to get the best matched with the modified base resilient modulus evaluation of geosynthetic benefits to improve the base resilient modulus (M_r). In this regard, the input material, load, conditions, thicknesses, and other parameters in the ME Pavement Design software were first calibrated for the unreinforced test section to achieve the best fit matched with the entire rut depth-load cycle curve. This fitting process was assessed in terms of the least square of errors between the predicted and measured values in the rut depth-load cycle curve (Abu-Farsakh and Chen 2018). Table 13 illustrates the mechanistic-empirical calibration parameters.

Table 13. Mechanistic-Empirical calibration parameters

Section	Br_1, Br_2, Br_3 (AC)	K_1 (AC)	K_1 (AC)	K_1 (AC)	Bs_1 (base)	K_1 (base)	p (base)	B (base)	Bs_1 (subgrade)	K_1 (subgrade)	p (subgrade)	B (subgrade)
1	1.00	-2.45	3.01	0.22	2.2	0.965	48E3	0.24	2.2	0.675	48 E3	0.24

Figure 121 shows the compared measured rut-load cycle curves and the best-fit match with calibrated ME Pavement Design software (MEPDG) ('Guide for Mechanistic-Empirical Design of New and Rehabilitatioed Pavement Structures', 2004) curves for the unreinforced test section.

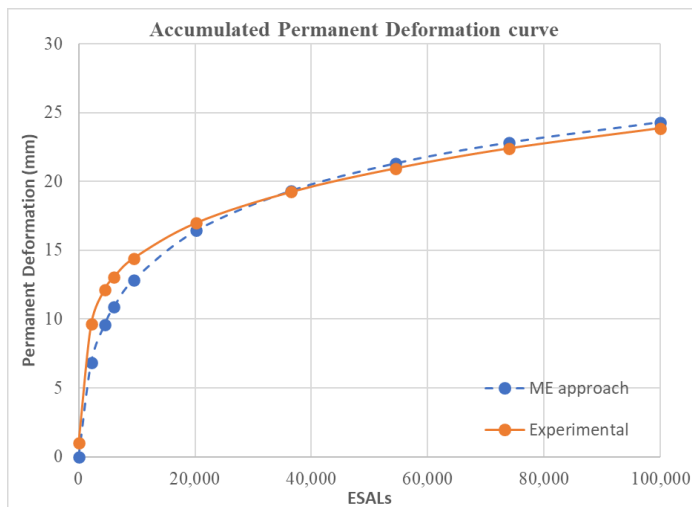


Figure 121. Calibrated permanent deformation of experimental results with mechanistic-empirical approach in unreinforced section

The calibrated mechanistic-empirical calibration parameters were then used to establish the rut depth-load cycle curve for the corresponding geosynthetic reinforced sections. The modified resilient modulus of the reinforced sections' aggregate base layer was increased deliberately until the entire predicted ME Pavement Design software rut depth-cyclic load curve reached the best-fit match with the entire relative measured curve. This base resilient modulus improved values showed for each section separately in

Table 13 and the related fitted curve for some of the reinforced sections according to the aforementioned method are illustrated in Figure 122 as well.

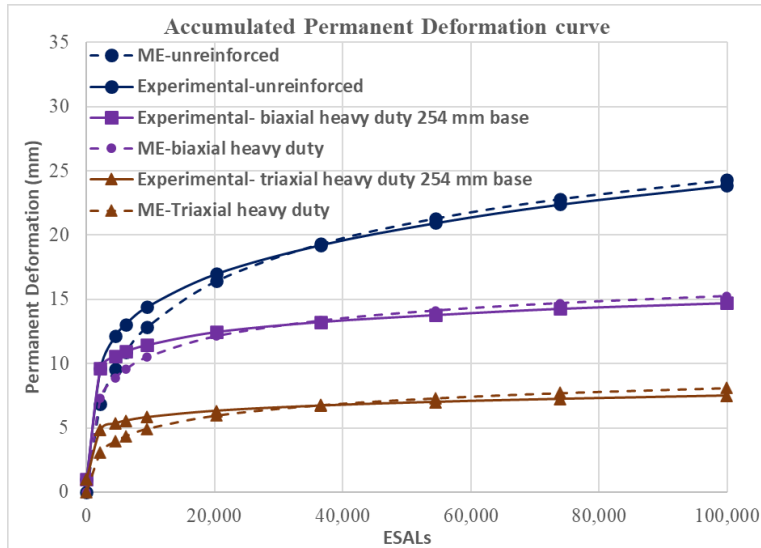


Figure 122. Calibrated permanent deformation of experimental results with mechanistic-empirical approach in unreinforced section

Also, the resilient modulus gain factor (α) calculated by dividing the increased resilient modulus of reinforced sections over resilient modulus of the control section illustrated in this table.

Finally, the GE gain factor value is assumed as zero for the unreinforced section. The GE gain factor values were evaluated by the back-calculation process using evaluated modified base resilient modulus for the reinforced sections and calculated GE gain factor values for each test section illustrated in Table 14.

Table 14. GE factors for geogrid-reinforced laboratory sections

Section No.	Base course thickness (mm)	Geogrid type/strength	Geogrid location	Geogrid tensile strength @5% strain (kN/m)	Aperture dimensions (mm)		Base resilient modulus (MPa)	Base resilient modulus gain factor (α)	GE factor (in.)	GE gain factor (in.)
					Longitudinal	Dimensional				
Section 1	254	unreinforced	unreinforced	unreinforced	unreinforced	unreinforced	230	0	10	0
Section 2	254	Biaxial, Light-duty	Interface	13.4	33	25	442	1.92	6.8	3.18
Section 3	254	Biaxial, Heavy-duty	Interface	19.6	33	25	243	1.93	6.7	3.3
Section 4	254	Triaxial, Heavy-duty	Interface	25	33	33	447	1.94	6.5	3.5
Section 5	254	Biaxial, Light-duty	Middle of base	13.4	33	25	291	1.26	8.26	1.73
Section 6	254	Triaxial, Light-duty	Middle of base	20	33	33	441	1.78	6.8	3.18
Section 7-control	406	unreinforced	unreinforced	unreinforced	unreinforced	unreinforced	230	0	16	0
Section 7	406	Triaxial, Light-duty	Middle of base	20	33	33	861	3.73	8.18	7.8
Section 8- control	152	unreinforced	unreinforced	unreinforced	unreinforced	unreinforced	230	0	6	0
Section 8	152	Triaxial, Heavy-duty	Interface	25	33	33	326	1.41	3.77	2.2

As can be seen in Table 14, the values of the GE gain factor range are from 30 to 198 mm for reinforced pavement sections, which means that the thickness of the aggregate base layer can be reduced with the inclusion of whether the high or low duty of biaxial and triaxial geosynthetics placed at the interface or mid-depth of the base layer. From the results, the best performance of geogrid identified by using triaxial geogrid at the middle of the base layers for sections with thick base thickness of 406 mm; however, the results of sections 2 and 5 indicate that the interface position of geogrid shows better performance than the middle of the thin base course layer for the same geogrid properties and type. Results also represent that generally triaxial geogrids have better performance in reinforcement than biaxial geogrids.

For design purposes, resilient modulus gain factor (α) could be used in the MnPave software to increasing the resilient modulus of the base layer in the pavement design for inclusion of the geosynthetic reinforcement in the pavement according to studied variables such as geosynthetic types, stiffness and locations. Also, the GE values can be used to decrease the designed base course for other design method instead.

4.5 FINITE ELEMENT EVALUATION OF SHORT-TERM GE FACTORS FOR GEOGRID REINFORCED SECTIONS

4.5.1 Introduction

One of Excessive surface rutting is one of the typical types of pavement distresses especially pavements which built over weak and wet subgrade soils. Strengthen the subgrade and upper part of the pavement layers with cement or lime is common method for stabilizing/treating in the pavement constructions (Abu-Farsakh et al. 2016). However, geosynthetics can provide environmentally friendly and potentially economical alternative ways to stabilize/reinforce pavement layers as well. The concept of using geosynthetics for pavement reinforcement initiated in the 1970s (Tang et al. 2014). Many experimental and numerical investigations have been developed to assess the benefits of application of geogrid and geotextile reinforcement in pavements (Wu et al. 2011, Gu et al. 2016a, Saghebfar et al. 2016, Alimohammadi and Abu-Farsakh 2019). The benefits provided by geosynthetics for reinforcement layers in pavements, especially geogrid, is due to their mechanism including the lateral confinement, tensioned membrane effect, increasing bearing capacity of the layers, and the separation (Abu-Farsakh and Chen 2011, Zornberg 2011, Alimohammadi et al. 2020c).

The results of performed investigations illustrated that benefits of geosynthetic reinforcement can be summarized as increasing the TBR and consequently extending the service life of pavements (Alimohammadi et al. 2020b), decreasing required thickness of the base course layer with the same performance (Nazzal 2007), increasing resilient modulus of the base course and subgrade layer (Perkins et al. 2009b, Kim and Lee 2013), reinforcement effect on base course layer and stabilization effects on the subgrade layer (Perkins et al. 2009b, Cuelho and Perkins 2017), better distribution of loading within the pavement layers, and postpone rutting distresses (Perkins et al. 2009b, Abu-Farsakh and Chen 2011).

Many numerical studies using the finite element approach were conducted to evaluate the geosynthetic reinforcement improvements in the pavement. (Perkins 2001) conducted finite element analysis using Abaqus software to evaluate pavement behavior sections presented in their previous report (Perkins and Ismeik 1997). They used elastic perfectly plastic model and a bounding surface model described by Dafalias and Hermann (Dafalias 1986) for simulating the HMA and the base course and subgrade layers respectively in their FE modeling. They used membrane element with an anisotropic linear elastic behavior for modeling the geogrid reinforcement as well. Their results reported reduction of the vertical strain on top of the subgrade and increasing of the bulk stresses by geosynthetic reinforcement in their pavement section.

Rahmani et al. (2020) used finite element method to simulate pavement layers response to repeating loads. They modeled pavement structure (2D plain-strain condition) in different layers incorporated with bulk and interface elements. Through their fully mechanistic analysis framework, the finite element modeling was used to link the mesoscale behavior of pavement materials to the macroscale pavement structural model to carry out a realistic performance evaluation of pavement layers. This can be reflected in the high level of conformity between their experimental and numerical results. Their structural pavement simulation results demonstrated the advantage of FE modeling through evaluating the behavior and performance of pavement layers at specific locations, particularly at weaker interfaces, beneath the tires, and adjacent to the joints that are more likely to get distressed. They also showed that finite element modeling is a promising approach to take into account the complex aspects of pavement response when cracks and preexisted discontinuities, different constitutive material models, and different pavement layer configurations are included. Generally, the presence of distresses on asphalt pavement surface not only reduces the ride quality but also intensifies the traffic noise level. In a study conducted by Khajehvand et al. (2021), it is shown that the presence of either functional or structure distresses on urban roads reduces the pavement smoothness that resulted in high sound pressure level generated by the tire and pavement interaction. Therefore, having pavement without defects could mitigate the traffic noise in urban area. There are couple of approaches to increase the road service life such as asphalt material modification or using geogrid between asphalt layers as well.

Geosynthetic and geocell have proven to provide improved soil reinforcement. For example, (Zadehmohamad and Bolouri Bazaz 2019) found that soil reinforcement with geocell dramatically reduced the peak lateral soil coefficient. (Gu et al. 2017) conducted a numerical analysis by validating their FE simulations with their large-scale tank test results. They used Prony series to simulate viscoelastic behavior of HMA material and a non-linear cross anisotropic constitutive model to mimic the behavior of base course layer plus linear elastic model for subgrade layer simulations. They illustrated that finite element models can accurately predict the unreinforced and geogrid-reinforced pavement section responses.

In this report, a series of laboratory and field tests were performed to evaluate and compute a geogrid gain factor, called the GE factor, and quantify the structural benefit of geogrids. The information and a brief description of performed laboratory and field tests were presented in the following section. This report aims to use performed geogrid laboratory and field test results to calibrate numerical models and then investigate the performance benefits of geogrids in other configurations by the varying location of

geogrids, geogrid type and stiffness, and aggregate base thicknesses. The finite element method was employed for analyzing the structural performance of the unreinforced and geosynthetic reinforced pavement. Finally, a series of GE factors were presented in this report, which can be used by design engineers and industrial designers to include geogrids in their pavement designs.

4.5.2 Finite Element Modeling

In this section, the steps follow for FE simulations, and input parameters were described in the details.

4.5.3 Geometry and Mesh Sizes

In this research, A sensitivity analysis performed to identify the pavement response with different dimension by using a 2D axisymmetric model for simulations through ten different dimension cases. The selected model for case studies shows less than 1% of stress and strain at the model's edges due to the loading with a radius of 2000 mm and depth of 1700 mm (Nazza 07). For all pavement layers, CAX8R Mesh type (8-node biquadratic axisymmetric quadrilateral reduced) and for Geogrid, 3-noded membrane elements were selected (Nazza 2007). Figure 123 illustrates selected FE model dimension and refined mesh size in this research. the bottom and right sides of the models were restrained by roller supports for kinematic boundary conditions in the models.

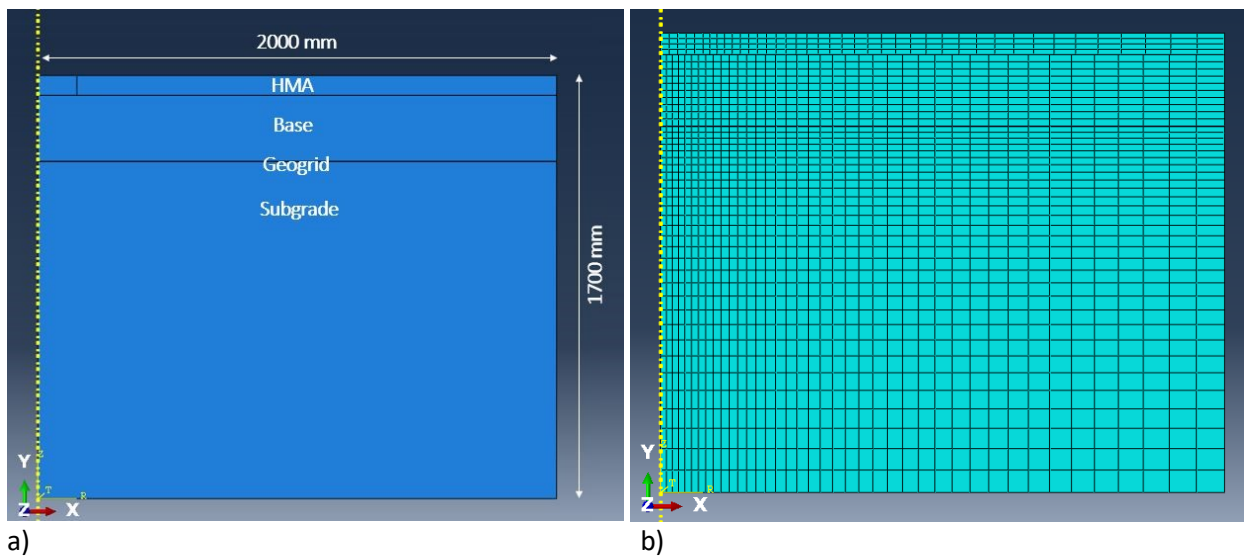


Figure 123. a) Dimension size of FE models and b) Refined mesh size of the FE model elements

Another sensitivity analysis performed to identify the optimum number of element sizes and element numbers of the axisymmetric model and assessing the effect of the mesh sizes on the model results (stresses, strains, etc.). The 1890 element model was selected based on performed mesh sensitivity analysis, which consists of 160 elements for HMA, 400 elements for the base, 1200 elements for the subgrade.

4.5.4 Material Input Parameters

In this section, each appropriately selected constitutive models for every three pavement layers and the input properties of the different layers were described in detail.

4.5.4.1 Hot-Mix Asphalt Layer

To evaluate viscoelastic behavior of the HMA layer, Prony series adapted to apply the numerical method in the time domain properties of HMA. For calculating Prony series parameters in this research, the results of a series of dynamic modulus tests performed on a typical HMA mixture used in the state of Iowa were selected (Alimohammadi et al. 2020a). The experimental dynamic modulus testing was conducted by research performed by Buss et al. (2020) in a project supported by the Iowa Department of Transportation (DOT) (Buss 2014). The detail of the performed experimental tests and the steps followed to convert test results to Prony series mentioned in the related reference (Alimohammadi et al. 2020b); however, Table 15 shows the Prony series parameters used to simulate HMA properties in this report.

Table 15. Prony series parameters in FE simulations in Abaqus software

Elastic Properties	Poisson's Ratio	0.35	Viscoelastic Properties (Prony Constant)	g_i	0.001259	0.012589	1.25893	12.5893	39.8107	79.4328
Elastic Properties	Instantaneous modulus (MPa)	8031		τ_i	0.517936	0.332679	0.07257	0.0246	0.013649	0.009533

In the first step, the master curves of the performed dynamic modulus test results were fitted with the Prony series parameters and then relevant (G) and (τ) for the HMA mixture have been calculated to use in HMA properties in FE simulations in Abaqus software.

4.5.4.2 Unbound Granular Base Course and Subgrade Layers

The base and subgrade layers were simulated using the Mohr-Coulomb model available in the Abaqus software package. Properties of Class 5 aggregates, classified as A-1 based on the AASHTO method, which is typically used in the state of Minnesota for the base course constructions, were used in FE simulations. Also, subgrade soil with a CBR equal to 2 prepared at a target moisture content of 16.6%, classified with A-7-6 (2) based on the AASHTO method, representing the common subgrade soil conditions in Minnesota in FE simulations as well. The mentioned aggregate and soil properties were conducted based on a series of geotechnical tests performed in the geotechnical laboratory of Iowa State University and DCP tests performed in the Ingios Geotechnics, Inc. laboratory. The average values of resilient modulus from DCP test results for the base and subgrade layers were selected to use in the FE simulations (Ceylan et al. 2009, Alimohammadi et al. 2020c). Table 16 shows the Mohr-Coulomb model properties for subgrade and unbound base layers.

Table 16. Base course, and subgrade layers properties used in FE simulation

Material	Gradation type	Elastic modulus (MPa)	ν	Friction angle (ϕ)	Cohesion (KPa)
Base	A-1	76	0.35	29	60
Subgrade	A-7-6 (2)	21	0.35	22	9

4.5.4.3 Geogrid Properties

Four types of geogrids, including biaxial and triaxial with high and low duty stiffnesses, are used in this research. Due to the machine and cross-machine stiffness of geosynthetics, a method developed by Perkins et al. (2004) was used to convert orthotropic linear elastic behavior of geosynthetic to an equivalent isotropic elastic property to use in FE simulations (Perkins et al. 2004). The properties of the geogrids are illustrated in Table 17.

Table 17. The geogrid equivalent modulus (MPa) quantifying geogrid properties

No.	Type of geogrid	Stiffness	Equivalent modulus (MPa)
1	Biaxial	Low duty	426
2	Biaxial	Heavy-duty	928
3	Triaxial	Low duty	1085
4	Triaxial	Heavy-duty	1260

4.5.5 Interface/Interlocking and Confinement Effect Modeling of Geogrid

Generally vertical stresses increase during the construction of pavement layers due to the granular pavement's compaction and consequently interlocking base coarse particles cause increasing in lateral residual stresses in base course layer as well. On the other hand, geogrid reinforcement in the pavements provide additional lateral residual stresses and confinement due to the interlocking of the aggregate particles. To evaluate mentioned interlocking and confining effects and additional lateral residual stresses, a Discrete Element Modeling (DEM) developed by previous researchers (Zadehmohamad and Bolouri Bazaz 2019). Their investigation showed the influence zone provided by geogrid-reinforcement in the base course layer is approximately 100 mm. same influence zone captured by other investigations (Nazzal 2007) by conducting triaxial tests as well. The maximum mentioned stress was 63 kPa at the geogrid location, linearly decrease to 21 kPa at the influence zone and then remains steady for the rest of the height of base course layer.

Recently an investigation performed by Gu et al. (2016b) including a series of triaxial tests and large-scale tank (LST) tests to better understand and evaluate the geosynthetic reinforcement influence zone and lateral residual stresses developed in the pavement layers. They developed equation (15) to calculate the mentioned maximum equivalent additional stress (Gu et al. 2016b):

$$\Delta\sigma_3 \max = \left(\frac{2M}{(1-\nu_g)\delta\alpha} \cdot \left[\frac{(\sigma_3 + \Delta\sigma_3 \max)}{E_H} - \frac{\nu_{13}\sigma_1}{E_V} - \frac{\nu_{33}(\sigma_3 + \Delta\sigma_3 \max)}{E_H} + 0.85\varepsilon_0 e^{-\left(\frac{r}{N}\right)^\beta} (\sqrt{J_2})^m \right] (\alpha I_1 + K)^n \right) \quad (15)$$

where $\Delta\sigma_3 \max$ is the maximum additional confining stress, M is geosynthetic sheet stiffness, ν_g is the Poisson's ratio of the geosynthetic, δ is the thickness of the influence zone (i.e., $\delta = 150$ mm), σ_3 is the initial confining pressure, E_H is the horizontal modulus of the specimen, E_V is the vertical modulus of the specimen, σ_1 is the axial stress applied to the specimen, ν_{13} is the Poisson's ratio, and ν_{33} is the Poisson's ratio to characterize the effect of lateral stress on the lateral strain, I_1 is the first invariant of the stress tensor, J_2 is the second invariant of the deviatoric stress tensor, and ε_0 , p , β , m , and n are permanent

deformation properties of the unbound base course material. From equation (15), the maximum additional confining stress, $\Delta\sigma_3 \text{ max}$, identified by an iteration method (Gu et al. 2016a).

The mechanism of geosynthetic reinforcement consist of vertical membrane effects and lateral confinement (Gu et al. 2016a, Gu et al. 2016b, Luo et al. 2017). Assuming membrane element in FE simulation can convince the reinforcement vertical membrane effect. Also, the lateral confinement simulated by assuming an additional confining stress distribution in the geosynthetic influence zone as described before. The maximum confining stress for different type and stiffness of geosynthetics in FE simulations in this report illustrated in Table 18.

Table 18. Maximum confining stress for different type and stiffness of geosynthetics

Geogrid stiffness	$\Delta\sigma_3 \text{ max}$ (KPa)
Biaxial, light-duty	29
Biaxial, heavy-duty	31
Triaxial, light-duty	32
Triaxial, heavy-duty	34

Geogrid interface properties of between Base and Subgrade layer was simulated by adapting an interface model in FE simulations. This interface model could be defined as a normal interaction interface with hard contact and tangential interaction with a frictional coefficient (μ) and elastic slip (E_{slip}) that could be used to illustrate shearing resistance and shearing displacement in the interaction surface. These interface properties defined according to experimental tests and related literature for FE simulation, typically as friction coefficient of $\mu = 1$, and $E_{\text{slip}} = 0.003$ for coulomb properties model between geogrid and unbound base material plus tie condition between geosynthetic and subgrade clay soil in the simulation (Perkins and Cuelho 1999, Perkins et al. 2004). All other FE simulations were assumed the same as the lab test conditions in the experimental large-scale laboratory experimental part of this research.

4.5.6 Calibration of the FE Simulations by Mechanistic-Empirical Approach with IMAS Experimental Tests, Parametric Study

As mentioned in Chapter 2 of this report, eight test sections were investigated to evaluate the unreinforced and reinforced base course behavior using different types of geogrids and under different locations in the performed laboratory tests. Figure 124 shows all these eight test sections consisting of GE0, GE1, GE2, GE4, GE5, GE7, GE12, and GE15 that were studied in both laboratory and field tests.

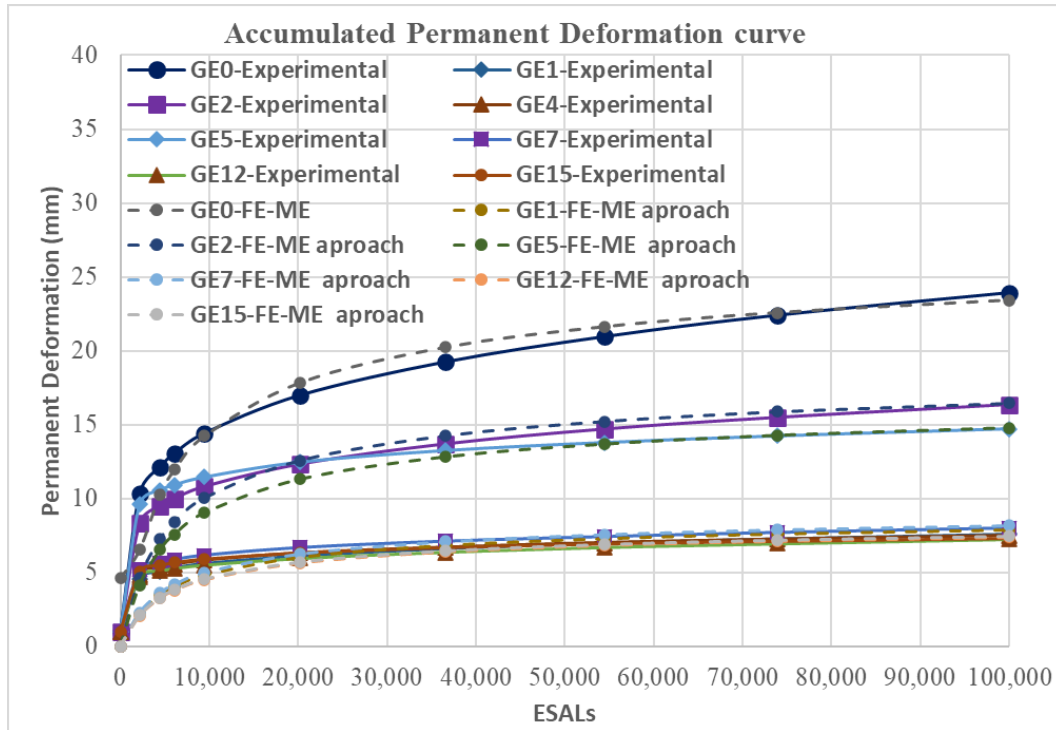


Figure 124. Calibrated permanent deformation of experimental test results with performed FE simulation sections evaluated by mechanistic empirical approach

These sections were used for calibration and then investigated in this research by finite element and mechanistic-empirical approach. For this purpose, all the eight sections with the same layer material properties, loading conditions, and boundary conditions described in Chapter 2 of this report were assumed in FE simulations. Then the results of permanent deformation of FE simulations were evaluated with empirical equations and calibrated with relative experimental IAMS test results. According to the Guide for Mechanistic-Empirical Design of New and Rehabilitated Pavement Structures (MEPDG for short) (ARA, Inc. 2004), the total rutting value in the pavement is calculated by the sum of individual layers deformations to obtain total deformation by equation (16) as (Gu et al. 2017):

$$D_{\text{Total}} = D_{\text{AC}} + D_{\text{B}} + D_{\text{S}} \quad (16)$$

Where D_{Total} is total surface permanent deformation, D_{AC} , D_{B} , and D_{S} are asphalt layer, base, and subgrade deformation, respectively. Also, permanent deformation for asphalt layer, base layer, and subgrade layer calculated by equations (17) and (18) respectively as:

$$\Delta_{p(HMA)} = \varepsilon_{p(HMA)} \times h_{HMA} = \beta_{1r} \times K_z \times \varepsilon_{r(HMA)} \times 10^{k_{1r}} \times n^{k_{2r}\beta_{2r}} \times T^{k_{3r}\beta_{3r}} \quad (17)$$

$$\Delta_{p(soil)} = \beta_{s1} \times K_{s1} \times \varepsilon_V \times h_{soil} \times \frac{\varepsilon_0}{\varepsilon_r} \times e^{\left(\frac{\rho}{n}\right)^\beta} \quad (18)$$

Where

$$K_2 = (C_1 + C_2 \times D) \times 0.328196^D \quad (19)$$

$$C_1 = -0.1039 \times H_{HMA}^2 + 2.4868 \times H_{HMA} - 17.342 \quad (20)$$

$$C_2 = 0.0172 \times H_{HMA}^2 - 1.7331 \times H_{HMA} + 27.428 \quad (21)$$

and

$$\log \beta = -0.61119 - 0.017638 \times (w_c) \quad (22)$$

$$\rho = 10^9 \times \left(\frac{c_0}{1 - (10^9)^\beta} \right)^{\frac{1}{\beta}} \quad (23)$$

$$c_0 = \text{Ln} \left(\frac{a_1 M_r^{b_1}}{a_9 M_r^{b_9}} \right) \quad (24)$$

Where Δp is accumulated permanent vertical deformation, ϵ_p is accumulated plastic strain in layers at n repetitions of the loads, ϵ_0 is intercept determined from laboratory-repeated load permanent deformation, ϵ_r is the elastic strain, n is the number of repetitions of the load, ϵ_v is the average vertical resilient strain, T is pavement temperature, W_c is water content, $a_{1,9}$ are regression constants, $b_{1,9}$ is regression constants, B_{s1} is local calibration factor, k_{s1} is global calibration factor, Depth is the depth below the surface, k_z is depth confinement factor, B_{r1} , B_{r2} , B_{r3} are local calibration factors for the rut model, and k_{1r} , k_{2r} , k_{3r} are global field calibration factors defined as -2.45, 3.01, and 0.22 respectively. Mechanistic-Empirical damage prediction functions (e.g. B, p, k, etc.) for unreinforced and reinforced sections were calibrated according to performed experimental laboratory test results for each section separately to get the best fit rutting graph matched with the relative experimental tests. Table 19 illustrates mechanistic-empirical calibration parameters for the best-fit match of rutting graph of mechanistic-empirical approach and laboratory test results for all test sections separately.

Table 19. Mechanistic-empirical calibration parameters for best-fit with field test sections

Section	B_{r1} , B_{r2} , B_{r3} (AC)	K_1 (AC)	K_2 (AC)	K_3 (AC)	B_{s1} (base)	K_1 (base)	p (base)	B (base)	B_{s1} (subgrade)	K_1 (subgrade)	p (subgrade)	B (subgrade)
0	1.00	-2.45	3.01	0.22	2.2	0.965	4,800	0.5	2.2	0.675	4,800	0.5
1	0.27	-2.45	3.01	0.22	0.59	0.965	4,800	0.5	0.59	0.675	4,800	0.5
2	0.55	-2.45	3.01	0.22	1.21	0.965	4,800	0.5	1.21	0.675	4,800	0.5
4	0.26	-2.45	3.01	0.22	0.57	0.965	4,800	0.5	0.57	0.675	4,800	0.5
5	0.38	-2.45	3.01	0.22	0.83	0.965	4,800	0.5	0.83	0.675	4,800	0.5
7	0.21	-2.45	3.01	0.22	0.46	0.965	4,800	0.5	0.46	0.675	4,800	0.5
12	0.22	-2.45	3.01	0.22	0.48	0.965	4,800	0.5	0.48	0.675	4,800	0.5
15	0.23	-2.45	3.01	0.22	0.49	0.965	4,800	0.5	0.49	0.675	4,800	0.5

Also, Figure 122 shows the calibrated permanent deformation of experimental test results with performed FE simulation sections evaluated by a mechanistic-empirical approach.

A parametric study with FE simulation and evaluated using the mechanistic-empirical approach performed on the sections GE3, GE6, GE8, GE9, GE10, GE11, GE13, GE14, and GE16 which mentioned by the red frame in Figure 119. By conducting this parametric study, the pavement's geosynthetic reinforcement benefits could be evaluated by getting new damage prediction functions for different assumed variables in reinforced sections. For this purpose, all mentioned sections with the same layer material properties, loading conditions, and boundary conditions as by the other experimental sections were assumed in FE simulations. Then the results of the permanent deformation of FE simulations were evaluated with empirical equations and calibrated with relative calibrated experimental test damage prediction coefficients. Table 20 illustrates the mechanistic-empirical evaluated parameters. Also, Figure 124 shows the evaluated permanent deformation of all test sections using the mentioned approach.

Table 20. Mechanistic-empirical calibration parameters for FE simulated sections

Section	Br ₁ , Br ₂ , Br ₃ (AC)	K ₁ (AC)	K ₂ (AC)	K ₃ (AC)	Bs ₁ (base)	K ₁ (base)	p (base)	B (base)	B _{s1} (subgrade)	K ₁ (subgrade)	p (subgrade)	B (subgrade)
3	0.26	-2.45	3.01	0.22	0.58	0.965	4,800	0.5	0.58	0.675	4,800	0.5
6	0.37	-2.45	3.01	0.22	0.81	0.965	4,800	0.5	0.81	0.675	4,800	0.5
8	0.2	-2.45	3.01	0.22	0.45	0.965	4,800	0.5	0.45	0.675	4,800	0.5
9	0.26	-2.45	3.01	0.22	0.53	0.965	4,800	0.5	0.53	0.675	4,800	0.5
10	0.25	-2.45	3.01	0.22	0.52	0.965	4,800	0.5	0.52	0.675	4,800	0.5
11	0.23	-2.45	3.01	0.22	0.49	0.965	4,800	0.5	0.49	0.675	4,800	0.5
13	0.26	-2.45	3.01	0.22	0.52	0.965	4,800	0.5	0.52	0.675	4,800	0.5
14	0.25	-2.45	3.01	0.22	0.51	0.965	4,800	0.5	0.51	0.675	4,800	0.5
16	0.22	-2.45	3.01	0.22	0.48	0.965	4,800	0.5	0.48	0.675	4,800	0.5

4.5.7 Developing GE Factors for Assessing Geogrid Reinforcement in Flexible Pavements

The GE factor is one of the MnDOT methods to characterize the pavement materials that enhanced their strength provided by geosynthetic reinforcement (MnDOT 1996). The GE factor can equate to the structural performance of all layers of the pavement structure. The GE factor concept is similar to the AASHTO structural number concept (AASHTO 1993); however, local materials and conditions are assumed in the ratio between material factors and normalized to the performance of Class 5 and 6 aggregate base materials used in MnDOT. The mentioned Class 5 and 6 aggregated could be classified as between the range of A-1 and A-2 according to AASHTO soil classification (AASHTO 1991). The total GE thickness in the pavement is defined by equation (25) as:

$$GE = a_1D_1 + a_2D_2 + a_3D_3 + \dots \quad (25)$$

Where GE is total aggregate thickness, D1 is the thickness of asphalt layer (mm), D2 is the thickness of base course layer (mm), D3 is the thickness of subbase course layer (mm), and a1, a2, a3 are the layer coefficients which for the base layer it defines as equation (26).

$$a_2 = 0.249 (\log Mr) - 0.977 \quad (26)$$

The Incorporation of geosynthetics in pavements can be beneficial by increasing the base and subgrade stiffness properties and resilient modulus and reduce pavements' permanent surface deformations (Hanandeh et al. 2016). Perkins (2001) developed a methodology to evaluate the TBR and geosynthetic reinforcement effects on the stabilization of the subgrade and reinforcement of base layer in pavement.

This method was adapted for a reinforced section by subtracting the reduction in permanent deformation of the base layer from the total surface permanent deformation curve in Figure 124 as shown in equations (27) through (29).

$$PD_{R-B} = PD_U - (PD_{B-U} - PD_{B-R}) \quad (27)$$

$$PD_{R-S} = PD_U - (PD_{S-U} - PD_{S-R}) \quad (28)$$

$$PD_R = PD_U - (PD_{B-U} - PD_{B-R} + PD_{S-U} - PD_{S-R}) \quad (29)$$

Where PD_U is the surface deformation for unreinforced section, PD_{R-B} illustrates the base layer reinforced surface deformation, PD_{R-S} show the subgrade layer reinforced surface deformation, PD_R is the reinforced section surface deformation, PD_{B-U} is the unreinforced section deformation of the base layer, PD_{B-R} is the reinforced section deformation of the base layer, PD_{S-U} is the unreinforced section deformation of subgrade layer, and PD_{S-R} is the reinforced section deformation of subgrade layer.

The effects of geosynthetic reinforcement on the base course layer can be incorporated into the Pavement Mechanistic-Empirical (ME) Design software (ARA, Inc. 2004) by enhancing stiffness of base layer and adjusting the base resilient modulus (M_r) in the designs. This approach utilized Pavement ME Design to back-calculate the adjusted reinforced section base resilient modulus to evaluate relevant TBR value.

In case that the reinforced pavement's design service life to be same as the unreinforced pavement (i.e., TBRB=1), the enhanced base resilient modulus cause reduction in required base layer's thickness. This reduction in base layer thickness can back-calculated by using the Minnesota pavement rutting distress equations. This benefit of geosynthetic reinforcement is commonly assessed in terms of the GE factor, which is defined as reducing the reinforced section's base thickness compared to the base thickness of the unreinforced section for a given traffic level. The corresponding GE factor estimated using the same methodology as described earlier by increase the base resilient modulus (M_r) to achieve the TBR.

The GE factor for geogrid reinforced calculated in this research based on the test results and the method discussed earlier illustrated in Table 21.

Table 21. Factors for geogrid reinforced sections

Section No.	Base course thickness (mm)	Geogrid type/strength	Geogrid location	Geogrid tensile strength @5% strain (KN/m)	Aperture dimensions (mm)		GE factor inches (mm)
					Longitudinal	Dimensional	
Section GE0	254	unreinforced	unreinforced	Unreinforced	unreinforced	unreinforced	0
Section GE1	254	Biaxial, Light-duty	Interface	13.4	33	25	3.2 (81)
Section GE2	254	Biaxial, Heavy-duty	Interface	19.6	33	25	3.3 (83)
Section GE3	254	Triaxial, Light-duty	Middle of base	20	33	33	3.3 (84)
Section GE4	254	Triaxial, Heavy-duty	Interface	25	33	33	3.4 (89)
Section GE5	254	Biaxial, Light-duty	Middle of base	13.4	33	25	1.7 (43)
Section GE6	254	Biaxial, Heavy-duty	Middle of base	19.6	33	25	1.8 (46)
Section GE7	406	Triaxial, Light-duty	Middle of base	20	33	33	3.2 (81)
Section GE8	254	Triaxial, Heavy-duty	Middle of base	25	33	33	3.4 (86)
Section GE9	152	Biaxial, Light-duty	Interface	13.4	33	25	1.9 (48)
Section GE10	152	Biaxial, Heavy-duty	Interface	19.6	33	25	2.0 (51)
Section GE11	152	Triaxial, Light-duty	Interface	20	33	33	2.1 (53)
Section GE12	152	Triaxial, Heavy-duty	Interface	25	33	33	2.2 (56)
Section GE13	406	Biaxial, Light-duty	Middle of base	13.4	33	25	6.9 (175)
Section GE14	406	Biaxial, Heavy-duty	Middle of base	19.6	33	25	7.2 (183)
Section GE15	406	Triaxial, Light-duty	Middle of base	20	33	33	7.8 (198)
Section GE16	406	Triaxial, Heavy-duty	Middle of base	25	33	33	8.0 (203)

As can be seen from this table, the range of GE factor from 43 to 203 mm for reinforced sections. These results indicated that the base layer's thickness could be decreased with the inclusion of geogrids (both triaxial and biaxial with light or heavy-duty stiffness) located at the subgrade interface or mid-depth of the base layer. From the results, it is obvious that the high-duty triaxial geogrid located at the middle of thick base layers has the best geogrid reinforcement performance, among other sections. Results also represent that triaxial geogrids have better performance than biaxial geogrids in geosynthetic reinforcement.

It should be mentioned that the results presented in this research represent a selected number of measurements per sample group. As a result, these test results apply to the specific testing point locations. Due to the subgrade and base stiffness variability in the site, some unexpected results were obtained; however, more experimental tests with low site variability or finite element simulation by adapting calibrated results with the experimental sections can be performed to identify more beneficial results of geosynthetic reinforcement.

4.6 COST-BENEFIT ANALYSIS

In this section, details of construction and maintenance procedures and their costs consist of aggregate, hauling, equipment, and geogrid costs were addressed. First, details of construction and maintenance costs were mentioned and then a visual comparison developed by providing graphs of maintenance and construction costs. Finally, calculations for life-cycle cost analysis are presented which can help engineers to design for lowest cost and constraints limit of the design and give them a better sense of perspective and design balance.

4.6.1 Lifecycle Cost Analysis

Various alternatives should be considered in providing base support for pavements, and cost effectiveness is an important consideration. Lifecycle cost analysis (LCCA) is useful because it considers construction, rehabilitation and maintenance as well as pavement service life to project the cost effectiveness of various solutions. Using LCCA method was initiated in the 1950s by state agencies for cost evaluations and comparing proposed pavement projects (AASHTO 1960). It is advantageous to compare various pavement types, qualities of pavement, in addition to rehabilitation and maintenance strategies (Walls and Smith 1998, Wilde et al. 1999). In this method, the net present value (NPV) can evaluate based on construction, maintenance, and salvage value costs of the pavement using equation (30).

$$NPV = \text{Construction Costs} + \sum_{k=1}^n \text{Maintenance Cost}_k \left[\frac{1}{(1+i)^{nk}} \right] - \text{Salvage Value} \left[\frac{1}{(1+i)^{nk}} \right] \quad (30)$$

where, n represents the service life of the project and i refers to the discount rate. The value of investment paving materials for each alternative at the end of the analysis period (salvage value), is often assumed to be zero; this coincides with the end of the service life for the pavement. Also, compared to initial construction or maintenance costs, routine annual maintenance costs usually do not

change the analysis noticeably and thus have negligible effects on the total NPV, especially for pavements with longer service lives (over 20 years).

Cost differences when using a geosynthetic reinforcement in a pavement system will vary by project. This analysis will compare the presented GE values for design recommendations of geosynthetic reinforced pavements with an unreinforced section with Class 5 aggregate base. The benefit of using geosynthetic reinforcement results from reduced base thickness as defined by GE value in this research. It should be noted that only the pay items that make the cost differences between different pavement sections will be included for analysis: cost of geosynthetic reinforcement, cost of aggregate base (i.e., we assume that the thickness of asphalt layer is the same for all sections). The calculated prices are based on each mile (5,280 ft) of the road with width of 24 ft and 10-in. base thickness and it will be represented for the other base thicknesses that assumed in this research as well.

4.6.2 Initial Cost Analysis

Class 5 aggregate materials were assumed to haul from local quarry with 15-miles distance in the calculations. The aggregate cost, haul time for round trip, Labor haul cost, and the delivered prices for the Class 5 aggregate are summarized in Table 22.

Table 22. Aggregate and hauling time costs for base material

Source	Aggregate cost (\$/ton)	Haul time (min)	Labor haul cost (\$/truck)	Labor haul cost (\$/ton)	Delivered price (\$/ton)
Class 5 aggregate	15.00	32	15.73	1.05	15.75

The labor haul rate was considered to be \$31.78/hr (AASHTO 1960) per 15-ton tandem-dump truck (Wilde et al. 1999) and the hourly truck rental rate was considered to be \$82.05/hr as well (Walls and Smith 1998). Haul times were estimated based on average distance from the local quarry to the construction site for round-trip travel.

Four types of geogrid preparation and transferring cost that used in this research are presented in Table 23. A value of 10% of area for overlapping the geogrids in the installation was assumed in the calculations in Table 23.

Table 23. Geogrid costs for the material installation in the road sections

Type	Light-duty biaxial geogrid (BX1100)	Heavy-duty biaxial geogrid (BX1200)	Light-duty triaxial geogrid (TX130S)	Heavy-duty triaxial geogrid (TX7)
Each roll (ft ² /roll)	3227	2151	3227	2151
Price (\$/roll)*	500	570	790	1720
Number of needed rolls in each mile	43	65	43	65

Type	Light-duty biaxial geogrid (BX1100)	Heavy-duty biaxial geogrid (BX1200)	Light-duty triaxial geogrid (TX130S)	Heavy-duty triaxial geogrid (TX7)
Geogrid price for each mile	21,598	36,938	34,124	111,462
Geogrid price (\$/yd ²)	1.56	2.63	2.46	7.94

*Source: Paramount Materials 2021

Typical base placement equipment (graders, dump trucks, tractors, and rollers) and labor hourly rates are presented in Table 24. Installation time including unrolling and securing the geogrid was estimated to be 6 minutes per square yard.

Table 24. Labor and equipment unit costs

Category	Unit cost per hour
On-site labor ¹	\$31.78
Grader ²	\$87.6
Bottom-dump truck ³	\$88.89
Tandem-dump truck ⁴	\$82.05
Loader ⁵	\$82.5
Tractor ⁶	\$96.36
Drum roller ⁷	\$59.41

Sources: ¹ MnDOT 2020a, ² MnDOT 2020b, ³ and ⁴ Minnesota Department of Labor and Industry 2021, ⁵ MnDOT 2012, ⁶ Minnesota Department of Labor and Industry 2021, ⁷ Cetin et al. 2019

In Table 25, the total tonnages and costs of granular aggregate material required for the road construction are summarized to calculate the initial construction costs.

Table 25. Weight of the aggregate materials required for construction

Source	Tonnage (ton)	Total cost (\$/ton)	Total cost (\$)
Class 5 aggregate	5,652	15.75	89,017

The costs in this table include the costs of the aggregate materials and the labor costs for hauling as well. The costs for preparing and setting the geogrids will be added to the final cost of construction. Also, Table 26 illustrates the costs of labor for aggregate and hauling.

Table 26. Class 5 aggregate and labor cost of hauling the Class 5 aggregate for construction

Source	Class 5 aggregate (ton)	labor haul rate /hr per 15-ton tandem-dump truck	Labor hauling (\$)
Class 5 aggregate	5,652	31.78	11,974

The hours for labor and equipment for construction of the test sites including preparation and compaction of subgrade and base layers are presented in Table 27.

Table 27. Labor and equipment required times for construction

Source	Labor (hr)	Grader (hr)	Bottom dump (hr)	Tandem dump (hr)	Loader (hr)	Tractor (hr)	Drum roller (hr)
Class 5 aggregate	72	16	8	21	10	15	8

Source: (Cetin et al. 2019)

Tables 28 and 29 show the calculated costs of the equipment and labor during road sites' construction, respectively.

Table 28. Equipment costs for each section for construction

Source	Grader (\$)	Bottom dump (\$)	Tandem dump (\$)	Loader (\$)	Tractor (\$)	Drum roller (\$)	Total (\$)
Class 5 aggregate	1,402	711	1,723	825	1,445	475	6,581

The labor costs in Table 29 included the costs for the construction and the cost of hauling labor

Table 29. Labor costs of the sections for construction

Source	On-site (\$)	Hauling (\$)	Total (\$)
Class 5 aggregate	2,288	11,974	14,263

Table 30 represents the final construction costs based on the equipment, labor, aggregate, and preparing and installation of geogrid costs.

Table 30. Equipment, Class 5 aggregate, and labor total costs for each geogrid type

Source	Equipment (\$/mile)	Class 5 aggregate (\$/mile)	Labor (\$/mile)	Total without geogrid (\$/mile)	Geogrid (\$/mile)	Total with geogrid(\$/mile)
Light-duty biaxial geogrid (BX1100)	6,581	89,017	14,263	109,861	21,598	131,459
Heavy-duty biaxial geogrid (BX1200)	6,581	89,017	14,263	109,861	36,938	146,799
Light-duty triaxial geogrid (TX130S)	6,581	89,017	14,263	109,861	34,124	143,986
Heavy-duty triaxial geogrid (TX7)	6,581	89,017	14,263	109,861	111,462	221,323

According to the types of geogrids, prices mentioned in Table 23 of geogrid including required overlap for installation are used for each mile of the road in Table 30.

4.6.3 Maintenance/Rehabilitation Costs Analysis

Future maintenance costs may be desirable to predict in circumstances such as lacking or unreliable historical data to vet historical data or under other certain circumstances. Local officials can also apply this method to evaluate cost estimates according to their local material sources and equipment and compare with historical data. In this section, the maintenance costs were evaluated economically for HMA road for yearly maintenance costs for one mile of road.

This economic analysis can be helpful for engineers in their evaluations and making decisions about upgrading flexible roads. The example presented here compares the cost of maintenance of an HMA road; however, it can be modified to present timing and cost of many other typical projects. The historical costs were used for the HMA road since predictable maintenance operations for HMA roads couldn't be identified in this project.

The analysis assumes regular preventing and maintenance actions at the first five years of the road life. Then for seven years the annual maintenance expenditure for \$1,600 per mile/ per year assumed and then Seal coat maintenance after seven years at an estimated cost of \$7600 per mile and continuing the annual maintenance expenditure at \$1,600 per mile/ per year for the second seven years presented in Table 31.

Table 31. HMA maintenance/seal coat costs for seven-year cycle

Maintenance/rehabilitation type:	Preventing actions and maintenance for the first 7 years	Seal coat maintenance after 7 years	Preventing actions and maintenance for the second 7 years
Maintenance/rehabilitation cost:	\$1,600 per mile per year	\$7,600/ mile	\$1,600 per mile per year

The information of this table is also presented in the Figure 125. It should be mentioned that the seal coat application is repeated on a seven-year cycle and continues until the road is expected for another type of rehabilitation which may be cold-in-place recycling or an overlay. Also, according to the budget available and the local conditions of the project, other upgrades may be more appropriate as well. Although the HMA maintenance costs vary in the state of Minnesota, a fair representation of the cost could be a cost of \$1,600 per mile/ per year for the purposes of analysis.

The maintenance plan in Figure 125 is being conducted assuming that the small maintenance and preventing activities between years 1 and 5 may occur in the constructed HMA road.

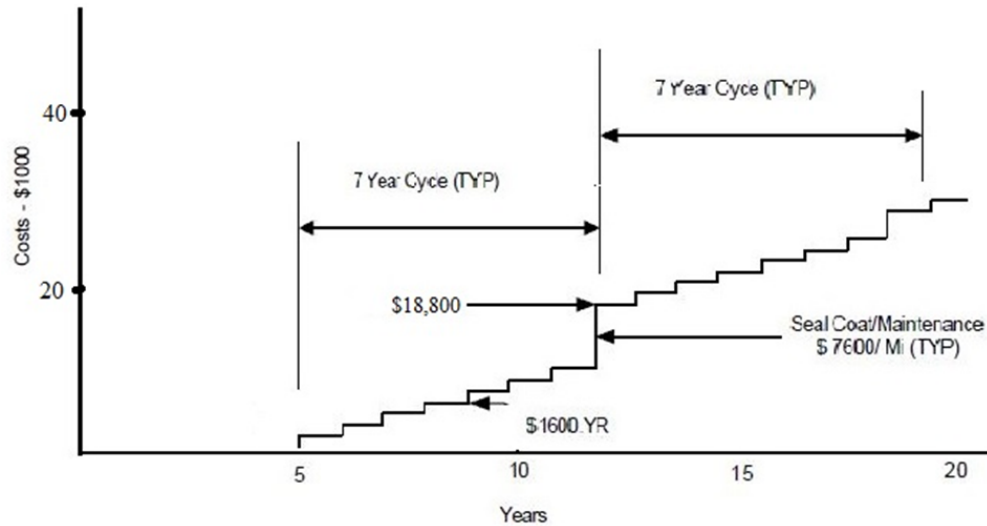


Figure 125. Maintenance/rehabilitation versus road life time

4.6.4 Calculation of Lifecycle Cost Analysis (LCCA)

According to performed cost analysis in sections 4.6.2 and 4.6.3, the life cycle cost analysis for each road type according to equation (30) is presented in this section. As mentioned before, geosynthetic reinforcement could both decrease the initial cost of construction of the pavement for same performance of a road and increase the life time of the pavement as well. The effect of benefits of geosynthetic reinforcement for each road section in this research is presented in this section. Section 0 is an unreinforced section, and the other sections are the reinforced sections including different variables of geosynthetic types, strengths, base thickness and geogrid locations. Table 32 presents the cost analysis of each section separately.

Table 32. Cost analysis of each section separately

Section	Initial construction cost (\$/mile)	Geogrid reinforcement cost (\$/mile)	GE gain factor (in.)	Initial construction cost by geogrid reinforcement (\$/mile)	Saving in initial construction cost by geogrid reinforcement (\$/mile)	Total savings in initial construction cost by including geogrid price (\$/mile)	Maintenance/rehabilitation costs (\$/mile)	TBR	Maintenance/rehabilitation costs with geogrid reinforcement (\$/mile)	Saving in maintenance/rehabilitation costs (\$/mile)	Total life cycle cost analysis (LCCA)	Total savings in construction and maintenance (\$/mile)	Total savings (%)
Section 0 3" Bituminous 10" Class 5 aggregate Subgrade	109,861	0	0.0	109,861	0	0	30,000	1	30,000	0	139,861	0	0
Section 1 3" Bituminous 10" Class 5 aggregate Biaxial light duty Subgrade	109,861	21,598	3.2	74,706	35,156	13,558	30,000	2.00	\$13,200	16,800	109,504	30,358	27.7
Section 2 3" Bituminous 10" Class 5 aggregate Biaxial heavy duty Subgrade	109,861	36,938	3.3	73,607	36,254	-684	30,000	2.04	\$13,090	16,910	123,635	16,226	13.1
Section 3 3" Bituminous 10" Class 5 aggregate Triaxial light duty Subgrade	109,861	34,124	3.3	73,607	36,254	2,130	30,000	2.04	\$13,090	16,910	120,822	19,040	15.8
Section 4 3" Bituminous 10" Class 5 aggregate Triaxial heavy duty Subgrade	109,861	111,462	3.5	71,410	38,451	-73,010	30,000	2.75	\$4,073	25,927	186,944	-47,083	-25.2
Section 5 3" Bituminous 10" Class 5 aggregate Biaxial light duty Subgrade	109,861	21,598	1.7	91,185	18,676	-2,921	30,000	2.01	13,172	16,828	125,955	13,907	11
Section 6 3" Bituminous 10" Class 5 aggregate Biaxial heavy duty Subgrade	109,861	36,938	1.8	90,086	19,775	-17,163	30,000	2.08	12,985	17,015	140,009	-147	-0.1

Section	Initial construction cost (\$/mile)	Geogrid reinforcement cost (\$/mile)	GE gain factor (in.)	Initial construction cost by geogrid reinforcement (\$/mile)	Saving in initial construction cost by geogrid reinforcement (\$/mile)	Total savings in initial construction cost by including geogrid price (\$/mile)	Maintenance/rehabilitation costs (\$/mile)	TBR	Maintenance/rehabilitation costs with geogrid reinforcement (\$/mile)	Saving in maintenance/rehabilitation costs (\$/mile)	Total life cycle cost analysis (LCCA)	Total savings in construction and maintenance (\$/mile)	Total savings (%)
Section 7 3" Bituminous 10" Class 5 aggregate Triaxial light duty Subgrade	109,861	34,124	3.2	74,706	35,156	1,031	30,000	2.12	12,883	17,117	121,713	18,148	14.9
Section 8 3" Bituminous 10" Class 5 aggregate Triaxial heavy duty Subgrade	109,861	111,462	3.4	72,509	37,353	-74,109	30,000	2.84	3,944	26,056	187,914	-48,053	-25.6
Section 9 3" Bituminous 6" Class 5 aggregate Biaxial light duty Subgrade	65,917	21,598	1.9	45,043	20,874	-724	30,000	3.12	3,590	26,410	70,231	25,686	36.6
Section 10 3" Bituminous 6" Class 5 aggregate Biaxial heavy duty Subgrade	65,917	36,938	2.0	43,945	21,972	-14,966	30,000	3.26	3,436	26,564	84,318	11,599	13.8
Section 11 3" Bituminous 6" Class 5 aggregate Triaxial light duty Subgrade	65,917	34124	2.1	42,846	23,071	-11,054	30,000	3.26	3,436	26,564	80,406	15,511	19.3
Section 12 3" Bituminous 6" Class 5 aggregate Triaxial heavy duty Subgrade	65,917	111,462	2.4	39,550	26,367	-85,095	30,000	4.45	2,517	27,483	153,529	-57,612	-37.5
Section 13 3" Bituminous 16" Class 5 aggregate Biaxial light duty Subgrade	175,778	21,598	6.9	99,974	75,804	54,207	30,000	1	30,000	0	151,572	54,207	35.8



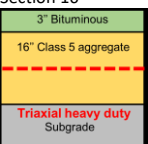
Section	Initial construction cost (\$/mile)	Geogrid reinforcement cost (\$/mile)	GE gain factor (in.)	Initial construction cost by geogrid reinforcement (\$/mile)	Saving in initial construction cost by geogrid reinforcement (\$/mile)	Total savings in initial construction cost by including geogrid price (\$/mile)	Maintenance/rehabilitation costs (\$/mile)	TBR	Maintenance/rehabilitation costs with geogrid reinforcement (\$/mile)	Saving in maintenance/rehabilitation costs (\$/mile)	Total life cycle cost analysis (LCCA)	Total savings in construction and maintenance (\$/mile)	Total savings (%)
Section 14 	175,778	36,938	7.2	96,678	79,100	42,162	30,000	1	30,000	0	163,616	42,162	25.8
Section 15 	175,778	34,124	7.8	90,086	85,692	51,567	30,000	1	30,000	0	154,211	51,567	33.4
Section 16 	175,778	111,462	8.0	87,889	87,889	-23,573	30,000	1	30,000	0	229,351	-23,573	-10.3

Table 32 shows the results from laboratory and field tests and finite element modeling of the 10-inch base course thickness sections. From the results in Table 32, it can be concluded that placing geosynthetic at the interface of the 10-inch base and subgrade layers can decrease the required base thickness of the pavement by an average of about 4 inches, which means the GE gain factor is about 4 inches. The minimum GE gain factor found in all the tests and simulations is 3.2 inches for the 10-inch base course reinforced at the interface. Geosynthetic reinforcement can also be incorporated into pavement design by assuming the average base resilient modulus gain factor (α) as two, which represents the lower bound of the test results. Also, geosynthetic reinforcement can prolong the service life of the pavement about two times that of unreinforced sections as indicated by the TRB factor. The results in Table 32 for geogrid placement at the center of the base course materials shows that the recommended GE gain factor for geogrids is about 2 inches but varies based on type and stiffness of geogrids. The average base resilient modulus gain factor (α) is about 1.5 and the TBR value will be about two times that of the unreinforced sections as well.

Table 32 shows the results for six inches of base course material with the geogrid placed at the interface of the base and the subgrade materials. The experimental and simulation results show that the GE gain factor is no more than 2 inches due to the required minimum thickness for the base layer. The average base resilient modulus gain factor (α) is about 1.4, also indicating a benefit of adding the geogrid to the base course. The TBR value in this case is always over three, indicating that the use of geosynthetic reinforcement with thin base course sections will significantly prolong the service life of the pavement.

Finally, Table 32 shows the results for 16 inches of base course material with the geogrid placed at the middle of the base course materials. The results in Table 32 reveal that the recommended GE gain factor for geogrids at the center of a thick base layer (16-in. base thickness) is about 6 inches due to the mechanism of geogrids in spreading stresses within the thick base layers. The average base resilient modulus gain factor (α) is more than 3, also indicative of the significant benefit of the geogrid to the system. The TBR value of one indicates that the same service life performance as unreinforced sections would be expected.

4.7 ENSAR SOFTWARE SIMULATION AND CALCULATION

The unreinforced section (section 0), light-duty biaxial geogrid reinforced section (section 1), and heavy-duty triaxial geogrid reinforced section (Section 4) from the field test were simulated by Tensar software to check, calibrate, and compare the software results to the results developed in this research. Details of assumptions in the calculations are included in the Appendix I.

4.7.1 Unreinforced Section

The length of road was assumed as 1 mile, AC thickness was 3 in., aggregate base course (ABC) thickness was 10 in., subgrade CBR strength was 3, AASHTO input parameters as reliability 95%, standard deviation 0.49, initial serviceability 4.2, terminal serviceability 2.0. the section of the pavement illustrated in Figure 126.

Unstabilized Pavement				
Layer	Di	ai	mi	SN
ACC1	3.00	0.420	N/A	1.260
ABC	10.00	0.140	1.0	1.400
Overall Structural Number (SN)				2.660
Calculated Traffic, ESALs				267,000

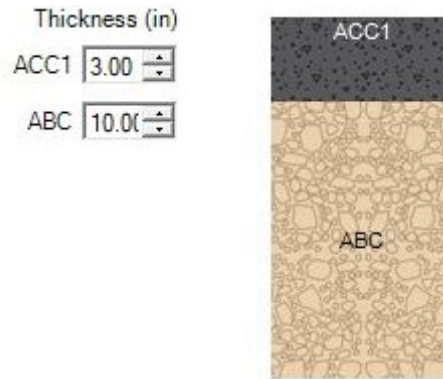


Figure 126. Unreinforced section

4.7.2 Section 1

This section has an aggregate MSL using triaxial heavy-duty geogrid BX1100 to provide mechanical stabilization reduced base thickness as 6.5 in. (GE as 3.5 in.) as recommended from results of this research geogrid located at the bottom of the base layer; the Section of the pavement illustrated in Figure 127.

Stabilized Pavement				
Layer	Di	ai	mi	SN
ACC1	3.00	0.420	N/A	1.260
MSL	6.80	0.254	1.0	1.727
Overall Structural Number (SN)				2.987
Calculated Traffic, ESALs				568,000

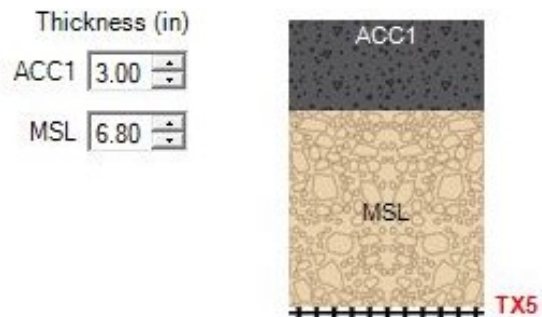
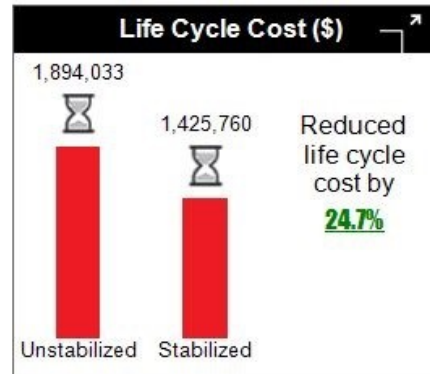
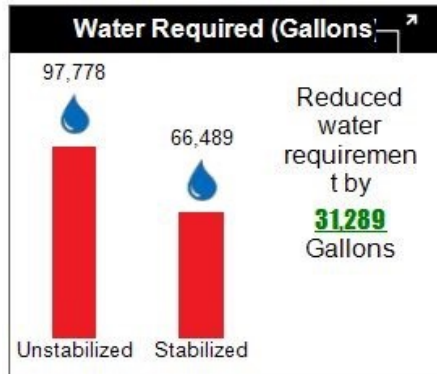
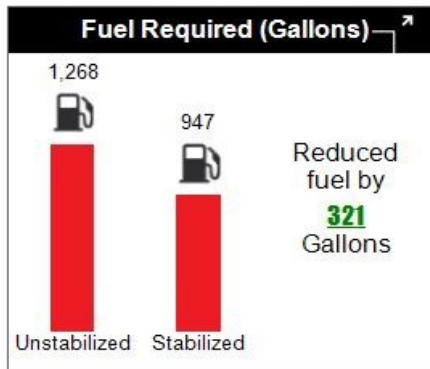
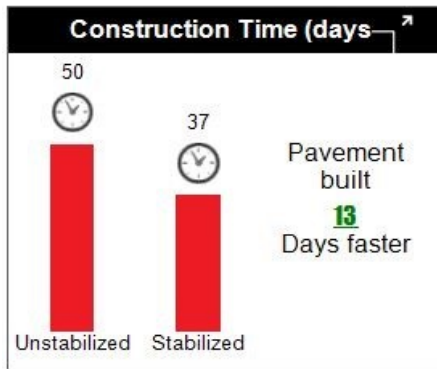
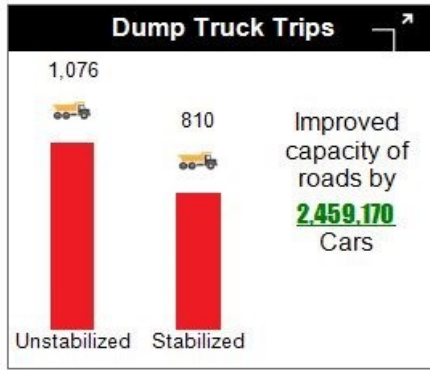


Figure 127. Section 1

Compared to the unreinforced section we will have these advantages as below in Figure 128.



Non-accounted impacts

- Carbon Emissions
- Safety
- Noise Pollution
- Effects on Local Business
- Utility Conflicts
- Public Inconvenience and Nuisance

Recommended resolution is 1920x1080 and scaling is 100% for the best viewing experience.

Figure 128. Section 1 comparison

It can be mentioned that by reinforcement of the section with geogrid BX1100 and then reduce base thickness as 6.5 in (GE as 3.5 in) as recommended from results of this research with geogrid located at the bottom of the base layer, the ESAL number will increase as 2 times (TBR as 2 for the same section thicknesses) consequently, the initial construction cost of the project decreases as 9%, and the life cycle cost reduced as 24.7% during the lifetime of the pavement. This reduction in our calculation in Table 32 was about 27.7%, which is very near to results of the Tensar software.

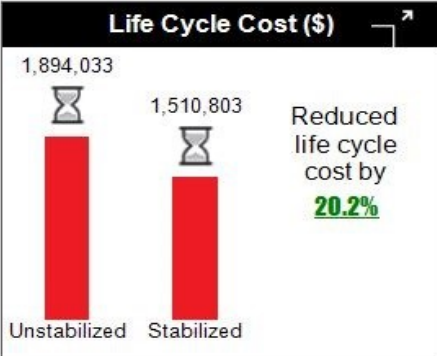
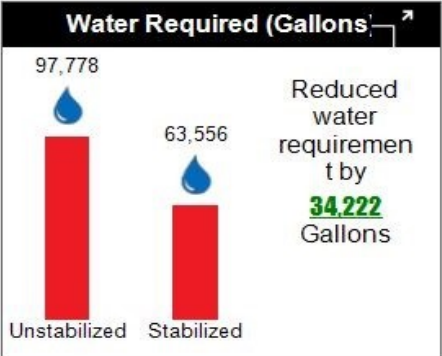
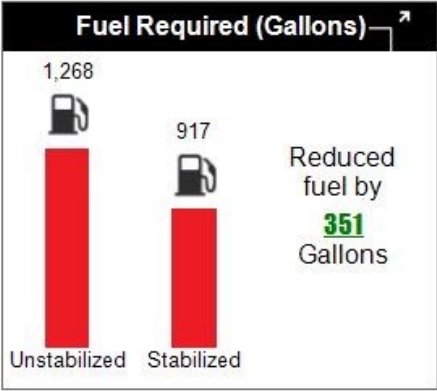
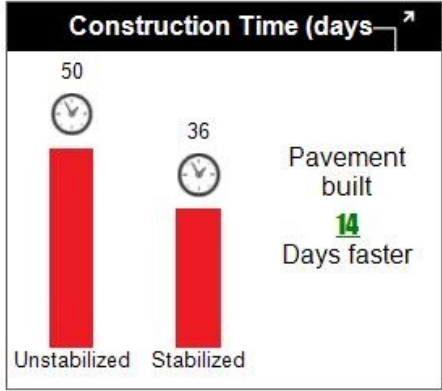
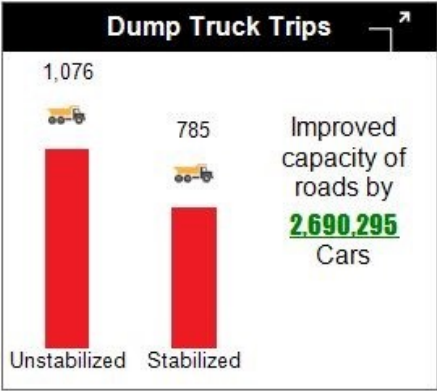
4.7.3 Section 4

This section’s MSL uses triaxial heavy-duty geogrid TX7 with a reduced base thickness as 6.5 in. (GE as 3.5 in.) as recommended from results of this research geogrid located at the bottom of the base layer; the section of the pavement illustrated in Figure 129.



Figure 129. Section 4

Compared to the unreinforced section we will have these advantages in Figure 130.



Non-accounted impacts

- Carbon Emissions
- Safety
- Noise Pollution
- Effects on Local Business
- Utility Conflicts
- Public Inconvenience and Nuisance

Recommended resolution is 1920x1080 and scaling is 100% for the best viewing experience

Figure 130. Section 4 comparison

It can be concluded that by reinforcement of the section with triaxial heavy-duty geogrid TX7 with reduced base thickness as 6.5 in. (GE as 3.5 in.) as recommended from results of this research with geogrid located at the bottom of the base layer, the ESAL number will increase as 2.75 times (TBR as 2.75 for the same section thicknesses). Although geosynthetic reinforcement increases the initial construction cost of the project as 16.6%, the life cycle cost reduced as 20.2% during the lifetime of the pavement. This section from our evaluation in the previous Table 32 is uneconomical at about 25%.

For Identifying additional design elements, construction practices, or maintenance strategies which could assist decision makers with improving the performance of its pavements, it can be mention that some of the additional design elements could mention the maintenance of the roads during t's lifetime and how we could postpone the required time for rehabilitation of the pavement as well. In this regard, geogrid reinforcement of pavement could increase the lifetime of the pavement and effect on the maintenance/rehabilitation cost of the pavement as well. Selecting of the appropriate (biaxial, triaxial, strength, and model of the geogrid, and so on) product of geogrid would help to save the budget of the construction and rehabilitation of the pavement according to the criteria of the selected pavement. It also could decrease producing the CO₂ from the trucks and equipment in the construction of the pavement, which could be an environmentally- friendly solution in the construction of the pavement as well.

Generally, geogrid reinforcement of the pavement could increase capacity roads by decreasing the dump truck trips, reduce water required for construction of the roads, decrease construction time of the reads, decrease fuel consumption required for construction of the pavement, decrease the cost of traffic delay during construction them by benefiting local economies, and finally reduce lifecycle cost as well.

CHAPTER 5: RESEARCH FINDINGS AND IMPLEMENTATION OF THE RESEARCH IN MNPAVE SOFTWARE

As mentioned before, in this report a series of large-scale laboratory tests, a full-scale experimental test plan, and the finite element method were conducted to determine the geogrids' effectiveness under various parameters. After plotting and comparing the results of performed investigations, a series of GE factors were presented in his study, which can be used by design engineers and industrial designers to include geogrids in their pavement designs. For design purposes, base resilient modulus gain factor (α) and calculated GE gain factor can be used in the MnPave software to increasing the resilient modulus of the base layer or decrease the thickness of base coarse aggregates in the pavement design for inclusion of the geosynthetic reinforcement in the pavement according to studied variables such as geosynthetic types, stiffness and locations.

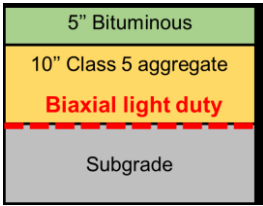
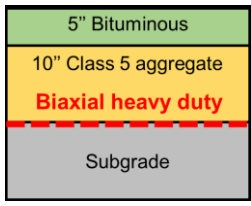
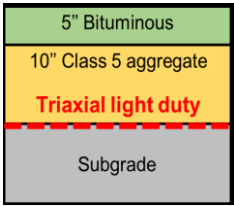
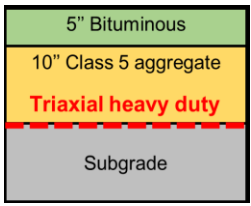
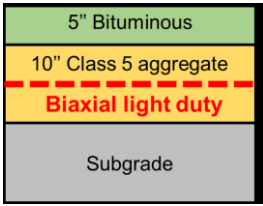
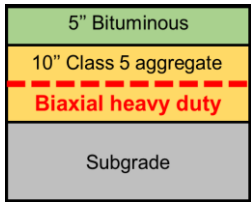
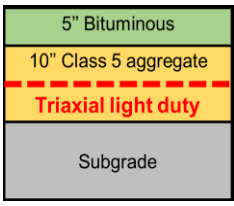
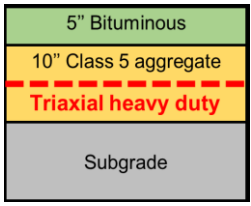
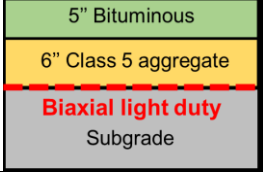

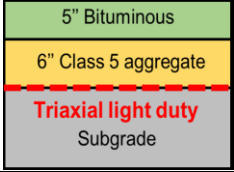
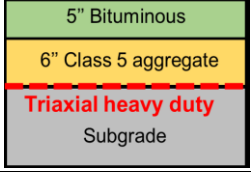
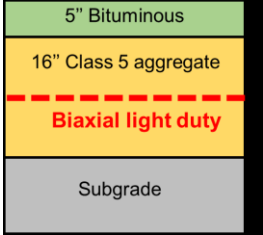
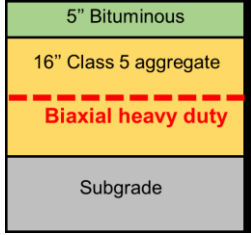
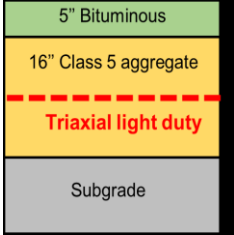
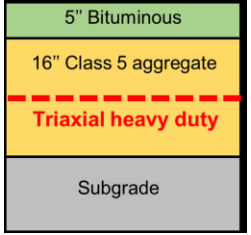
The materials evaluated in this report are geogrids. From the information gathered, it has given a design method detailed. The first recommendation given is that before deciding to use a geogrid reinforced pavement, project conditions are assessed and determine whether the favorable use of these materials.

Below is a step-by-step procedure will be detailed this design method. This task will also list the key steps that the Local Road Research Board and MnDOT could take to implement the research. The qualitative discussion includes how the incorporation of geogrid in MnPave would result in consistent in pavement structure design in Minnesota and better QA/QC testing of road systems. The key implementation steps include: (1) Using the accurate GE of geogrid in design, (2) Using geogrid gain factor to consider geogrid in MnPave

5.1.1 First Method of Implementation of Research Findings in Incorporation of Geogrid in MnPave

MnPave software could be used to design the road according to assumptions and specifications of the location and material of the designed road, then for the sake of incorporation of geogrid in pavement design, the calculated base thickness could be decreased according to the GE value mentioned in Table 33.

Table 33. GE gain factors for geogrid reinforced sections

				
Section	Section 1	Section 2	Section 3	Section 4
GE gain factor (in)	3.2	3.3	3.3	3.5
				
Section	Section 5	Section 6	Section 7	Section 8
GE gain factor (in)	1.7	1.8	3.2	3.4
				
Section	Section 9	Section 10	Section 11	Section 12
GE gain factor (in)	1.9	2.0	2.1	2.4
				
Section	Section 13	Section 14	Section 15	Section 16
GE gain factor (in)	6.9	7.2	7.8	8.0

The value of GE is different according to valuables assumed for the geogrids such as base thickness, geogrid type and stiffness, and geogrid location. The best case according to the road situation can be used and the final calculation of the road layer thickness can be revised based on the updated thickness for base course layer of geogrid reinforced section.

As can be seen in Table 33, when using 10 inches of Class 5 aggregate with the geogrid placed at the bottom of the aggregate, the GE gain factor varies from 3.2 to 3.5 inches, depending on the type of geogrid used, compared to the unreinforced case. Based on these results, using geogrids in the configuration shown in the first row (sections 1 to 4), a GE gain factor of 3 can be used. When the

geogrid is placed at the center of a 10-inch layer of Class 5 aggregate (sections 5 to 8), the results are less clear, with values of GE gain factor of 1.7 and 1.8 inches for biaxial geogrids, and 3.2 and 3.4 inches for triaxial geogrids. For this configuration, the GE gain factor will depend on the type of geogrid, 2 inches for biaxial geogrids and 3 inches for triaxial geogrids.

When using six inches of Class 5 aggregates and the geogrid placed at the interface of the aggregate and the subgrade (section 9 to 12), the GE gain factors range from 1.9 to 2.2 in. This indicates that when using geogrids in such configurations the Class 5 thickness can be reduced to four inches in combination with either biaxial or triaxial geogrids.

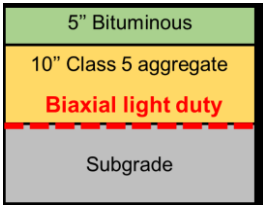
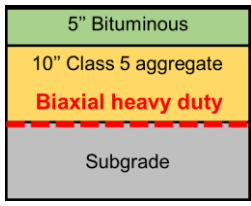
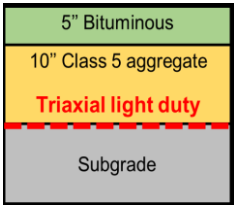
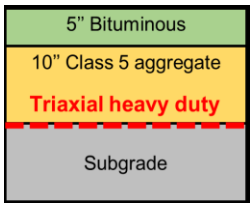
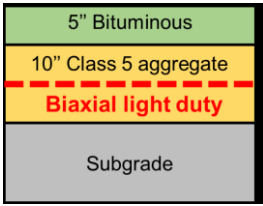
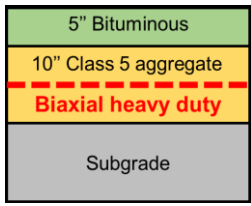
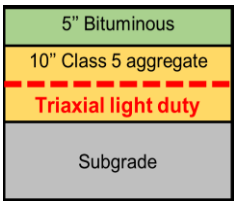
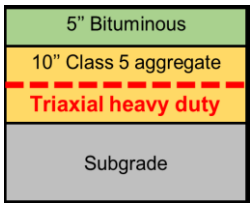
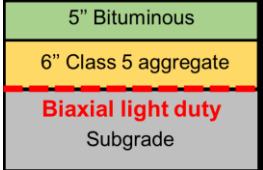
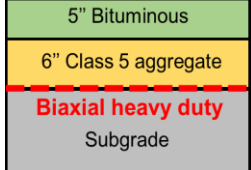
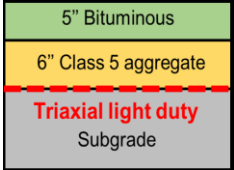
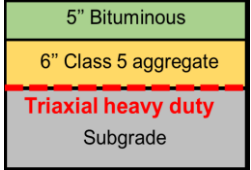
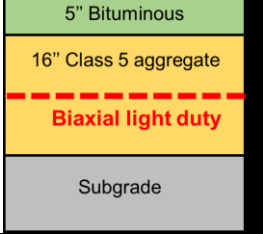
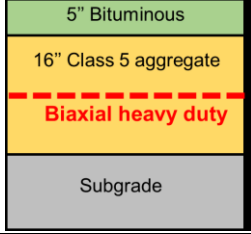
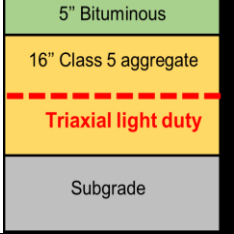
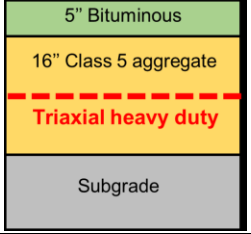
When using sixteen inches of Class 5 aggregates and the geogrid placed at the center of the aggregate (sections 13 to 16), the GE gain factors ranged from 6.9 to 8.0 in. The triaxial grids had higher GE gain factors indicating that the type of geogrid influences the system response.

The GE gain factors found in Table 33 can be used in conjunction with MnPave to reduce aggregate thicknesses for pavement section solutions from MnPave.

5.1.2 Second Method of Implementation of Research Findings in Incorporation of Geogrid in MnPave

A second way of incorporating geogrid effects into MnPave is suggested as a tentative alternative by using the geogrid resilient modulus gain factor (α), calculated by dividing the increased resilient modulus of reinforced sections over resilient modulus of the control section. This is achieved by multiplying the resilient modulus of the aggregate base by base resilient modulus gain factor for geogrid reinforced sections to account for the performance improvement due to the use of geogrids. The increased resilient modulus of an aggregate base can be input into MnPave to design geogrid in pavement structure and quantify geogrid's ability to reduce asphalt fatigue and rutting. The short-term and long-term geogrid base resilient modulus gain factors were determined in Task 6. The base resilient modulus gain factors to incorporate geogrids into MnPave for geogrid design are shown in Table 34.

Table 34. Base resilient modulus gain factor for geogrid reinforced sections

				
Section	Section 1	Section 2	Section 3	Section 4
Base resilient modulus gain factor (α)	1.92	1.93	1.92	1.94
				
Section	Section 5	Section 6	Section 7	Section 8
Base resilient modulus gain factor (α)	1.26	1.28	1.78	1.80
				
Section	Section 9	Section 10	Section 11	Section 12
Base resilient modulus gain factor (α)	1.38	1.39	1.39	1.41
				
Section	Section 13	Section 14	Section 15	Section 16
Base resilient modulus gain factor (α)	3.21	3.23	3.73	3.75

In practice, geosynthetic reinforcement effects can be illustrated by increasing the base resilient modulus of flexible pavement instead of decreasing the base thickness directly as shown on the first method above.

For design purposes, the resilient modulus gain factor (α) can be used in the MnPave software to increase the resilient modulus of the base layer in the pavement design for inclusion of the geosynthetic reinforcement in the pavement according to variables such as geosynthetic types, stiffness and locations.

Either the proposed GE gain factors or the resilient modulus gain factor (α) can be used by design engineers and industrial applications to incorporate geosynthetics in their pavement designs.

As can be seen in Table 34, when using 10 inches of Class 5 aggregate with the geogrid placed at the bottom of the aggregate (sections 1 to 4), the base resilient modulus gain factor varies from 1.92 to 1.94, a very narrow range, depending on the type of geogrid used, compared to the unreinforced case. This is a very narrow range and indicates a nearly two-fold increase in the base resilient modulus with the use of geogrid reinforcement. When the geogrid is placed at the center of a 10-in. layer of Class 5 aggregate (sections 5 to 8), the values of resilient modulus gain factor range from 1.26 to 1.28 for biaxial geogrids, and 1.78 to 1.80 for triaxial geogrids. Clearly the triaxial geogrids have a larger effect on the base course than the biaxial geogrids for this configuration.

When using 6 in. of Class 5 aggregates and the geogrid placed at the interface of the aggregate and the subgrade (section 9 to 12), the resilient modulus gain factors range from 1.38 to 1.41, again a very narrow band. For this configuration the use of either biaxial or triaxial geogrid and light or heavy-duty geogrid has similar effects on the resilient modulus.

When using 16 in. of Class 5 aggregates and the geogrid placed at the center of the aggregate (sections 13 to 16), the resilient modulus gain factors ranged from 3.21 to 3.75, substantial improvements in the base course resilient modulus values.

CHAPTER 6: CONCLUSIONS, KEY FINDINGS AND RECOMMENDATIONS

This is a comprehensive study including laboratory and field experiments plus numerical studies to evaluate the benefits of geosynthetic reinforcement of flexible pavement. This research fills gaps in research performed by previous researchers and has a strong literature review in the field of research. Researchers have found that the main appreciable improvement of geosynthetics reinforcement depends on various factors such as subgrade stiffness, base aggregate thickness and quality, hot mix asphalt thickness and quality, geogrid stiffness/location, and so on.

In this research, an IMAS, experimental APLTs, and finite element simulations were used to evaluate the reinforcement effects of geogrids. A total of eight test configurations constructed by varying geogrid types (i.e., light-duty biaxial, heavy-duty biaxial, light-duty triaxial, and heavy-duty triaxial geogrids), geogrid locations in base course (i.e., at the interface between base and subgrade or in the base course), and base aggregate thicknesses were used in the laboratory and field experimental tests to evaluate the reinforced base course behavior using different types of geogrids at different locations. The FEM models were calibrated based on the results of the laboratory and field tests and were used to determine GE values of an additional nine sections. The results of cyclic deformation, permanent deformation, elastic modulus, stiffness, resilient modulus, cyclic stresses, and the number of cycles calculated in real-time were presented. The GE factor was determined based on the results of the geosynthetic reinforced, and the unreinforced section was compared to obtain the GE factors based on the mentioned factors of reinforcements. The results of this report can be used by the designers to evaluate the geosynthetic reinforcement of flexible pavements in their designs.

A table of GE factors based on different parameters was presented in this report, based on the comparison of the results of the laboratory and field experimental tests plus the numerical studies. All of the calculated GE factors including GE gain factor laboratory, GE gain factor field, GE gain factor FE simulation, base resilient modulus gain factor (α), and related TBR are presented in Table 32. Table 32 also shows the cost analysis for each section. The geogrid benefits for the pavement structure can be incorporated into MnPave by using the geogrid gain factor and base resilient modulus gain factor (α). The MnPave software can be used to design a road according to conditions and specifications of the location and material of the designed road, then for the sake of incorporation of geogrid in pavement design, the calculated base thickness can be decreased according to the GE gain factor value shown in Tables 32 and 33. The value of GE gain varies according to assumed values for the geogrids such as base thickness, geogrid type and stiffness, and geogrid location, However, the subgrade stiffness in all test sections is the same with CBR of about 3%. The optimal case according to road conditions can be used, and the final calculation of the road layer thickness can be revised based on updated thickness for the base course layer of the geogrid reinforced section.

Alternately, the resilient modulus gain factor (α), calculated by dividing the increased resilient modulus of reinforced sections over resilient modulus of the control section is illustrated in Tables 32 and 34. For design purposes, the resilient modulus gain factor (α) can be used in the MnPave software to increase

the resilient modulus of the base layer in the pavement design to include the benefit of geosynthetic reinforcement in the pavement based on the studied variables such as geosynthetic types, stiffness, and geogrid locations. The proposed GE gain factors or resilient modulus gain factor (α) can be used by design engineers and industrial applications to incorporate geosynthetics into pavement designs.

The GE gain factor values developed from the literature review conducted for short-term and long-term tests are in excellent agreement with the values developed in this research. This provides corroboration that the GE gain factors determined in this study are reasonable.

By comparing an unreinforced section with a reinforced section from the results illustrated in Table 32, it can be calculated that reinforcement of the section with biaxial light-duty geogrid BX1100, reduced base thickness as calculated by the GE gain factor (GE as 3.5, 1.7, 1.9, and 6.9 in. for sections 1, 5, 9, and 13 respectively) as recommended from results of this research, and it can result in the greatest cost savings with an average of 27.8% more than an unreinforced section (cost saving as 27.7, 11, 36.6, and 35.8 in for sections 1, 5, 9, and 13 respectively). Light-duty biaxial at the interface of the thin base layer with 6 inches performed well due to the mechanism of geosynthetics in prolonging the service life of the pavement and decreasing the maintenance/rehabilitation of the pavement during their service lives. Also, biaxial light-duty geogrids at the center of thick base thicknesses could have a significant effect on decreasing the required base thickness and increasing the GE gain factor, consequently decreasing the initial construction cost of the pavement.

It was also found that triaxial high duty are not cost effective in any case. Based on the performed life-cycle cost analysis shown in Table 32, sections 4, 8, 12, and 16 with triaxial high duty have -25.2, -25.6, -37.5, and -10.3, respectively. That might be due to the high initial cost of preparing the high duty triaxial geogrids compared to other types and strengths of the geogrids.

6.1 CONCLUSIONS AND KEY FINDINGS

From analyzing the results of the studies described herein, the following conclusions and key findings are made:

- Geosynthetic reinforcement in flexible pavements can extend the service life of pavements by increasing the TBR factor; reducing the thickness of the base course layer with the same performance by increasing the BCR factor; developing the base course and subgrade stiffness by increasing their resilient modulus; having reinforcement effects on the base materials and decreasing base course layer thickness by increasing resilient modulus; having stabilization effects on the subgrade materials by decreasing permanent deformation on the top of subgrade; and providing better distribution of loads, delay rutting development, and increase the number of load repetitions until failure in pavement sections.
- Three main benefits of the application of geogrid reinforcement in flexible pavement are: aiding in the construction of pavements, especially over soft/wet subgrades; improving or extending the pavement's designed service life; and for a given service life, decreasing the thickness of pavement layer cross-sections (basically the base course layer).

- Many of the reviewed laboratory studies showed that marked reduction in surface deformation can be obtained by putting the geosynthetics at the interface position of the aggregate base course and subgrade layer for thin course base sections. This reduction increased with the stiffness of the geogrid. Also, it was observed that geogrid reinforcement of flexible pavement performed better than geotextile.
- Most of the experimental field studies discussed herein show that the location of geosynthetics, strength of geosynthetics, the aperture size of geogrid, base layer thickness, the strength of subgrade materials, and magnitude of enforcing traffic and loads have a significant effect on the performance of geosynthetic-reinforced flexible pavements.
- Placing the geosynthetic layer at the base and subgrade interface layer or within the base layer can significantly reduce permanent deformation (or rutting) and improve the performance of the subgrade and the base layers of flexible pavement sections.
- The results of the tests conducted show that geogrids can significantly improve the performance of pavement sections. These performances primarily are in terms of reducing the permanent surface deformation and extending the service life of the pavement sections.
- The strain gauges results illustrate that due to the base aggregate compaction, the residual strain in both triaxial and biaxial geogrid is about 1%; however, the amount for biaxial geogrids is slightly more than for triaxial geogrids.
- From the permanent deformation versus the number of loading cycles, it can be stated that geosynthetic reinforcement can significantly decrease permanent deformation of the sections. Generally, it seems that triaxial geogrids can be more beneficial than biaxial geogrids to decrease permanent deformation of the sections.
- The test sections with heavy-duty geogrid always had higher-pressure cell data than the light-duty. For example, under the same location, the maximum pressure in the section with the light-duty geogrid was 62 KPa; however, the maximum pressure in the section with the heavy-duty reached 103 KPa. This may be due to the heavy-duty geogrid having a higher stiffness than the light-duty geogrid, where the high-strength geogrid can provide more confinement. For the overall earth pressure cell results, the earth pressure cell data was increasing as the loading occurred, both in the subgrade and base course layer, but the increasing rate and magnitude were higher in the base course layer than the subgrade layer. This evidence supports that the geogrids can stabilize both the subgrade and the base course layer, but more so the base course.
- The average earth pressure cell data in triaxial geogrid tests was higher than the biaxial geogrid tests which means that the triaxial geogrid would have more effectiveness than the biaxial.
- A method using the back-calculation of the Mechanical-Empirical approach by using AASHTO's Pavement ME Design software was developed in this research and a series of GE factors presented. The proposed GE factors can be used for design engineers and industrial applications to incorporate geosynthetics in their pavement designs.

- The evaluation was based on the GE gain factors and designs developed using the MnPave application. The cost of geogrids and the cost of the reduced amount of aggregate base materials and asphalt materials was evaluated and compared. This research represents an establishment of a geogrid design criterion for incorporating geogrids in flexible pavement designs using the MnPave application, by validating the geogrid vendor's technical design information and by evaluating cost effectiveness of geogrids in different conditions.
- Geogrids can be incorporated into MnPave by using the geogrid gain factor. This is achieved by multiplying the resilient modulus of the aggregate base by the granular gain factor to account for the performance improvement due to the use of geogrids. The increased resilient modulus of an aggregate base can be input into MnPave to design geogrid in pavement structure and quantify the ability of geogrid to reduce asphalt fatigue and rutting. The short-term and long-term geogrid gain factors determined and used to incorporate geogrids into MnPave for geogrid design are shown in Table 32.

6.2 RECOMMENDATIONS

Based on the results of the studies described herein, including the cost analyses conducted, the following general recommendation for design and use of geogrids in flexible pavements sections are made:

Generally, it can be stated that triaxial geogrids especially with higher duty stiffnesses perform better than biaxial geogrids in decreasing permanent deformation of the sections and illustrate higher GE than biaxial geogrids; however, high duty triaxial geogrids are expensive and they are not economical to use in the pavements.

The best performance of geogrid reinforcement in a thick base section is illustrated when it is located at the center of the base layer; this can prolong service life of the pavement compared to locating the geogrid at the bottom of a thin base layer.

Biaxial light-duty and then triaxial light-duty are the most economical geogrids to use in the pavements unless the assumed economic condition at the time of this publication changes.

For typical road sections (10-inch base), light-duty biaxial and light-duty triaxial geogrids located at the bottom of the base layer are recommended.

For thin base layers, light-duty biaxial geogrids located at the bottom of base layer are recommended.

REFERENCES

- AASHTO. 1960. *Road User Benefit Analyses for Highway Improvements*. American Association of State Highway Officials, Committee on Planning and Design Policies, Washington, DC.
- AASHTO M 145-91. 1991. *Standard Specification for Classification of Soils and Soil-Aggregate Mixtures for Highway Construction Purposes*. American Association of State and Highway Transportation Officials, Washington, DC.
- AASHTO. 1993. *AASHTO Guide for Design of Pavement Structures*. American Association of State Highway and Transportation Officials, Washington, DC.
- AASHTO. 2001. American Association of State Highway and Transportation Officials, Washington, DC.
- Abu-Farsakh, M. Y., and M. Nazzal. 2009. *Evaluation of the Base/Subgrade Soil under Repeated Loading: Phase 1 – Laboratory Testing and Numerical Modeling of Geogrid Reinforced Bases in Flexible Pavement*. Louisiana Transportation Research Center, Louisiana State University, Baton Rouge, LA.
- Abu-Farsakh, M. Y., and Q. Chen. 2011. Evaluation of Geogrid Base Reinforcement in Flexible Pavement Using Cyclic Plate Load Testing. *International Journal of Pavement Engineering*, Vol. 12, No. 3, pp. 275–288.
- Abu-Farsakh, M. Y., and Q. Chen. 2012. *Evaluation of the Base/Subgrade Soil under Repeated Loading: Phase II–In-Box and ALF Cyclic Plate Load Tests*. Louisiana Transportation Research Center, Louisiana State University, Baton Rouge, LA.
- Abu-Farsakh, M., S. Hanandeh, L. Mohammad, and Q. Chen. 2016. Performance of Geosynthetic Reinforced/Stabilized Paved Roads Built Over Soft Soil Under Cyclic Plate Loads. *Geotextiles and Geomembranes*, Vol. 44, No. 6, pp. 845–853.
- Abu-Farsakh, M. Y., Q. Chen, and S. Hanandeh. 2019. *Accelerated Load Testing of Geosynthetic Base Reinforced/Stabilized Unpaved and Pavement Test Sections*. Louisiana Department of Transportation Research Center, Louisiana State University, Baton Rouge, LA.
- ACRP. 2019. Flexible Pavement Distresses (Project No. 09-11). Retrieved from <https://acrp-pavement-tool.tti.tamu.edu/browse-full-list.htm>
- Al-Qadi, I. L., T. L. Brandon, R. J. Valentine, B. A. Lacina, and T. E. Smith. 1994. Laboratory Evaluation of Geosynthetic-Reinforced Pavement Sections. *Transportation Research Record: Journal of the Transportation Research Board*, No. 1439, pp. 25–31.
- Alimohammadi, H. 2020. A Framework for Evaluation of Existing Pavement Conditions and Selection of Feasible Maintenance/Rehabilitation Alternatives; A Case Study in Some Routes of Livingston Parish in the State of Louisiana. *Springer Nature Applied Sciences*, Vol. 2, No. 289, pp. 1–13.

Alimohammadi, H., and M. Abu-Farsakh. 2019. Finite Element Parametric Study on Rutting Performance of Geosynthetic Reinforced Flexible Pavements. Paper presented at the 98th Annual Meeting of the Transportation Research Board, January 13–17, Washington, DC.

Alimohammadi, H., J. Zheng, V. R. Schaefer, J. Siekmeier, and R. Velasquez. 2020a. Evaluation of Geogrid Reinforcement of Flexible Pavement Performance: A Review of Large-Scale Laboratory Studies. *Transportation Geotechnics*, Vol. 27, March 2021. <https://doi.org/10.1016/j.trgeo.2020.100471>

Alimohammadi, H., J. Zheng, A. Buss, V. R. Schaefer, C. Williams, and G. Zheng. 2020b. Field and Simulated Rutting Behavior of Hot Mix and Warm Mix Asphalt Overlays. *Construction and Building Materials*, Vol. 265, pp. 1–9.

Alimohammadi, H., V. R. Schaefer, J. Zheng, and H. Li. 2020c. Performance Evaluation of Geosynthetic Reinforced Flexible Pavement: A Review of Full-Scale Field Studies. *International Journal of Pavement Research and Technology*, Vol. 14, pp. 30–42.

ARA, Inc. ERES Consultants Division. 2004. *Guide for Mechanistic-Empirical Design of New and Rehabilitated Pavement Structures*. National Cooperative Highway Research Program, Washington, DC.

ASTM. 2008. Determining the Aperture Stability Modulus of Geogrids (Standardization of ASM Test Method in Progress by ASTM. WK24635). ASTM International, West Conshohocken, PA.

Berg, R. R., and Associates. 1992. *Guidelines for Design, Specification, and Contracting of Geosynthetic Mechanically Stabilized Earth Slopes on Firm Foundations*. Industrial Fabrics Association International (IAFI), Geotextile Division, St. Paul, MN and Federal Highway Administration, Office of Technology Applications, Washington, DC.

Berg, R. R., B. R. Christopher, and S. Perkins. 2000. *Geosynthetic Reinforcement of the Aggregate Base/Subbase Courses of Pavement Structures* (GMA White Paper II, prepared for AASHTO Committee 4E). Geosynthetic Materials Association, Roseville, MN.

Buss, A. F. 2014. Investigation of Sustainable Pavement Technologies Evaluating Warm Mix Asphalt Using Recycled Asphalt Materials. PhD dissertation. Iowa State University, Ames, IA. Retrieved from <https://lib.dr.iastate.edu/etd/13652>.

Cancelli, A., and F. Montanelli. 1999. In-Ground Test for Geosynthetic Reinforced Flexible Paved Roads. Paper presented at the Geosynthetics '99: Specifying Geosynthetics and Developing Design Details, April 28–April 30, Boston, MA.

Cetin, B., S. Satvati, J. C. Ashlock, and C. Jahren. 2019. *Performance-Based Evaluation of Cost-Effective Aggregate Options for Granular Roadways*. Institute for Transportation, Iowa State University, Ames, IA. Retrieved from https://intrans.iastate.edu/app/uploads/2019/12/cost-effective_aggregate_options_for_granular_roadways_eval_w_cvr.pdf

- Ceylan, H., K. Gopalakrishnan, and S. Kim. 2009. *MEPDG Work Plan Task No. 5: Characterization of Unbound Materials (Soils/Aggregates) for Mechanistic-Empirical Pavement Design Guide*. Center for Transportation Research and Education, Institute for Transportation, Iowa State University, Ames, IA. Retrieved from https://intrans.iastate.edu/app/uploads/2018/03/MEPDG_task_5_w_cvr1.pdf
- Chiglo, J. M. 2013. Technical Memorandum No. 14-11-T-02. Minnesota Department of Transportation, Engineering Services Division, St. Paul, MN.
- Cuelho, E. V., and S. W. Perkins. 2017. Geosynthetic Subgrade Stabilization – Field Testing and Design Method Calibration. *Transportation Geotechnics*, Vol. 10, pp. 22–34.
- Dafalias, Y. F. 1986. Bounding Surface Plasticity. I: Mathematical Foundation and Hypoplasticity. *Journal of Engineering Mechanics*, Vol. 112, No. 9, pp. 966–987.
- FHWA. 2019. *FHWA FY 2019 Budget and Summary Overview*. Federal Highway Administration, Washington, DC. Retrieved from <https://www.fhwa.dot.gov/cfo/fhwa-fy-2019-cj-final.pdf>
- Fredrickson, F. C., P. J. Diethelm, and D. M. Zwiers. 1970. Minnesota Department of Highways Flexible Pavement Design–1969. *Highway Research Record*, No. 329, pp. 55–64.
- Ghafoori, N., and M. Sharbaf. 2016. *Use of GEOGRID for Strengthening and Reducing the Roadway Structural Sections*. Nevada Department of Transportation, Carson City, NV.
- Gu, F., X. Luo, R. Luo, R. L. Lytton, E. Y. Hajj, and R. V. Siddharthan. 2016a. Numerical Modeling of Geogrid-Reinforced Flexible Pavement and Corresponding Validation Using Large-Scale Tank Test. *Construction and Building Materials*, Vol. 122, pp. 214–230.
- Gu, F., Y. Zhang, C. V. Drodody, R., and R. L. Lytton. 2016b. Development of a New Mechanistic Empirical Rutting Model for Unbound Granular Material. *Journal of Materials in Civil Engineering*, Vol. 28, No. 8.
- Gu, F., X. Luo, R. Luo, E. Y. Hajj, and R. L. Lytton. 2017. A Mechanistic-Empirical Approach to Quantify the Influence of Geogrid on the Performance of Flexible Pavement Structures. *Transportation Geotechnics*, Vol. 13, pp. 69–80.
- Haas, R., J. Walls, and R. G. Carroll. 1988. Geogrid Reinforcement of Granular Bases in Flexible Pavements. *Transportation Research Record: Journal of the Transportation Research Board*, No. 1188, pp. 19–27.
- Hanandeh, S. 2016. Performance Evaluation of Instrumented Geosynthetics Reinforced Paved Test Sections Built Over Weak Subgrade Using Accelerated Load Testing (PhD dissertation). Louisiana State University, Baton Rouge, LA.
- Hanandeh, S., M. Y. Abu-Farsakh, L. N. Mohammad, Q. Chen, and M. Saghebfar. 2016. *Full-Scale Accelerated Load Testing of Geosynthetics Reinforced/Stabilized Paved Roads Built Over Native Soft Subgrade*. Paper presented at the GeoAmericas, 3rd Pan-American Conference on Geosynthetics, April 10–13, Miami, FL.

- Holtz, R. D., B. R. Christopher, and R. R. Berg. 1998. *Geosynthetic Design and Construction Guidelines*. FHWA-HRT-17-080. Federal Highway Administration, Washington, DC.
- Hossain, M. S., and B. N. Schmidt. 2009. *Benefits of Using Geotextile Between Subgrade Soil and Base Course Aggregate in Low-Volume Roads in Virginia*. Virginia Transportation Research Council, Charlottesville, VA.
- Huang, Y. H. 1993. *Pavement Analysis and Design*. Prentice Hall College Division, New York, NY.
- Ibrahim, E. M., S. M. El-Badawy, M. H. Ibrahim, A. Gabr, and A. Azam. 2017. Effect of Geogrid Reinforcement on Flexible Pavements. *Innovative Infrastructure Solutions*, Vol. 2, Article No. 54. <https://doi.org/10.1007/s41062-017-0102-7>
- Ingle, G. S., and S. S. Bhosale. 2017. Geosynthetics Reinforced Flexible Pavement: Review of Laboratory Model Studies. *International Journal of Engineering and Technology*, Vol. 6, No. 4, pp. 103–107.
- Khajehvand, M., A. A. Rassafi, and B. Mirbaha. 2021. Modeling Traffic Noise Level Near at-Grade Junctions: Roundabouts, T, and Cross Intersections. *Transportation Research Part D: Transport and Environment*. Vol. 93, No. 102752.
- Kim, M., and J. H. Lee. 2013. Effects of Geogrid Reinforcement in Low Volume Flexible Pavement. *Journal of Civil Engineering and Management*, Vol. 19, No. 1, pp. S14–S22.
- Koerner, R. M. 1997. *Designing with Geosynthetics*. Prentice Hall College Division, New York, NY.
- Leng, J., and M. A. Gabr. 2002. Characteristics of Geogrid-Reinforced Aggregate Under Cyclic Load. *Transportation Research Record: Journal of the Transportation Research Board*, No. 1786, pp. 29–35.
- Ling, H. I., and Z. Liu. 2001. Performance of Geosynthetic-Reinforced Asphalt Pavements. *Journal of Geotechnical and Geoenvironmental Engineering*, Vol. 127, No. 2, pp. 99–102.
- Lukanen, E. O. 1980. *Application of AASHTO Road Test Results to Design of Flexible Pavement in Minnesota*. Minnesota Department of Transportation, St. Paul, MN.
- Luo, R., F. Gu, X. Luo, R. L. Lytton, E. Y. Hajj, R. V. Siddharthan, S. Elfass, M. Piratheepan, and S. Pournoman. 2017. *NCHRP Web-Only Document 235: Quantifying the Influence of Geosynthetics on Pavement Performance*. National Cooperative Highway Research Program, Washington, DC.
- Mahaffay, B., J. Robinson, J. Gagnon, and G. Norwood. 2019. Using Geosynthetics in Flexible Airport Pavements. *Geosynthetics Magazine*. Retrieved from <https://geosyntheticsmagazine.com/2019/06/01/using-geosynthetics-in-flexible-airport-pavements/>
- Mallela, J., L. T. Glover, M. I. Darter, H. L. Von Quintus, A. Gotlif, M. Stanley, and S. Sadasivam. 2009. *Guidelines for Implementing NCHRP 1-37A M-E Design Procedures in Ohio: Volume 1— Summary of Findings, Implementation Plan, and Next Steps*. Ohio Department of Transportation Research and Development, Columbus, OH.

Maxwell, S., W.-H. Kim, C. H. Benson, and T. Edil. 2005. *Effectiveness of Geosynthetics in Stabilizing Soft Subgrades*. University of Wisconsin-Madison, WI.

Minnesota Department of Labor and Industry. 2021. Prevailing Wage: Region 7 Minimum Truck Rental Rates. Retrieved from <http://www.dli.mn.gov/business/employment-practices/prevailing-wage-region-7-minimum-truck-rental-rates>

MnDOT. 1996. *Pavement Manual*. Minnesota Department of Transportation, St. Paul, MN.

TONN2010. 2010. Pavement Design, TONN2010 Manual Installation. Retrieved from <https://www.dot.state.mn.us/materials/pvmtdesign/tonn2010.html>

Sweeney, M. 2012. *Articulating Wheel Loader Price Schedule*. Minnesota Department of Transportation, St. Paul, MN. Retrieved from <http://www.dot.state.mn.us/maintenance/pdf/loader/Nuss/Volvo L150G.pdf>

Labor Compliance. 2020a. Labor Compliance, Overtime Requirements. Retrieved from <https://www.dot.state.mn.us/const/labor/overtime.html>

Fahey S. 2020b. *Exhibit D: Price Schedule Motor Graders Fixed Pricing-Options Specification 4.0*. Minnesota Department of Transportation, St. Paul, MN.

Mitchell, J. K., T.-C. Kao, and E. Kavazanjian, Jr. 1979. *Analysis of Grid Cell Reinforced Pavement Bases* (Report No. GL-79-8). U.S. Army Engineer Waterways Experiment Station Geotechnical Laboratory, Vicksburg, MS.

Moghaddas-Nejad, F., and J. C. Small. 1996. Effect of Geogrid Reinforcement in Model Track Tests on Pavements *Journal of Transportation Engineering*, Vol. 122, No. 6, pp. 468–474.

Mousavi, S. H. 2016. Experimental and Numerical Investigation of the Performance of Geosynthetics-Reinforced Unsaturated Subgrade Soils under Cyclic Loading. PhD dissertation. North Carolina State University, Raleigh, NC.

Nair, A. M., and G. M. Latha. 2016. Repeated Load Tests on Geosynthetic Reinforced Unpaved Road Sections. *Geomechanics and Geoengineering*, Vol. 11, No. 2, pp. 95–103.

Nazzal, M. D. 2007. Laboratory Characterization and Numerical Modeling of Geogrid Reinforced Bases in Flexible Pavements (PhD dissertation). Louisiana State University, Baton Rouge, LA.

Palmeira, E. M., and I. A. G. Góngora. 2016. Assessing the Influence of Some Soil–Reinforcement Interaction Parameters on the Performance of a Low Fill on Compressible Subgrade. Part I: Fill Performance and Relevance of Interaction Parameters. *International Journal of Geosynthetics and Ground Engineering*, Vol. 2, Article No. 1, pp. 1–17.

Paramount Materials. 2021. Tensar Geogrid Fabric. Retrieved from <https://www.paramountmaterials.com/collections/tensar-geogrid-fabric>

- Paterson, W. D. O., and T. Scullion. 1990. *Information Systems for Road Management: Draft Guidelines on System Design and Data Issues*. The World Bank Infrastructure and Urban Development Department, Washington, DC.
- Penner, R. 1985. Geogrid Reinforcement of the Granular Base Layer in Conventional Three-Layer Pavement Sections (Master's thesis). University of Waterloo, ON.
- Perkins, S. W. 1999. *Geosynthetic Reinforcement of Flexible Pavements: Laboratory Based Pavement Test Sections*. Western Transportation Institute, Montana State University, Bozeman, MT.
- Perkins, S. W. 2001. *Numerical Modeling of Geosynthetic Reinforced Flexible Pavements*. Montana Department of Transportation, Helena, MT.
- Perkins, S. W. 2002. *Evaluation of Geosynthetic Reinforced Flexible Pavement Systems Using Two Pavement Test Facilities*. Western Transportation Institute, Montana State University, Bozeman, MT.
- Perkins, S. W., and E. V. Cuelho. 1999. Soil-Geosynthetic Interface Strength and Stiffness Relationships from Pullout Tests. *Geosynthetics International*, Vol. 6, No. 5, pp. 321–346.
- Perkins, S. W., and M. Ismeik. 1997. A Synthesis and Evaluation of Geosynthetic-Reinforced Base Layers in Flexible Pavements: Part I. *Geosynthetics International*, Vol. 4, No. 6, pp. 549–604.
- Perkins, S. W., B. R. Christopher, E. L. Cuelho, G. R. Eiksund, I. Hoff, C. W. Schwartz, G. Svano, and A. Watn. 2004. *Development of Design Methods for Geosynthetic Reinforced Flexible Pavements*. Western Transportation Institute, Montana State University, Bozeman, MT.
- Perkins, S. W., B. R. Christopher, E. L. Cuelho, G. R. Eiksund, C. W. Schwartz, and G. Svano. 2009. A Mechanistic-Empirical Model for Base-Reinforced Flexible Pavements. *International Journal of Pavement Engineering*, Vol. 10, No. 2, pp. 101–114.
- Propex®. 2019. The Best Geosynthetic for Pavement Separation/Stabilization. *Civil + Structural Engineer magazine*. Retrieved from <https://cseengineermag.com/the-best-geosynthetic-for-pavement-separation-stabilization/>
- Qian, Y., J. Han, S. K. Pokharel, and R. L. Parsons. 2013. Performance of Triangular Aperture Geogrid-Reinforced Base Courses over Weak Subgrade under Cyclic Loading. *Journal of Materials in Civil Engineering*, Vol. 25, No. 8, pp. 1013–1021.
- Rahmani, M., Y. Kim, and J. Jung. 2020. Mechanistic Analysis of Pavement Damage and Performance Prediction Based on Finite Element Modeling with Viscoelasticity and Fracture of Mixtures. *LHI Journal of Land, Housing, and Urban Affairs*, Vol. 11, No. 2, pp. 95–104.
- Rajagopal, K., S. Chandramouli, A. Parayil, and K. Iniyan. 2014. Studies on Geosynthetic-Reinforced Road Pavement Structures. *International Journal of Geotechnical Engineering*, Vol. 8, No. 3, pp. 287–298.

- Reck, N. C. 2009. *Mechanistic-Empirical Design of Geogrid Reinforced Paved Flexible Pavements*. Paper presented at the 2009 Geogrid Jubilee Symposium, September 8, London, England. Retrieved from <https://www.jubilee-symposium.co.uk/-/media/Files/Jubilee/Pdf/Proceedings/9Reck.ashx?la=en>
- Robinson, W. J., B. J. Mahaffay, I. L. Howard, and G. J. Norwood. 2019. Cyclic Plate Testing of Geosynthetic-Reinforced Airfield Pavements. *Proceedings of the Institution of Civil Engineers - Ground Improvement*, Vol. 172, No. 4, pp. 229–243.
- Sævarsdóttir, Þ. 2014. Performance Modelling of Flexible Pavements Tested in a Heavy Vehicle Simulator (PhD dissertation). University of Iceland, Reykjavik.
- Saghebfar, M., M. Hossain, and B. A. Lacina. 2016. Performance of Geotextile-Reinforced Bases for Paved Roads. *Transportation Research Record: Journal of the Transportation Research Board*, No. 2580, pp. 27–33.
- Siekmeier, J. 2018. *Performance Specification for Geogrid Reinforced Aggregate*. Minnesota Department of Transportation, St. Paul, MN.
- Siekmeier, J., and J. Casanova. 2016. *Geogrid Reinforced Aggregate Base Stiffness for Mechanistic Pavement Design*. Minnesota Department of Transportation, St. Paul, MN.
- Tang, X., M. Y. Abu-Farsakh, S. Hanandeh, and Q. Chen. 2014. *Use of Geosynthetics for Reinforcing/Stabilizing Unpaved Roads under Full-Scale Truck Axle Loads*. Shale Energy Engineering Conference 2014, July 21–23, Pittsburgh, PA.
- Tranquist, B. 2019. *MnPAVE Flexible - Odemark's Equivalent Thickness Method*. Minnesota Department of Transportation, Office of Materials and Road Research, Maplewood, MN. Retrieved from https://edocs-public.dot.state.mn.us/edocs_public/DMResultSet/download?docId=12278570
- Walls, J., III, and M. R. Smith. 1998. *Life-Cycle Cost Analysis in Pavement Design: Pavement Division Interim Technical Bulletin (FHWA-SA-98-079)*. Federal Highway Administration, Washington, DC.
- Webster, S. L. 1993. *Geogrid Reinforced Base Courses for Flexible Pavements for Light Aircraft: Test Section Construction, Behavior under Traffic, Laboratory Tests, and Design Criteria*. U.S. Army Corps of Engineers, Waterways Experiment Station, Vicksburg, MS.
- Wilde, W. J., S. Waalkes, and R. Harrison. 1999. *Life Cycle Cost Analysis of Portland Cement Concrete Pavements*. Center for Transportation Research, University of Texas at Austin, TX.
- Wu, Z., X. Chen, and X. Yang. 2011. *Finite Element Simulation of Structural Performance on Flexible Pavements with Stabilized Base/Treated Subbase Materials under Accelerated Loading*. Louisiana Transportation Research Center, Louisiana State University, Baton Rouge, LA.
- Zadehmohamad, M., and J. Bolouri Bazaz. 2019. Cyclic Behavior of Geocell-Reinforced Backfill behind Integral Bridge Abutment. *International Journal of Geotechnical Engineering*, Vol. 13, No. 5, pp. 438–450.

Zornberg, J. G. 2011. Advances in the Use of Geosynthetics in Pavement Design. Keynote Paper *Proceedings of the Second National Conference on Geosynthetics, Geosynthetics India '11*, September 23–24, Chennai, India, Vol. 1, pp. 3–21.

Zornberg, J. G. 2017. Functions and Applications of Geosynthetics in Roadways. *Procedia Engineering*, Vol. 189, pp. 298–306.

Zornberg, J. G., and R. Gupta. 2010. Geosynthetics in Pavements: North American Contributions. Theme Speaker Lecture. *Proceedings of the 9th International Conference on Geosynthetics: Advanced Solutions for a Challenging World*, May 22–28, Guarujá, Brazil, Vol. 1, pp. 379–400.

Zornberg, J. G., J. Prozzi, R. Gupta, R. Luo, J. S. McCartney, J. Z. Ferreira, and C. Nogueira. 2008. *Validating Mechanisms in Geosynthetic Reinforced Pavements*. Center for Transportation Research, University of Texas at Austin, TX.